ISTANBUL TECHNICAL UNIVERSITY ★ GRADUATE SCHOOL OF SCIENCE ENGINEERING AND TECHNOLOGY

DYNAMIC AND AEROELASTIC ANALYSIS OF A HELICOPTER BLADE WITH AN ACTIVELY CONTROLLED TRAILING EDGE FLAP IN FORWARD FLIGHT

Ph.D. THESIS

Özge ÖZDEMİR ÖZGÜMÜŞ

Department of Aeronautical and Aerospace Engineering

Aeronautical and Aerospace Engineering Programme

Anabilim Dalı : **Herhangi Mühendislik, Bilim**
Programı : **Herhangi Program**

MAY 2012

ISTANBUL TECHNICAL UNIVERSITY ★ GRADUATE SCHOOL OF SCIENCE ENGINEERING AND TECHNOLOGY

DYNAMIC AND AEROELASTIC ANALYSIS OF A HELICOPTER BLADE WITH AN ACTIVELY CONTROLLED TRAILING EDGE FLAP IN FORWARD FLIGHT

Ph.D. THESIS

Özge ÖZDEMİR ÖZGÜMÜŞ
(511052012)

Department of Aeronautical and Aerospace Engineering

Aeronautical and Aerospace Engineering Programme

Thesis Advisor: Prof. Dr. Metin Orhan KAYA
Anabilim Dalı : Herhangi Mühendislik, Bilim
Programı : Herhangi Program

MAY 2012

İSTANBUL TEKNİK ÜNİVERSİTESİ ★ FEN BİLİMLERİ ENSTİTÜSÜ

AKTİF OLARAK KONTROL EDİLEN FİRAR KENARI FLABINA SAHİP BİR HELİKOPTER PALİNİN İLERİ UÇUŞ ŞARTLARI ALTINDA DİNAMİK VE AEROELASTİK İNCELEMESİ

DOKTORA TEZİ

Özge ÖZDEMİR ÖZGÜMÜŞ
(511052012)

Uçak ve Uzay Mühendisliği Anabilim Dalı

Uçak ve Uzay Mühendisliği Programı

Tez Danışmanı: Prof. Dr. Metin Orhan KAYA
Anabilim Dalı : Herhangi Mühendislik, Bilim
Programı : Herhangi Program

MAYIS 2012

Özge Özdemir Özgümüş, **a Ph.D.** student of ITU **Institute of Engineering Science** student ID 511052012, successfully defended the **dissertation** entitled "**DYNAMIC AND AEROELASTIC ANALYSIS OF A HELICOPTER BLADE WITH AN ACTIVELY CONTROLLED TRAILING EDGE FLAP IN FORWARD FLIGHT**", which she prepared after fulfilling the requirements specified in the associated legislations, before the jury whose signatures are below

Thesis Advisor : Prof. Dr. Metin Orhan KAYA
Istanbul Technical University

Jury Members : Prof. Dr. İbrahim ÖZKOL..
Istanbul Technical University

Prof. Dr. Ata MUĞAN..
Istanbul Technical University

Prof. Dr. Erol UZAL..
Istanbul University

Assoc.Prof. Dr. Serdar BARIŞ...
Istanbul University

Date of Submission : 21 February 2012
Date of Defense : 7 May 2012

To my lovely little daughter Defne Zeynep ÖZGÜMÜŞ who has brought cheer, happiness and patience to our lives.…

FOREWORD

First and foremost, I would like to express my sincere thanks to my dissertation advisor, Prof. Dr. Metin O. Kaya for his continuous guidance and endless patience during my studies. He has always been near to support me and to lead me to the right way with his deep knowledge of beam theories, vibration and aeroelasticity. Besides being an advisor, he has been a good friend with whom I can share and discuss my ideas about life. I learnt from him that patience is the most powerful way to reach success. This work would not have been possible without all the insightful discussions with him.

I would like to thank to Prof. Dr. Dewey Hodges fromthe School of Aerospace Engineering, Georgia Institute of Technology. During my studies in Georgia Institute of Technology, he was an excellent advisor for me. He helped me a lot on defining the title of my dissertation through long discussions and he shared his deepknowledge on helicopters, aeroelasticity and beam theories with me without any hesitation. Additionally, he and his beloved wife Margaret opened the doors of their house and make me feel home when I am away from my family.

I thank my committee members, Prof.Dr. İbrahim Özkol, Prof.Dr. Ata Muğan, Prof.Dr. Erol Uzal, Prof.Dr. Yavuz Yaman and Assoc.Prof.Dr. Serdar Barış for taking their time to read and evaluate my thesis. Their valuable ideas and enlightening suggestions were essential in improving the quality of this work.

I thank to Prof. Dr. Zahit Mecitoğlu who shared his deep knowledge of finite element methods with me and who gave me very useful ideas that keep my finite element studies go on.

I also would like to thank to my friend, Seher Durmaz for her valuable academic and moral support and to Namık Kemal Alpaydın from Rotorcraft Center of Excellence (ROTAM) for his valuable technical assistance.

I wish to express my thankfulness to the Scientific and Technological Research Council of Turkey (TUBITAK) for supporting my dissertation in Istanbul Technical University, Turkey and my academic studies in Georgia Institute of Technology, USA under the National Scholarship Programmes for Ph.D. Student.

Above all, I would like to express my gratitude to my dear husband, Emrah Özgümüş for his love, patience and support during this research work. He has always been there to calm me down. Moreover, I want to express my deepest respect and gratefulness to my beloved parents Asuman and Sezgin Özdemir for their loveand unbelievable patience. I also want to thank to my dear brother, Özgür Özdemir who has always been a very good friend and a very good listener for me. Lastly, but most importantly I want to express my deepest love for my little daughter, Defne ZeynepÖzgümüş. This work is dedicated to this adorable, little girl who has given me strength and determination with a cute smile on her beautiful face.

May 2012 Özge ÖZDEMİR ÖZGÜMÜŞ

TABLE OF CONTENTS

ABBREVIATIONS

ACSR	**:**Active Control of Structural Response
ACF	**:** Actively Controlled Flap
AFC	**:** Active Fiber Composite
ATR	**:** Active Twist Rotors
cg	**:** Center of gravity
DTM	**:** Differential Transform Method
HHC	**:** Higher Harmonic Control
IBC	**:** Individual Blade Control
LE	**:** Leading edge
MFC	**:** Macro Fiber Composite
MS	**:** Magnetostrictive
PVDF	**:** Polyvinylidine Fluoride
PZT	**:** Lead Zirconate Titanate
SMA	**:** Smart Memory Alloy
App	**:** Appendix

LIST OF TABLES

LIST OF FIGURES

DYNAMIC AND AEROELASTIC ANALYSIS OF A HELICOPTER BLADE WITH ACTIVELY CONTROLLED TRAILING EDGE FLAP IN FORWARD FLIGHT

SUMMARY

The main focus of the present research is on the development of a computer code that carries out the dynamic and aeroelastic analysis of a hingeless helicopter blade under hover and forward flight conditions. The blade has a trailing edge flap to reduce blade vibration and the flap mechanism is actuated by a piezoelectric bender type actuator that is connected to the flap by a linkage arm.

The present dissertation is organised in four main sections, i.e. introduction part, structural formulation, aerodynamic formulation and aeroelastic formulation.

In the introduction part, information is given about smart structures, smart materials, rotor types, rotor aerodynamic environment, rotor vibration control techniques, smart rotors, and actuators. Additionally, blade and actuator types that are preferred in this research are introduced and objectives of the dissertation are mentioned about. Moreover, a brief literature review is given. The aim of the *Introduction*section is to introduce smart structures, vibration reduction techniques, helicopter rotor systems, etc. to the reader so it is going to be easier and more meaningful for the reader to understand all the derivations carried out in the following sections.

In the first part of the structural formulation, some information is given about the mechanics of a piezolaminated beam and expressions of the mechanical and the electrical loads that act on this beam model are derived in detail. The resulting expressions of this subsection are used in the analytical formulation of the bender type piezoelectric actuator. In the second part of the structural formulation, analytical beam models are developed both for the piezoelectric actuator and for the helicopter blade, seperately. Since the actuator is modeled as a short beam, Timoshenko beam theory is used for the actuator while Euler-Bernoulli beam theory is used for the helicopter blade that is modeled as a long, slender beam. Both the bender type actuator and the hingeless blade are modeled as cantilever beams that have fixed-free end conditions. Related strain fields and the energy expressions are derived step by step by introducing several explanatory tables and figures. Afterwards, Hamilton's principle is applied to these energy expressions to obtain the governing differential equations of motion and the boundary conditions. An efficient semi-analytic, mathematical technique called the Differential Transform Method (DTM), is applied to these equations as a solution procedure. Effects of several parameters, i.e. rotational speed, vibration coupling, ply orientation, boundary conditions, voltage, etc. on the natural frequencies or tip deflection are investigated and whenever it is possible, the calculated results are validated by making comparisons with the studies in open literature. When the related results are not available in open literature, the examined beam model is modeled in the commercial finite element programme ABAQUS and validation is made by using the results calculated by ABAQUS. After

the validation of the analytical models, finite element method is applied to these models to get the element matrices, i.e. element stiffness and mass matrices. Depending on the number of elements used in the structural modeling code, all the element matrices are assembled by considering the finite element rules to obtain the global matrices. The boundary conditions at the fixed end are applied to the global matrices to get the reduced matrices and the matrix systems of equations are obtained for the structural models.Modal analysis is used to solve the matrix equations and the results that are obtained by solving these matrix equations of motion are compared with the previously validated analytical ones to check the accuracy and the correctness of finite element formulation and a very good agreement between the results is observed. After the validation of the structural models, length of the linkage arm between the piezoelectric bender type actuator and the flap mechanism is calculated and this length is used in the aeroelastic part for the calculations made to examine the effect of the applied voltage on the tip deflection.

In the aerodynamic formulation, Theodorsen’s unsteady aerodynamic theory for a two dimensional thin airfoil with a trailing edgeflap is used. Firstly, the flap mechanism is discarded to model the aerodynamic loads on a plain helicopter blade. Secondly, the terms of the Theodorsen formulation that are related only to the flap deflection are considered to model the flap aerodynamics. Variation of the flap induced aerodynamic moment coefficient and flap induced aerodynamic lift coefficient with respect to time are plotted and the calculated results are compared with the ones in open literature for validation and a good agreement between the results is observed. Lastly, the two aerodynamic formulation, i.e. plain blade aerodynamics and trailing edge flap aerodynamics, are combined to model the aerodynamic loads on a helicopter blade with a trailing edge flap. Afterwards, several steps including coordinate transformations are performed to adapt the Theodorsen’s theory to the aerodynamic environment of the helicopter blade.

In the aeroelastic formulation part, the aerodynamic loads that act on the helicopter blade with a trailing edge flap are applied on the structural model of the hingeless helicopter blade. Aerodynamic matrices are assembled with the structural ones to obtain the aeroelastic matrix system of equations. Both hover and forward flight conditions are considered. Runge Kutta method is applied to the system of equations and the effects of several parameters, i.e. advance ratio, rotor disk angle of attack, trailing edge flap deflection angle, voltage applied to the piezoelectric actuator, on the vibration characteristics of the helicopter blade are inspected. Consequently, all the effort succeeded and the blade tip vibration is reduced in forward flight by deflecting the trailing edge flap.

AKTİF OLARAK KONTROL EDİLEN FİRAR KENARI FLABINA SAHİP BİR HELİKOPTER PALİNİN İLERİ UÇUŞTA DİNAMİK VE AEROELASTİK İNCELEMESİ

ÖZET

Bu doktora tezinin asıl amacı, askıda kalma ve ileri uçuş koşulları altında menteşesiz bir helikopter palinin dinamik ve aeroelastik incelemesini yapan bir bilgisayar programı geliştirmektir. Helikopter palinin firar kenarında pal titreşimlerinin azaltılması için kullanılacak flap yer almaktadır ve flap, flap mekanizmasına bir bağlantı kolu ile etki eden piezoelektrik eyleyici yardımıyla hareket ettirilmektedir.

Bu çalışmada; giriş bölümü, yapısal formülasyon, aerodinamik formülasyon ve aeroelastik formülasyon olmak üzere dört ana bölüm yer almaktadır.

Giriş bölümünde, akıllı yapılar, akıllı malzemeler, helikopter rotor tipleri, rotor çevresi aerodinamik ortamları, titreşim kontrol teknikleri, akıllı rotorlar ve eyleyici tipleri, vb. konularda bilgi verilmektedir. Ayrıca, bu çalışmada kullanılması tercih edilen eyleyici ve rotor tipinden bahsedilmekte ve literatürde yapılan çalışmalar hakkında bilgi verilmektedir. Bu *Giriş* bölümünün amacı; akıllı malzemeler, rotor sistemleri, titreşim azaltma yöntemleri, vb. konularda okuyucuya gerekli bilgileri vererek daha sonraki bölümlerde yapılan formül çıkarımlarının ve anlatılan konuların okuyu tarafından daha kolay anlaşılmasını ve daha anlamlı olmasını sağlamaktır.

Yapısal formülasyon, piezoelektrik katmanlı kiriş mekaniği, analitik formülasyon ve sonlu elemanlar formülasyonu olmak üzere iki alt bölümden oluşmaktadır. Yapısal formülasyonun ilk kısmında, piezoelektrik katmanlı kirişlerin mekaniği hakkında temel bilgilerin verilmesinin yanısıra bu kirişlere etkiyen yük ifadelerinin çıkarımı detaylı bir biçimde yapılmıştır. Bu alt bölümden elde edilen sonuçlar, eğilen kiriş tipi piezoelektrik eyleyici için oluşturulan kiriş modelinin analitik formülasyonunda kullanılmaktadır. Yapısal formülasyonun ikinci alt bölümü olan analitik formülasyon kısmında, piezoelektrik eyleyici ve helikopter pali için kiriş modelleri ayrı ayrı geliştirilmiştir. Piezoelektrik eyleyici,kısa bir kiriş olarak modellendiği için eyleyici için eğilme-uzama etkileşimli Timoshenko kiriş modeli kullanılırken uzun bir kiriş olarak modellenen helikopter pali için düzlemiçi eğilme-düzlemdışı eğilme ve burulma etkileşimli Euler-Bernoulli kiriş modeli kullanılmaktadır. Ayrıca hem piezoelektrik eyleyici hem de helikopter pali, ankastre kirişler olarak modellenmiştir. İlgili birim uzama alanları, potansiyel enerji ve kinetik enerji ifadeleri, çeşitli ve açıklayıcı tablolar ve grafikler kullanılarak adım adım elde edilmiştir. Elde edilen enerji ifadelerine bir sonraki adımda Hamilton prensibi uygulanarak diferansiyel hareket denklemlerinin ve sınır şartlarının çıkarımı yapılmıştır. Literatürde var olan çalışmalarla karşılaştırma yapabilmek amacıyla boyutsuz parametreler tanımlanmış ve elde edilen denklemler boyutsuz hale getirilmiştir. Etkin bir matematiksel teknik olan yarı-analitik Diferansiyel Dönüşüm Yöntemi, elde edilen boyutsuz hareket denklemlerine ve sınır şartlarına uygulanarak çözüm yapılmıştır. Dönme hızı, titreşim etkileşimleri, katman düzeni, sınır şartları ve voltaj gibi çok çeşitli

değişkenlerin, doğal frekanslar ve kiriş uç deplasmanları üzerindeki etkileri incelenmiş ve mümkün olduğunca literatürde var olan sonuçlar ilekarşılaştırmalar yapılmıştır. Elde edilen sonuçların doğrulanması için ilgili örnekler literatürde bulunamadığı taktirde kiriş modelleri, ticari sonlu elemanlar programı ABAQUS ile modellenmiş ve hesaplanan sonuçlar ile ABAQUS'ten alınan sonuçların karşılaştırması yapılmıştır. Analitik olarak elde edilen sonuçların, hem literatür hem de ABAQUS sonuçları ile oldukça uyumlu olduğu gözlenmiştir. Analitik modellerin doğrulaması yapıldıktan sonra, yapısal formülasyonun son bölümü olan sonlu elemanlar modellemesine başlanmıştır. İlk olarak deplasman alanları, polinomlar ile tanımlanmıştır. Tanımlanan deplasman alanları, eleman düğüm noktalarındaki deplasman ifadeleri cinsinden yazılarak şekil fonksiyonları elde edilmiştir. Bu şekil fonksiyonları, daha önce analitik kısımda elde edilen potansiyel ve kinetik enerji ifadelerinde kullanılarak sırasıyla eleman katılık ve eleman kütle matrisleri gibi eleman seviyesindeki matrislerin çıkarımı yapılmıştır. Eleman matrislerinin, sonlu elemanlar yöntemine uygun olarak toplanması ile tüm yapıya ait global matrisler elde edilmiş ve bu matrislere gerekli sınır şartları uygulanarak indirgeme yapılmıştır. İndirgenmiş global matrislerin oluşturduğu denklem sistemleri Modal Analiz uygulanarak çözülmüş ve elde edilen sonuçlar, uygulanan sonlu elemanlar formülasyonunun doğruluğunu teyit etmek amacıyla daha önce analitik kısımda elde edilen sonuçlar ile karşılaştırılmıştır ve sonuçlar arasında çok iyi bir uyum olduğu gözlenmiştir. Piezoelektrik eyleyici ve helikopter pali için kurulan yapısal modellerin doğrulanması tamamlandıkan sonra, eyleyiciyi flap mekanizması ile ilişkilendiren baglantı kolunun olası uzunluğu hesaplanmıştır. Hesaplanan bağlantı kolu uzunluğu daha sonra aeroelastik kısımda incelenen voltaj etkisi ile ilgili hesaplamalarda kullanılmıştır.

Aerodinamik formülasyon bölümünde, iki boyutlu, flaplı, ince kanat profili için geliştirilmiş Theodorsen teorisi kullanılmıştır. Bu teoride kanat profili kanat çırpma, burulma ve flap sapması olmak üzere üç titreşime maruz kalmaktadır. İlk olarak, flap mekanizması hesaba katılmayarak sade bir helikopter palinin üzerine etkiyen aerodinamik yüklerin çıkarımı yapılmıştır. İkinci olarak, Theodorsen teorisinde yer alan ve sadece flap titreşimini içeren terimler göz önüne alınarak flap aerodinamiği modellenmiştir. Flap taşıma katsayısı ile flap moment katsayısının zamanla değişimini gösteren grafikler çizilerek literatürdeki sonuçlar ile karşılaştırma yapılmıştır. Sonuçlar arasındaki uyum, uygulanan formülasyonun doğruluğunu kanıtlamıştır. Aerodinamik formülasyonun son bölümünde, flapsız pal aerodinamiği ile flap aerodinamiği birleştirilerek hem askıda kalma hem de ileri uçuş koşulları altında flaplı helikopter paline etkiyen aerodinamik yüklerin hesabı yapılmıştır. Daha sonra, Theodorsen teorisini helikopter aerodinamiğine uygun hale getirebilmek amacıyla çeşitli adımlar gerçekleştirilmiştir. Bu uygulama çerçevesinde; pal üzerindeki hız ifadesi bileşenlerine ayrıldıktan sonra, teoride tanımlanan taşıma ve moment ifadeleri bu hız bileşenleri cinsinden yazılmıştır. Çeşitli koordinat dönüşümleri yapıldıktan sonra pal üzerine etkiyen taşıma ve moment ifadeleri; ileri uçuş oranı, önkoniklik açısı, yunuslama kontrol açısı, azimut açısı ve pal deplasmanları cinsinden ifade edilmiştir.

Aeroelastik formülasyon bölümünde, flaplı helikopter paline ait aerodinamik formülasyon sonucu elde edilen aerodinamik yükler, helikopter palinin modellenmesinde kullanılan eğilme-eğilme-burulma etkileşimli Euler-Bernoulli kirişine uygulanmıştır. Aerodinamik matrisler ile yapısal matrislerin birleştirilmesi sonucunda aeroelastik denklem sistemlerine ulaşılmıştır. Denklem sistemlerinin çözümünde Runge Kutta yönteminden yararlanılmıştır ve hem askıda kalma hem de ileri uçuş durumları göz önünde bulundurulmuştur. Yapılan çözümler sonucunda askıda kalma durumunda yapının kendi kendini sönümlediği ve bu nedenle flap mekanizmasının, askıda kalma durumunda titreşim sönümleme amacıyla kullanılmasının anlamsız olacağı görülmüştür. Ancak, ileri uçuş koşulları altında zamana bağlı ek terimlerin varlığı sebebiyle yapının kendi kendini sönümlemesi engellendiğinden firar kenarı flabı hareket ettirildiğinde helikopter pal ucu titreşiminin azaldığı gözlenmiştir. Daha önce yapısal kısımda piezoelektrik eyleyici ile flap mekanizması arasında yer alan bağlantı kolunun boyutlandırılmasında göz önünde bulundurulan flap açısının pal titreşiminin azaltılmasında yeterli olduğu, aeroelastik hesaplamalarda görülmüştür. İlerleme oranı, rotor diski hücum açısı, flap sapma açısı ve piezoelektrik eyleyiciye uygulanan voltaj gibi parametrelerin helikopter pal titreşimine nasıl etki ettiği incelenmiştir.

Sonuçta, bu tezin asıl amacı olan pal titreşiminin firar kenarı flabı ile azaltılması konusunda başarılı olunmuştur ve bu konuda çok sayıda yapısal, aerodinamik ve aeroelastik bilgisayar kodu yazılmıştır.

1. INTRODUCTION

Helicopters experience large vibration because of the unsteady aerodynamic environment acting on highly flexible rotating blades soin forward flight, periodic aerodynamic loading of the blades is the primary source of vibratory loads. Since vibration has several important effects, i.e. poor performance, short fatigue life of onboard equipment, passenger and crew discomfort, high maintenance cost, etc. on a helicopter; designers are required to model structures and control surfaces that have more acceptable vibration levels (Viswamurthy and Ganguli, 2008). Various passive vibration reduction techniques were suggested by the early studies in this field (Loewy, 1984).Nevertheless, these traditional passive techniques, i.e. absorbers and isolators, blade structural optimization, etc., have not been effective and/or efficient enough to maintain the desired comfort level. Therefore, active approaches that have relative advantages on the traditionl passive techniques have received considerable attention in the last two decades (Lee and Chopra, 1999; Friedmann et al.,2001; Wilber et al., 2002).

In this section, brief information is given about intelligent structures, smart materials, active vibration reduction techniques, smart helicopter blade configurations,smart actuator types, rotor types and rotor aerodynamic environment. Additionally, the concept downselection, literature survey and roadmap of the disserttaion are presented.

The aim of this section is to introduce some basic information smart materials/structures and helicopter rotor to the reader so it is going to be easier and more meaningful for the reader to understand all the derivations carried out in the following sections.

1.1 Intelligent Structures

Intelligent structuresare a subset of a much larger field of research,as shown in Figure 1.1.

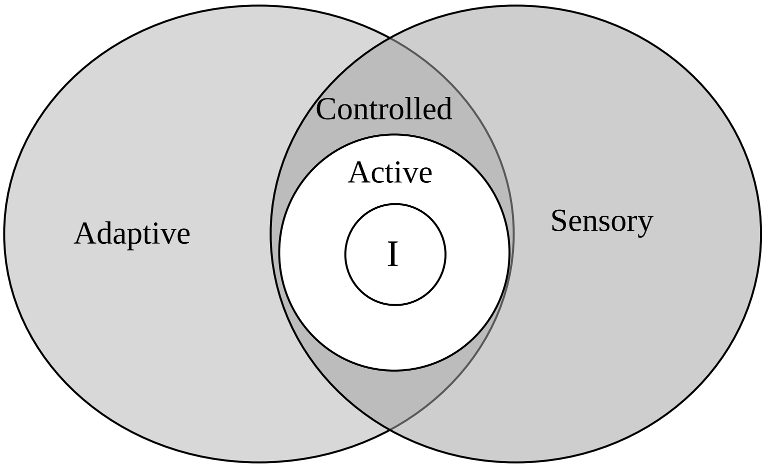

Figure 1.1: Intelligent structures as a subset of controlled and activestructures,adapted from (Crawley, 1994).

1.1.1 Adaptive structures

Adaptive, in other words actuated structures have distributed actuators. Leading- and trailing-edge control surfaces on a wing or articulated manipulators of a robotic system are good examples for adaptive structures.

1.1.2 Sensory structures

Sensory structures have distributed sensors which detect mechanical states such as displacements, strains, etc. or electromagnetic states, temperature, heat flow, etc. Damage detection is one of the application areas of sensory structures.

1.1.3 Controlled structures

Structures that have both distributed sensors and actuators linked by closed-loop control are called controlled structures.

1.1.4 Active structures

Active structures take place in the subset of controlled structures and distinguished from the controlled structures by distributed actuators that have structural functionality and that are part of the load bearing system.

1.1.5 Intelligent structures

Intelligent structures,are a subset of active structures and they have highly distributed actuator and sensor systems with structural functionality. Additionally, distributed control functions and computing mechanism are present in the intelligent structures (Crawley, 1994).

In Table 1.1, which is adapted from (Loewy, 1997), subsets of smart structures are defined briefly in a table format which makes it easier to understand their differences.

Table 1.1: Subsets of smart structures.

Subset Classification	Function	Implementation
(Self-) Adaptive	Sensor	Nonstructural
	Controller	Nonstructural, external
	Actuator	Embedded, integrated
(Self-) Sensing	Sensor	Load carrying, embedded, integrated
	Controller	Nonstructural, external
	Actuator	Traditional, concentrated, external to structure
Active	Sensor	Embedded, integrated
	Controller	Nonstructural, external
	Actuator	Embedded, integrated
Intelligent	Sensor	Embedded, integrated
	Controller	Load carrying, embedded, integrated
	Actuator	Embedded, integrated

The interest in intelligent structures has steadily increased during the last 20 years due to the fact that this new generation of structural systems has special functionalities, i.e. sensing, actuation, shape morphing, health monitoring, vibration control, etc. Moreover, these structures have the capability of developing special stiffness and strength characteristics which are generally not present in other materials (Gaudenzi, 2005).Key elements in the application of intelligent structures technology to a system are actuators, sensors, control methodology and hardware, i.e. computer and power electronics (Chopra, 2002). Sensors, actuators and controllers of these systems are seamlessly integrated with structural materials at the macroscopic or mesoscopic level (Tani and Qui, 1998).

Due to the following reasons, intelligent structures are becoming feasible:

- Commercial availability,
- Easily embeded in laminated structures,
- Utility of material couplings such as between mechanical and electrical properties,
- Potential of a substantial jump in performance improvement at a small price,
- Advances in microelectronics, information processing and sensor technology.

1.2 Smart Materials

Components of smart structures, i.e sensors, controllers and actuators, are made of smart materials which are functional materials and fluids such as piezoelectric materials, magnetostrictive materials, shape memory alloys, electro-and magneto-rheological fluids and so on. In this section, some brief information is given about some of the outstanding ones of these materials.

1.2.1 Piezoelectric materials

Piezoelectricmaterials are one of the most popular smart materials. Mechanically strained piezoelectric materials become polarized and electrical charge is produced on the surface of the material. This property is called the “direct piezoelectric effect” and makes piezoelectric materials to beavailable as sensors. On the other hand, when an electric field is applied across the material, the material deforms and strain is produced. This property is called the “converse piezoelectric effect” and makes piezoelectric materials to beavailable as actuators.Quartz, Rochelle salt and Tourmaline are some of the naturally occurring piezoelectric materials. Two of the most popular man-made piezoelectric materials are PZT (Lead Zirconate Titanate), a ceramic, and PVDF (Polyvinylidine Fluoride) a polymer. The most widely used piezoceramicssuch as leadzirconatetitanate are in the form of thin sheets that can be readily attached or embedded in composite structures or stackedto form discretepiezostackactuators. Piezoelectric materials are relatively linear at low fields and bipolar,but exhibit hysteresis.

1.2.2 Magnetostrictive materials

Magnetostrictive (MS) materials such as Terfenol-D exhibit the dual properties that strain is generated in response to a magnetic field and conversely, mechanical stress produces domain changes which yield measurable magnetic effects. These materials are nonlinear and exhibit hysteresis. Over a wide range of frequency, they generate low strains and moderate forces. These actuators are often bulky due to the coil and magnetic return path.

1.2.3 Shape memory alloys

Shape memory alloys (SMA) appear attractive as actuators because of the possibility of achieving large excitation forces and displacements. These materials undergo phase transformation at a specific temperature. When plastically deformed at a low temperature, these alloys recover to their original undeformed condition if its temperature is raised above the transformation temperature. This process can be repeated again. A remarkable characteristic of SMA is its large change of modulus of elasticity with heating, typically three to five times of room temperature value. The most common SMA material is Nitinol, nickel titanium alloy and is available in the form of wires of different diameters. Though heating is carried out internally (electrically), response is very slow (less than 1 Hz).

1.2.4. Electrostrictive materials

Electrostrictive materials are quite identical to piezoelectric materials, with slightly better strain capability, but they are very sensitive to temperature. They are available in the form of thin layers and stacks.Electrostrictive materials have a nonlinear relation between an applied field and induced strain, but exhibit negligible hysteresis.

1.2.5. Rheological fluids

Rheological fluids consist of suspensions of fine dielectric particles in an insulating fluid that exhibit controlled rheological behavior in the presence of large applied electric fields. Application of an electric field results in a significant change of shear loss factor, viscosity that helps to alter damping of the system (Tani and Qiu, 1998).

In Table 1.2, which is adapted from (Loewy, 1997), brief information is given about the energy exchange capabilities of smart structures. Ticks in more than one row per column indicate energy-exchange capability for each structure. Additionally, response of several materials to different inputs are given in Table 1.3, which is adapted from (Preumont, 2006). Here, the smart materials correspond to non-diagonal cells.

Table 1.2: Energy exchange capabilities of smart materials**.**

Energy Form	Piezoelectric	Magnetostrictive	Shape memory alloy	Rheological fluid
Strain	√	√		
Stress				√
Temperature			√	
Voltage field	√			√
Magnetic field		√		
Chemical (material phase)			√	

Table 1.3: Input – output effects in materials.

INPUT	**OUTPUT**			
	Strain	Electric Charge	Magnetic Flux	Temperature
Stress	**Elasticity**	Piezo-electricity	Magneto-striction	
Electric Field	Piezo-electricity	**Permittivity**		
Magnetic Field	Magneto-striction	Magneto-electric Effect	**Permeability**	
Heat	Thermal Expansion	Pyroelectricity		**Specific Heat**

1.3 Rotor Blades

1.3.1 Rotor blade motions

The simplest model of a rotating blade involvesa rigid blade that is hinged at the root to the rotor hub and that undergoesrotations,i.e. flapping, lead-lag and feathering, about the root as shown in Figure 1.2.

In Figure 1.2(a), flapping motion, i.e. the degree of freedom that produces motion of the rotor disk plane, is shown. This motion appears about either a hinge or a region of structural flexibility at the root and is represented by the flapping angle, β. The flapping angle is positive upwards since the main reason of this motion is the thrust force on the blade that is also in the upwards direction.

In Figure 1.2(b), lead-lag motion, i.e. the degree of freedom that appears in the plane of the rotor disk is shown and is represented by the lead-lag angle, ξ. Since lead-lag motion is the result of the drag force, it is positive when opposing the direction of rotation.

In Figure 1.2(c), feathering motion or blade pitching, i.e. the degree of freedom that appears about a bearing at the root is shown and is represented by the pitching angle, Φ. The axis of the bearing is parallel to the blade spanwise direction and the pitching angle is positive when the blade leading edge rotates upwards (Johnson, 1946).

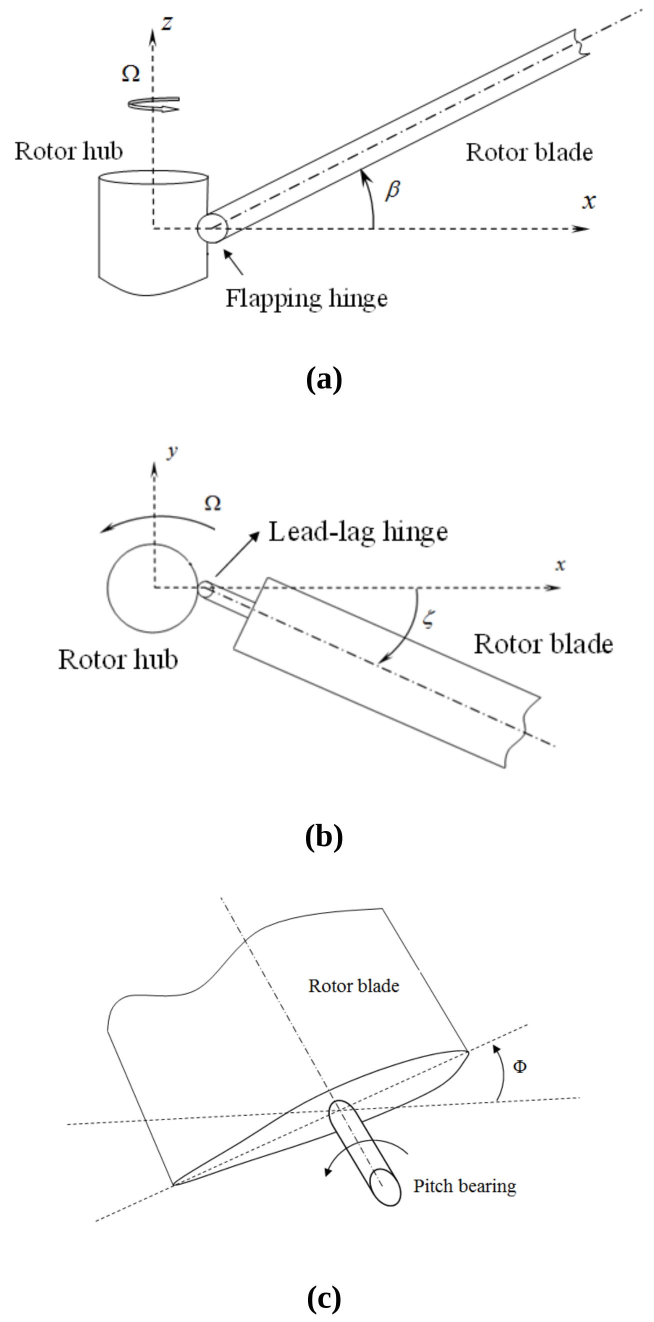

Figure 1.2: (a) Flapping (flapwise bending) motion**(b)**Lead-lag(chordwisebending) motion, adapted from (Leishman, 2000) **(c)**Feathering(pitching, torsion)motion of the rotor blade, adapted from (Bramwell, 1976).

1.3.2 Rotor hinges

The loads on the rotor blades are large and time variant and the hinges were developed to minimize these loads. Additionally, hinges reduce the rate at which the rotor blade responds to the controls. A detailed representation of each blade motion and the configuration of the hinges areillustrated in Figure 1.3.

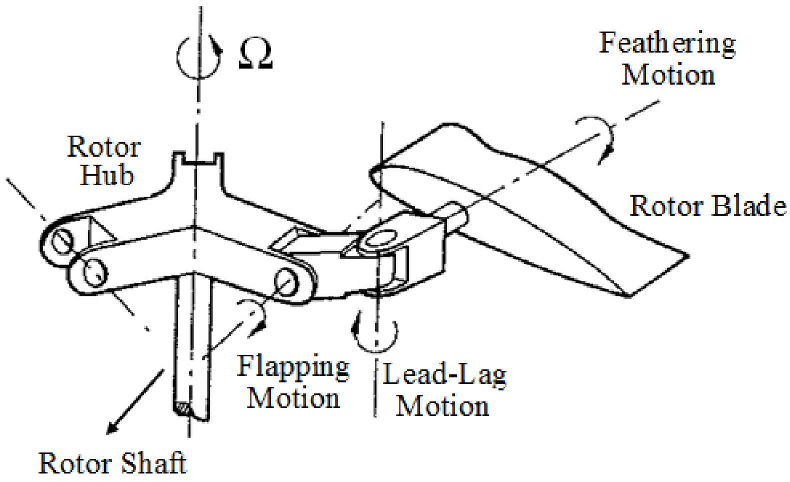

Figure 1.3: Rotor blade motions and hinges, adapted from (Bramwell, 1976).

In 1904, Renard suggested to use hinges to relieve the large bending stresses at the blade root and to eliminate the rolling moment that appears in forward flight. However in 1920s, Cierva was the first one who practically and successfully applied hinges. The hinge axes are not always mutually perpendicular and the sequence of the hinges may change . Usually, the flapping hinge is the one that is the most inboard and the feathering bearing is the most outboard. However, in some configurations the lead-lag hinge is located outside the feathering bearing. Additionally, some helicopters have the flapping and the lead-lag hinges at the same location as shown in Figure1.4 (Bramwell, 1976).

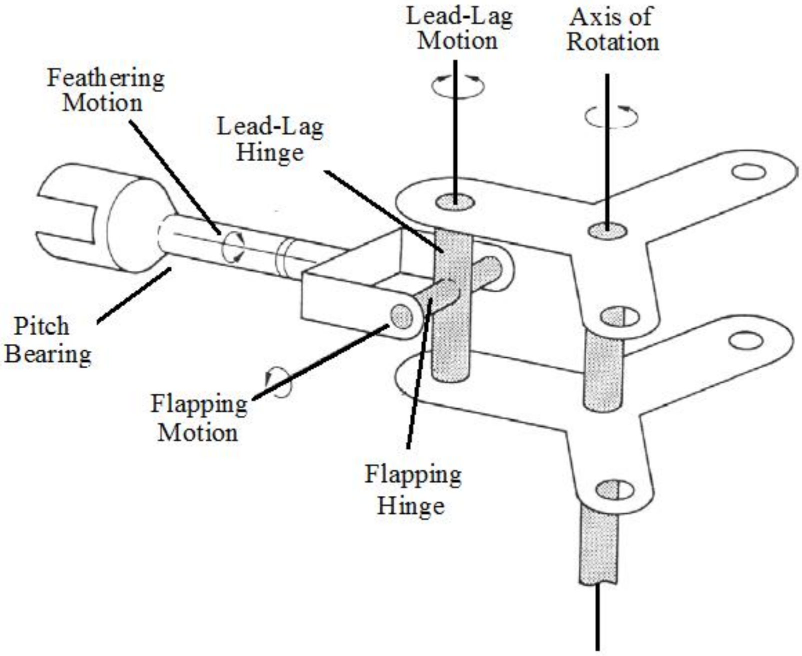

Figure 1.4: Flapping and lead-lag hinges at the same location, adapted from(Watkinson, 2004).

1.3.3 Rotor types

Commonly there are four types of rotor hub configurations, which are teetering (see-saw) rotor, fully articulated rotor, hingeless and bearingless rotors.

1.3.3.1 Teetering (see-saw) rotor

Teetering rotor whose configuration is given in Figure 1.5 has two blades that are hinged on the rotor shaft and that have no independent flapping and lead-lag hinges. However, each blade has a separate feathering bearing, which makes the cyclic and the collective pitch possible.

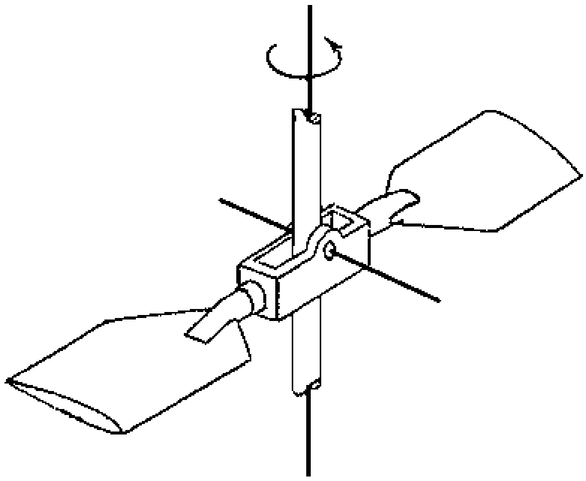

Figure 1.5: Teetering rotor, adapted from (Bramwell, 1976).

Advantage of this rotor configuration is its mechanical simplicity due to low part count while high parasitic drag in forward flight is the main disadvantage (Leishman, 2000)

1.3.3.2 Articulated rotor

A large number of helicopters have fully articulated rotor configuration where each blade has separate flapping hinge, lead-lag hinge and feathering bearing as shown in Figure 1.4. Various sequences of hinges and bearings are used by different types of helicopters which affect the dynamics of the rotor system. For instance, many Sikorsky helicopters use coincident flap and lead-lag hinges with the feathering bearing located outboard while the Boeing CH-46 and CH-47 machines use lead-lag hinge outside the feathering bearing. Due to high part count, the articulated rotor design is complicated and its maintenance is expensive.

1.3.3.3 Hingeless rotor

Improvements in blade design and construction have made it possible to eliminate the flapping and the lead-lag hinges by using a flexure to accommodate blade motion. The hingeless rotor type has blades that are connected to the rotor shaft in a cantilevered fashion. The feathering bearing is usually located outboard of the flexible root elements. Mechanical simplicity and low aerodynamic drag are the main advantages of a hingeless rotor. Moreover, stiffer hub design gives the helicopter an outstanding maneuvering capability as a response to control inputs. However, design of these rotors is more complicated because of the fact that elastic flexing of a beam structure is used to achive the balde articulation (Leishman, 2000). In Figure 1.6, the hingeless rotor configuration is compared with a fully articulated rotor configuration which examplifies the mechanical simplicity of a hingeless rotor (Bramwell, 1976).

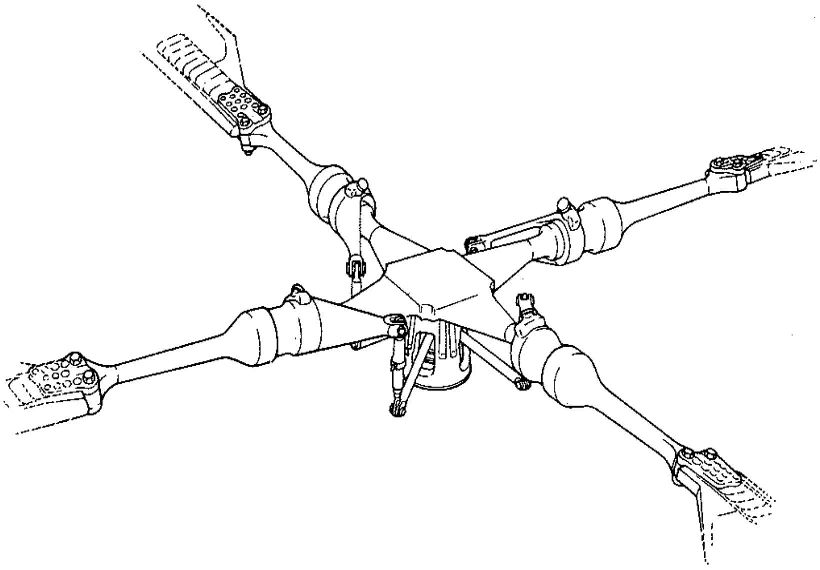

(a)

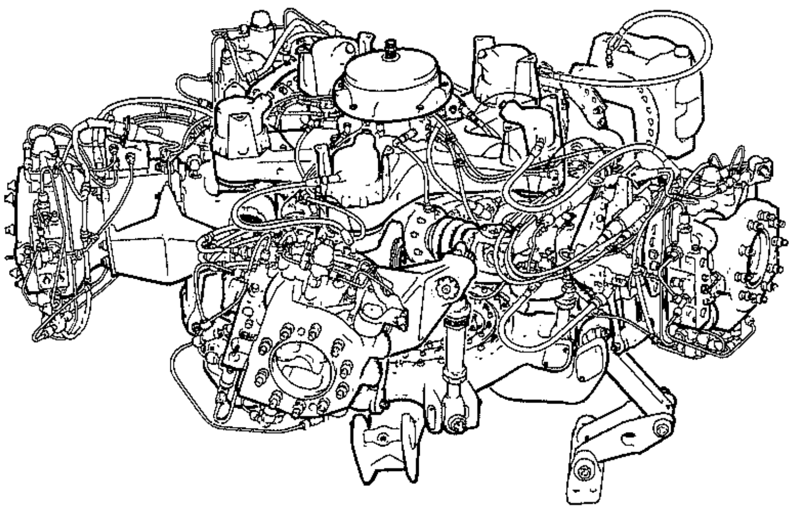

(b)

Figure 1.6:(a) Hingeless rotor configuration, Lynx **(b)** Fully articulated rotorconfiguration, Sea King, adapted from (Bramwell, 1976).

1.3.3.4 Bearingless rotor

In bearingless hub designs, besides eliminating the flapping and the lead-lag hinges, feathering bearing is also eliminated as shown in Figure 1.7. Therefore; flapping, lead-lag and feathering motions of the blade are obtained by bending, flexing and torsion of the hub structure.

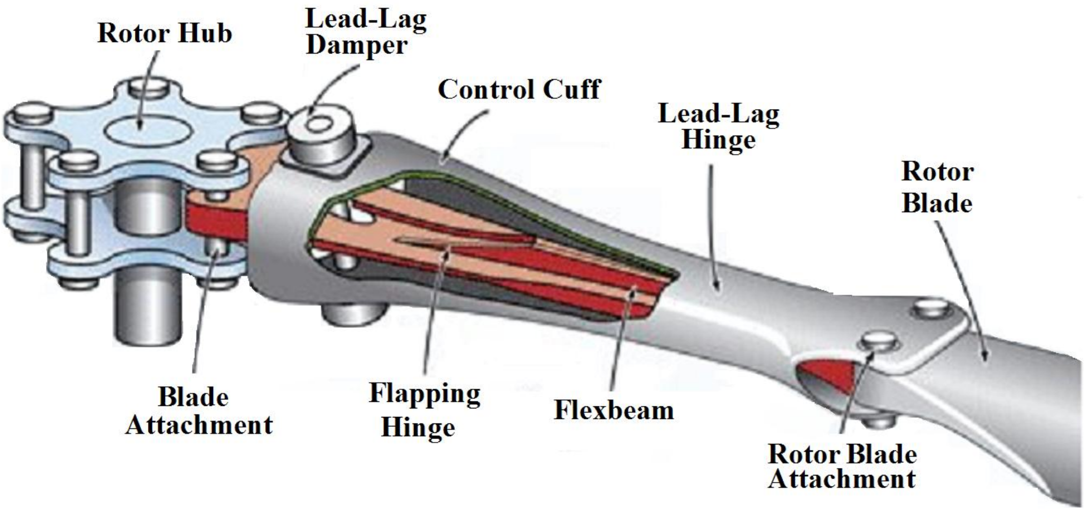

Figure 1.7: Bearingless five-blade rotor configuration, EC 145, adapted from **(**Coppinger, 2006).

High strength composite materials such as glass, carbon and Kevlar are used in the construction of this rotor type to be able to obtain the required stiffness. Additionally, these materials can be arranged in such a way that stiffnesses, load paths and couplings can be controlled. Thus, designing a bearingless hub is difficult and it requires finite element based structural dynamics analysis. Bearingless rotor configuration is mechanically simple and the aerodynamic drag is low as a hingeless rotor configuration. However, in bearingless rotor configuration the lead-lag damping is low which results in aeromechanical instability.

1.4 Aerodynamic Environment About A Rotor Blade

1.4.1 Aerodynamic environmentin hovering flight

In Figure 1.8, top view of a rotor disk under hover conditins is illustrated.

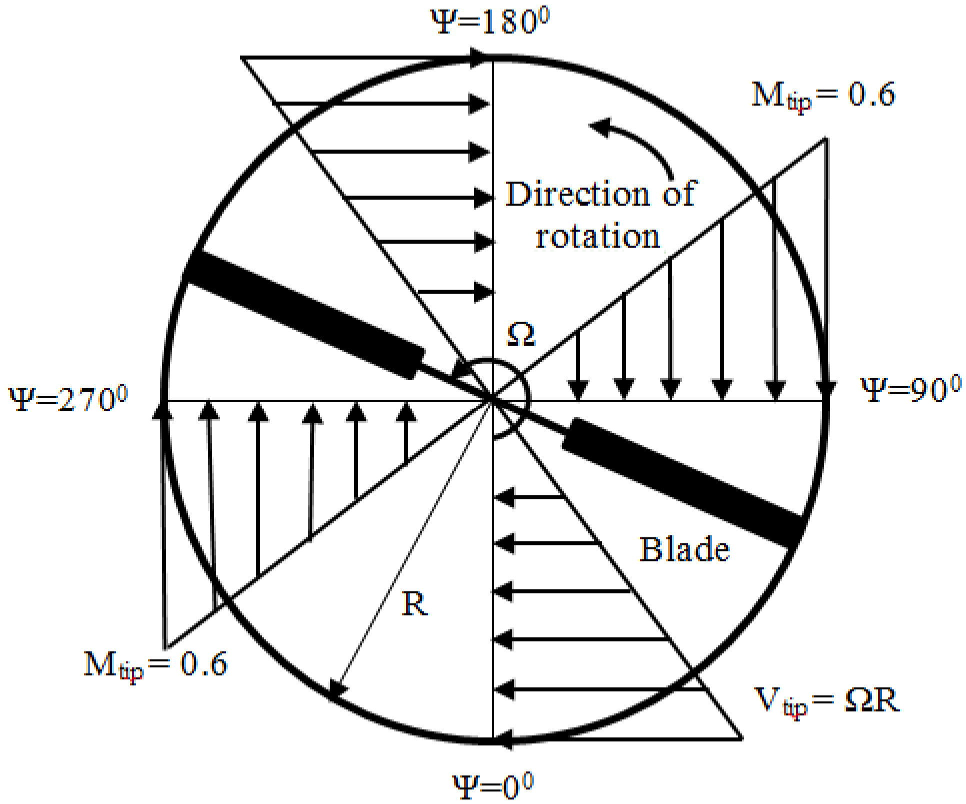

Figure 1.8: Aerodynamic environment about a rotor disk under hover conditions,adapted from (Leishman, 2006).

As it is seen here, under hover conditions, velocity varies in an azimuthally axisymmetric and radially linear manner, i.e.velocity is zero at the hub while it reaches a maximum value at the blade tip. Therefore, independent of the azimuth angle, Ψ, a blade encounters the same velocity field under hover conditions.

1.4.2 Aerodynamic environment in forward flight

In Figure 1.9, top view of a rotor disk in forward flight and variation of the velocity field through the rotor disk with respect to the azimuth angle, Ψ,are illustrated.

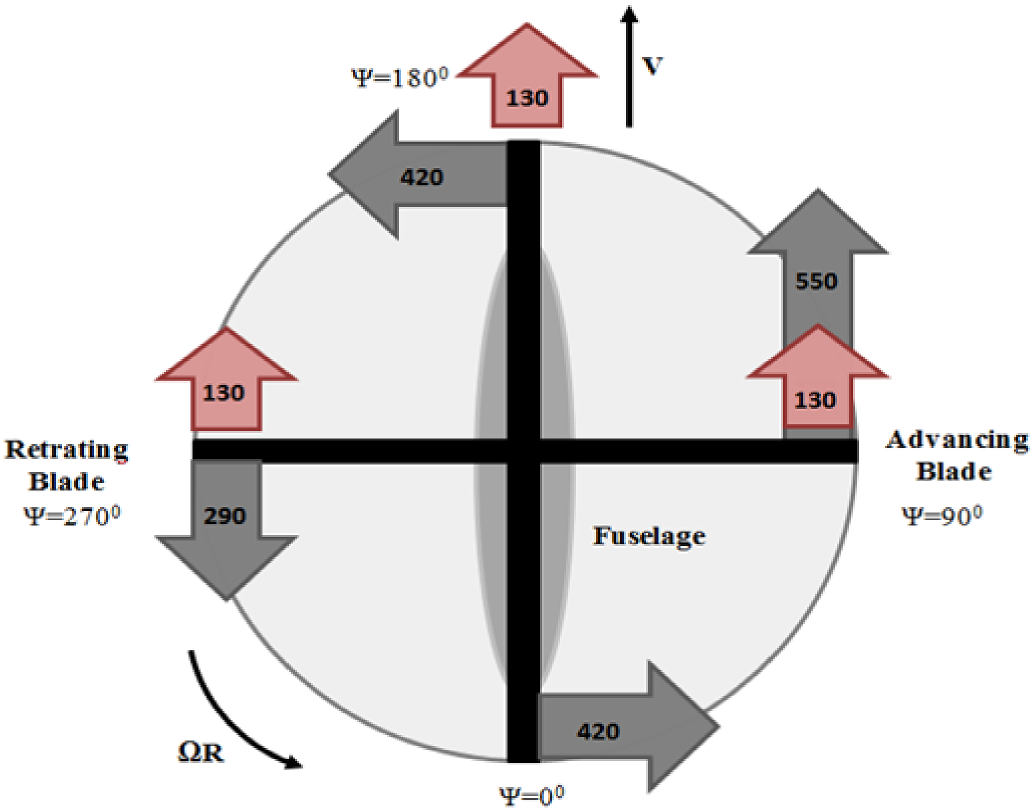

Figure 1.9: Velocity distribution over a rotor in forward flight, adapted from (Gunston and Spick, 1986).

Here, the forward flight velocity, V, of the helicopter is 130 mph and the blade rotates in the counter-clockwise direction with a constant angular velocity, Ω. The tip speed of the blade is 420 mph.

As it is seen in Figure 1.9, the forward flight velocity adds to the blade tip velocity on the advancing side of the disk, $\Psi=90^0$. However, on the retreating side, $\Psi=270^0$, the forward flight velocity substracts from the blade tip velocity. Therefore, the velocity distribution is no longer azimuthally axisymmetric and it varies in magnitude with respect to the azimuth angle as it is illustrated in Figure 1.10. However, the distribution of velocity along the blade is still linear.

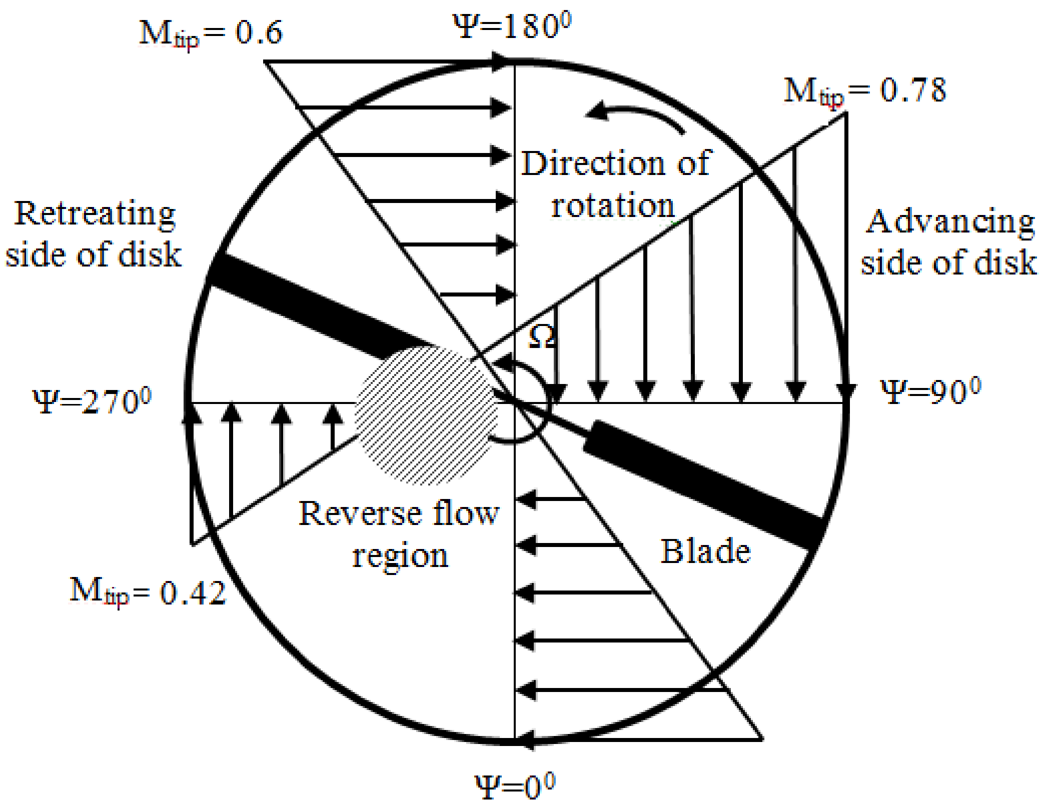

Figure 1.10: Aerodynamic environment about a rotor disk in forward flight, adaptedfrom (Leishman, 2006).

Consequently, depending on the azimuth angle, each blade encounters a periodically changing aerodynamic environment in forward flight which is the primary reason of vibration.

1.5 Active Vibration Control

Vibratory loads in helicopters arise mainly from the main rotor system and lead to the fatigue damage of structural components, human discomfort and reduced effectiveness of weapons systems. The traditional approaches that have been used for long years are passive approaches which involve a large weight penalty and poor off-design performance. Active vibration control allows the vibration system to be able to adapt to several flight conditions, at a lower weight than passive devices. In contrast to traditional passive systems, active control systems are designed to cancel the vibratory loads at their source. On blade actuation mechanisms are much more attractive than passive actuation mechanisms such as hydraulics, electric motors,etc. Therefore, active actuation of helicopter blades by means of smart materials have been a subject of interest for many authors so far. A detailed review of the application of smart materials to helicopters have been presented by Chopra (2000). Active rotor controls, which use active materials especially piezoelectric materials, directly modify the periodic aerodynamic loads that are present on a helicopter blade. In this section, active control techniques are considered.

Active control techniques generally fall into one of two categories: (1) Active control approaches implemented in the fuselage (2) Active control approaches whose primary objective is to reduce vibrations in the rotor before they propagate into the fuselage. An overview of the active control techniques is given schematically in Figure 1.11(Friedmann, 2004).

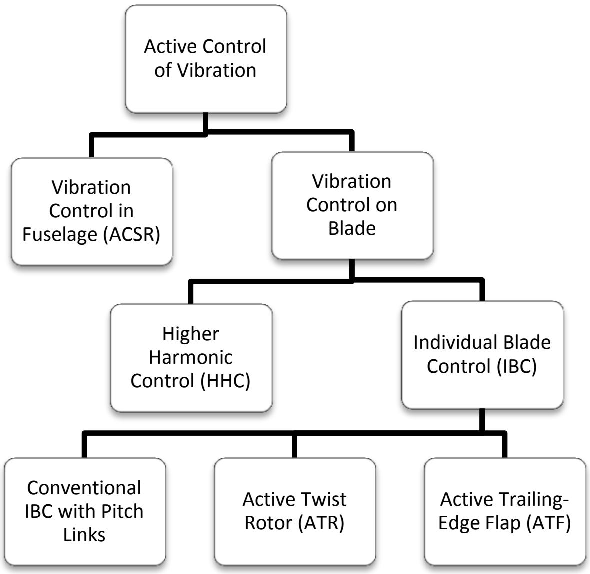

Figure 1.11: Active vibration control scheme, adapted from (Friedmann, 2004).

1.5.1 Vibration control in the fuselage

In the first branch of Figure 1.11, active control of structural response (ACSR), which is aimed at vibrations in the fuselage, or the fixed frame takes place. In this technique, stiff actuators introduce small-amplitude excitations between the rotor and the the fuselage. Therefore, the sum of the airframe response at specified locations due to the rotor loads and control excitations is minimized. ACSR is illustrated in Figure 1.12(Friedmann, 2004).

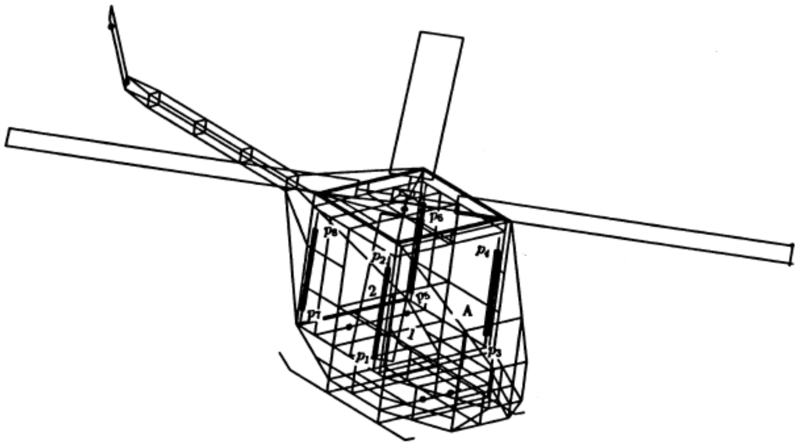

Figure 1.12: Vibration control on fuselage, adapted from (Friedmann, 2004).

1.5.2 Vibration control on the blade

In the second branch of Figure 1.11, there are two outstanding methods, i.e. higher harmonic control (HHC) and individual blade control (IBC).

Before giving information about these vibration control techniques, it is essential to mention about the main components of a swashplate which are illustrated in Figure 1.13.

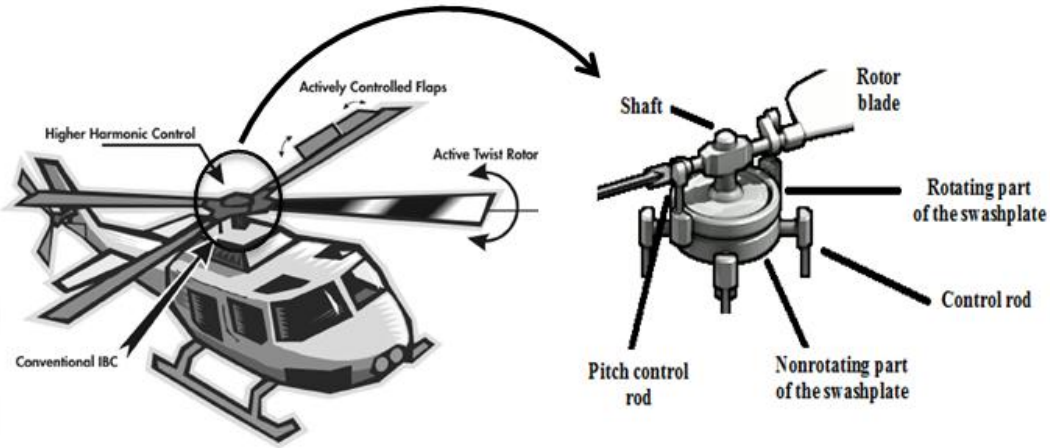

Figure 1.13: Components of swashplate, adapted from (Liu et al., 2006).

As it is seen in Figure 1.13, a swashplate has rotating and nonrotating rings which have bearings between. The rotating ring is gimballed to the shaft in an arrangement that allows an arbitrary orientation of the plane of the swashplate relative to the rotor shaft while one ring is stationary and the other is rotating. Pitch control rods are attached to the rotating ring while the pilot’s control rods are attached to the stationary one. Pilot’s control motion in the nonrotating frame are transmitted to the blades pitch motion in the rotating frame by the mechanical device called the swashplate (Johnson, 1980).

In HHC, the blades are activated in the nonrotating part of the swashplate by introducing pitch commands by the pilot**.** The controller applies pitch inputs through a conventional swashplate. All blades experience the same inputs, and the vibratory aerodynamic loads are modified at their source, before they propagate into the fuselage.

In IBC, which is a more promising alternative, an actuator is installed in each blade so each blade can be controlled independently in the rotating frame and time-varying pitch is introduced.This control concept is a more general approach than HHC since it removes some of the limitations of active control through a conventional swashplate. Besides controlling each blade independently, IBC alsoinvolves a feedback loop for each blade in the rotating frame. Three different techniques of IBC implementation are possible (1) The conventional or earliest implementation that is based on pitch actuation at the root of the blade, (2) the active-twist rotor (ATR), and (3) actively controlled flaps (ACF). All of these control mechanisms are illustrated in Figure 1.14(Liu et al., 2006).

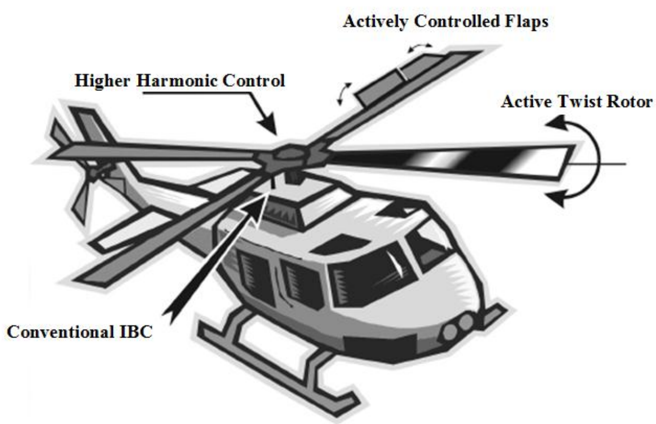

Figure 1.14: Vibration control on rotor, adapted from (Liu et al., 2006).

1.6.Smart Rotor Blades

Advances in smart material technologies has increased the potential to implement smart actuation methods for helicopter vibration reduction (Chopra, 2000). Active twist rotor (ATR) and actively controlled flaps (ACF) are two of the most outstanding active vibration reduction techniques applied to helicopter blades. In this section, some information is given about these smart rotor types and about the actuator types used to actively control them.

1.6.1. Active twist rotor

A detailed literature review about ATR blades has been prepared by Thakkar and Ganguli (2005).Initial proof-of-concept studies on active twist control using piezoelectric materials are based on experimental analysis and/or simple analytical modeling (Chen and Chopra 1996, 1997; Derham and Hagood, 1996). Later, a considerable amount of research has been focused on improving the blade-twisting performance to suppress vibrations. One of the promising concepts for the active twist rotor is the active fiber composite (AFC) (Ghiringhelli et al., 2000; Rodgers and Hagood, 1997) which has been developed by integrating the active fibers into composite laminates to induce a twisting moment along the blade as shown in Figure 1.15(Pawar and Jung, 2009). These specially-cut piezoelectric actuators are attached under the skin at an orientation so that a pure twisting of blade occurs when the same potential is applied to both top and bottom actuators (Chopra, 2000). Due to the opposing polarity, elongation occurs along fibers while there is contraction in the transverse direction to the fibers.Despite many advantages, the AFC still needs more study to overcome its drawbacks, such as the manufacturing difficulty, higher production cost and large power requirement(Wickramasinghe and Hagood, 2004). In Figure 1.16, active fiber composite configuration is introduced in detail.

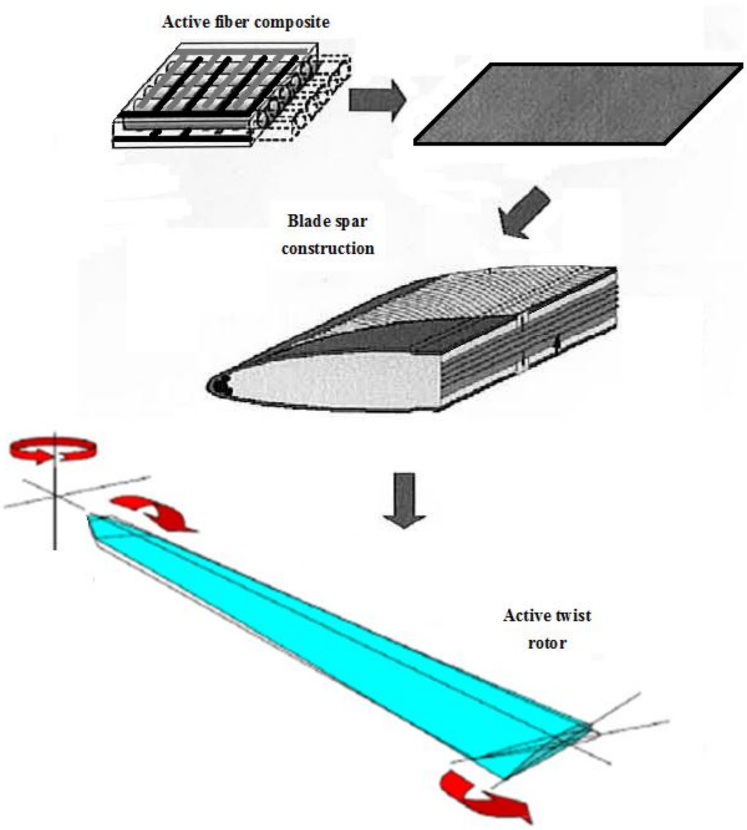

Figure 1.15: Active twist rotor, adapted from (Booth and Wilbur, 2004).

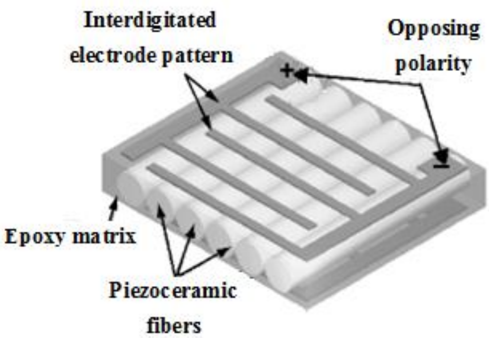

Figure 1.16: Active fiber composite, adapted from (Wickramasinghe and Hagood, 2004).

1.6.2. Actively controlled flaps

Actively controlled flaps (ACF) whose configuration is given in Figure 1.17is another method used to reduce vibration.

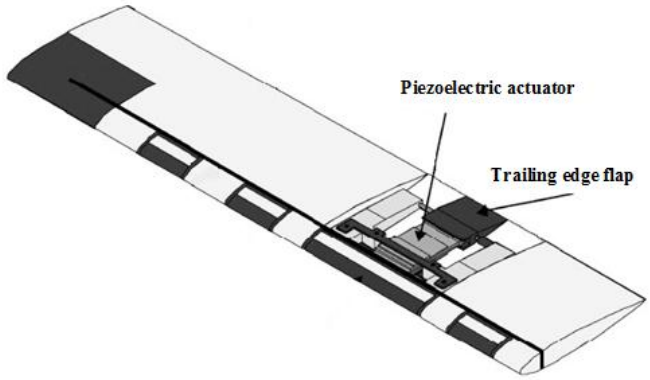

Figure 1.17: Smart rotor with bender type actuated deflected trailing edge flaps, adapted from (Koratkar and Chopra, 2002).

Here, the trailing edge flap is deflected by a bender type piezoelectric actuator.

In ACF concept, one or more trailing-edge flaps are actuated by smart actuators to induce blade twist or to increase local section lift. Flaps dynamically modify the aerodynamic loading along the span which is similar to HHC and conventional IBC. However, the advantage of actively controlled flaps over these methods is that there is no need to oscillate the entire blade or modify the primary control system (Friedmann and de Terlizzi, 2001). Studies indicate that the actively controlled flap (ACF) has remarkable potential for reducing vibration at high advance ratios and alleviation of vibrations due to blade vortex interaction (BVI) at low advance ratios (Yi et al., 2011). Advantages of the ACF approach are low power consumption and enhanced airworthiness, since the control system employed for vibration reduction is independent of the primary control system, which uses the conventional swashplate. A detailed survey paper by Chopra (2000) reviews in detail many studies that have attempted to combine piezoelectric actuation with trailing edge flaps for vibration reduction. Experimental studies on ACF include the design and development of trailing-edge flaps with minimum control efforts (Ben-Zeev and Chopra, 1996), stroke improvement of ACF using piezostack-based actuators (Lee and Chopra, 2001) and full-scale testing of the rotor with ACF (Straub et al. 2001; Koratkar and Chopra, 2001). Theoretical analysis on ACF includes simulating the ACF concept (Milgram et al., 1998) and optimal configuration of multiple flaps (Viswamurthy and Ganguli, 2007).Some of the outstanding actuation mechanisms used to deflect actively controlled flaps are bender type actuators and stack type actuators.

Bimorphs cause larger displacement and smaller force as compared to single piezo element. Therefore, bender type actuators consist of two or more layers of piezoelectric material that are poled and activated such that layers on opposite sides of the neutral axis have opposing strain. The opposing strain from the piezoelectric layers creates an internal bending momentthat causes the entire bender to bend in the flapwise directionas shown in Figure 1.18(a)(Christopher et al., 2001). As a result of the pure bending of the actuator, tip displacement appears and the tip displacement provides the actuation mechanism for the flap as it is seen in Figure 1.18 (b). The tip displacement of the bender is amplified using a mechanical leverage mechanism whose details are given in Figure 1.19(Koratkar and Chopra, 2002).

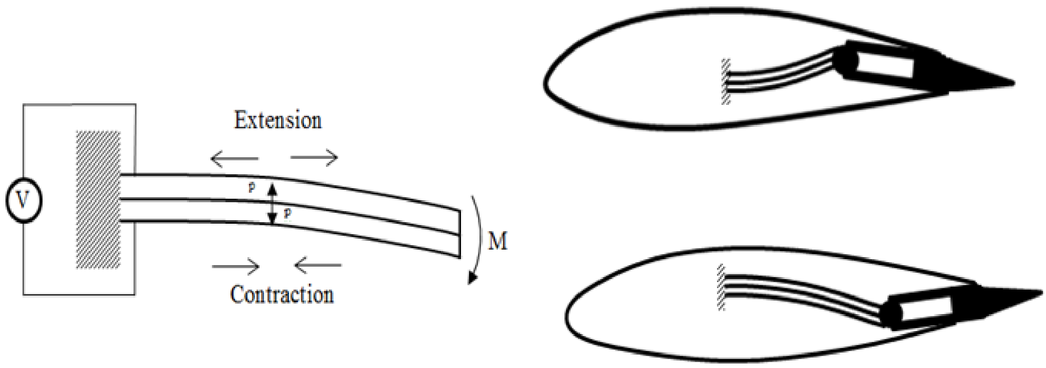

Figure 1.18:(a) Bender type bimorph piezoelectric actuator**(b)** Actuator linkage mechanism, adapted from (Christopher et al., 2001).

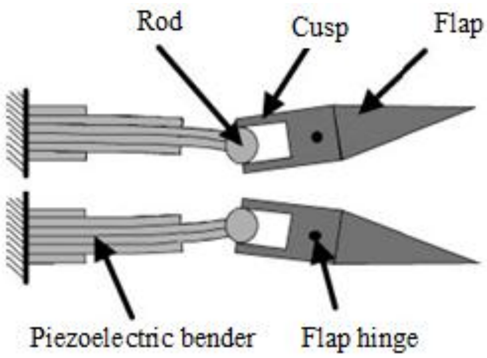

Figure 1.19: Bender type actuator-trailing edge flap assembly, adapted from (Koratkar and Chopra, 2002).

As it is illustrated in the figures, the bender is cantilevered, Most benders have piezoelectric material extending the full length of the beam. One deviation of this concept is the tapered bender, Figure 1.19, that staggers the thickness of the material, with the thickest portion at the root, to more efficiently utilize the material for bending (Christopher et al., 2001).

Piezoelectric actuators are also available in the form of “stacks,” where a large number of thin piezoceramic sheets are bonded together in a series arrangement by means of conducting adhesivesas shown in Figure 1.20.Voltage is applied through electrodes attached lengthwise on opposite sides of stack. With an electric field, each sheet expands in the thickness direction thus causing stack elongation. Bond layer thickness between sheets reduces the effective deflection. It is important to note that for a given piezoceramic material, a higher value of transverse displacement (stroke) can be obtained by using a large number of piezoceramic sheets and by reducing the bond thickness (Chopra, 2002). The stack makes use of the expansion of the piezoelectric material in the thickness direction. Stacks are characterized by having much larger block forces but smaller free displacements than bimorphs or individual piezoelectric sheets (Spencer and Chopra, 1996). Stacks generate large forces but small displacements in the direction normal to the top and bottom surfaces. Due to the limited displacement capabilities multiple stacks might be used in a series to produce desired output. In addition, mechanical amplification devices are used to increase actuation displacement by reducing the actuation force (Mitrovic et al., 1999). Piezoelectric stack actuator and trailing edge flap connection is illustrated in detail in Figure 1.21. The stacks are rigidly restrained on theoutboard end while the inboard end of the stacks press against the L-arm. Acompression spring is used to provide a precompression inthe stack and to provide the restoring force needed to keepthe L-arm and stack firmly in contact with each otherwhen the stack contracts. A pushrod connects the L-arm to flap hinge tube. The movement of the pushrod causes the flap to rotate.

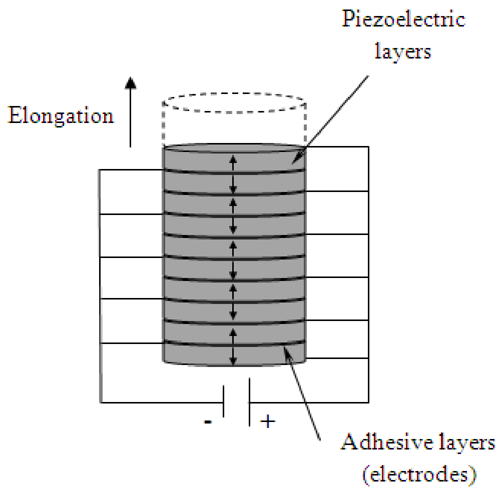

Figure 1.20: Stack type actuator, adapted from (Lee and Chopra, 2000).

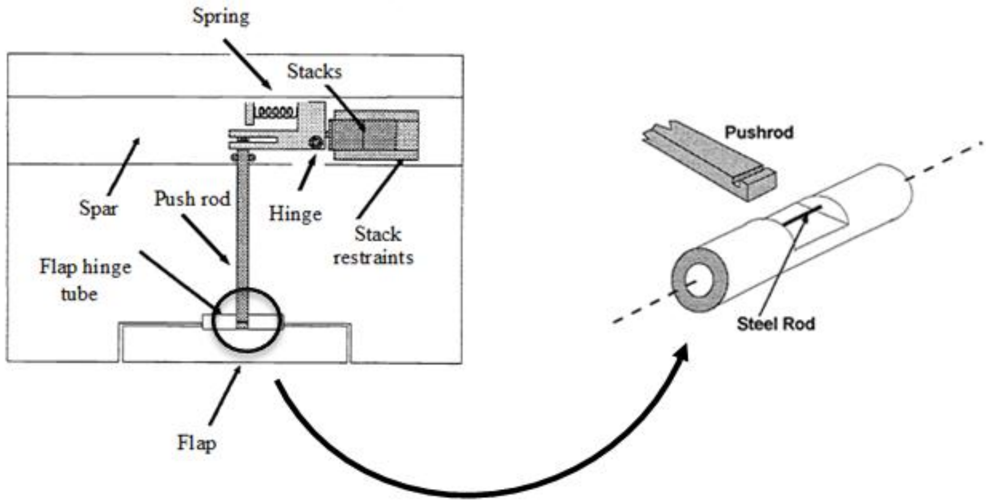

Figure 1.21: Stack type actuator-trailing edge flap assembly, adapted from (Spencer and Chopra, 1996).

1.7 Present Study

1.7.1 Rotor configuration

One of the new generation rotor configurations, hingeless rotor, is preferred to be used in the analyses carried out in this dissertation because of the following reasons

- Mechanical simplicity,
- Low aerodynamic drag,
- Outstanding maneuvering capability.

Since flapping and lead-lag hinges are discarded from this rotor configuration, in the structural formulation of the rotor, Section 2.4, the blade is modeled as a cantilevered beam with fixed-free end conditions.

1.7.2 Active vibration reduction technique

Among the concepts of active vibration reduction of a helicopter blade, actively controlled trailing-edge flaps are chosen to be useddue to the following advantages of this concept (Zhang et al., 2004)

- Compact size
- Light weight
- Enhanced airworthiness
- Low power consumption
- High adaptation

1.7.3 Actuator concept

After the selection of trailing edge flap concept for vibration reduction, selection of the actuation mechanism is made and bender type piezoelectric actuators are considered to deflect the trailing edge flaps. The advantages of this type of actutaors are (Koratkar and Chopra, 2000)

- The compact actuator assembly property makes it possible to locate flaps at optimal points along the blade.
- Almost all the energy stored in the piezoelectric structure is directly used to deflect the flap mechanism with small loses. Thus, the mechanical efficiency of the actuator is high.
- Addition of the actuator to the blade makes a moderate increase in blade mass.
- Low voltage values which are less than 400V are enough for this actuator
- The actuator is discrete and has no embedded or surface bonded components. Therefore, maintanence of the actuator mechanism is easy.

1.8 Objectives of The Thesis

The primary motivation for the present thesis is that a noncommercial analysis code that can be used for the dynamic and aeroelastic analysis of a helicopter blade under hover conditions or in forward flight is not available in the Istanbul Technical University. The commercial codes are either too expensive to be used as a licensed product or too difficult to be used without technical and/or academic support. Therefore, for a long time it has been a necessity to write our own computer code to be able to carry out aeroelastic studies about helicopters.The purpose of the present thesis is to develope the necessary computer code to carry out the mentioned analyses. The code is written for one blade that has a trailing edge flap which is actively deflected by a piezoelectric actuator to reduce the vibration of the blade.Additionally, during the development of the computer code; a huge formulation is carried out for the structural, aerodynamic and aeroelastic sections.Considering all of these, the objectives of the present thesis can be defined as follows

- Both the structural and the aerodynamic formulas are derived in detail and they are combined for the aeroelastic analysis.
- A basic computer code is developed for the aeroelastic analysis and vibration reduction of a helicopter blade under hover conditions and in forward flight.
- This basic computer code is organised in such a way that it can be modified easily. Therefore, adding new modules to the present code is going to give us the opportunity to develop the code according to our needs in the future.

1.9 Literature Review

Since the 1990's, the advancement of smart materials opens a new domain of active trailing-edge flap systems driven by smart material actuators. The emergence of these compact, lightweight, high bandwidth, and low power requirement actuators has revived the interest in active trailing-edge flap rotors (Chopra, 2000). Several small scale rotors with a trailing-edge flap system actuated by embedded smart materials have been developed by various researchers, including Bernhard and Chopra (1999) and Fulton and Ormiston (2001). A full scale rotor with a smart trailing-edge flap system has been designed by Straub, et al. (2001). Wind tunnel experiments (Koratkar and Chopra, 2001) have shown that helicopter hub vibratory loads can be successfully minimized with actively controlled, trailing-edge flaps with smart actuators. In analytical simulation, Millott and Friedmann (1994) investigated servo-flaps using a flexible blade model and modified Theodorsen aerodynamics. The servo flap system was found to be as effective as conventional multicyclic control, but with greatly reduced power requirements. The study included parametric studies of flap size, flap location, and blade torsional stiffness. The flap location was determined to be a significant design parameter. Viswamurthy and Ganguli presented optimal locations of dual trailing-edge flaps to achieve minimum hub vibration levels in a helicopter, while incurring low penalty in terms of required trailing edge flap control power (Viswamurthy and Ganguli, 2007). Kim *et al.*(2007) developed a resonant trailing edge flap actuation system (includes the piezoelectric actuator and the related mechanical and electrical elements for actuation) for helicopter rotors and evaluated experimentally. Myrtle and Friedmann (1998) presented a rotor code for the active flap using an unsteady aerodynamic model (Myrtle and Friedmann, 1997) for airfoil/flap based on a rational function approximation approach. Similar levels of vibration reduction are obtained when using quasi-steady Theodorsen aerodynamics and the new unsteady aerodynamic model. Zhang*et al.*(1999) presented an active/passive hybrid method for vibration reduction by integrating active flap design with blade structural optimization. The study concluded that hybrid design could achieve more vibration reduction with less control efforts compared to retrofit or sequential design. Other vibration reduction studies using the ACF were also conducted (Straub and Charles, 1999; Chopra et al. 1996). Additional information on vibration reduction using the ACF can be found in a recent survey paper (Friedmann, 2001).

1.10 Road Map

The present dissertation is organized in 5 chapters and 4 appendices.

In Chapter 1 (Introduction), the reader is informed about smart structures, smart materials, rotor types, rotor aerodynamic environment, rotor vibration control techniques, smart rotors, and actuators. Additionally, blade and actuator types that are preferred in this research are introduced and objectives of the dissertation are mentioned about. Moreover, a brief literature review is given. The aim of Chapter 1 is to introduce smart structures, vibration reduction techniques, helicopter rotor systems, etc. to the reader so it is going to be easier and more meaningful for the reader to understand all the derivations carried out in the following sections.

In Chapter 2 (Structural Formulation), structural models built for the piezoelectric actuator and the helicopter blade are introduced. Detailed description of the formula derivations are presented and the obtained results are validated. Additionally, length of the linkage arm between the actuator beam and the flap mechanism is calculated.

In Chapter 3 (Aerodynamic Formulation), aerodynamic formulation is given for a plain nonrotating blade, for trailing edge flaps and for a rotatinghelicopterblade with a trailing edge flap both under hover and forward flight conditions. Whenit ispossible, the results of this section are also validated.

InChapter 4 (Aeroelastic Formulation), the structural model developed in Chapter 2 and the aerodynamic models developed in Chapter 3 are combined for aeroelastic analysis. Flutter speed of the Goland wing is calculated and validated with the results in open literature. Moreover, effects of several parameters, i.e. advance ratio, rotor disk angle of attack, flap deflection angle, voltage applied to the piezoelectric actuator on the vibration characteristics of the rotor blade are inspected.

In Chapter 5 (Conclusion and Recommendations), a summary of the previous chapters are given and a conclusion is presented for all the results. Additionally, new titles are given for future studies.

In Appedix A, expressions of the constants used in Theodorsen’s theory, i.e. T_1, T_2,....,T_{14}, are given.

In Appendix B, components of the aerodynamic matrix that are assembled with the structural matrices to be used in the flutter speed calculation of a nonrotating blade, Goland wing, are introduced.

In Appendix C, components of the aerodynamic matrix that are assembled with the structural matrices to be used in the aeroelastic analysis of the helicopter blade that has a trailing edge flap underhoverconditions are introduced.

In Appendix D, components of the aerodynamic matrix that are assembled with the structural matrices to be used in the aeroelastic analysis of the helicopter blade that has a trailing edge flap in forward flight are introduced.

2. STRUCTURAL FORMULATION

2.1 Overview

The purpose of the present section is to build the structural modelsfor both the piezoelectric actuator and the helicopter blade and to make the related formula derivations correctly and accurately. The results of this section are going to be assembled with the results of the aerodynamic formulation to be used in the aeroelastic section.

In the first part of the structural formulation, some information is given about the mechanics of a piezolaminated beam.Expressions of the mechanical and the electrical loads that act on this beam model are derived in great detail. The resulting expressions are used in the analytical formulation of the bender type piezoelectric actuator. In the second part of the structural formulation, analytical beam models are developed both for the bender type piezoelectric actuator and for the helicopter blade, seperately. The structural formulation of the beam models starts by introducing the displacement fields before and after the deformation of the beams.Related strain fields and energy expressions are derived step by step by introducing several explanatory tables and figures. Afterwards, Hamilton’s principle is applied to these energy expressions to obtain the governing differential equations of motion and the boundary conditions. An efficient, semi-analytical mathematical technique called the Differential Transform Method (DTM), is applied to these equations as thesolution procedure. Effects of several parameters, i.e. rotational speed, vibration coupling, lamina orientation, voltage, etc. on the natural frequencies or tip deflection are investigated and whenever it is possible, the calculated results are validated by making comparisons with the studies in open literature. When the related results are not available in open literature, the examined beam model is modeled in the commertial finite element programme, ABAQUS and validation is made by using the results calculated by ABAQUS. After the validation of the analytical models, finite element method is applied to these models to get the element level structural matrices, i.e. element stiffness and mass matrices. Depending on the number of elements used in the developed structural modeling code, element matrices are assembled by considering the finite element rules to get the global matrices. Boundary conditions are applied to the global matrices to get the reduced global matrix expressions. Results that are obtained by solving these matrix equations of motion are compared with the previously validated semi-analytical ones to check the accuracy and the correctness of finite element formulation and a very good agreement between the results are observed.

This section includes derivations that have been achieved step by step in the previous studies of the doctorate student and his advisor through several years. These studies include uncoupled/coupled Euler Bernoulli or Timoshenko beam models (Ozdemir and Kaya (2006a, 2006b); Ozdemir Ozgumus and Kaya (2007c, 2008, 2010, 2012a); Kaya and Ozdemir (2010)), composite beams (Kaya and Ozdemir (2007)) and piezolaminated composite beams (Ozdemir Ozgumus and Kaya (2012b)).

2.2 Piezolaminated Composite Materials

Well known advantages of composite materials over other traditional materials have increased the utility of these materials in the design of rotating structures such as turbine and helicopter blades, tilt rotors, robotic manipulator arms, etc. Some of these advantages are given below.

- Composite materials have better damage tolerance.
- The manufacturing processes of composite blades provide the designer with the freedom to incorporate more refined platforms and airfoil geometries.
- These materials provide opportunities for structural simplicity of hingeless and bearingless rotor blade designs and structural couplings.
- Composite rotor blades also offer the potential for aeroelastic tailoring since they enable the introduction of favorable structural couplings to improve the aeroelastic stability and response of hingeless and bearinglessrotor blade configurations.

2.2.1 Piezoelectric effects

Piezoelectric materials are one of the most popular subset of intelligent materials. As mentioned in the Subsection 1.2.1., due to their “direct piezoelectric effect” property, these materials are used as sensors and due to their "converse piezoelectric effect", they are used as actuators which gives a designer the opportunity to utilize these materials in the control of rotor blades.

Poling process of the piezoelectric materials is shown in Figure 2.1 as three stages, i.e. before, during and after polarization. During polarization, dipoles are formed and similarly oriented dipoles start grouping together. Application of a high electric field and a high temperature makes these dipoles align and in the absence of the electrical field, these dipoles remain roughly aligned even after cooling the material to room temperature (Moheimani and Fleming, 2006).

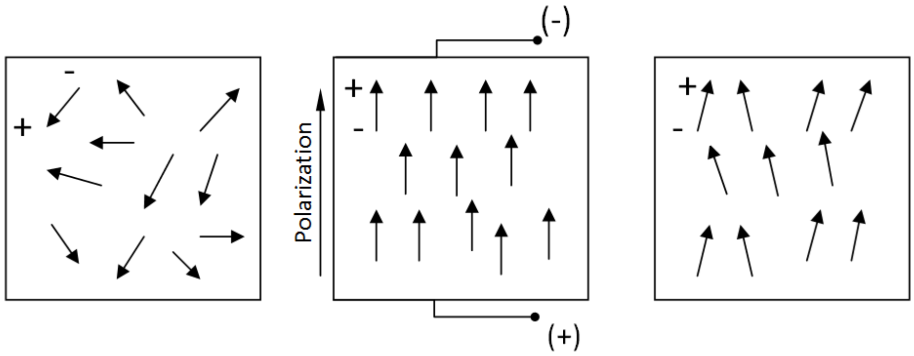

Figure 2.1: Stages of polarization of a piezoelectric material **(a)**before polarization**(b)** during polarization **(c)** polarized, adapted from (Moheimani and Fleming, 2006).

Piezoelectric properties, size and shape of the material and the direction in which forces or electrical fields are applied relative to the material axis are some of the properties that determine the relationship between the applied forces and resultant responses of a piezoelectric material. Figure 2.2 shows an element of piezoelectric material.

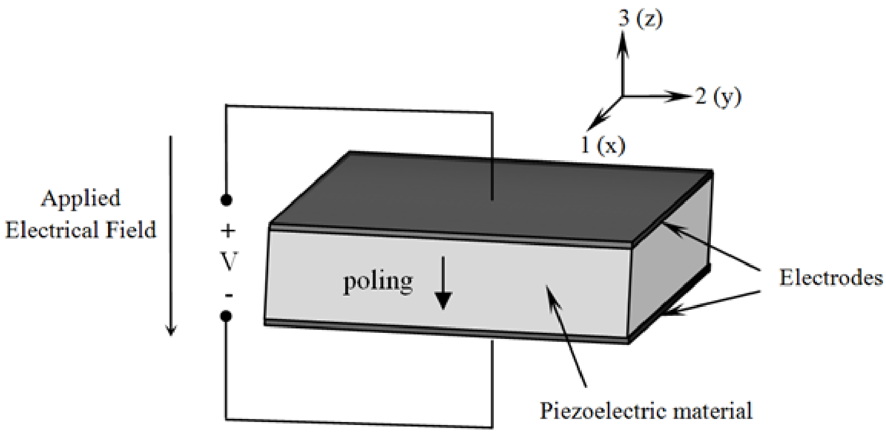

Figure 2.2: Poling direction and the coordinate axes for a piezoelectric element.

As it is seen in Figure 2.2,three axes which are set during the poling process are used to identify directions in the piezoelectric element.The z axis is parallel to the direction of polarization. The polarization vector points from the positive to negative poling electrode or in the negative z direction (Fuller et al., 1996).

Properties of a poled piezoelectric element can be explained by the series of images in Figure 2.3 and Figure 2.4. Mechanical compression or tension on the element changes the dipole moment associated with that element which creates voltage. Compression along the direction of polarization or tension perpendicular to the direction of polarization, generates voltage of the same polarity as the poling voltage, i.e. Figure 2.3(a). Tension along the direction of polarization, or compression perpendicular to that direction, generates a voltage with polarity opposite to that of the poling voltage, i.e. Figure 2.3(b).When operating in this tension/compression mode, the device is used as a sensor which means that the piezoelectric element converts the mechanical energy of compression or tension into electrical energy.

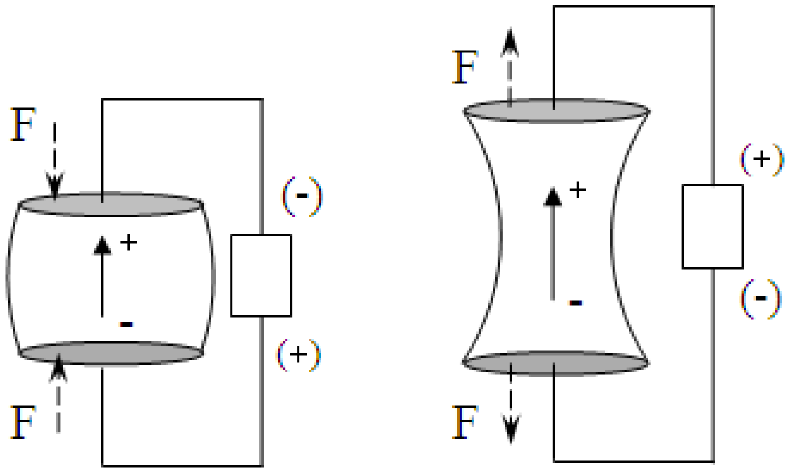

Figure 2.3: Utility of piezoelectric materials as sensors**(a)** under compression **(b)**under tension, adapted from (Moheimani and Fleming, 2006).

If the applied voltage and the polarization voltage of the piezoelectric material have opposite signs, the element will become shorter and broader, i.e. Figure 2.4(a).However, if the applied voltage and the polarization voltage of the piezoelectric material have the same sign, the element will lengthen and its diameter will become smaller, i.e. Figure 2.4(b). If an alternating voltage is applied to the device, the element will expand and contract cyclically, at the frequency of the applied voltage.

When operated in this mode, the piezoelectric material is used as an actuator. That is, electrical energy is converted into mechanical energy (Moheimani and Fleming, 2006).

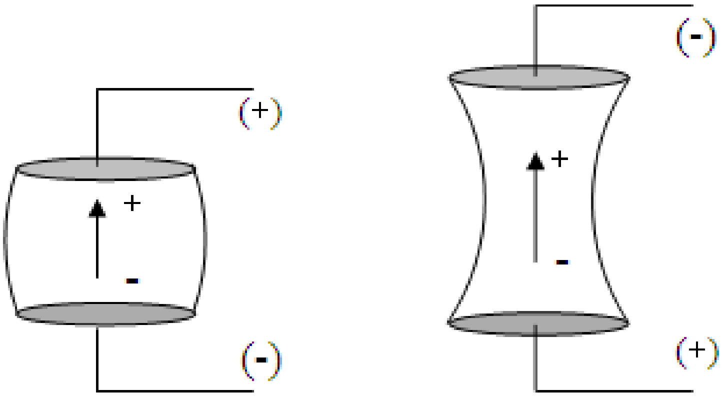

Figure 2.4: Utility of piezoelectric materials as actuators**(a)** voltages with oppositesigns **(b)** voltages with the same sign,adapted from (Moheimani andFleming, 2006).

2.2.2 Constitutive equations for a piezoelectric layer

Up to a specific stress value, the relation between the stress that is applied to the piezoelectric material and the voltage that is generated as a result of this stress is linear. The same linear relationship exists between the applied voltage and the strain that is generated as the result of this voltage. Therefore, when the applied electric field and the generated stress are not large, the constitutive equations for a linear piezoelectric material can be written as follows

$$\varepsilon_i = S_{ij}^E \sigma_j + d_{mi} E_m \qquad \textbf{(2.1)}$$

$$D_m = d_{mi} \sigma_i + \zeta_{ik}^{\sigma} E_k \qquad \textbf{(2.2)}$$

where ε is the strain, σ is the stress, D is the electrical displacement (charge per unit area), E is the electrical field (volts per unit length), S is the elastic compliance (the inverse of elastic modulus), d is the piezoelectric strain constant and ζ is the permittivity of the material respectively (Fuller et al., 1996). Eq.(2.1)expresses the converse piezoelectric effect, which describe the situation when the piezoelectric layer is being used as an actuator. Eq.(2.2)expresses the direct piezoelectric effect, which deals with the case when the piezoelectric layer is being used as a sensor.

2.2.3 Stress and moment resultants on a piezoelectric layer

In this study, piezoelectric materials are used as actuators to deflect the trailing edge flap on the helicopter blade. Therefore, Eq.(2.1)is used and it can be written in its full form as follows

$$\begin{Bmatrix} \varepsilon_1 \\ \varepsilon_2 \\ \varepsilon_3 \\ \varepsilon_4 \\ \varepsilon_5 \\ \varepsilon_6 \end{Bmatrix}_k = \begin{bmatrix} S_{11} & S_{12} & S_{13} & S_{14} & S_{15} & S_{16} \\ S_{21} & S_{22} & S_{23} & S_{24} & S_{25} & S_{26} \\ S_{31} & S_{32} & S_{33} & S_{34} & S_{35} & S_{36} \\ S_{41} & S_{42} & S_{43} & S_{44} & S_{45} & S_{46} \\ S_{51} & S_{52} & S_{53} & S_{54} & S_{55} & S_{56} \\ S_{61} & S_{62} & S_{63} & S_{64} & S_{65} & S_{66} \end{bmatrix}_k \begin{Bmatrix} \sigma_1 \\ \sigma_2 \\ \sigma_3 \\ \sigma_4 \\ \sigma_5 \\ \sigma_6 \end{Bmatrix}_k + \begin{bmatrix} d_{11} & d_{21} & d_{31} \\ d_{12} & d_{22} & d_{32} \\ d_{13} & d_{23} & d_{33} \\ d_{14} & d_{24} & d_{34} \\ d_{15} & d_{25} & d_{35} \\ d_{16} & d_{26} & d_{36} \end{bmatrix}_k \begin{Bmatrix} E_1 \\ E_2 \\ E_3 \end{Bmatrix}_k \qquad \textbf{(2.3)}$$

where k refers to the k^{th} lamina as illustrated in Figure 2.5.

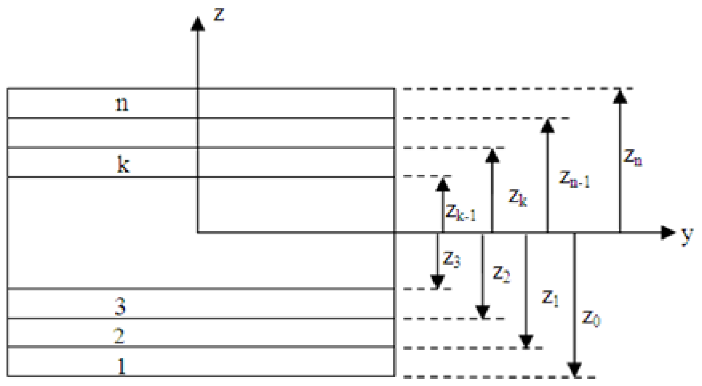

Figure 2.5: Lamina coordinates and distribution of the laminates.

Here, z_k and z_{k-1} represent the location of the upper and the lower surfaces of the k^{th} layer with respect to the middle plane, respectively and n is the total number of the layers.

Plane stress: When inplane loading is applied to a thin structure, the stresses with respect to the thin surface are zero and the structure is said to be under plane stress.

Piezolaminated beams have thin piezoelectric layers and these layers are under either compression or tension. Therefore, plane stress assumption is appropriate for this study and for a thin piezoelectric layer that is under a plane stress, the following equalities can be written.

$$\sigma_3 = \sigma_4 = \sigma_5 = 0 \qquad \textbf{(2.4)}$$

Referring Eq.(2.4), the constitutive equation , Eq.(2.3), can be written as follows

$$\begin{Bmatrix} \varepsilon_x \\ \varepsilon_y \\ \gamma_{xy} \end{Bmatrix}_k = \begin{bmatrix} S_{11} & S_{12} & S_{16} \\ S_{12} & S_{22} & S_{26} \\ S_{16} & S_{26} & S_{66} \end{bmatrix}_k \begin{Bmatrix} \sigma_x \\ \sigma_y \\ \tau_{xy} \end{Bmatrix}_k + \begin{bmatrix} d_{11} & d_{21} & d_{31} \\ d_{12} & d_{22} & d_{32} \\ d_{16} & d_{26} & d_{36} \end{bmatrix}_k \begin{Bmatrix} E_x \\ E_y \\ E_z \end{Bmatrix}_k \quad \textbf{(2.5)}$$

In this dissertation, bending type actuator is used. Therefore, it is enough to consider only extension and flapwise bending displacements. In the extension-flapwise bending vibration analysis, it is enough to consider only the electric field that is applied in z-direction, i.e. $E_x = E_y = 0$, so Eq.(2.5)can be simplified as follows

$$\begin{Bmatrix} \varepsilon_x \\ \varepsilon_y \\ \gamma_{xy} \end{Bmatrix}_k = \begin{bmatrix} S_{11} & S_{12} & S_{16} \\ S_{12} & S_{22} & S_{26} \\ S_{16} & S_{26} & S_{66} \end{bmatrix}_k \begin{Bmatrix} \sigma_x \\ \sigma_y \\ \tau_{xy} \end{Bmatrix}_k + \begin{Bmatrix} d_{31} \\ d_{32} \\ d_{36} \end{Bmatrix}_k (E_z)_k \quad \textbf{(2.6)}$$

As mentioned before, $[S]$is the inverse of the stiffness matrix, i.e. $[S]=[Q]^{-1}$ so Eq.(2.6) can be rewritten as follows

$$\begin{Bmatrix} \sigma_x \\ \sigma_y \\ \tau_{xy} \end{Bmatrix}_k = [Q]_k \begin{Bmatrix} \varepsilon_x^0 \\ \varepsilon_y^0 \\ \gamma_{xy}^0 \end{Bmatrix}_k + [Q]_k \, z \begin{Bmatrix} \kappa_x \\ \kappa_y \\ \kappa_{xy} \end{Bmatrix}_k - [Q]_k \begin{Bmatrix} d_{31} \\ d_{32} \\ d_{36} \end{Bmatrix}_k (E_z)_k \quad \textbf{(2.7)}$$

where Q_{ij} are the reduced stiffness constants, ε_x^0, ε_y^0, γ_{xy}^0 are the uniform strains and κ_x, κ_y, κ_{xy} are the curvatures (Gibson, 2007).

Local and global coordinate axis of a laminate is shown in Figure 2.6.

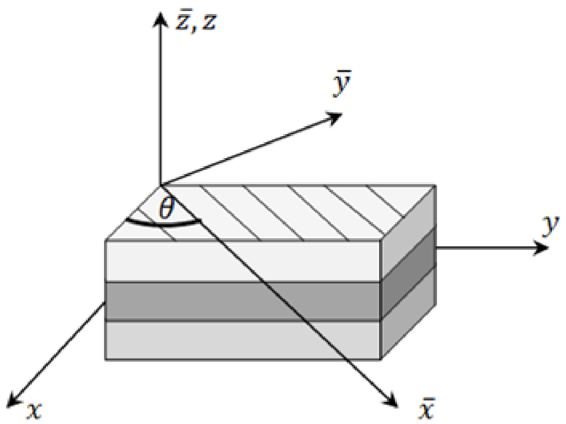

Figure 2.6: Local and global coordinate systems.

Here, xyz coordinate axes are referred to as global coordinates while $\overline{xyz}$ coordinate axes are referred to as local coordinates that depend on the fiber orientation of each lamina of the laminate. Additionally, θ , i.e. skew angle, is the fiber orientation angle of each lamina.

In local coordinates, Eq.(2.7) can be written as follows

$$\begin{Bmatrix} \sigma_{\bar{x}} \\ \sigma_{\bar{y}} \\ \tau_{\overline{xy}} \end{Bmatrix}_k = [Q]_k \begin{Bmatrix} \varepsilon^0_{\bar{x}} \\ \varepsilon^0_{\bar{y}} \\ \gamma^0_{\overline{xy}} \end{Bmatrix}_k + [Q]_k\, z \begin{Bmatrix} \kappa_{\bar{x}} \\ \kappa_{\bar{y}} \\ \kappa_{\overline{xy}} \end{Bmatrix}_k - [Q]_k \begin{Bmatrix} d_{\overline{31}} \\ d_{\overline{32}} \\ d_{\overline{36}} \end{Bmatrix}_k (E_z)_k \qquad \textbf{(2.8)}$$

A lamina has several laminates each of which may have different fiber orientations that are defined in the local coordinates of the laminate. In order to incorporate arbitrary fiber directions in the considered plane, a coordinate transformation is necessary. Therefore, transformation from local lamina coordinates to global laminate coordinates has to be considered. Stress transformation matrix, $[R]_\sigma$ and strain transformation matrix, $[R]_\varepsilon$, are given by(Kollar and Springer, 2003)

$$[R]_\sigma = \begin{bmatrix} Cos^2\theta & Sin^2\theta & 2Cos\theta Sin\theta \\ Sin^2\theta & Cos^2\theta & -2Cos\theta Sin\theta \\ -Cos\theta Sin\theta & Cos\theta Sin\theta & Cos^2\theta - Sin^2\theta \end{bmatrix} \qquad \textbf{(2.9)}$$

$$[R]_\varepsilon = \begin{bmatrix} Cos^2\theta & Sin^2\theta & Cos\theta Sin\theta \\ Sin^2\theta & Cos^2\theta & -Cos\theta Sin\theta \\ -2Cos\theta Sin\theta & 2Cos\theta Sin\theta & Cos^2\theta - Sin^2\theta \end{bmatrix} \qquad \textbf{(2.10)}$$

Transformation from the local coordinates to the global coordinates is performed by substituting Eq.(2.9) and Eq.(2.10) into Eq.(2.8)which gives

$$\begin{Bmatrix} \sigma_x \\ \sigma_y \\ \tau_{xy} \end{Bmatrix}_k = [\bar{Q}]_k \begin{Bmatrix} \varepsilon^0_x \\ \varepsilon^0_y \\ \gamma^0_{xy} \end{Bmatrix}_k + [\bar{Q}]_k\, z \begin{Bmatrix} \kappa_x \\ \kappa_y \\ \kappa_{xy} \end{Bmatrix}_k - [\bar{Q}]_k \begin{Bmatrix} d_{\overline{31}} \\ d_{\overline{32}} \\ d_{\overline{36}} \end{Bmatrix}_k (E_z)_k \qquad \textbf{(2.11)}$$

where

$$\left[\bar{Q}\right]_k = \left[R\right]_\sigma^{-1} \left[Q\right]_k \left[R\right]_\varepsilon \tag{2.12}$$

$$\left[\bar{\bar{Q}}\right]_k = \left[R\right]_\sigma^{-1} \left[Q\right]_k \tag{2.13}$$

The axial force, N, the bending moment, M and the shear force, Q_s that act on a laminate at the midplane are expressed as follows (Kollar and Springer, 2003)

$$N = b\int_{-h/2}^{h/2} \sigma dz \tag{2.14}$$

$$M = b\int_{-h/2}^{h/2} \sigma z dz \tag{2.15}$$

$$Q_S = b\int_{-h/2}^{h/2} \tau dz \tag{2.16}$$

where b and h are the width and the thickness of the laminate, respectively.

Substituting Eq.(2.11) into Eqs.(2.14)-(2.16) gives

$$\begin{aligned}\begin{Bmatrix} N_x \\ N_y \\ N_{xy} \end{Bmatrix} = b\int_{-h/2}^{h/2} \left[\bar{Q}\right]_k \begin{Bmatrix} \varepsilon_x^0 \\ \varepsilon_y^0 \\ \gamma_{xy}^0 \end{Bmatrix} dz + b\int_{-h/2}^{h/2} z\left[\bar{Q}\right]_k \begin{Bmatrix} \kappa_x \\ \kappa_y \\ \kappa_{xy} \end{Bmatrix} dz - \\ b\int_{-h/2}^{h/2} \left[\bar{\bar{Q}}\right]_k \begin{Bmatrix} d_{\bar{3}\bar{1}} \\ d_{\bar{3}\bar{2}} \\ d_{\bar{3}\bar{6}} \end{Bmatrix}_k \left(E_z\right)_k dz\end{aligned} \tag{2.17}$$

$$\begin{aligned}\begin{Bmatrix} M_x \\ M_y \\ M_{xy} \end{Bmatrix} = b\int_{-h/2}^{h/2} z\left[\bar{Q}\right]_k \begin{Bmatrix} \varepsilon_x^0 \\ \varepsilon_y^0 \\ \gamma_{xy}^0 \end{Bmatrix} dz + b\int_{-h/2}^{h/2} z^2\left[\bar{Q}\right]_k \begin{Bmatrix} \kappa_x \\ \kappa_y \\ \kappa_{xy} \end{Bmatrix} dz - \\ b\int_{-h/2}^{h/2} z\left[\bar{\bar{Q}}\right]_k \begin{Bmatrix} d_{\bar{3}\bar{1}} \\ d_{\bar{3}\bar{2}} \\ d_{\bar{3}\bar{6}} \end{Bmatrix}_k \left(E_z\right)_k dz\end{aligned} \tag{2.18}$$

In the analysis of a laminate, lamina level stiffness matrix $[\bar{Q}]_k$ is used to calculate the laminate level stiffness matrices whose components can be defined as follows(Vinson and Sierakowski, 2002)

$$\bar{A}_{ij} = b\int_{-h/2}^{h/2} \bar{Q}_{ij} dz = b\sum_{k=1}^{n} \left(\bar{Q}_{ij}\right)_k \left(z_k - z_{k-1}\right) \tag{2.19}$$

$$\bar{B}_{ij} = b\int_{-h/2}^{h/2} z\bar{Q}_{ij} dz = \frac{b}{2}\sum_{k=1}^{n} \left(\bar{Q}_{ij}\right)_k \left(z_k^2 - z_{k-1}^2\right) \tag{2.20}$$

$$\bar{D}_{ij} = b\int_{-h/2}^{h/2} z^2\bar{Q}_{ij} dz = \frac{b}{3}\sum_{k=1}^{n} \left(\bar{Q}_{ij}\right)_k \left(z_k^3 - z_{k-1}^3\right) \tag{2.21}$$

Referring the definitions in Eqs.(2.19)-(2.21), forces and moments acting on a laminate, i.e. Eq.(2.17)and Eq. (2.18)can be given as follows

$$\begin{Bmatrix} N_x \\ N_y \\ N_{xy} \end{Bmatrix} = \begin{bmatrix} \bar{A}_{11} & \bar{A}_{12} & \bar{A}_{16} \\ \bar{A}_{12} & \bar{A}_{22} & \bar{A}_{26} \\ \bar{A}_{16} & \bar{A}_{26} & \bar{A}_{66} \end{bmatrix} \begin{Bmatrix} \varepsilon_x^0 \\ \varepsilon_y^0 \\ \gamma_{xy}^0 \end{Bmatrix} + \begin{bmatrix} \bar{B}_{11} & \bar{B}_{12} & \bar{B}_{16} \\ \bar{B}_{12} & \bar{B}_{22} & \bar{B}_{26} \\ \bar{B}_{16} & \bar{B}_{26} & \bar{B}_{66} \end{bmatrix} \begin{Bmatrix} \kappa_x \\ \kappa_y \\ \kappa_{xy} \end{Bmatrix} - b\sum_{k=1}^{n_p} \left[\bar{Q}\right]_k \begin{Bmatrix} d_{\bar{3}\bar{1}} \\ d_{\bar{3}\bar{2}} \\ d_{\bar{3}\bar{6}} \end{Bmatrix}_k h_k \left(E_z\right)_k \tag{2.22}$$

$$\begin{Bmatrix} M_x \\ M_y \\ M_{xy} \end{Bmatrix} = \begin{bmatrix} \bar{B}_{11} & \bar{B}_{12} & \bar{B}_{16} \\ \bar{B}_{12} & \bar{B}_{22} & \bar{B}_{26} \\ \bar{B}_{16} & \bar{B}_{26} & \bar{B}_{66} \end{bmatrix} \begin{Bmatrix} \varepsilon_x^0 \\ \varepsilon_y^0 \\ \gamma_{xy}^0 \end{Bmatrix} + \begin{bmatrix} \bar{D}_{11} & \bar{D}_{12} & \bar{D}_{16} \\ \bar{D}_{12} & \bar{D}_{22} & \bar{D}_{26} \\ \bar{D}_{16} & \bar{D}_{26} & \bar{D}_{66} \end{bmatrix} \begin{Bmatrix} \kappa_x \\ \kappa_y \\ \kappa_{xy} \end{Bmatrix} - b\sum_{k=1}^{n_p} \left[\bar{Q}\right]_k \begin{Bmatrix} d_{\bar{3}\bar{1}} \\ d_{\bar{3}\bar{2}} \\ d_{\bar{3}\bar{6}} \end{Bmatrix}_k z_k^0 h_k \left(E_z\right)_k \tag{2.23}$$

where n_p represents the number of the piezoelectric layers.

In the analysis of a beam problem, it is enough to consider only the N_x and M_x components. Therefore, Eq.(2.22) and Eq.(2.23) can be simplified as follows

$$N_x = \bar{A}_{11}\varepsilon_x^0 + \bar{A}_{12}\varepsilon_y^0 + \bar{A}_{16}\gamma_{xy}^0 + \bar{B}_{11}\kappa_x + \bar{B}_{12}\kappa_y + \bar{B}_{16}\kappa_{xy} - b\sum_{k=1}^{n_p}\left(\bar{\bar{Q}}_{11}d_{\bar{3}\bar{1}} + \bar{\bar{Q}}_{12}d_{\bar{3}\bar{2}} + \bar{\bar{Q}}_{16}d_{\bar{3}\bar{6}}\right)_k \left(V_z\right)_k \tag{2.24}$$

$$M_x = \bar{B}_{11}\varepsilon_x^0 + \bar{B}_{12}\varepsilon_y^0 + \bar{B}_{16}\gamma_{xy}^0 + \bar{D}_{11}\kappa_x + \bar{D}_{12}\kappa_y + \bar{D}_{16}\kappa_{xy} - b\sum_{k=1}^{n_p}\left(\bar{\bar{Q}}_{11}d_{\bar{3}\bar{1}} + \bar{\bar{Q}}_{12}d_{\bar{3}\bar{2}} + \bar{\bar{Q}}_{16}d_{\bar{3}\bar{6}}\right)_k z_k^0 \left(V_z\right)_k \tag{2.25}$$

where the applied voltage, $(V_z)_k$ and the z coordinate of the midplane of the k^{th} layer,z_k^0 are defined as follows

$$\left(V_z\right)_k = h_k\left(E_z\right)_k \tag{2.26}$$

$$z_k^0 = \frac{z_k + z_{k-1}}{2} \tag{2.27}$$

Terms of Eq.(2.24)and Eq.(2.25)can be classified as mechanical terms and piezoelectric terms which are given by

$$N_x^m = \bar{A}_{11}\varepsilon_x^0 + \bar{A}_{12}\varepsilon_y^0 + \bar{A}_{16}\gamma_{xy}^0 + \bar{B}_{11}\kappa_x + \bar{B}_{12}\kappa_y + \bar{B}_{16}\kappa_{xy} \tag{2.28}$$

$$N_x^p = \bar{E}_{11} = b\sum_{k=1}^{n_p}\left(\bar{\bar{Q}}_{11}d_{\bar{3}\bar{1}} + \bar{\bar{Q}}_{12}d_{\bar{3}\bar{2}} + \bar{\bar{Q}}_{16}d_{\bar{3}\bar{6}}\right)_k \left(V_z\right)_k \tag{2.29}$$

$$M_x^m = \bar{B}_{11}\varepsilon_x^0 + \bar{B}_{12}\varepsilon_y^0 + \bar{B}_{16}\gamma_{xy}^0 + \bar{D}_{11}\kappa_x + \bar{D}_{12}\kappa_y + \bar{D}_{16}\kappa_{xy} \tag{2.30}$$

$$M_x^p = \bar{F}_{11} = b\sum_{k=1}^{n_p}\left(\bar{\bar{Q}}_{11}d_{\bar{3}\bar{1}} + \bar{\bar{Q}}_{12}d_{\bar{3}\bar{2}} + \bar{\bar{Q}}_{16}d_{\bar{3}\bar{6}}\right)_k z_k^0 \left(V_z\right)_k \tag{2.31}$$

where $\bar{E}_{11}$ and $\bar{F}_{11}$ are the actuator induced axial force and bending moment, respectively(Edery-Azulay and Abramovich, 2006). However, during the calculation of the stiffness coefficients, i.e. $\bar{A}_{ij}$, $\bar{B}_{ij}$ and $\bar{D}_{ij}$, properties of the piezoelectric material are also used.

In the analysis of extension-flapwise bending vibrations, ε_y^0, γ_{xy}^0, κ_y and κ_{xy} can be taken to be zero. Thus, Eq.(2.28) and Eq.(2.30)can be simplified as follows

$$N_x^m = \bar{A}_{11}\varepsilon_x^0 + \bar{B}_{11}\kappa_x \quad \textbf{(2.32)}$$

$$M_x^m = \bar{B}_{11}\varepsilon_x^0 + +\bar{D}_{11}\kappa_x \quad \textbf{(2.33)}$$

Where $\bar{A}_{11}$, $\bar{B}_{11}$ and $\bar{D}_{11}$ are the extension, coupled extension-bending and bending stiffness coefficients.

Piezoelectric actuator is modeled as a short beam. Therefore, using Timoshenko beam formulation is more appropriate for the structural formulation of the actuator. Thus, shear effect is included and the shear force is expressed as follows

$$Q_{xz} = \bar{A}_{55}\gamma_{xz} \quad \textbf{(2.34)}$$

where $\bar{A}_{55}$ is the transverse shear stiffness coefficient given by

$$\bar{A}_{55} = \bar{k}b\int_{-h/2}^{h/2}\bar{Q}_{ij}dz = \bar{k}b\sum_{k=1}^{n}\left(\bar{Q}_{ij}\right)_k\left(z_k - z_{k-1}\right) \quad \textbf{(2.35)}$$

Here, $\bar{k}$ is the shear correction factor.

The piezoelectric strain constant, d ,is defined as the ratio of developed free strain to the applied electric field. The subscripts of d_{ij} imply that the electric field is applied or charge is collected in the i direction for a displacement or force in the j direction (Moheimani and Fleming, 2006)**.** In this study, extension-flapwise bending vibration analysis is performed. When electrical field is applied in the z direction, E_z, extension and flapwise bending deflections occur as a result of elongation of the piezoelectric layers in the x directions. Thus, all the piezoelectric strain constants except $d_{\bar{3}\bar{1}}$ are neglected in Eq.(2.29)and Eq.(2.31). Consequently, the resulting force and moment expressions are

$$N_x = \bar{A}_{11}\varepsilon_x^0 + \bar{B}_{11}\kappa_x - b\sum_{k=1}^{n_p}\left(\bar{\bar{Q}}_{11}d_{\bar{3}\bar{1}}\right)_k\left(V_z\right)_k \quad \textbf{(2.36)}$$

$$M_x = \bar{B}_{11}\varepsilon_x^0 + \bar{D}_{11}\kappa_x - b\sum_{k=1}^{n_p}\left(\bar{\bar{Q}}_{11}d_{\bar{3}\bar{1}}\right)_k z_k^0 \left(V_z\right)_k \qquad \textbf{(2.37)}$$

2.3 Piezoelectric Actuator Structural Model

In this section, structural model for a bender type piezoelectric actuator is built and results are obtained analytically. Both the potential and the kinetic energy expressions are derived step by step using explanatory tables and figures. The parameters for the ply orientation and voltage are incorporated into the energy expressions. The governing differential equations of motion and the related boundary conditions are obtained by applying the Hamilton's principle. In order to solve the derived equations, a semi-analytical technique called the Differential Transform Method (DTM) is used.After the validation of the analytical model, finite element formulation is carried out by using the analytically derived energy expressions. Effects of the applied voltage and ply orientation on the actuator tip deflection and on the natural frequencies are inspected (Ozdemir Ozgumus and Kaya, 2012).

2.3.1 Beam model

The bender type actuator is modeled as a cantilever, solid-cross section piezolaminated composite beam that is shown in Figure 2.7. The beam has a composite core and two piezoelectric layers. The piezoelectric layers are continuous along the beam and they are located on the top and bottom faces of the composite core.

Governing differential equations of motion and the boundary conditions are derived for this solid cross-sectionbeam model that undergoes extension and flapwise bending displacements.

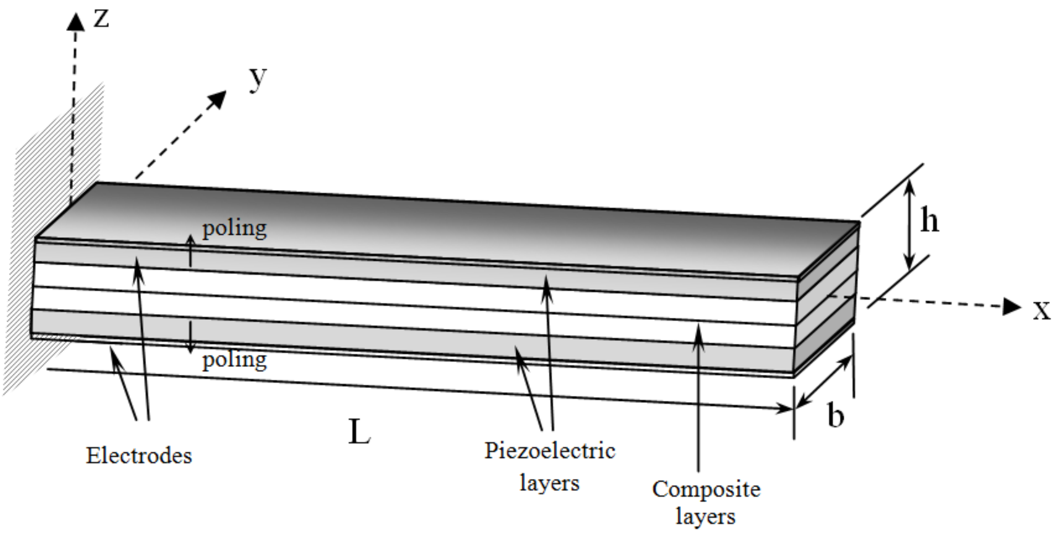

Figure 2.7: Bender type piezoelectric actuator.

Here, L is the length, b is the width and h is the thickness of the beam. The xyz axes represent a global orthogonal coordinate system with its origin at the root of the beam.

2.3.2 Energy expressions

The cross-sectional and the longitudinal views of a Timoshenko beam that undergoes extension and flapwise bending vibrations are introduced in Figure 2.8 and Figure 2.9, respectively. Here, a reference point is chosen and is represented by P_0 before deformation and by P after deformation.

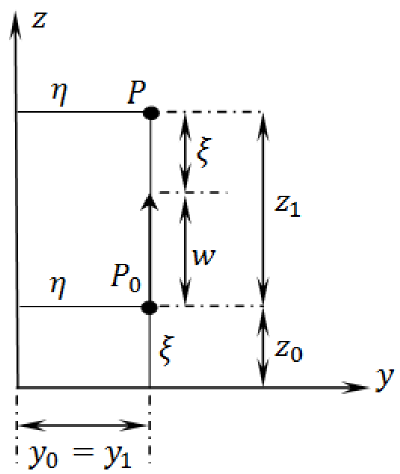

Figure 2.8: Cross-sectional view of the actuator beam.

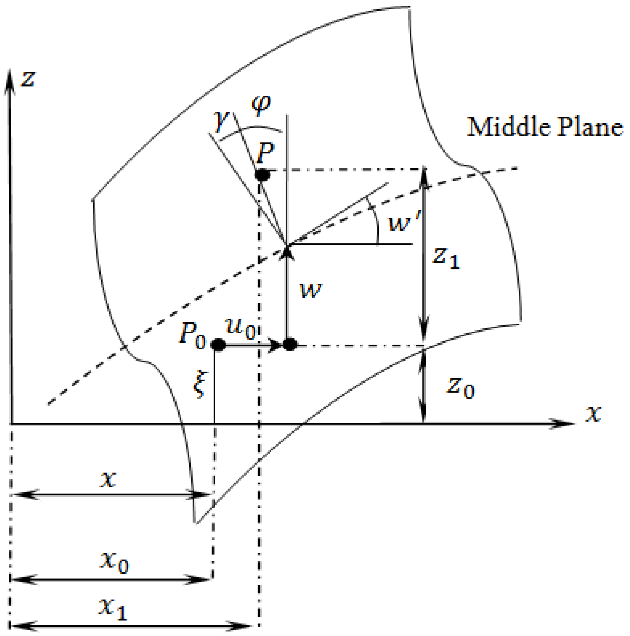

Figure 2.9: Longitudinal view of the actuator beam.

Here, η is the offset of the reference point from the z- axis, ξ is the offset of the reference point from the middle plane, x is the offset of the reference point from the z-axis, u_0 is extension, w is the flapwise bending displacement, φ is the rotation due to bending and γ is the shear angle.

Considering Figure 2.8 and Figure 2.9, the coordinates of the reference point can be written as follows

Before deformation (coordinates of P_0 *):*

$$x_0 = x \tag{2.38}$$

$$y_0 = \eta \tag{2.39}$$

$$z_0 = \xi \tag{2.40}$$

After deformation (coordinates of P *):*

$$x_1 = x + u_0 + \xi\varphi \tag{2.41}$$

$$y_1 = \eta \tag{2.42}$$

$$z_1 = w + \xi \tag{2.43}$$

The position vectors of the reference point are represented by $\overrightarrow{r_0}$ and $\overrightarrow{r_1}$ before and after deformation, respectively. Therefore, $d\overrightarrow{r_0}$ and $d\overrightarrow{r_1}$ can be written as follows

$$d\vec{r}_0 = dx\vec{i} + d\eta\vec{j} + d\xi\vec{k} \tag{2.44}$$

$$d\vec{r}_1 = \left[\left(1 + u_0' + \xi\varphi'\right)dx + \varphi d\xi\right]\vec{i} + d\eta\vec{j} + \left(w'dx + d\xi\right)\vec{k} \tag{2.45}$$

where $(\quad)'$ denotes differentiation with respect to the spanwise coordinate, x.

The classical strain tensor ε_{ij} may be obtained as follows (Eringen, 1980)

$$d\vec{r}_1.d\vec{r}_1 - d\vec{r}_0.d\vec{r}_0 = 2\left[dx \quad d\eta \quad d\xi\right]\left[\varepsilon_{ij}\right]\begin{bmatrix} dx \\ d\eta \\ d\xi \end{bmatrix} \tag{2.46}$$

where

$$\left[\varepsilon_{ij}\right] = \begin{bmatrix} \varepsilon_{xx} & \varepsilon_{x\eta} & \varepsilon_{x\xi} \\ \varepsilon_{\eta x} & \varepsilon_{\eta\eta} & \varepsilon_{\eta\xi} \\ \varepsilon_{\xi x} & \varepsilon_{\xi\eta} & \varepsilon_{\xi\xi} \end{bmatrix} \tag{2.47}$$

Substituting Eq. (2.44) and Eq. (2.45) into Eq. (2.46), the components of the strain tensor ε_{ij} are obtained as follows

$$\varepsilon_{xx} = u_0' + \frac{\left(u_0'\right)^2}{2} + \frac{\left(w'\right)^2}{2} + u_0'\varphi'\xi + \varphi'\xi + \frac{\left(\varphi'\right)^2}{2}\xi^2 \tag{2.48}$$

$$\gamma_{x\eta} = 0 \tag{2.49}$$

$$\gamma_{x\xi} = \left(w' + \varphi\right) + \varphi\varphi'\xi - u_0'\varphi \tag{2.50}$$

Where ε_{xx}, $\gamma_{x\eta}$ and $\gamma_{x\xi}$ are the axial strain and the shear strains, respectively.

In order to obtain simpler expressions for the strain components given by Eqs.(2.48)-(2.50), higher order terms can be neglected so an order of magnitudeanalysis is performed by using the ordering scheme, given by Hodges and Dowell (1974) and introduced inTable 2.1.

Table 2.1: Ordering scheme for the Timoshenko beam model**.**

Term	Order
w'	$O(\varepsilon)$
φ	$O(\varepsilon)$
$w'+\varphi$	$O(\varepsilon^2)$
u_0'	$O(\varepsilon^2)$
φ'	$O(\varepsilon^2)$

Hodges and Dowell (1974) carried out a formulation for an Euler-Bernoulli beam so in this study, their formulation is modified for a Timoshenko beam and a new expression, $w'+\varphi = O(\varepsilon^2)$is added to their ordering scheme as a contribution to literature.

ConsideringTable 2.1, Eqs. (2.48)-(2.50) are simplified as follows

$$\varepsilon_{xx} = u_0' + \frac{(w')^2}{2} + \varphi'\xi \tag{2.51}$$

$$\gamma_{x\eta} = 0 \tag{2.52}$$

$$\gamma_{x\xi} = w' + \varphi \tag{2.53}$$

The potential energy expression is given by

$$U = \frac{1}{2}\int_0^L\int_A \left(\sigma_{xx}\varepsilon_{xx} + \tau_{x\xi}\gamma_{x\xi}\right) dA dx = \frac{b}{2}\int_0^L\int_{-h/2}^{h/2} \left(\sigma_{xx}\varepsilon_{xx} + \tau_{x\xi}\gamma_{x\xi}\right) d\xi\, dx \tag{2.54}$$

Substituting Eq. (2.51)and Eq. (2.53)into Eq. (2.54)and considering the definitions in Eqs. (2.14)-(2.16), the following expression is obtained.

$$U = \frac{1}{2}\int_0^L \left\{ N_x \left[u_0' + \frac{(w')^2}{2} \right] + M_x\varphi' + Q_{xz}\left(w'+\varphi\right) \right\} dx \tag{2.55}$$

Substituting Eqs. (2.32)-(2.34) into Eq. (2.55)gives

$$U=\frac{1}{2}\int_0^L\left\{\overline{A}_{11}\left(u_0'\right)^2+2\overline{B}_{11}\left(u_0'\varphi'\right)+\overline{D}_{11}\left(\varphi'\right)^2+\overline{A}_{55}\left(w'+\varphi\right)^2\right.$$
$$\left.-\overline{E}_{11}\left[u_0'+\frac{\left(w'\right)^2}{2}\right]-\overline{F}_{11}\varphi'\right\}dx \qquad \textbf{(2.56)}$$

ReferringEq.(2.56),variation of the potential energy is obtained as follows

$$\delta U=\frac{1}{2}\int_0^L\left\{\left(\overline{A}_{11}u_0'+\overline{B}_{11}\varphi'-\overline{E}_{11}\right)\delta u_0'+\left[\overline{A}_{55}\left(w'+\varphi\right)-\right.\right.$$
$$\left.\left.\overline{E}_{11}w'\right]\delta w'+\left(\overline{B}_{11}u'+\overline{D}_{11}\varphi'-\overline{F}_{11}\right)\delta\varphi'+\overline{A}_{55}\left(w'+\varphi\right)\delta\varphi\right\}dx \qquad \textbf{(2.57)}$$

The position vector of point P shown in Figure 2.9 is given by

$$\vec{r}=\left(x+u_0+\xi\varphi\right)\vec{i}+w\vec{k} \qquad \textbf{(2.58)}$$

The velocity vector of this point is obtained as follows

$$\vec{V}=\frac{\partial\vec{r}}{\partial t}=\left(\dot{u}_0+\xi\dot{\varphi}\right)\vec{i}+\dot{w}\vec{\mathrm{k}} \qquad \textbf{(2.59)}$$

Hence, the velocity components are

$$V_x=\dot{u}_0+\xi\dot{\varphi} \qquad \textbf{(2.60)}$$

$$V_y=0 \qquad \textbf{(2.61)}$$

$$V_z=\dot{w} \qquad \textbf{(2.62)}$$

The kinetic energy expression is given by

$$T=\frac{1}{2}\int_0^L\iint_A\rho\left(V_x^2+V_y^2+V_z^2\right)dAdx=\frac{b}{2}\int_0^L\int_{-h/2}^{h/2}\rho\left(V_x^2+V_y^2+V_z^2\right)d\xi\,dx \qquad \textbf{(2.63)}$$

where ρ is the material density.

Substituting the velocity components into Eq.(2.63)and taking the variation of the kinetic energy give

$$\delta T = \int_0^L \left\{ I_1 \left(\dot{u}_0 \delta \dot{u}_0 + \dot{w} \delta \dot{w} \right) + I_2 \left[\dot{u}_0 \delta \dot{\varphi} + \dot{\varphi} \delta \dot{u}_0 \right] + I_3 \left(\dot{\varphi} \delta \dot{\varphi} \right) \right\} dx \quad \textbf{(2.64)}$$

whereI_1, I_2 and I_3 are the inertial characteristics of the beam given by

$$I_1 = b \int_{-h/2}^{h/2} \rho \, d\xi \quad \textbf{(2.65)}$$

$$I_2 = b \int_{-h/2}^{h/2} \rho \xi \, d\xi \quad \textbf{(2.66)}$$

$$I_3 = b \int_{-h/2}^{h/2} \rho \xi^2 \, d\xi \quad \textbf{(2.67)}$$

2.3.3 Governing equations of motion and boundary conditions

The Hamilton's principle is expressed as follows

$$\int_{t_1}^{t_2} \delta \left(U - T \right) dt = 0 \quad \textbf{(2.68)}$$

Eq.(2.57)and Eq.(2.64)are substituted into Eq.(2.68)to obtain the equations of motion and the boundary conditions.

Equations of motion:

$$\bar{A}_{11} u_0'' + \bar{B}_{11} \varphi'' = I_1 \ddot{u}_0 + I_2 \ddot{\varphi} \quad \textbf{(2.69)}$$

$$\left(\bar{A}_{55} - \bar{E}_{11} \right) w'' + \bar{A}_{55} \varphi' = I_1 \ddot{w} \quad \textbf{(2.70)}$$

$$\bar{D}_{11} \varphi'' + \bar{B}_{11} u_0'' - \bar{A}_{55} \left(w' + \varphi \right) = I_2 \ddot{u}_0 + I_3 \ddot{\varphi} \quad \textbf{(2.71)}$$

Boundary conditions:

At x=0 $$u_0(0,t) = w(0,t) = \varphi(0,t) = 0 \quad \textbf{(2.72)}$$

At x=L $$\bar{A}_{11}u_0'(L,t) + \bar{B}_{11}\varphi'(L,t) - \bar{E}_{11} = 0 \quad \textbf{(2.73)}$$

$$\left(\bar{A}_{55} - \bar{E}_{11}\right)w'(L,t) + \bar{A}_{55}\varphi(L,t) = 0 \quad \textbf{(2.74)}$$

$$\bar{B}_{11}u_0'(L,t) + \bar{D}_{11}\varphi'(L,t) - \bar{F}_{11} = 0 \quad \textbf{(2.75)}$$

2.3.4 Simple harmonic motion and dimensionless parameters

In order to investigate the free vibration of the beam model considered in this study, a sinusoidal variation of $u_0(x,t)$, $w(x,t)$ and $\varphi(x,t)$ with a circular natural frequency, ω, is assumed and the functions are approximated as

$$u_0(x,t) = \bar{u}(x)e^{i\omega t} \quad \textbf{(2.76)}$$

$$w(x,t) = \bar{w}(x)e^{i\omega t} \quad \textbf{(2.77)}$$

$$\varphi(x,t) = \bar{\varphi}(x)e^{i\omega t} \quad \textbf{(2.78)}$$

Substituting Eqs. (2.76)-(2.78)into Eqs. (2.69)-(2.75) gives

Equations of motion:

$$\bar{A}_{11}\bar{u}'' + \bar{B}_{11}\bar{\varphi}'' + \omega^2\left(I_1\bar{u} + I_2\bar{\varphi}\right) = 0 \quad \textbf{(2.79)}$$

$$\left(\bar{A}_{55} - \bar{E}_{11}\right)\bar{w}'' + \bar{A}_{55}\bar{\varphi}' + \omega^2 I_1\bar{w} = 0 \quad \textbf{(2.80)}$$

$$\bar{D}_{11}\bar{\varphi}'' + \bar{B}_{11}\bar{u}'' - \bar{A}_{55}\left(\bar{w}' + \bar{\varphi}\right) + \omega^2\left(I_2\bar{u} + I_3\bar{\varphi}\right) = 0 \quad \textbf{(2.81)}$$

Boundary Conditions:

At x=0 $$\bar{u}\left(0,t\right)=\bar{w}\left(0,t\right)=\bar{\varphi}\left(0,t\right)=0 \qquad \textbf{(2.82)}$$

At x=L $$\bar{A}_{11}\bar{u}'\left(L,t\right)+\bar{B}_{11}\bar{\varphi}'\left(L,t\right)-\bar{E}_{11}=0 \qquad \textbf{(2.83)}$$

$$\left(\bar{A}_{55}-\bar{E}_{11}\right)\bar{w}'\left(L,t\right)+\bar{A}_{55}\bar{\varphi}\left(L,t\right)=0 \qquad \textbf{(2.84)}$$

$$\bar{B}_{11}\bar{u}'\left(L,t\right)+\bar{D}_{11}\bar{\varphi}'\left(L,t\right)-\bar{F}_{11}=0 \qquad \textbf{(2.85)}$$

In order to simplify the equations of motion and to make comparisons with open literature, the dimensionless parameters,introduced in Table 2.2,are used.

Table 2.2 : Dimensionless parameters for the actuator beam model.

Dimensionless Parameters			
$\gamma^2=\dfrac{\bar{A}_{11}L^2}{\bar{D}_{11}}$	$\alpha^2=\dfrac{\bar{B}_{11}L}{\bar{D}_{11}}$	$\tilde{w}=\dfrac{\bar{w}}{L}$	$\mu^2=\dfrac{I_2}{I_1 L}$
$\tau^2=\dfrac{\bar{D}_{11}}{\bar{A}_{55}L^2}$	$e_0=\dfrac{\bar{E}_{11}L^2}{\bar{D}_{11}}$	$\tilde{u}=\dfrac{\bar{u}}{L}$	$r^2=\dfrac{I_3}{I_1 L^2}$
$f_0=\dfrac{\bar{F}_{11}L}{\bar{D}_{11}}$	$\bar{x}=\dfrac{x}{L}$	$\lambda^2=\dfrac{I_1 L^4\omega^2}{\bar{D}_{11}}$	

where λ is the frequency parameter and r is the inverse of the slenderness ratio.

Substituting the dimensionless parameters into Eqs. (2.79)-(2.85)gives

Equations of motion:

$$\gamma^2\tilde{u}^{**}+\alpha^2\tilde{\varphi}^{**}+\lambda^2\left(\tilde{u}+\mu^2\tilde{\varphi}\right)=0 \qquad \textbf{(2.86)}$$

$$\left(\frac{1}{\tau^2}-\mathrm{e}_0\right)\tilde{w}^{**}+\lambda^2\tilde{w}+\frac{1}{\tau^2}\tilde{\varphi}^{*}=0 \qquad \textbf{(2.87)}$$

$$\alpha^2\tau^2\tilde{u}^{**}+\tau^2\tilde{\varphi}^{**}+\mu^2\tau^2\lambda^2\tilde{u}+\left(\mathrm{r}^2\tau^2\lambda^2-1\right)\tilde{\varphi}-\tilde{w}^{*}=0 \qquad \textbf{(2.88)}$$

Boundary Conditions:

At x=0 $$\tilde{u}(0,t)=\tilde{w}(0,t)=\tilde{\varphi}(0,t)=0 \qquad \textbf{(2.89)}$$

At x=L $$\gamma^2\tilde{u}^*(L,t)+\alpha^2\tilde{\varphi}^*(L,t)=0 \qquad \textbf{(2.90)}$$

$$\left(\frac{1}{\tau^2}-\mathrm{e}_0\right)\tilde{w}^*(L,t)+\frac{1}{\tau^2}\tilde{\varphi}(L,t)=0 \qquad \textbf{(2.91)}$$

$$\alpha^2\tilde{u}^*(L,t)+\tilde{\varphi}^*(L,t)-\mathrm{f}_0=0 \qquad \textbf{(2.92)}$$

where $(\ )^*$ denotes differentiation with respect to the dimensionless spanwise position, $\bar{x}$.

2.3.5 Application of the differential transform method

The differential transform method is a transformation technique based on the Taylor series expansion and is a useful tool to obtain semi-analytical solutions of the differential equations. In this method, certain transformation rules are applied and the governing differential equations and the boundary conditions of the system are transformed into a set of algebraic equations in terms of the differential transforms of the original functions and the solution of these algebraic equations gives the desired solution of the problem.

Consider a function $f(x)$ which is analytic in a domain D and let $x=x_0$ represent any point in D. The function $f(x)$ is then represented by a power series whose center is located at x_0 . The differential transform of the function $f(x)$ is given by

$$F[k]=\frac{1}{k!}\left(\frac{d^k f(x)}{dx^k}\right)_{x=x_0} \qquad \textbf{(2.93)}$$

where $f(x)$ is the original function and $F[k]$ is the transformed function. The inverse transformation is defined as

$$f(x)=\sum_{k=0}^{\infty}(x-x_0)^k F[k] \tag{2.94}$$

Combining Eq. (2.93)and Eq. (2.94), we get

$$f(x)=\sum_{k=0}^{\infty}\frac{(x-x_0)^k}{k!}\left(\frac{d^k f(x)}{dx^k}\right)_{x=x_0} \tag{2.95}$$

Referring Eq.(2.95), it is noticed that the concept of differential transform is derived from Taylor series expansion. However, the method does not evaluate the derivatives symbolically.

In actual applications, the function $f(x)$ is expressed by a finite series and Eq. (2.95) can be written as follows

$$f(x)=\sum_{k=0}^{m}\frac{(x-x_0)^k}{k!}\left(\frac{d^k f(x)}{dx^k}\right)_{x=x_0} \tag{2.96}$$

which means that the rest of the series

$$f(x)=\sum_{k=m+1}^{\infty}\frac{(x-x_0)^k}{k!}\left(\frac{d^k f(x)}{dx^k}\right)_{x=x_0} \tag{2.97}$$

is negligibly small. Here, the value of m depends on the convergence of the natural frequencies.

Theorems that are frequently used in the transformation of equations of motion are introduced inTable 2.3 and theorems that are used for boundary conditions are introduced inTable 2.4 (Ozdemir Ozgumus and Kaya, 2007).

Table 2.3: DTM theorems used for equations of motion.

Original Function	**Transformed Function**
$f(x)=g(x)\pm h(x)$	$F[k]=G[k]\pm H[k]$
$f(x)=\lambda g(x)$	$F[k]=\lambda G[k]$
$f(x)=g(x)h(x)$	$F[k]=\sum_{l=0}^{k}G[k-l]H[l]$
$f(x)=\dfrac{d^n g(x)}{dx^n}$	$F[k]=\dfrac{(k+n)!}{k!}G[k+n]$
$f(x)=x^n$	$F[k]=\delta(k-n)=\begin{cases}0 & if \quad k\neq n\\ 1 & if \quad k=n\end{cases}$

Table 2.4: DTM theorems used for boundary conditions.

$x=0$		$x=1$	
Original B.C.	**Transformed B.C.**	**Original B.C.**	**Transformed B.C.**
$\dfrac{df}{dx}(0)=0$	$F(0)=0$	$f(1)=0$	$\sum_{k=0}^{\infty}F(k)=0$
$\dfrac{df}{dx}(0)=0$	$F(1)=0$	$\dfrac{df}{dx}(1)=0$	$\sum_{k=0}^{\infty}kF(k)=0$
$\dfrac{d^2 f}{dx^2}(0)=0$	$F(2)=0$	$\dfrac{d^2 f}{dx^2}(1)=0$	$\sum_{k=0}^{\infty}k(k-1)F(k)=0$
$\dfrac{d^3 f}{dx^3}(0)=0$	$F(3)=0$	$\dfrac{d^3 f}{dx^3}(1)=0$	$\sum_{k=0}^{\infty}(k-1)(k-2)kF(k)=0$

After applying the differential transform method to Eqs.(2.86)-(2.92), the transformed equations of motion and boundary conditions are obtained as follows

Equations of motion:

$$\gamma^2(k+1)(k+2)U[k+2]+\alpha^2(k+1)(k+2)\varphi[k+2]+\lambda^2\left(U[k]+\mu^2\varphi[k]\right)=0 \tag{2.98}$$

$$\left(\frac{1}{\tau^2}-e_0\right)(k+1)(k+2)W[k+2]+\lambda^2 W[k]+\frac{1}{\tau^2}(k+1)\varphi[k+1]=0 \tag{2.99}$$

$$\alpha^2(k+1)(k+2)U[k+2]+(k+1)(k+2)\varphi[k+2]+\mu^2\lambda^2U[k]+ \left(r^2\lambda^2-\frac{1}{\tau^2}\right)\varphi[k]-\frac{1}{\tau^2}(k+1)W[k+1]=0 \quad \textbf{(2.100)}$$

Boundary Conditions:

At x=0 $$U[k]=W[k]=\varphi[k]=0 \quad \textbf{(2.101)}$$

At x=L $$\gamma^2\sum_{k=0}^{\infty}kU[k]+\alpha^2\sum_{k=0}^{\infty}k\varphi[k]=0 \quad \textbf{(2.102)}$$

$$\left(\frac{1}{\tau^2}-e_0\right)\sum_{k=0}^{\infty}kW[k]+\frac{1}{\tau^2}\sum_{k=0}^{\infty}\varphi[k]=0 \quad \textbf{(2.103)}$$

$$\alpha^2\sum_{k=0}^{\infty}kU[k]+\sum_{k=0}^{\infty}k\varphi[k]-f_0=0 \quad \textbf{(2.104)}$$

2.3.6 Semi-analytical results and discussions

Effects of ply orientation and voltage on the natural frequencies and the tip deflection of the piezolaminated beam are investigated and the results are presented in related graphics and tables. In order to validate the calculated results, comparisons with the studies in open literature are made and a very good agreement between the results are observed which proves the correctness and accuracy of the developed beam model.

2.3.6.1 Bimorph beam example

A bimorph piezoelectric beam which consists of two layers of KYNAR piezofilm, illustrated in Figure 2.10, is considered to validate the piezoelectric beam model developed in this section. In the present example, an external voltage is applied to the beam and the induced strain generates control forces that bend the bimorph beam. As shown in Figure1.18(a), the bimorphbender consists of two piezoelectric thin plates with opposite polarities. When the electric field is applied, one layer expands while the other contracts. Due to the constraint at the interface of these two layers,bending deformation occurs in the whole structure.

In Table 2.5, the material and geometrical properties of the beam model that is studied in this example are introduced.

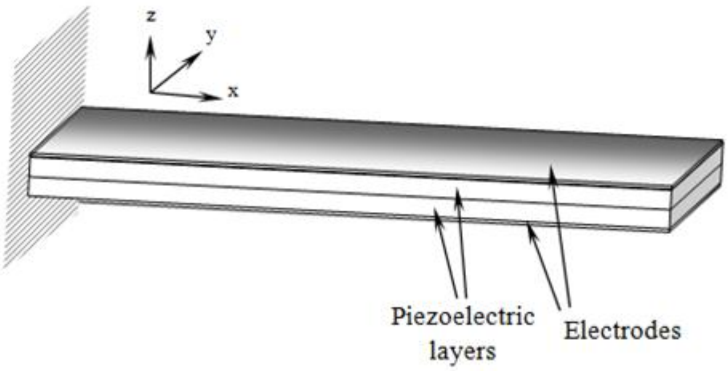

Figure 2.10: Bimorph beam model.

Table 2.5: Material and geometric properties of the bimorph beam, analytical model.

Material and Geometrical Properties			
$E_1\left(N/m^2\right)$	6.85×10^9	$L(m)$	0.08
$E_2\left(N/m^2\right)$	6.85×10^9	$b(m)$	0.01
$G_{12}\left(N/m^2\right)$	0.078×10^9	$h(m)$	0.00011
$G_{13}\left(N/m^2\right)$	–	$d_{31}(m/V)$	22.99×10^{-12}
$G_{23}\left(N/m^2\right)$	–	$d_{32}(m/V)$	4.6×10^9
ν_{12}	0.29		

Variation of the bimorph beam tip deflection with respect to the applied voltage is given in Figure 2.11. The calculated results are validated with the ones of Donthireddy and Chandrashekhara**(**1996) who used finite element method in their study**.**

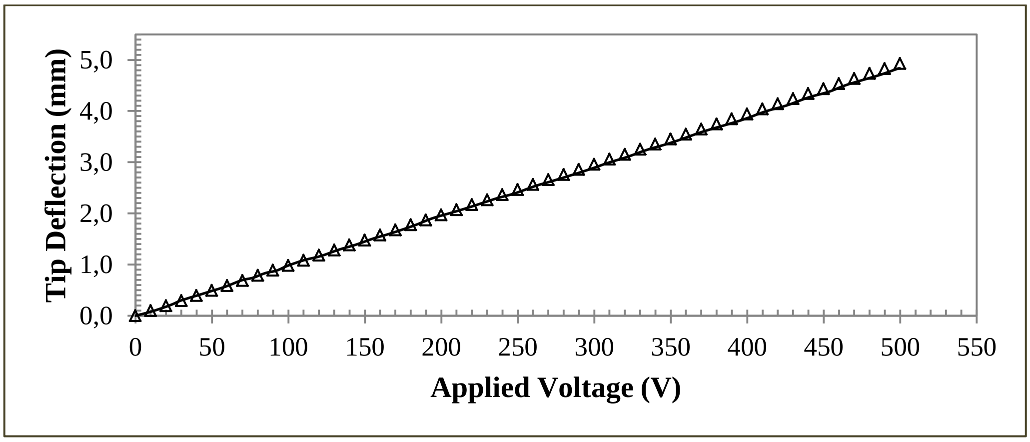

Figure 2.11: Variation of the tip deflection of the bimorph beam with respect to the appliedvoltage(—— : Present Study, △: Donthireddy and Chandrashekhara).

As illustrated in Figure 2.11, when the voltage that is applied to the piezoelectric layers increases, the piezolaminated composite beam has a larger tip deflection.

2.3.6.2 Piezolaminated composite beam example

A composite Timoshenko beam with one layer of piezoelectric material bonded to the top and bottom faces is considered to validate the derived piezolaminated composite beam formulation. The beam model is illustrated in Figure 2.12 and the layer distribution of the beam is $\left[PZT/0/90/90/0/PZT\right]$.

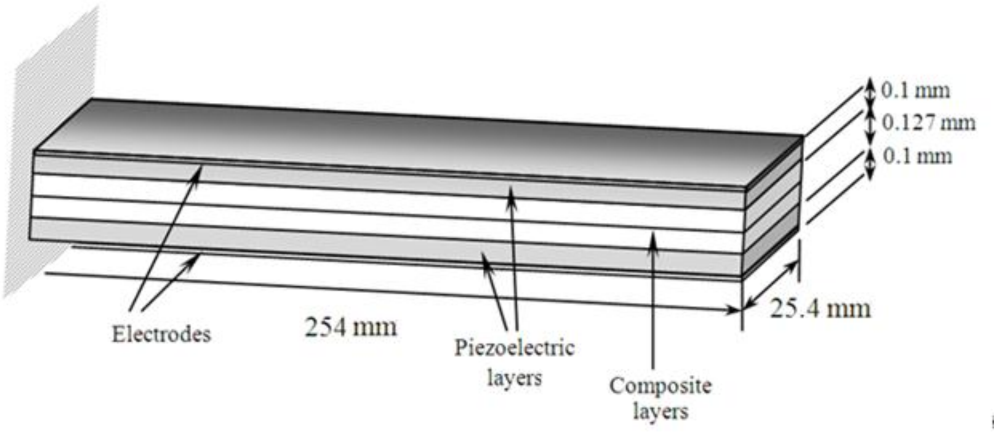

Figure 2.12: Piezolaminated composite beam model.

In Table 2.6, the material and geometrical properties of the piezolaminated composite Timoshenko beam model are given.

Table 2.6: Material and geometrical properties of the piezolaminated composite Timoshenko beam model.

Material and Geometrical Properties	Graphite Epoxy	PZT-5H
$E_1\left(N/m^2\right)$	144.8×10^{9}	63×10^{9}
$E_2\left(N/m^2\right)$	9.65×10^{9}	63×10^{9}
$G_{12}=G_{13}\left(N/m^2\right)$	7.1×10^{9}	24.8×10^{9}
$G_{23}\left(N/m^2\right)$	5.92×10^{9}	–
ν_{12}	0.3	0.28
$\rho\left(kg/m^3\right)$	1560	7600
$\bar{k}$	5/6	5/6
$L(m)$	0.254	0.254
$b(m)$	0.0254	0.0254
$h(m)$	1.27×10^{-4}	2×10^{-4}
$d_{31}=d_{32}\left(m/V\right)$	–	-166×10^{-12}

Firstly, natural frequencies are calculated for clamped-free boundary conditions and in Table 2.7, the calculated results are conpared with the ones given by Fridman and Abramovich(2008) who worked analytically in their study.

Table 2.7: Natural frequencies calculated for clamped-free boundary conditions.

Natural Frequencies (Hz)	
Present	Reference*
9.831	9.78
61.6012	61.11
172.452	171.17

* Fridman and Abramovich(2008)

In Table 2.7, it is seen that there is a very good agreement between the calculated results and the ones in open literature. Additionally, in Ozdemir Ozgumus and Kaya (2012), natural frequencies are also calculated and validated for the other boundary conditions, i.e. clamped-simply supported (CS) and simply supported (SS).

Secondly, effect of the ply orientation of piezolaminated composite beam on the first three natural frequencies is studied. The example is restricted to symmetric and nonsymmetric lay-up configurations and the results are given inTable 2.8.

Table 2.8: Variation of the first three natural frequencies with respect to ply orientation.

Ply Orientations		
PZT/0/30/30/0/PZT	PZT/0/60/60/0/PZT	PZT/0/90/90/0/PZT
9.9377	9.8456	9.8309
62.2441	61.6701	61.6015
174.1320	172.5370	172.4520
PZT/0/30/0/30/PZT	PZT/0/60/0/60/PZT	PZT/0/90/0/90/PZT
9.6966	9.2620	9.1815
60.7664	58.0426	57.5330
170.1410	162.5150	161.0650

Considering Table 2.8, it is noticed that when the composite core beam has symmetric ply configuration, the beam is stiffer and the natural frequencies are higher than the ones of nonsymmetric ply configuration. Additionally, it is noticed that increasing the value of the ply angle of the laminas has the same decreasing effect in both symmetric and nonsymmetric laminates. However, changing the ply angle in a nonsymmetric laminate makes a more dominant change in the beam frequencies.

In Figure 2.13, effect of ply orientation on the tip deflection is illustrated.

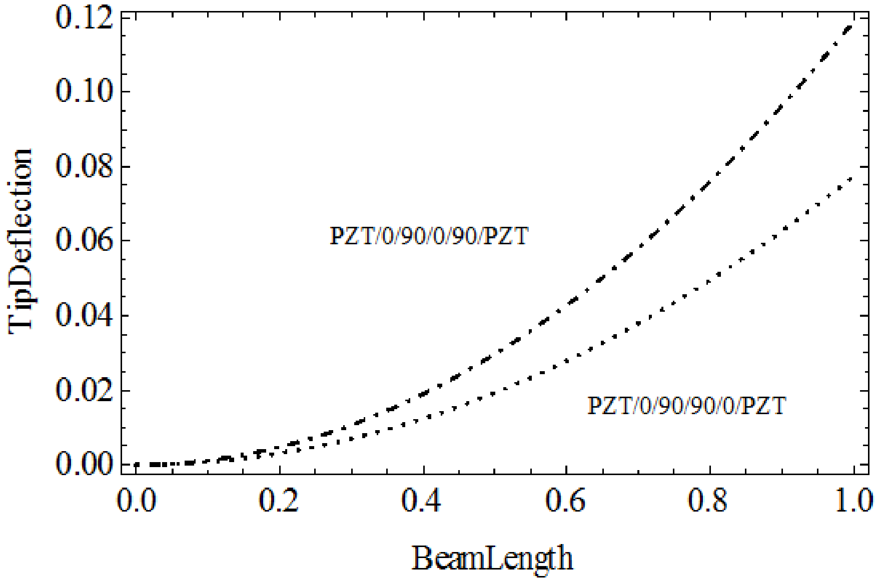

Figure 2.13: Effect of ply orientation on the tip deflection.

Here, it is noticed that symmetric laminates have smaller tip deflections than nonsymmetric laminates.

2.3.7 Finite element formulation

Finite element formulation of the piezoelectric actuator beam that undergoes extension and flapwise bending deflections is carried out in this section. The finite element model of the beam that is used for the formulation is illustrated in Figure 2.14.

Figure 2.14: Piezoelectric actuator beam finite element model.

Here, it is seen that a two noded simple beam element that has eight degrees of freedom is preferred to model the piezoelectric actuator.

Polinomials of appropriate order are used to define the displacement field as follows

$$u = a_0 + a_1 x \quad \textbf{(2.105)}$$

$$w = a_2 + a_3 x + a_4 x^2 + a_5 x^3 \quad \textbf{(2.106)}$$

$$\varphi = a_6 + a_7 x \quad \textbf{(2.107)}$$

$$\theta_y = w' - \varphi = a_3 - a_6 + (2a_4 - a_7)x + 3a_5 x^2 \quad \textbf{(2.108)}$$

where u is the elongation, w is the flapwise bending, θ_y is the angle due to bending and φ is the shear angle.

The nodal displacements are determined as the displacement values at the first node of the beam element, $x = 0$ and at the second node, $x = L$, respectively. These are given in matrix form as follows

$$\begin{Bmatrix} u_1 \\ w_1 \\ \theta_{y1} \\ \varphi_1 \\ u_2 \\ w_2 \\ \theta_{y2} \\ \varphi_2 \end{Bmatrix} = \begin{bmatrix} 1 & 0 & 0 & 0 & 0 & 0 & 0 & 0 \\ 0 & 0 & 1 & 0 & 0 & 0 & 0 & 0 \\ 0 & 0 & 0 & 1 & 0 & 0 & -1 & 0 \\ 0 & 0 & 0 & 0 & 0 & 0 & 1 & 0 \\ 1 & L & 0 & 0 & 0 & 0 & 0 & 0 \\ 0 & 0 & 1 & L & L^2 & L^3 & 0 & 0 \\ 0 & 0 & 0 & 1 & 2L & 3L^2 & -1 & -L \\ 0 & 0 & 0 & 0 & 0 & 0 & 1 & L \end{bmatrix} \begin{Bmatrix} a_0 \\ a_1 \\ a_2 \\ a_3 \\ a_4 \\ a_5 \\ a_6 \\ a_7 \end{Bmatrix} \quad \textbf{(2.109)}$$

Expressing the displacement field in terms of the nodal displacements gives

$$\{q\} = [N]\{q_e\} \quad \textbf{(2.110)}$$

where $\{q\}$ is the displacement field, $\{q_e\}$ is the nodal displacements and [N] is the matrix of shape functions whose expressions are given as follows

$$\{q\} = \{u \quad w \quad \theta_y \quad \varphi\}^T \quad \textbf{(2.111)}$$

$$\{q_e\} = \{u_1 \quad w_1 \quad \theta_{y1} \quad \varphi_1 \quad u_2 \quad w_2 \quad \theta_{y2} \quad \varphi_2\}^T \quad \textbf{(2.112)}$$

$$[N] = \{N_u \quad N_w \quad N_{\theta y} \quad N_\varphi\}^T \tag{2.113}$$

Components of the matrix of shape functions are

$$[N_u] = \left\{1-\frac{x}{L} \quad 0 \quad 0 \quad 0 \quad \frac{x}{L} \quad 0 \quad 0 \quad 0\right\} \tag{2.114}$$

$$\begin{aligned}[N_w] = \Bigg\{0 \quad & 1-\frac{3x^2}{L^2}+\frac{2x^3}{L^3} \quad x-\frac{2x^2}{L}+\frac{x^3}{L^2} \quad x-\frac{2x^2}{L}+\frac{x^3}{L^2} \\ 0 \quad & \frac{3x^2}{L^2}-\frac{2x^3}{L^3} \quad -\frac{x^2}{L}+\frac{x^3}{L^2} \quad -\frac{x^2}{L}+\frac{x^3}{L^2}\Bigg\}\end{aligned} \tag{2.115}$$

$$\begin{aligned}[N_{\theta y}] = \Bigg\{0 \quad & -\frac{6x}{L^2}+\frac{6x^2}{L^3} \quad 1-\frac{4x}{L}+\frac{3x^2}{L^2} \quad -\frac{3x}{L}+\frac{3x^2}{L^2} \\ 0 \quad & \frac{6x}{L^2}-\frac{6x^2}{L^3} \quad -\frac{2x}{L}+\frac{3x^2}{L^2} \quad -\frac{3x}{L}+\frac{3x^2}{L^2}\Bigg\}\end{aligned} \tag{2.116}$$

$$[N_\varphi] = \left\{0 \quad 0 \quad 0 \quad 1-\frac{x}{L} \quad 0 \quad 0 \quad 0 \quad \frac{x}{L}\right\} \tag{2.117}$$

where $[N_u]$, $[N_w]$, $[N_{\theta y}]$ and $[N_\varphi]$ are the shape functions associated with elongation, u, flapwise bending, w, rotation due to bending, θ_y and the shear angle φ, respectively.

Displacement field of a Timoshenko beam that undergoes extension and flapwise bending deflections is given by

$$u = u_0 - z\varphi \tag{2.118}$$

$$w = w_0 \tag{2.119}$$

Strain expressions are obtained as follows

$$\varepsilon_x = \frac{\partial u}{\partial x} = u_0' - z\varphi' \tag{2.120}$$

$$\gamma_{xz} = \frac{\partial w}{\partial x} + \frac{\partial u}{\partial z} = w' - \varphi = \theta_y \qquad \textbf{(2.121)}$$

Considering Eq.(2.120) and Eq.(2.121), the finite element formulation of the strain field is given by

$$\{\varepsilon\} = \begin{Bmatrix} \varepsilon_x \\ \gamma_{xz} \end{Bmatrix} = \begin{Bmatrix} [N_u]' - z[N_\varphi]' \\ [N_{\theta y}] \end{Bmatrix} \{q^e\} = [B]\{q^e\} \qquad \textbf{(2.122)}$$

where

$$[B] = \begin{bmatrix} 0 & -\frac{1}{L} \\ -\frac{6x}{L^2} + \frac{6x^2}{L^3} & 0 \\ 1 - \frac{4x}{L} + \frac{3x^2}{L^2} & 0 \\ -\frac{3x}{L} + \frac{3x^2}{L^2} & \frac{z}{L} \\ 0 & \frac{1}{L} \\ \frac{6x}{L^2} - \frac{6x^2}{L^3} & 0 \\ -\frac{2x}{L} + \frac{3x^2}{L^2} & 0 \\ -\frac{3x}{L} + \frac{3x^2}{L^2} & -\frac{z}{L} \end{bmatrix}^T \qquad \textbf{(2.123)}$$

The constitutive equations for a linear piezoelectric material, Eq.(2.1) and Eq.(2.2), can be written in matrix form as follows

$$\{D\} = [e]\{\varepsilon\} + [\in]\{\mathrm{E}\} \qquad \textbf{(2.124)}$$

$$\{\sigma\} = [\bar{Q}]\{\varepsilon\} - [e]^T\{\mathrm{E}\} \qquad \textbf{(2.125)}$$

where $\{D\}$ is the electric displacement vector, $[e]$ is the piezoelectric constant matrix, $\{\varepsilon\}$ is the strain vector, $[\in]$ is the permittivity matrix, $\{E\}$ is the electric field vector, $\{\sigma\}$ is the stress vector and $[Q]$ is the elastic stiffness matrix (Fuller et al., 1996).Eq.(2.124) and Eq. (2.125)express the direct piezoelectric effect used for sensors and the converse piezoelectric effect used for actuators, respectively.

In this section structural model for a piezoelectric actuator is built so Eq.(2.125) is going to be used for the finite element formulation.The first term in Eq.(2.125) is the mechanical part while the second term is the piezoelectric part. For the displacement field given by Eqs. (2.105)-(2.108), the stress-strain relationship related to the mechanical part isgiven by

$$\begin{Bmatrix} \sigma_1 \\ \sigma_5 \end{Bmatrix} = \begin{bmatrix} \bar{Q}_{11} & 0 \\ 0 & \bar{Q}_{55} \end{bmatrix} \begin{Bmatrix} \varepsilon_1 \\ \varepsilon_5 \end{Bmatrix} \tag{2.126}$$

Matrix form of the potential energy, Eq.(2.54), is

$$U = \frac{1}{2} \iint_A \int_x \{\varepsilon\}^T \{\sigma\} \, dxdA \tag{2.127}$$

Substituting Eq.(2.125) into Eq.(2.127) gives

$$U = \frac{1}{2} \iint_A \int_x \{\varepsilon\}^T \left[\bar{Q}\right] \{\varepsilon\} \, dxdA - \frac{1}{2} \iint_A \int_x \{\varepsilon\}^T [e]^T \{\mathrm{E}\} \, dxdA \tag{2.128}$$

The first term of Eq.(2.128) gives the element stiffness matrix while the second term contributes to the equation of motion as a damping term. Thus, the first term is considered to obtain the element stiffness matrix. Substituting Eq.(2.122) and Eq.(2.126) into the first part of Eq.(2.128) gives

$$U = \frac{1}{2} \iint_A \int_x \{q_e\}^T [B]^T \begin{bmatrix} \bar{Q}_{11} & 0 \\ 0 & \bar{Q}_{55} \end{bmatrix} [B] \{q_e\} \, dxdA \tag{2.129}$$

ReferringEq.(2.129), the element stiffness matrix that includes both mechanical and piezoelectric effects is obtained as follows

$$\left[K^e\right] = \iint_A [B]^T \begin{bmatrix} \bar{Q}_{11} & 0 \\ 0 & \bar{Q}_{55} \end{bmatrix} [B] dA \tag{2.130}$$

Considering the definitions given in Eqs.(2.19)-(2.21), the element stiffness matrix can be written in terms of the stiffness coefficients A_{11}, B_{11}, D_{11} and A_{55} as follows

$$
\left[K^e\right]=\begin{bmatrix}
\frac{A11}{L} & 0 & 0 & -\frac{B11}{L} & -\frac{A11}{L} & 0 & 0 & \frac{B11}{L} \\
0 & \frac{6A55}{5L} & \frac{A55}{10} & \frac{3A55}{5} & 0 & -\frac{6A55}{5L} & \frac{A55}{10} & \frac{3A55}{5} \\
0 & \frac{A55}{10} & \frac{2A55L}{15} & \frac{A55L}{20} & 0 & -\frac{A55}{10} & -\frac{A55L}{30} & \frac{A55L}{20} \\
-\frac{B11}{L} & \frac{3A55}{5} & \frac{A55L}{20} & \frac{D11}{L}+\frac{3A55L}{10} & \frac{B11}{L} & -\frac{3A55}{5} & \frac{A55L}{20} & -\frac{D11}{L}+\frac{3A55L}{10} \\
-\frac{A11}{L} & 0 & 0 & \frac{B11}{L} & \frac{A11}{L} & 0 & 0 & -\frac{B11}{L} \\
0 & -\frac{6A55}{5L} & -\frac{A55}{10} & -\frac{3A55}{5} & 0 & \frac{6A55}{5L} & -\frac{A55}{10} & -\frac{3A55}{5} \\
0 & \frac{A55}{10} & -\frac{A55L}{30} & \frac{A55L}{20} & 0 & -\frac{A55}{10} & \frac{2A55L}{15} & \frac{A55L}{20} \\
\frac{B11}{L} & \frac{3A55}{5} & \frac{A55L}{20} & -\frac{D11}{L}+\frac{3A55L}{10} & -\frac{B11}{L} & -\frac{3A55}{5} & \frac{A55L}{20} & \frac{D11}{L}+\frac{3A55L}{10}
\end{bmatrix} \qquad \textbf{(2.131)}
$$

Matrix form of the kinetic energy, Eq.(2.63), is

$$
T=\frac{1}{2}\iint_A\int_x \rho\{\dot{q}\}^T\{\dot{q}\}dxdA \qquad \textbf{(2.132)}
$$

Substituting Eq.(2.110) into Eq.(2.132) gives

$$
T=\frac{1}{2}\iint_A\int_x \rho\{\dot{q}_e\}^T[N]^T[N]\{\dot{q}_e\}dxdA \qquad \textbf{(2.133)}
$$

Referring Eq.(2.133), the element mass matrix is obtained as follows

$$
\left[M^e\right]=\frac{1}{2}\iint_A \rho[N]^T[N]dA \qquad \textbf{(2.134)}
$$

Considering the definitions given in Eqs. (2.65)-(2.67), the element mass matrix can be written in terms of the inertial terms I_0, I_1 and I_2 as follows

$$
\left[M^e\right]=\frac{L}{420}\begin{bmatrix}
140I_0 & 0 & 0 & -140I_1 & 70I_0 & 0 & 0 & -70I_1 \\
0 & 156I_0 & 22LI_0 & 22LI_0 & 0 & 54I_0 & -13LI_0 & -13LI_0 \\
0 & 22LI_0 & 4L^2I_0 & 4L^2I_0 & 0 & 13LI_0 & -3L^2I_0 & -3L^2I_0 \\
-140I_1 & 22LI_0 & 4L^2I_0 & 4(L^2I_0+35I_2) & -70I_1 & 13LI_0 & -3L^2I_0 & -3L^2I_0+70I_2 \\
70I_0 & 0 & 0 & -70I_1 & 140I_0 & 0 & 0 & -140I_1 \\
0 & 54I_0 & 13LI_0 & 13LI_0 & 0 & 156I_0 & -22LI_0 & -22LI_0 \\
0 & -13LI_0 & -3L^2I_0 & -3L^2I_0 & 0 & -22LI_0 & 4L^2I_0 & 4L^2I_0 \\
-70I_1 & -13LI_0 & -3L^2I_0 & -3L^2I_0+70I_2 & -140I_1 & -22LI_0 & 4L^2I_0 & 4(L^2I_0+35I_2)
\end{bmatrix} \qquad \textbf{(2.135)}
$$

Depending on the number of elements used in the structural modeling code, all the element matrices are assembled by considering the finite element rules to obtain the global matrices. The boundary conditions at the fixed end of the actuator, Eq.(2.72), are applied to the global matrices to get the reduced matrices and the following matrix system of equations are obtained for the structural model of the bender type piezoelectric actuator.

$$[M]\{\ddot{q}\}+[K]\{q\}=\{0\} \tag{2.136}$$

Modal analysis is applied to Eq.(2.136) to calculate the natural frequencies. Firstly, the modal matrix, $[\Phi]$, is calculated by using the eigenvectors obtained by solving the following determinant

$$\left|-\omega^2[M]+[K]\right|=0 \tag{2.137}$$

Premultiplying Eq.(2.136) by the transpose of the model matrix and postmultiplying it by the modal matrix give

$$-\omega^2[I]+\left[\lambda^2\right]=\{0\} \tag{2.138}$$

where $[I]$ is the identity matrix, $\left[\lambda^2\right]$ is the diagonal matrix of natural frequencies.

2.3.8 Finite element results and validation

2.3.8.1 Bimorph beam example

Voltage is applied across the thickness of a bimorph beam and the tip deflection is calculated by the finite element method. The tip deflection of the beam is calculated for various voltage values from 0 to 100 V. Material and geometrical properties of the beam is given in Table 2.9.

Table 2.9: Material and geometrical properties of the bimorph beam model,finite element model.

Material and Geometrical Properties			
$E_1\left(N/m^2\right)$	2×10^9	ν_{12}	0.29
$E_2\left(N/m^2\right)$	2×10^9	$L(m)$	0.1
$G_{12}\left(N/m^2\right)$	0.775×10^9	$b(m)$	0.005
$G_{13}\left(N/m^2\right)$	–	$h(m)$	0.0005
$G_{23}\left(N/m^2\right)$	–	$d_{31}(m/V)$	2.3×10^{-11}

Mode shape of the bimorph beam that is plotted for V = 0.5 is shown in Figure 2.15 and variation of the tip deflection with respect to the applied voltage is shown in Figure 2.16. Both of the figures reveal that there is a very good agreement between the calculated results and the results of Hwang and Park (1993)who used afour-node, 12-degree-of-freedom quadrilateral plate bending element for finite element formulation.

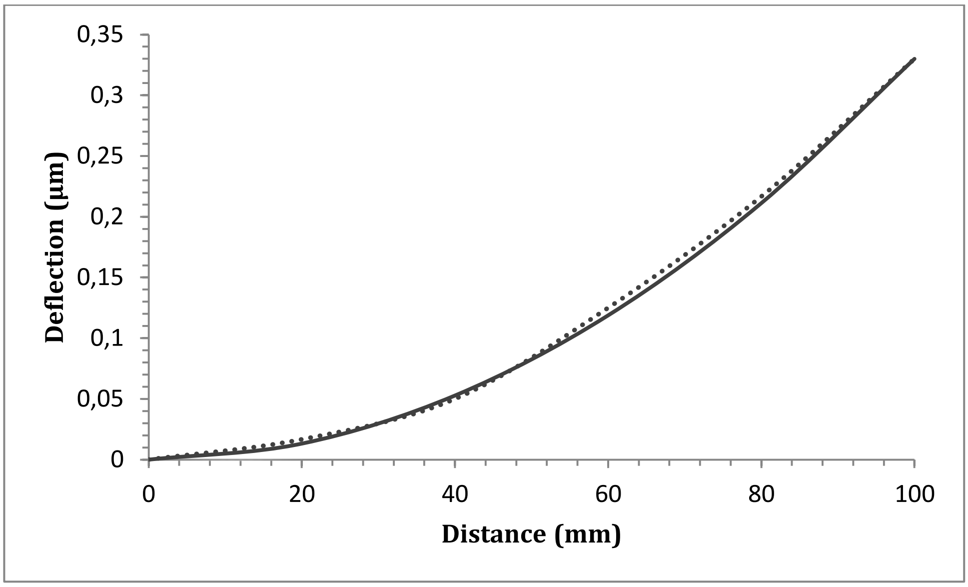

Figure 2.15 : Mode shape of the piezoelectric PVDF bimorph beam (input V=0.5), (.......: Present, ——: Hwang and Park).

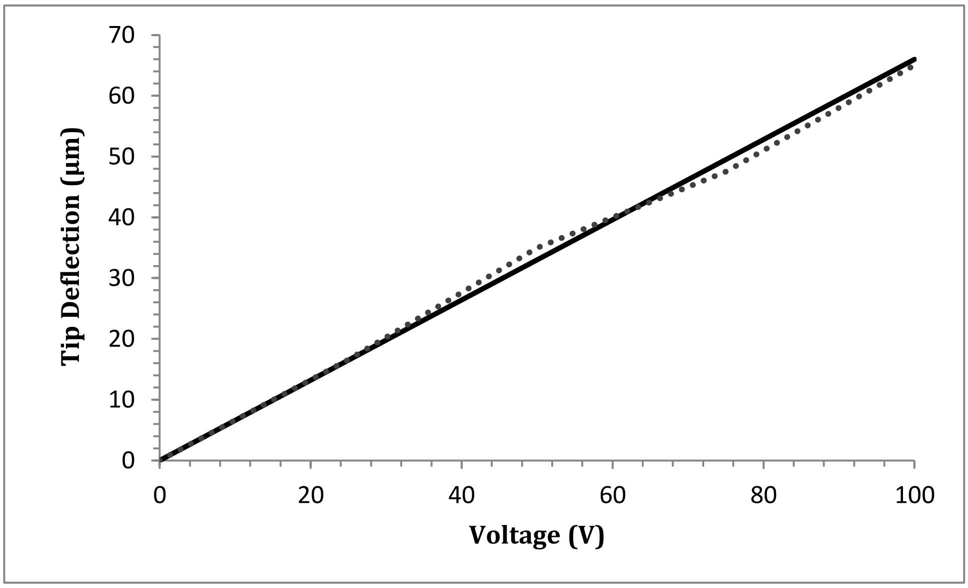

Figure 2.16: Tip deflection of the piezoelectric PVDF bimorph beam with respect to the input voltage, (.......: Present, ——:Hwang and Park).

2.3.8.2 Piezolaminated composite beam example

Dimensionless natural frequencies of the piezolaminated composite timoshenko beam whose properties are given in Table 2.6 are calculated for clamped-free boundary conditions and are given in Table 2.10. The ply orientation of the beam is $[PZT/0/90/90/0/PZT]$.

The calculated results are compared with ones that are obtained semi-analytically in Section 2.3.5 and that have already been validated with the ones of Fridmen and Abramovich (2008) who worked analytically in their study.

Table 2.10: Natural frequencies of graphite epoxy beam with two piezoelectriclayers.

Natural Frequencies (Hz)		
Present (FEM)	**Present (Semi-Analytical)**	**Reference***
9.83564	9.83088	9.78
61.8103	61.6015	61.11
173.851	172.72	171.17

* Fridman and Abramovich(2008)

2.4 Rotor Blade Structural Model

In this section, structural modeling of a rotating bending-bending-torsion coupled Euler-Bernoulli beam is carried out for the helicopter blade. Both the potential and the kinetic energy expressions are derived step bystep using explanatory tables and figures. The parameters for the hub radius, rotationalspeed and bending- bending-torsion coupling are incorporated into the energy expressions. The governing differential equations of motion and the related boundary conditions are obtained by applying the Hamilton's principle. In order to solve the derived equations, the Differential Transform Method (DTM) whose details are given in Section 2.3.5 is used. After the analytical part is completed, finite element formulation starts by considering the energy expressions that are derived analytically. A displacement field is defined for the coupled beam and the shape functions are obtained. These shape functions are substituted into the energy expressions to get the element matrices which are assembled to obtain the global matrices. This system of equations are solved to get the results of finite element formulation. Moreover, rotation is added to both the analytical and the finite element formulation. At the end of this section, validation of both formulations, i.e. sei-manalytical and finite element, is made by comparing the results with open literature and it is noticed that there is a very good agreement between the results.

2.4.1 Beam model

When the cross-sections of an isotropic beam have two symmetry axes, the shear center and the centroid of the cross-sections coincide. Therefore, flapwise bending and chordwise bending vibrations are not coupled with the torsional vibration. However, for a monosymmetric cross-section, the shear center and the centroid do not coincide and the bending vibration that is in the direction of the symmetry axis is independent of the other vibrations while the bending vibration that is perpendicular to the symmetry axis is coupled with the torsional vibration (Li et al., 2004). Thus, for structures with asymmetric cross-section, bending vibrations, i.e., flapwise bending and chordwise bending, get coupled with the torsion vibration.

The governing differential equations of motion are derived for a beam model that has such an asymmetric cross-section and that undergoes coupled flapwise bending-chordwise bending-torsion vibrations. The beam that is illustrated in Figure 2.17, is modeled as anEuler-Bernoulli beam since helicopter blades are long and slender structures.

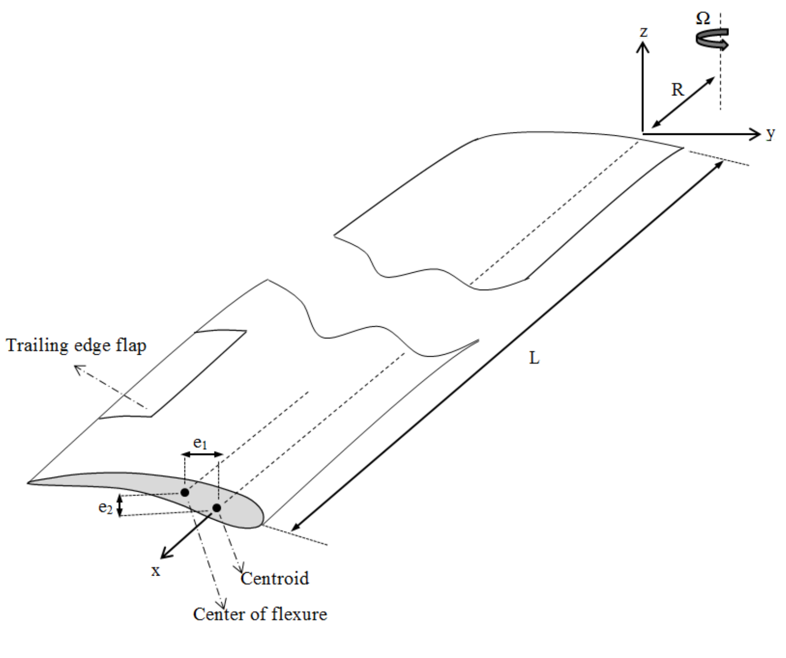

Figure 2.17: Helicopter blade with asymmetric cross-section.

Here, a cantilever beam of length L, with hub radius R, is shown. The xyz axes represent a global orthogonal coordinate system.The beam is assumed to be rotating at a constant angular velocity, Ω. In the right-handed Cartesian coordinate system, the z-axis is parallel to the axis of rotation, but not coincident and the y-axis lies in the plane of rotation.The principal axes of the beam cross-sections are, therefore, parallel to y and z directions, respectively. Since the beam has an asymmetric cross-section, the center of flexure and the centroid are not coincident. The e_1 and e_2 represent the offsets of the center of flexure from the centroid in the y and z directions, respectively.

2.4.2 Energy expressions

The cross-sectional view, longitudinal views in the x-y and x-z planes of the bending- bending-torsion coupled motion of the Euler-Bernoulli beam model are given in Figure 2.18, Figure 2.19 and Figure 2.20, respectively.

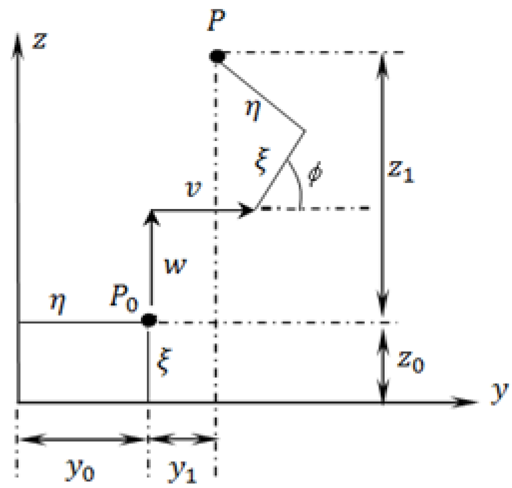

Figure 2.18: Cross-sectional viewof bending-bending-torsion coupled Euler-Bernoulli beam.

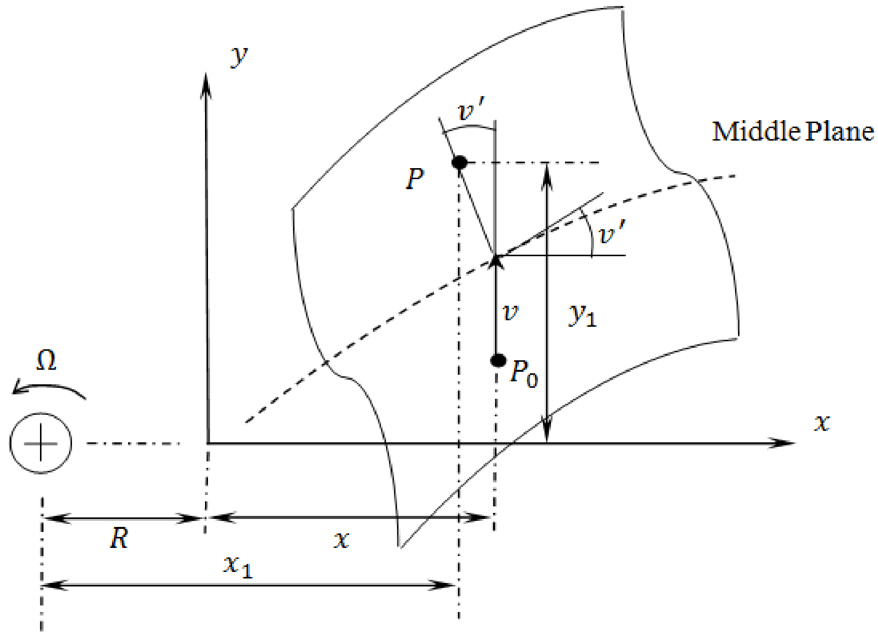

Figure 2.19: Longitudinal view of bending-bending-torsion coupledEuler-Bernoulli beam in the x-y plane.

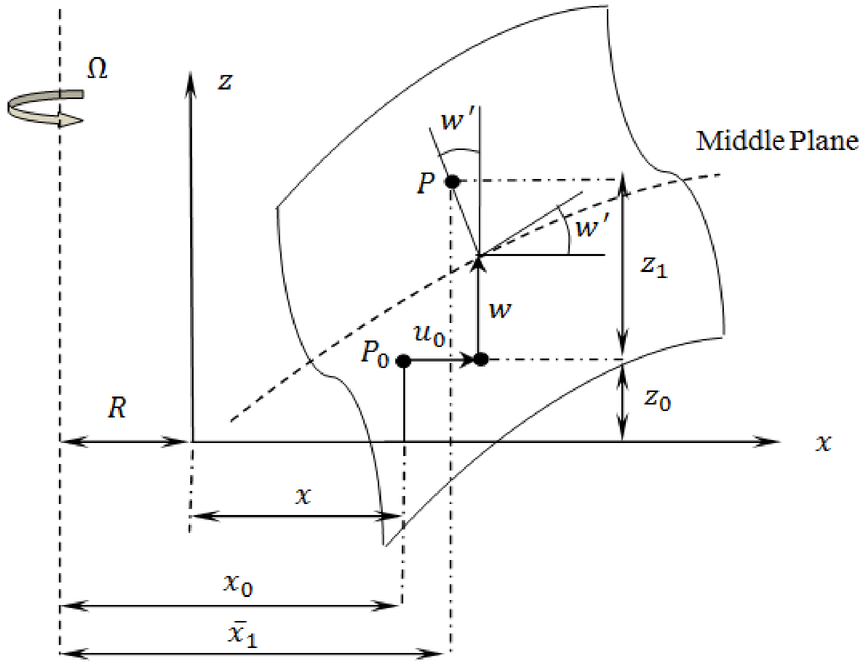

Figure 2.20: Longitudinal view of bending-bending-torsion coupled Euler-Bernoulli beam in the x-z plane.

Here, a reference point is chosen and is represented by P_0 before deformation and by P after deformation. The beam undergoes flapwise bending, chordwise bending and torsion vibrations, respectively. Thus, $\bar{x}_1$ is the spanwise coordinate of the reference point after the flapwise bending displacement and x_1 is the spanwise coordinate of the reference point after the chordwise bending displacement. In other words, x_1 has all the terms of $\bar{x}_1$ and it also has additional terms.

Considering Figures 2.18-2.20, the coordinates of the reference point are obtained

Before deflection (coordinates of P_0):

$$x_0 = R + x \tag{2.139}$$

$$y_0 = \eta \tag{2.140}$$

$$z_0 = \xi \tag{2.141}$$

After deflection (coordinates of P):

$$\bar{x}_1 = R + x + u_0 - (\eta Sin\phi + \xi Cos\phi) Sinw' \tag{2.142}$$

$$\begin{aligned} x_1 = R + x + u_0 - (\eta Sin\phi + \xi Cos\phi) Sinw' - \\ (\eta Cos\phi - \xi Sin\phi) Sinv' \end{aligned} \tag{2.143}$$

$$y_1 = v + \eta Cos\phi - \xi Sin\phi \tag{2.144}$$

$$z_1 = w + \eta Sin\phi + \xi Cos\phi \tag{2.145}$$

where x is the offset of the reference point, P_0, from the hub, u_0 is the axial displacement due to the centrifugal force, η is the offset of the reference point from the axis of rotation, ξ is the offset of the reference point from the middle plane, v is the chordwise bending displacement, v' is the rotation due to chordwise bending, w is the flapwise bending displacement, w' is the rotation due to flapwise bending and ϕ is the torsion angle.

The rotations due to chordwise and flapwise bending displacements, v' and w', are small so it is assumed that $Sinv' \cong v'$ and $Sinw' \cong w'$. The torsion angle ϕ is also small so $Sin\phi \cong \phi$ but in order to investigate the torsional stability, the second order terms are kept for $Cos\phi$ so it is assumed that $Cos\phi \cong 1 - \frac{\phi^2}{2}$ (Hodges and Dowell, 1974). Considering these assumptions, Eqs. (2.143)-(2.145) can be rewritten as follows

$$x_1 = R + x + u_0 - \left[\eta\phi + \xi(1-\frac{\phi^2}{2})\right]w' - \left[\eta(1-\frac{\phi^2}{2}) - \xi\phi\right]v' \qquad \textbf{(2.146)}$$

$$y_1 = v + \eta(1-\frac{\phi^2}{2}) - \xi\phi \qquad \textbf{(2.147)}$$

$$z_1 = w + \eta\phi + \xi(1-\frac{\phi^2}{2}) \qquad \textbf{(2.148)}$$

The position vectors of the reference point before and after deformation are $\vec{r}_0$ and $\vec{r}_1$, respectively and the differentials of these position vectors are given by

$$d\vec{r}_0 = (dx_0)\vec{i} + (dy_0)\vec{j} + (dz_0)\vec{k} \qquad \textbf{(2.149)}$$

$$d\vec{r}_1 = (dx_1)\vec{i} + (dy_1)\vec{j} + (dz_1)\vec{k} \qquad \textbf{(2.150)}$$

where the derivatives of the coordinates are

$$dx_0 = dx \qquad \textbf{(2.151)}$$

$$dy_0 = d\eta \qquad \textbf{(2.152)}$$

$$dz_0 = d\xi \qquad \textbf{(2.153)}$$

$$\begin{aligned} dx_1 = &\left\{1 + u_0' - \left[\xi(1-\frac{\phi^2}{2}) + \eta\phi\right]w'' + (\xi\phi\phi' - \eta\phi')w' + (\eta\phi\phi' + \xi\phi')v'\right\} - \\ &\left[\phi w' + (1-\frac{\phi^2}{2})v'\right]\mathrm{d}\eta + \left[\phi v' - (1-\frac{\phi^2}{2})w'\right]d\xi \end{aligned} \qquad \textbf{(2.154)}$$

$$dy_1 = (v' - \eta\phi\phi' - \xi\phi')dx + (1-\frac{\phi^2}{2})d\eta - \phi d\xi \qquad \textbf{(2.155)}$$

$$dz_1 = (w' - \xi\phi\phi' + \eta\phi')dx + \phi d\eta + (1-\frac{\phi^2}{2})d\xi \qquad \textbf{(2.156)}$$

Here, dx, $d\eta$ and $d\xi$ are the increments along the deformed elastic axis and two cross sectional axes, respectively.

Substituting Eqs. (2.151)-(2.156) into Eq. (2.46), the components of the strain tensor ε_{ij} are obtained as follows

$$\varepsilon_{xx} = u_0' + \frac{(v')^2}{2} + \frac{(w')^2}{2} - \eta v'' - \xi w'' + \xi\phi v'' - \eta\phi w'' + \frac{1}{2}\left(\eta^2 + \xi^2\right)\left(\phi'\right)^2 \quad \textbf{(2.157)}$$

$$2\gamma_{x\eta} = -\xi\phi' + \eta\phi\phi' - u_0'v' + \eta v'v'' + \xi v'w'' \quad \textbf{(2.158)}$$

$$2\gamma_{x\xi} = \eta\phi' + \xi\phi\phi' - u_0'w' + \xi w'w'' + \eta w'v'' \quad \textbf{(2.159)}$$

In order to obtain simpler expressions for the strain components, Eqs.(2.157)-(2.159), higher order terms can be neglected so an order of magnitude analysis is performed by using the ordering scheme, used by Hodges and Dowell (1974) and introduced in Table 2.11.

Table 2.11: Ordering scheme for bending-bending-torsion coupled Euler-Bernoullibeam formulation.

Term	Order
u_0'	$O(\varepsilon^2)$
v'	$O(\varepsilon)$
w'	$O(\varepsilon)$
ϕ	$O(\varepsilon)$
ϕ'	$O(\varepsilon^2)$
v''	$O(\varepsilon^2)$
w''	$O(\varepsilon^2)$

Referring Table 2.11, Eqs.(2.157)-(2.159) can be simplified as follows

$$\varepsilon_{xx} = u_0' + \frac{(v')^2}{2} + \frac{(w')^2}{2} - \eta v'' - \xi w'' \quad \textbf{(2.160)}$$

$$2\gamma_{x\eta} = -\xi\phi' \quad \textbf{(2.161)}$$

$$2\gamma_{x\xi} = \eta\phi' \quad \textbf{(2.162)}$$

The uniform strain, ε_0, and the associated axial displacement, u_0, due to the centrifugal force, $F_{CF}(x)$, are related to each other as follows

$$u_0' = \varepsilon_0 = \frac{F_{CF}(x)}{EA} \quad \textbf{(2.163)}$$

where the expression of the centrifugal force, $F_{CF}(x)$, is given by

$$F_{CF}(x) = \int_x^L \rho A(R+x)\Omega^2 dx \quad \textbf{(2.164)}$$

The potential energy expression is given as follows

$$\begin{aligned} U &= \frac{1}{2}\int_0^L \iint_A \left(\sigma_{xx}\varepsilon_{xx} + \tau_{x\eta}\gamma_{x\eta} + \tau_{x\xi}\gamma_{x\xi}\right) d\eta d\xi dx = \\ &\frac{1}{2}\int_0^L \iint_A \left[E\varepsilon_{xx}^2 + G\left(\gamma_{x\eta}^2 + \gamma_{x\xi}^2\right)\right] d\eta d\xi dx \end{aligned} \quad \textbf{(2.165)}$$

where A is the cross-sectional area, E is the Young's modulus and G is the shear modulus.

The area integrals that are frequently used in the derivation of energy expressions are given in Table 2.12(Hodges and Dowell, 1974).

Table 2.12: Area integrals for energy expressions.

Area Integrals	
$I_\alpha = \iint_A \rho(\eta^2 + \xi^2) d\eta d\xi$	$I_z = \iint_A \eta^2 d\eta d\xi$
$J = \iint_A (\eta^2 + \xi^2) d\eta d\xi$	$I_y = \iint_A \xi^2 d\eta d\xi$
$Ae_1 = \iint_A \eta d\eta d\xi$	$I_{yz} = \iint_A \xi\eta d\eta d\xi$
$Ae_2 = \iint_A \xi d\eta d\xi$	

where I_α is the mass moment of inertia about the elastic axis, I_z, I_y and I_{yz} are the second moments of inertia.

Substituting Eqs. (2.157)-(2.159)into Eq.(2.165), taking integration over the blade cross-section and referring to the definitions given inTable 2.12, the following expression for the potential energy is obtained.

$$U = \frac{1}{2}\int_0^L \Big\{F_{CF}(x)\left[\left(v'\right)^2 + \left(w'\right)^2 + \frac{I_\alpha}{\rho A}\left(\phi'\right)^2\right] + EI_z\left(v''\right)^2 + EI_y\left(w''\right)^2 + GJ(\phi')^2\Big\}dx \qquad \textbf{(2.166)}$$

where EI_z and EI_y are the bending rigidities and GJ is the torsional rigidity of the beam cross section.

Variation of the potential energy, Eq.(2.166), is given by

$$\delta U = \int_0^L \Big\{F_{CF}(x)\left[v'\delta v' + w'\delta w' + \frac{I_\alpha}{\rho A}\phi'\delta\phi'\right] + EI_z v''\delta v'' + EI_y w''\delta w'' + GJ\phi'\delta\phi'\Big\}dx \qquad \textbf{(2.167)}$$

In order to obtain the kinetic energy expression, the velocity field has to be determined. The velocity vector of the point P due to rotation of the beam is given by

$$\vec{V} = \frac{\partial \vec{r}}{\partial t} + \Omega\vec{k}\times\vec{r} \qquad \textbf{(2.168)}$$

where

$$\vec{r} = \left\{R + x + u_0 - \left[\eta\phi + \xi(1-\frac{\phi^2}{2})\right]w' - \left[\eta(1-\frac{\phi^2}{2}) - \xi\phi\right]v'\right\}\vec{i} + \left[v + \eta(1-\frac{\phi^2}{2}) - \xi\phi\right]\vec{j} + \left[w + \eta\phi + \xi(1-\frac{\phi^2}{2})\right]\vec{k} \qquad \textbf{(2.169)}$$

Substituting Eq. (2.169)into Eq.(2.168), the total velocity vector expression can be obtained as follows

$$\vec{V} = V_x\vec{i} + V_y\vec{j} + V_z\vec{k} \qquad \textbf{(2.170)}$$

where the velocity components are

$$V_x = \dot{u}_0 + (\xi\phi\dot{\phi} - \eta\dot{\phi})w' - \left[\eta(1-\frac{\phi^2}{2}) - \xi\phi\right]\dot{v}' + (\eta\phi\dot{\phi} + \xi\dot{\phi})v' - \left[v + \eta(1-\frac{\phi^2}{2}) - \xi\phi\right]\Omega \qquad \textbf{(2.171)}$$

$$V_y = \dot{v} - (\eta\phi + \xi)\dot{\phi} + \left\{ R + x + u_0 - \left[\eta\phi + \xi(1 - \frac{\phi^2}{2}) \right] w' - \left[\eta(1 - \frac{\phi^2}{2}) - \xi\phi \right] v' \right\} \Omega \quad \textbf{(2.172)}$$

$$V_z = \dot{w} + (\eta - \xi\phi)\dot{\phi} \quad \textbf{(2.173)}$$

Here, $(\dot{\ })$ represents derivation with respect to time, t.

The kinetic energy expression is given by

$$T = \frac{1}{2}\int_0^L \iint_A \rho\left(V_x^2 + V_y^2 + V_z^2\right) d\eta d\xi dx \quad \textbf{(2.174)}$$

Substituting Eqs. (2.171)-(2.173)into Eq. (2.174)and using the definitions given in Table 2.12, the following kinetic energy expression is obtained

$$\begin{aligned} T = \int_0^L \{ & 2\rho A e_1 \left[\dot{w}\dot{\phi} - \Omega^2 (R + x)\phi w' \right] - \\ & 2\rho A e_2 \left[\Omega^2 v\phi + \dot{v}\dot{\phi} - \Omega^2 (R + x) v'\phi + \right. \\ & 2\rho I_{yz}\Omega^2 v' w' + \rho I_z \Omega^2 (v')^2 + \rho I_y \Omega^2 \left[\phi^2 + (w')^2 \right] + \\ & \rho A \left[(\dot{v})^2 + (\dot{w})^2 + \Omega^2 (v)^2 \right] + I_\alpha (\dot{\phi})^2 \} dx \end{aligned} \quad \textbf{(2.175)}$$

Variation of the kinetic energy, Eq.(2.175), is given by

$$\begin{aligned} \delta T = \int_0^L \{ & \rho A e_1 \left[\left(\dot{w}\delta\dot{\phi} + \dot{\phi}\delta\dot{w} \right) - \Omega^2 (R + x)\left(\phi\delta w' + w'\delta\phi \right) \right] - \\ & \rho A e_2 \left[\Omega^2 (v\delta\phi + \phi\delta v) + \left(\dot{v}\delta\dot{\phi} + \dot{\phi}\delta\dot{v} \right) - \right. \\ & \left. \Omega^2 (R + x)\left(\phi\delta v' + v'\delta\phi \right) \right] + \rho I_z \Omega^2 v'\delta v' + \\ & \rho I_y \Omega^2 \left[\phi\delta\phi + w'\delta w' \right] + \rho I_{yz}\Omega^2 \left(v'\delta w' + w'\delta v' \right) + \\ & \rho A \left(\dot{v}\delta\dot{v} + \dot{w}\delta\dot{w} + \Omega^2 v\delta v \right) + I_\alpha \dot{\phi}\delta\dot{\phi} \end{aligned} \quad \textbf{(2.176)}$$

2.4.3 Governing equations of motion and boundary conditions

The equations of motion and the associated boundary conditions are obtained by applying the Hamilton's principle given in Eq. (2.68). Substituting Eq.(2.167) and Eq.(2.176)into Eq. (2.68), the equations of motion and the related boundary conditions are obtained as follows

Equations of motion:

$$
\begin{aligned}
&EI_z v^{IV} - (F_{CF} v')' + \rho I_z \Omega^2 v'' - \rho A \Omega^2 v + \rho I_{yz} \Omega^2 w'' + 2\rho A \Omega^2 e_2 \phi + \\
&\rho A \Omega^2 e_2 \left(R + x\right) \phi' + \rho A \left(\ddot{v} - e_2 \ddot{\phi}\right) = 0
\end{aligned} \tag{2.177}
$$

$$
\begin{aligned}
&EI_y w^{IV} - (F_{CF} w')' + \rho I_y \Omega^2 w'' + \rho I_{yz} \Omega^2 v'' - \rho A \Omega^2 e_1 \phi - \\
&\rho A \Omega^2 e_1 \left(R + x\right) \phi' + \rho A \left(\ddot{w} + e_1 \ddot{\phi}\right) = 0
\end{aligned} \tag{2.178}
$$

$$
\begin{aligned}
&-\frac{I_\alpha}{\rho A}\left(F_{CF}\phi'\right)' - GJ\phi'' - \rho A \Omega^2 \left[\left(R + x\right)\left(e_1 w' + e_2 v'\right) - e_2 v\right] + \\
&\rho \Omega^2 I_y \phi + \rho A \left(e_1 \ddot{w} - e_2 \ddot{v}\right) + I_\alpha \ddot{\phi} = 0
\end{aligned} \tag{2.179}
$$

Boundary conditions:

At x=0 $$v\left(0,t\right) = w\left(0,t\right) = \phi\left(0,t\right) = v'\left(0,t\right) = w'\left(0,t\right) = 0 \tag{2.180}$$

At x=L $$-F_{CF} v' + EI_z v''' + \rho A \Omega^2 e_2 \left(R + x\right) \phi + \rho I_z \Omega^2 v' + \rho I_{yz} \Omega^2 w' = 0 \tag{2.181}$$

$$-F_{CF} w' + EI_y w''' - \rho A \Omega^2 e_1 \left(R + x\right) \phi + \rho I_y \Omega^2 w' + \rho I_{yz} \Omega^2 v' = 0 \tag{2.182}$$

$$\phi' = v'' = w'' = 0 \tag{2.183}$$

The boundary conditions expressed by Eq. (2.181) and Eq. (2.182) can be written in a simpler form by noting that the centrifugal force is zero at the free end of the beam, $F_{CF}\left(L\right) = 0$. Thus,

$$EI_z v''' + \rho A \Omega^2 e_2 \left(R + x\right) \phi + \rho I_z \Omega^2 v' + \rho I_{yz} \Omega^2 w' = 0 \tag{2.184}$$

$$EI_y w''' - \rho A \Omega^2 e_1 \left(R + x\right) \phi + \rho I_y \Omega^2 w' + \rho I_{yz} \Omega^2 v' = 0 \tag{2.185}$$

2.4.4 Simple harmonic motion and dimensionless parameters

In order to investigate the free vibration of the beam model considered in this study, a sinusoidal variation of $v(x,t)$, $w(x,t)$ and $\phi(x,t)$ with a circular natural frequency, ω, is assumed and the functions are approximated as

$$v(x,t) = \bar{v}(x)e^{i\omega t} \quad \textbf{(2.186)}$$

$$w(x,t) = \bar{w}(x)e^{i\omega t} \quad \textbf{(2.187)}$$

$$\phi(x,t) = \bar{\phi}(x)e^{i\omega t} \quad \textbf{(2.188)}$$

Substituting Eqs. (2.186)-(2.188) into Eqs. (2.177)-(2.179) and into the boundary conditions results in the following expressions

Equations of motion:

$$\begin{gathered} EI_z\bar{v}^{iv} - (F_{CF}\bar{v}')' + \rho I_z\Omega^2\bar{v}'' - \rho A\Omega^2\bar{v} + \rho I_{yz}\Omega^2\bar{w}'' + 2\rho A\Omega^2 e_2\bar{\phi} + \\ \rho A\Omega^2 e_2(R+x)\bar{\phi}' + \rho A\omega^2\left(e_2\bar{\phi} - \bar{v}\right) = 0 \end{gathered} \quad \textbf{(2.189)}$$

$$\begin{gathered} EI_y\bar{w}^{iv} - (F_{CF}\bar{w}')' + \rho I_y\Omega^2\bar{w}'' + \rho I_{yz}\Omega^2\bar{v}'' - \rho A\Omega^2 e_1\bar{\phi} - \\ \rho A\Omega^2 e_1(R+x)\bar{\phi}' - \rho A\omega^2\left(\bar{w} + e_1\bar{\phi}\right) = 0 \end{gathered} \quad \textbf{(2.190)}$$

$$\begin{gathered} -\frac{I_\alpha}{\rho A}\left(F_{CF}\bar{\phi}'\right)' - GJ\bar{\phi}'' - \rho A\Omega^2\left[(R+x)\left(e_1\bar{w}' + e_2\bar{v}'\right) - e_2\bar{v}\right] + \\ \rho\Omega^2 I_y\bar{\phi} + \rho A\omega^2\left(e_2\bar{v} - e_1\bar{w}\right) + I_\alpha\bar{\phi} = 0 \end{gathered} \quad \textbf{(2.191)}$$

Boundary conditions:

At x=0 $\quad \bar{v}(0,t) = \bar{w}(0,t) = \bar{\phi}(0,t) = \bar{v}'(0,t) = \bar{w}'(0,t) = 0 \quad$ **(2.192)**

At x=L $\quad EI_z\bar{v}''' + \rho A\Omega^2 e_2(R+x)\bar{\phi} + \rho I_z\Omega^2\bar{v}' + \rho I_{yz}\Omega^2\bar{w}' = 0 \quad$ **(2.193)**

$$EI_y\bar{w}''' - \rho A\Omega^2 e_1(R+x)\bar{\phi} + \rho I_y\Omega^2\bar{w}' + \rho I_{yz}\Omega^2\bar{v}' = 0 \quad \textbf{(2.194)}$$

$$\bar{\phi}' = \bar{v}'' = \bar{w}'' = 0 \quad \textbf{(2.195)}$$

In order to simplify the equations of motion and tobe able to make comparisons with open literature, dimensionless parameters are defined as given in Table 2.13.

Table 2.13: Dimensionless parameters for bending-bending-torsion coupledhelicopter blade.

Dimensionless Parameters		
$\bar{x} = \dfrac{x}{L}$	$\tilde{v} = \dfrac{\bar{v}}{L}$	$\lambda^2 = \dfrac{\rho A \Omega^2 L^4}{EI_y}$
$\sigma = \dfrac{R}{L}$	$\tilde{\phi} = \bar{\phi}$	$\mu^2 = \dfrac{\rho A \omega^2 L^4}{EI_y}$
$\bar{e}_1 = \dfrac{e_1}{L}$	$\Lambda_1 = \dfrac{I_z}{I_y}$	$r^2 = \dfrac{I_y}{AL^2}$
$\bar{e}_2 = \dfrac{e_2}{L}$	$\Lambda_2 = \dfrac{I_{yz}}{I_y}$	$e^2 = \dfrac{GJ}{EI_y}$
$\tilde{w} = \dfrac{\bar{w}}{L}$	$\Lambda_3 = \dfrac{I_{yz}}{I_z}$	$r_\alpha^2 = \dfrac{I_\alpha}{\rho AL^2}$

Substituting the dimensionless parameters into Eqs.(189)-(195), the dimensionless equations of motion and the dimensionless boundary conditions are expressed as follows

Equations of motion:

$$\begin{aligned} &-\frac{\Lambda_1}{\eta^2}\tilde{v}^{****} + \left[\sigma(1-\bar{x}) + \frac{1}{2}(1-\bar{x}^2) - \Lambda_1 r^2\right]\tilde{v}^{**} - \left(\sigma + \bar{x}\right)\tilde{v}^{*} + \\ &\left(1 + \frac{\mu^2}{\lambda^2}\right)\tilde{v} - \Lambda_2 r^2 \tilde{w}^{**} - \tilde{e}_2\left(2 + \frac{\mu^2}{\lambda^2}\right)\tilde{\phi} - \tilde{e}_2\left(\sigma + \bar{x}\right)\tilde{\phi}^{*} = 0 \end{aligned} \quad \textbf{(2.196)}$$

$$\begin{aligned} &-\frac{1}{\eta^2}\tilde{w}^{****} + \left[\sigma(1-\bar{x}) + \frac{1}{2}(1-\bar{x}^2) - r^2\right]\tilde{w}^{**} - \left(\sigma + \bar{x}\right)\tilde{w}^{*} + \\ &\frac{\mu^2}{\lambda^2}\tilde{w} - \Lambda_2 r^2 \tilde{v}^{**} + \tilde{e}_1\left(1 + \frac{\mu^2}{\lambda^2}\right)\tilde{\phi} + \tilde{e}_2\left(\sigma + \bar{x}\right)\tilde{\phi}^{*} = 0 \end{aligned} \quad \textbf{(2.197)}$$

$$\begin{aligned} &\left[\sigma(1-\bar{x}) + \frac{1}{2}(1-\bar{x}^2) + \frac{e^2}{r_\alpha^2\lambda^2}\right]\tilde{\phi}^{**} - \left(\sigma + \bar{x}\right)\tilde{\phi}^{*} + \left(\frac{r^2}{r_\alpha^2} + \frac{\mu^2}{\lambda^2}\right)\tilde{\phi}^{*} + \\ &\frac{\tilde{e}_1}{r_\alpha^2}\left(\sigma + \bar{x}\right)\tilde{w}^{*} + \frac{\mu^2\tilde{e}_1}{\lambda^2 r_\alpha^2}\tilde{w} + \frac{\tilde{e}_2}{r_\alpha^2}\left(\sigma + \bar{x}\right)\tilde{v}^{*} - \frac{\tilde{e}_2}{r_\alpha^2}\left(1 + \frac{\mu^2}{\lambda^2}\right)\tilde{v} = 0 \end{aligned} \quad \textbf{(2.198)}$$

Boundary conditions:

At x=0 $$\tilde{v}(0,t)=\tilde{w}(0,t)=\tilde{\phi}(0,t)=\tilde{v}^{*}(0,t)=\tilde{w}^{*}(0,t)=0 \quad \textbf{(2.199)}$$

At x=L $$\tilde{v}^{***}+\frac{\eta^{2}}{\Lambda_{1}}\tilde{e}_{2}(\sigma+\bar{x})\tilde{\phi}+\eta^{2}r^{2}\left(\tilde{v}^{*}+\Lambda_{3}\tilde{w}^{*}\right)=0 \quad \textbf{(2.200)}$$

$$\tilde{w}^{***}-\eta^{2}\tilde{e}_{1}(\sigma+\bar{x})\tilde{\phi}+\eta^{2}r^{2}\left(\tilde{w}^{*}+\Lambda_{2}\tilde{v}^{*}\right)=0 \quad \textbf{(2.201)}$$

$$\tilde{\phi}^{*}=\tilde{v}^{**}=\tilde{w}^{**}=0 \quad \textbf{(2.202)}$$

where $(\ )^{*}=\dfrac{d(\ )}{d\bar{x}}$.

2.4.5 Application of the differential transform method

After applying the differential transform method whose details are given in Section 2.3.5 to Eqs.(2.196)-(2.202) the transformed equations of motion and boundary conditions are obtained as follows

Equations of motion:

$$\begin{aligned}
&-\frac{\Lambda_{1}}{\eta^{2}}k_{14}V[k+4]+\left(\sigma+\frac{1}{2}-\Lambda_{1}r^{2}\right)k_{12}V[k+2]\\
&-\sigma(k+1)^{2}V[k+1]-\left[\frac{1}{2}k(k+1)-\left(1+\frac{\mu^{2}}{\lambda^{2}}\right)\right]V[k]-\\
&\Lambda_{2}r^{2}k_{12}W[k+2]-\tilde{e}_{2}\sigma(k+1)\Phi[k+1]-\\
&\tilde{e}_{2}\left(2+\frac{\mu^{2}}{\lambda^{2}}+k\right)\Phi[k]=0
\end{aligned} \quad \textbf{(2.203)}$$

$$\begin{aligned}
&-\frac{1}{\eta^{2}}k_{14}W[k+4]+\left(\sigma+\frac{1}{2}-r^{2}\right)k_{12}W[k+2]-\\
&\sigma(k+1)^{2}W[k+1]-\left[\frac{1}{2}k(k+1)-\frac{\mu^{2}}{\lambda^{2}}\right]W[k]-\\
&\Lambda_{2}r^{2}k_{12}V[k+2]+\tilde{e}_{1}\sigma(k+1)\Phi[k+1]+\\
&\tilde{e}_{1}\left(1+\frac{\mu^{2}}{\lambda^{2}}+k\right)\Phi[k]=0
\end{aligned} \quad \textbf{(2.204)}$$

$$\left(\sigma+\frac{1}{2}+\frac{e^2}{r_\alpha^2\lambda^2}\right)k_{12}\Phi\left[k+2\right]-\sigma\left(k+1\right)^2\Phi\left[k+1\right]-\left[\frac{1}{2}k\left(k+1\right)-\right.$$
$$\left.\left(\frac{r^2}{r_\alpha^2}+\frac{\mu^2}{\lambda^2}\right)\right]\Phi\left[k\right]+\frac{\tilde{e}_1}{r_\alpha^2}\sigma\left(k+1\right)W\left[k+1\right]+\frac{\tilde{e}_1}{r_\alpha^2}\left(k+\frac{\mu^2}{\lambda^2}\right)W\left[k\right]+ \quad \textbf{(2.205)}$$
$$\frac{\tilde{e}_2}{r_\alpha^2}\sigma\left(k+1\right)V\left[k+1\right]+\frac{\tilde{e}_1}{r_\alpha^2}\left(k-1-\frac{\mu^2}{\lambda^2}\right)V\left[k\right]=0$$

where $k_{12}=\left(k+1\right)\left(k+2\right)$ and $k_{14}=\left(k+1\right)\left(k+2\right)\left(k+3\right)\left(k+4\right)$

Boundary conditions:

At x=0
$$V\left[k\right]=W\left[k\right]=\Phi\left[k\right]=\theta_y\left[k\right]=\theta_z\left[k\right]=0 \quad \textbf{(2.206)}$$

At x=L
$$\sum_{k=0}^{\infty}\left\{(k-1)(k-2)kV\left[k\right]+\eta^2r^2kV\left[k\right]+\right.$$
$$\left.\eta^2r^2\Lambda_3kW\left[k\right]+\frac{\eta^2\tilde{e}_2}{\Lambda_1}\left[\sigma+\left(k-1\right)\right]\Phi\left[k\right]\right\}=0 \quad \textbf{(2.207)}$$
$$\sum_{k=0}^{\infty}\left\{(k-1)(k-2)kW\left[k\right]+\eta^2r^2kW\left[k\right]+\right.$$
$$\left.\eta^2r^2\Lambda_2kV\left[k\right]-\eta^2\tilde{e}_1\left[\sigma+\left(k-1\right)\right]\Phi\left[k\right]\right\}=0 \quad \textbf{(2.208)}$$

$$\sum_{k=0}^{\infty}k\Phi\left[k\right]=\sum_{k=0}^{\infty}\left(k-1\right)kV\left[k\right]=\sum_{k=0}^{\infty}\left(k-1\right)kW\left[k\right]=0 \quad \textbf{(2.209)}$$

2.4.6 Finite element formulation

Finite element formulation of the rotor blade that undergoes chorwise bending, flapwise bending and torsion is carried out in this section.

The finite element model of the beam that is used for the formulation is illustrated in Figure 2.21. Here, it is seen that a two noded simple beam element that has ten degrees of freedom is preferred to model the helicopter blade.

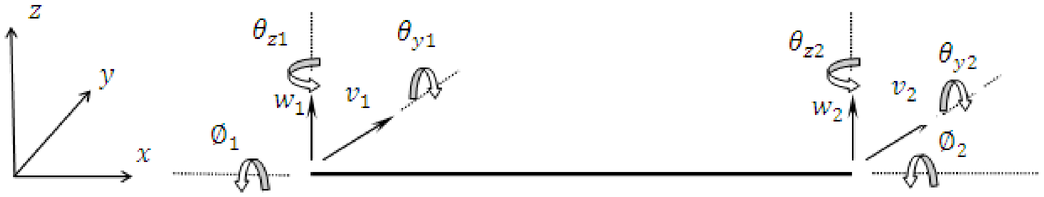

Figure 2.21: Rotor blade finite element model.

where v is the chorwise bending, w is the flapwise bending, θ_y is the angle due to flapwise bending, θ_z is the angle due to chordwise bending and ϕ is the torsion angle.

Polinomials of appropriate order are defined for the displacement field as follows

$$v = a_0 + a_1 x + a_2 x^2 + a_3 x^3 \qquad \textbf{(2.210)}$$

$$w = a_4 + a_5 x + a_6 x^2 + a_7 x^3 \qquad \textbf{(2.211)}$$

$$\theta_z = v' = a_1 + 2a_2 x + 3a_3 x^2 \qquad \textbf{(2.212)}$$

$$\theta_y = w' = a_5 + 2a_6 x + 3a_7 x^2 \qquad \textbf{(2.213)}$$

$$\phi = a_8 + a_9 x \qquad \textbf{(2.214)}$$

The nodal displacements are determined as the displacement values at the first node of the element, $x = 0$ and at the second node, $x = L$, respectively. These are given in matrix form as follows

$$\begin{Bmatrix} v_1 \\ w_1 \\ \theta_{z1} \\ \theta_{y1} \\ \phi_1 \\ v_2 \\ w_2 \\ \theta_{z2} \\ \theta_{y2} \\ \phi_2 \end{Bmatrix} = \begin{bmatrix} 1 & 0 & 0 & 0 & 0 & 0 & 0 & 0 & 0 & 0 \\ 0 & 0 & 0 & 0 & 1 & 0 & 0 & 0 & 0 & 0 \\ 0 & 1 & 0 & 0 & 0 & 0 & 0 & 0 & 0 & 0 \\ 0 & 0 & 0 & 0 & 0 & 1 & 0 & 0 & 0 & 0 \\ 0 & 0 & 0 & 0 & 0 & 0 & 0 & 0 & 1 & 0 \\ 1 & L & L^2 & L^3 & 0 & 0 & 0 & 0 & 0 & 0 \\ 0 & 0 & 0 & 0 & 1 & L & L^2 & L^3 & 0 & 0 \\ 0 & 1 & 2L & 3L^2 & 0 & 0 & 0 & 0 & 0 & 0 \\ 0 & 0 & 0 & 0 & 0 & 1 & 2L & 3L^2 & 0 & 0 \\ 0 & 0 & 0 & 0 & 0 & 0 & 0 & 0 & 1 & L \end{bmatrix} \begin{Bmatrix} a_0 \\ a_1 \\ a_2 \\ a_3 \\ a_4 \\ a_5 \\ a_6 \\ a_7 \\ a_8 \\ a_9 \end{Bmatrix} \qquad \textbf{(2.215)}$$

Relation between the displacement field and the nodal displacements is obtained as in Eq.(2.110). For the present beam model, expressions of the displacements, {q}, the nodal displacements, $\{q_e\}$and the matrix of the shape functions, $[N]$ are

$$\{q\} = \{v \quad w \quad \theta_z \quad \theta_y \quad \phi\}^T \qquad \textbf{(2.216)}$$

$$\{q_e\} = \{v_1 \quad w_1 \quad \theta_{z1} \quad \theta_{y1} \quad \phi_1 \quad v_2 \quad w_2 \quad \theta_{z2} \quad \theta_{y2} \quad \phi_2\}^T \qquad \textbf{(2.217)}$$

$$[N] = \left[[N_v] \quad [N_w] \quad [N_{\theta z}] \quad [N_{\theta y}] \quad [N_\phi]\right] \qquad \textbf{(2.218)}$$

Components of the matrix of shape functions are

$$\left[N_v\right]=\Bigg[1-\frac{3x^2}{L^2}+\frac{2x^3}{L^3} \quad 0 \quad 0 \quad x-\frac{2x^2}{L}+\frac{x^3}{L^2} \quad 0 \quad \frac{3x^2}{L^2}-\frac{2x^3}{L^3} \quad 0 \quad 0 \quad -\frac{x^2}{L}+\frac{x^3}{L^2} \quad 0\Bigg] \tag{2.219}$$

$$\left[N_w\right]=\Bigg[0 \quad 1-\frac{3x^2}{L^2}+\frac{2x^3}{L^3} \quad x-\frac{2x^2}{L}+\frac{x^3}{L^2} \quad 0 \quad 0 \quad 0 \quad \frac{3x^2}{L^2}-\frac{2x^3}{L^3} \quad -\frac{x^2}{L}+\frac{x^3}{L^2} \quad 0 \quad 0\Bigg] \tag{2.220}$$

$$\left[N_{\theta z}\right]=\Bigg[-\frac{6x}{L^2}+\frac{6x^2}{L^3} \quad 0 \quad 0 \quad 1-\frac{4x}{L}+\frac{3x^2}{L^2} \quad 0 \quad \frac{6x}{L^2}-\frac{6x^2}{L^3} \quad 0 \quad 0 \quad -\frac{2x}{L}+\frac{3x^2}{L^2} \quad 0\Bigg] \tag{2.221}$$

$$\left[N_{\theta y}\right]=\Bigg[0 \quad -\frac{6x}{L^2}+\frac{6x^2}{L^3} \quad 1-\frac{4x}{L}+\frac{3x^2}{L^2} \quad 0 \quad 0 \quad 0 \quad \frac{6x}{L^2}-\frac{6x^2}{L^3} \quad -\frac{2x}{L}+\frac{3x^2}{L^2} \quad 0 \quad 0\Bigg] \tag{2.222}$$

$$\left[N_\phi\right]=\Bigg[0 \quad 0 \quad 0 \quad 0 \quad 1-\frac{x}{L} \quad 0 \quad 0 \quad 0 \quad 0 \quad \frac{x}{L}\Bigg] \tag{2.223}$$

where $\left[N_v\right]$, $\left[N_w\right]$,$\left[N_{\theta z}\right]$, $\left[N_{\theta y}\right]$, $\left[N_\phi\right]$ are the shape functions associated with chordwise bending, v, flapwise bending, w, angle due to chordwise bending, θ_z, angle due to flapwise bending, θ_y and torsion ϕ, respectively.

Substituting the obtained shape functions into analytically derived energy expressions, Eq.(2.166) and Eq.(2.175), the element stiffness and mass matrices are found as follows

$$\left[K^e\right]=\int_0^L\left\{F_{CF}(x)\left(\left[\frac{dN_w}{dx}\right]^T\left[\frac{dN_w}{dx}\right]+\left[\frac{dN_v}{dx}\right]^T\left[\frac{dN_v}{dx}\right]+\right.\right.$$
$$\frac{I_\alpha}{\rho A}\left[\frac{dN_\phi}{dx}\right]^T\left[\frac{dN_\phi}{dx}\right]+I_z\left[\frac{d^2N_v}{dx^2}\right]^T\left[\frac{d^2N_v}{dx^2}\right]+ \tag{2.224}$$
$$\left.EI_y\left[\frac{d^2N_w}{dx^2}\right]^T\left[\frac{d^2N_w}{dx^2}\right]+GJ\left[\frac{dN_\phi}{dx}\right]^T\left[\frac{dN_\phi}{dx}\right]\right\}dx$$

$$\left[M^e\right]=\int_0^L\left\{\rho A\left(\left[N_w\right]^T\left[N_w\right]+\left[N_v\right]^T\left[N_v\right]\right)+I_\alpha\left[N_\phi\right]^T\left[N_\phi\right]+\right.$$
$$\left.\rho Ae_1\left(\left[N_w\right]^T\left[N_\phi\right]+\left[N_\phi\right]^T\left[N_w\right]\right)-\rho Ae_2\left(\left[N_v\right]^T\left[N_\phi\right]+\left[N_\phi\right]^T\left[N_v\right]\right)\right\}dx \tag{2.225}$$

where $\left[K^e\right]$ is the element stiffness matrixobtained from the kinetic energy and $\left[M^e\right]$ is the element mass matrix obtained from the potential energy.

Depending on the number of elements used in the structural modeling code, all the element matrices are assembled by considering the finite element rules to obtain the global matrices. The boundary conditions at the fixed end of the helicopter blade, Eq.(2.206), are applied to the global matrices to get the reduced matrices and the following matrix system of equations are obtained for the structural model of the helicopter blade.

$$\left[M^S\right]\{\ddot{q}\}+\left[K^S\right]\{q\}=\{0\} \tag{2.226}$$

In the case of a rotating beam, additional terms appear in the element matrices due to the centrifugal force. These terms are considered by using finite element formulation for the centrifugal force. Thus, finite element representation of a rotating beam that is given in Figure 2.22 can be used.

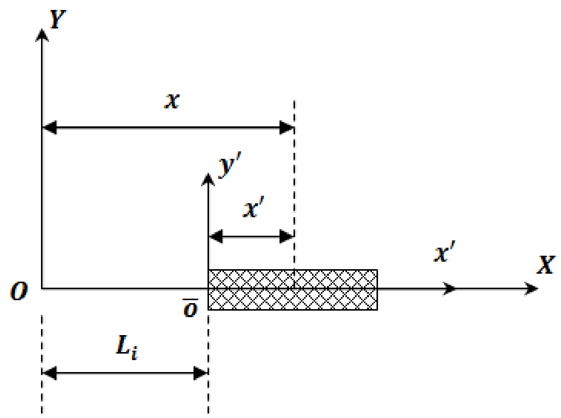

Figure 2.22: Finite element representation of a rotating beam, adapted from (Yang et al., 2004).

where L_i is the offset of each element from the rotational axis, XYZ is the global coordinate system while $x'y'z'$ is the local coordinate system.

Referring Figure 2.22, the centrifugal force given by Eq.(2.164) can be expressed in finite element form as follows

$$F_{CF}(x) = \rho A \Omega^2 \left[R(L - L_i - x') + \frac{1}{2}(L - L_i - x')(L + L_i - x') \right] \quad \textbf{(2.227)}$$

where

$$L_i = (i-1)\frac{L}{n} \quad \textbf{(2.228)}$$

and n is the number of elements.

After addingthe rotation effect to the finite element formulation, modal analysis is applied to Eq.(2.226) to calculate the natural frequencies. Firstly, the modal matrix, $[\Phi]$, is calculated by using the eigenvectors obtained by solving the following determinant

$$\left| -\omega^2 \left[M^S \right] + \left[K^S \right] \right| = 0 \quad \textbf{(2.229)}$$

Premultiplying Eq.(2.226) by the transpose of the model matrix and postmultiplying it by the modal matrix give

$$-\omega^2 [I] + \left[\lambda^2 \right] = \{0\} \quad \textbf{(2.230)}$$

where $[I]$ is the identity matrix, $\left[\lambda^2 \right]$ is the diagonal matrix of natural frequencies.

2.4.7 Validation of the structural model

2.4.7.1 Nonrotating bending-bending-torsion coupled beam example

An illustrative example that studies a rotating bending-bending-torsion coupled Euler Bernoulli beam is not present in open literature. Therefore firstly, a nonrotating coupled beam example that is available in open literature is solved to validate the built structural model. The material and the geometrical properties of this beam model are given in Table 2.13.

Table 2.14: Material and geometrical properties of the nonrotatingbending-bending-torsion coupledbeam model.

Property	Value	Property	Value
E	213.9×10^{9}N/m^{2}	e_2	1.1938×10^{-3} m
I_y	34.96×10^{-12}m^{4}	A	58.97×10^{-6} m^{2}
I_z	2.7928×10^{-9}m^{4}	L	0.1524 m
GJ	9.14 N/m^{2}	ρ	7.859×10^{3} kg/m^{3}
e_1	0.1930×10^{-3} m		

The calculated results are compared with the results of Rao and Carnegie (1970) and Carnegie and Dawson (1971)in Table 2.15 for validation.The results are given as coupled, i.e. $e_1 \neq 0$ and $e_2 \neq 0$ and uncoupled, i.e. $e_1 = 0$ and $e_2 = 0$, natural frequencies. When Table 2.15 is examined, it is seen that there is a very good agreement between the results.

Table 2.15: Coupled and uncoupled bending-bending-torsion frequencies.

Mode Shapes	Present (Hz)		Analytical Process*		Galerkin's Process**	
	Uncoupled	**Coupled**	**Uncoupled**	**Coupled**	**Uncoupled**	**Coupled**
1st ZZ Bending	96.7816	96.7813	96.9	96.9	96.9	96.9
2nd ZZ Bending	606.52	606.504	607	606.5	607.3	607.3
1st YY Bending	865.022	844.354	869	841.2	868.4	845.8
Torsion	1052.02	1093.08	1048.5	1072.9	1048.23	1074.8
3rd ZZ Bending	1698.27	1698.18	1699	1699	1701.7	1701.6

* Rao and Carnegie (1970), **Carnegie and Dawson (1971)

In Table 2.15, it is noticed that coupling does not have a significant effect on the first three flapwise bending modes, ZZ Bending, because e_1 has a very small value while it has a significant reducing effect on the first chordwise bending mode, YY Bending since e_2 is much larger than e_1. Additionally, the coupled torsion mode is larger than the uncoupled mode. Consequently, coupling has a reducing effect on the bending modes while it has an increasing effect on the torsion modes(Rao and Carnegie, 1970).

2.4.7.2 Helicopter rotor blade example

As mentioned before, any paper that studies a rotating coupled Euler-Bernoulli beam is not present in open literature. Therefore, such a beam model is built in ABAQUS to validate the results of the present research. The material and the geometrical properties of this beam model are given in Table 2.16.

Table 2.16: Material and geometrical properties of the rotating bending-bending-torsion coupled beam model.

Property	Value	Property	Value
E	70×10^9 N/m^2	e_1	9.361×10^{-3} m
I_y	1.172×10^{-5} m^4	A	22.5×10^{-3} m^2
I_z	1.45×10^{-9} m^4	L	3 m
I_α	0.502 kg m	ρ	3200 kg/m^3
GJ	1.126×10^9 N/m^2		

In Table 2.17, variation of the coupled natural frequencies with respect to the rotational speed is introduced and the results are compared with the ones given by ABAQUS.

Table 2.17: Variation of the natural frequencies with respect to the rotational speed.

Rotational Speed (rad/sec)					
0		***50***		***100***	
Natural Frequencies (Hz)					
Present	**ABAQUS**	**Present**	**ABAQUS**	**Present**	**ABAQUS**
6.63569	6.7163	10.8827	10.88	18.2559	18.274
23.31	23.355	24.8713	23.835	24.476	24.406
41.5474	41.603	46.2117	46.256	58.1207	57.181
116.152	116.46	120.873	121.2	126.744	125.65
125.679	125.65	125.969	125.65	134.012	134.36
144.653	145.36	146.03	146.58	150.087	150.09
227.164	228.21	232.075	233.14	246.137	247.32

In Table 2.17, it is seen that rotational speed has an increasing effect on the natural frequencies due to the increasing centrifugal force that makes the beam stiffer. Additionally, it is noticed that there is a very good agreement between the results of the present study and the results of ABAQUS which proves the correctness and accuracy of the built structural model.

2.5 Goland Wing Structural Model

2.5.1 Energy expressions and element matrices

In the aerodynamic formulation part; derivations are made for three different cases, i.e. a plain blade that has no trailing edge flap, a trailing edge flap and a blade with a trailing edge flap. Additionally, in the aeroelastic formulation part, validation of the plain blade aerodynamics is carried out by calculating the flutter speed of a Goland wing. Therefore, in this section structural formulation of the beam model that is used for the Goland wing is carried out. Goland wing is a wing model that is used in fixed-wing aircrafts and thisnonrotating wing structure undergoes only flapwise bending and torsion deflections since chordwise bending degree of freedom is mostly neglected in fixed-wing aircrafts. As a result, the flapwise bending-chordwise bending-torsion coupled beam model that is developed in Section 2.4 has to be simplified to model the Goland wing structure by eliminating the chorwise bending displacement and the rotational effect. This simpler beam model has been developed in the previous studies of the doctorate student and her advisor which are Ozdemir Ozgumus and Kaya (2007c), Kaya and Ozdemir (2007, 2010). However, Timoshenko beam model is studied in these references and in the present study, the simpler structural model is developed for an Euler-Bernoulli beam by referring these previous studies.The potential and the kinetic energy expressions of the flapwise bending-torsion coupled Euler-Bernoulli beam are given as follows

$$U = \frac{1}{2}\int_0^L \left[EI_y \left(w''\right)^2 + GJ\left(\phi'\right)^2 \right] dx \qquad \textbf{(2.231)}$$

$$T = \frac{1}{2}\int_0^L \left(2\rho A e_1 \dot{w}\dot{\phi} + \rho A \dot{w}^2 + I_\alpha \dot{\phi}^2 \right) dx \qquad \textbf{(2.232)}$$

The finite element model that is built in the Section 2.4.6 has to be simplified for the Goland wing as illustrated in Figure2.23.

Figure 2.23: Goland wing finite element model.

Here it is seen that a two noded simple beam element that has six degrees of freedom is used for the finite element model of the Goland wing.

Following the previously mentioned procedure, polinomials of appropriate order are defined for the displacement field as given below

$$w = a_0 + a_1 x + a_2 x^2 + a_3 x^3 \quad \textbf{(2.233)}$$

$$\theta_y = w' = a_1 + 2a_2 x + 3a_3 x^2 \quad \textbf{(2.234)}$$

$$\phi = a_4 + a_5 x \quad \textbf{(2.235)}$$

The nodal displacements are determined as the displacement values at the first node, and the $x = 0$ second node, $x = L$, of the beam element, respectively. These are given in matrix form as follows

$$\begin{Bmatrix} w_1 \\ \theta_{y1} \\ \phi_1 \\ w_2 \\ \theta_{y2} \\ \phi_2 \end{Bmatrix} = \begin{bmatrix} 1 & 0 & 0 & 0 & 0 & 0 \\ 0 & 1 & 0 & 0 & 0 & 0 \\ 0 & 0 & 0 & 0 & 1 & 0 \\ 1 & L & L^2 & L^3 & 0 & 0 \\ 0 & 1 & 2L & 3L^2 & 0 & 0 \\ 0 & 0 & 0 & 0 & 1 & L \end{bmatrix} \begin{Bmatrix} a_0 \\ a_1 \\ a_2 \\ a_3 \\ a_4 \\ a_5 \end{Bmatrix} \quad \textbf{(2.236)}$$

Relation between the displacement field and the nodal displacements is obtained as in Eq.(2.110). For the present beam model, expressions of the displacements, {q}, the nodal displacements, $\{q_e\}$and the matrix of the shape functions, $[N]$ are

$$\{q\} = \{v \quad w \quad \theta_z \quad \theta_y \quad \phi\}^T \quad \textbf{(2.237)}$$

$$\{q_e\} = \{v_1 \quad w_1 \quad \theta_{z1} \quad \theta_{y1} \quad \phi_1 \quad v_2 \quad w_2 \quad \theta_{z2} \quad \theta_{y2} \quad \phi_2\}^T \quad \textbf{(2.238)}$$

$$\{q\} = \{w \quad \theta_y \quad \phi\}^T \quad \textbf{(2.239)}$$

$$\{q_e\} = \{w_1 \quad \theta_{y1} \quad \phi_1 \quad w_2 \quad \theta_{y2} \quad \phi_2\}^T \quad \textbf{(2.240)}$$

$$[N] = \left[[N_w] \quad [N_{\theta y}] \quad [N_\phi] \right] \quad \textbf{(2.241)}$$

Components of the matrix of shape functions are

$$\left[N_w\right]=\left[1-\frac{3x^2}{L^2}+\frac{2x^3}{L^3} \quad x-\frac{2x^2}{L}+\frac{x^3}{L^2} \quad 0 \right.$$
$$\left. \frac{3x^2}{L^2}-\frac{2x^3}{L^3} \quad -\frac{x^2}{L}+\frac{x^3}{L^2} \quad 0\right] \tag{2.242}$$

$$\left[N_{\theta y}\right]=\left[-\frac{6x}{L^2}+\frac{6x^2}{L^3} \quad 1-\frac{4x}{L}+\frac{3x^2}{L^2} \quad 0 \right.$$
$$\left. \frac{6x}{L^2}-\frac{6x^2}{L^3} \quad -\frac{2x}{L}+\frac{3x^2}{L^2} \quad 0\right] \tag{2.243}$$

$$\left[N_{\phi}\right]=\left[0 \quad 0 \quad 1-\frac{x}{L} \quad 0 \quad 0 \quad \frac{x}{L}\right] \tag{2.244}$$

where $\left[N_w\right]$, $\left[N_{\theta y}\right]$ and $\left[N_{\phi}\right]$ are the shape functions associated with flapwise bending, w, angle due to flapwise bending, θ_y and torsion ϕ, respectively.

Substituting the related shape functions into Eq.(2.231) and Eq.(2.232), the element stiffness and mass matrices are obtained as follows for a flapwise bending-torsion coupled Euler-Bernoulli beam.

$$\left[K^e\right]=\int_0^L\left\{\frac{I_\alpha}{\rho A}\left(\left[\frac{dN_\phi}{dx}\right]^T\left[\frac{dN_\phi}{dx}\right]\right)+EI_y\left[\frac{d^2N_w}{dx^2}\right]^T\left[\frac{d^2N_w}{dx^2}\right]+\right.$$
$$\left. GJ\left[\frac{dN_\phi}{dx}\right]^T\left[\frac{dN_\phi}{dx}\right]\right\}dx \tag{2.245}$$

$$\left[M^e\right]=\int_0^L\left\{\rho Ae_1\left(\left[N_w\right]^T\left[N_\phi\right]+\left[N_\phi\right]^T\left[N_w\right]\right)+\rho A\left[N_w\right]^T\left[N_w\right]+\right.$$
$$\left. I_\alpha\left[N_\phi\right]^T\left[N_\phi\right]\right\}dx \tag{2.246}$$

Depending on the number of elements used in the developed structural modeling code, the element matrices are assembled by considering the finite element rules to obtain the global matrices. The boundary conditions at the cantilever end, i.e. $w(0,t)=w'(0,t)=\phi(0,t)=0$, are applied to the global matrices to get the reduced matrix equations of motion that are given below

$$\left[M^S\right]\{\ddot{q}\}+\left[K^S\right]\{q\}=\{0\} \tag{2.247}$$

Firstly, the modal matrix, $\left[\Phi\right]$, is calculated by using the eigenvectors obtained by solving the following determinant

$$\left|-\omega^2\left[M^S\right]+\left[K^S\right]\right|=0 \tag{2.248}$$

Premultiplying Eq.(2.239) by the transpose of the model matrix and postmultiplying it by the modal matrix give

$$-\omega^2\left[I\right]+\left[\lambda^2\right]=\{0\} \tag{2.249}$$

where $\left[I\right]$ is the identity matrix, $\left[\lambda^2\right]$ is the diagonal matrix of natural frequencies.

2.5.2 Validation of the Goland wing structural model

In this section, the structural model developed for the Goland wing is validated by comparing the calculated natural frequencies with the ones obtained by Eslimy-Isfahany et al., (1996). Properties of the Goland wing is given in Table 2.18 and the results are validated in Table 2.19.

Table 2.18: Goland wing structural properties.

Property	Value
Chord	6 ft (1.829 m)
Semispan	20 ft (6.096 m)
Mass/span	11.249 slug/ft (539.6 kg/m)
Elastic axis	2 ft (0.6096m) from the LE
Elastic axis, a_h	-1/3, relative to the LE
Centroidal axis	2.6 ft (0.7925m) from the LE
Mass moment of inertia/span, I_y	0.24921 slug-ft^2/ft (1.111 kg-m^2/m), about cg
Mass moment of inertia/span, I_z	25.170 slug-ft^2/ft (112.2 kg-m^2/m), about cg
EI_y	23.647×10^6 lb/ft^2 (345.9×10^6 N/m^2)
GJ	2. 3899×10^6 lb/ft^2 (34.95×10^6 N/m^2)

Table 2.19: Validation of the structural model for flapwise bending – torsion coupledEuler Bernoulli beam.

Natural Frequencies (Hz)	
Present	**Eslimy-Isfahany et al., (1996)**
49.6149	49.6
97.0391	97.0
248.943	248.9
355.657	355.6
451.858	451.5

2.6 Piezoelectric Bender Type Actuator – Trailing Edge Flap Connection

As mentioned before, bender type piezoelectric actuator is chosen to deflect the trailing edge flap. In this section, assembly process of the piezoelectric actuator and the trailing edge flap mechanism is studied. Locations of the piezoelectric actuator and the flap mechanism in the blade are shown in Figure 2.24.

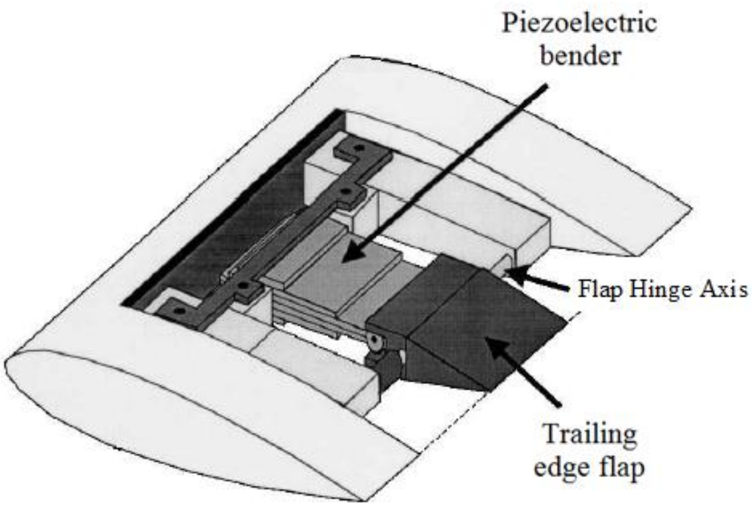

Figure 2.24: Piezoelectric actuator – trailing edge flap connection, adapted from (Koratkar and Chopra, 2000).

The linkage mechanism that connects the bender type actuator to the trailing edge flap is shown in Figure 2.25.

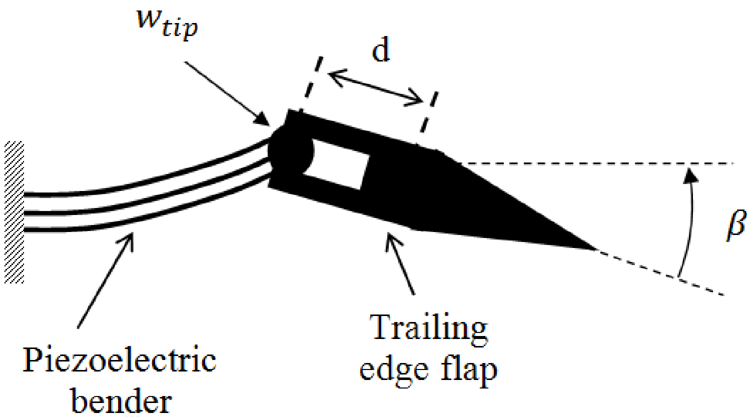

Figure 2.25: Linkage mechanism between the piezoelectric actuator and the trailing edge flap.

Here, d represents the length of the linkage arm and w_{tip} represents the tip deflection of the bender type actuator.

Considering Figure 2.24, the relation between the flap deflection angle and the actuator tip deflection is given by(Koratkar, 2000).

$$\beta = \frac{w_{tip}}{d} \qquad \textbf{(2.250)}$$

The bimorph beam model whose material and geometrical properties are given in Table 2.9 can be used as the bending type piezoelectric actuator that deflects the flap mechanism. When Figure 2.16 that illustrates the tip deflection of the bimorp beam with respect to the voltage is examined, it is seen that $w_{tip} = 0.066mm$ for the voltage value of 100 V.

It is assumed that flap deflection angle of 1^0 will be enough to reduce the blade vibration. Therefore, the tip deflection value of $w_{tip} = 0.066mm$ is substituted into Eq.(2.248) and the the length of the linkage arm is found to be $d = 3.78mm$.

Considering the previously studied bimorph beam example, calculation of the linkage arm length is made for the assumed flap deflection angle, $\beta=1^0$. In the aeroelastic analysis, it is going to be seen that the assumed flap deflection is enough to reduce the blade vibration.

3. AERODYNAMIC FORMULATION

3.1 Overview

The purpose of the present section is to build the aerodynamic models and to make the related formula derivations correctly and accurately. The results of this section are going to be assembled with the results of the structural formulation to be used in the aeroelastic analysis.

Through the whole section, Theodorsen's theory for unsteady aerodynamics is used to model the aerodynamic loads. Firstly, aerodynamic formulation is carried out for a plain blade that has no trailing edge flaps and derivation of the aerodynamic loads are made. Using the derived aerodynamic loads in the virtual work principle gives the components of the aerodynamic matrix, i.e. aerodynamic mass matrix, aerodynamic stiffness matrix and aerodynamic damping matrix. Secondly, only aerodynamics of the flap mechanism is considered and an illustrative example is solved for validation. Thirdly, the aerodynamic loads are obtained for a rotating helicopter blade that has a trailing edge flap. In order to apply the Theodorsen's theory to helicopter aerodynamic environment, several steps whose details are given in the related sections are performed and several coordinate transformations are made. Moreover, the aerodynamic formulation is carried out both for the hover and the forward flight conditions.

This section includes derivations that have been achieved step by step in the previous studies of the doctorate student and her advisor through several years. These studies include Ozdemir Ozgumus and Kaya (2007a, 2007b); Ozdemir Ozgumus et al. (2011).

3.2 Theodorsen's Theory

Theodorsen's theory is widely used for the analysis of fixed-wing aircrafts. However, it also takes place among several theories that are used for helicopter analysis. In this theory, a large aspect ratio wing is considered to move in an incompressible and inviscid flow.The lift and pitching moment are expressed for a thin airfoil that undergoes small harmonic oscillations.

The wing undergoes three degrees of freedom, i.e. plunging motion, h, pitching motion, α and flap deflection, βas illustrated in Figure 3.1.

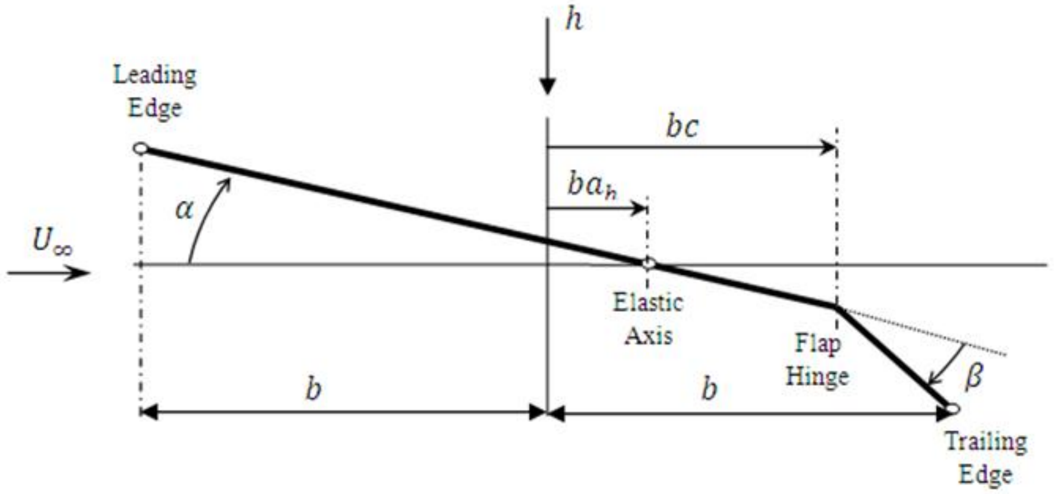

Figure 3.1: Typical wing cross-section with a trailing edge flap.

In Figure 3.1,U_∞ is the free stream velocity, b is the semi-chord length, h is the plunging deflection, α is the pitching angle, β is the flap deflection angle, ba_h, is the distance between the semichord and the elastic axis, bc, is the distance between the semichord and the flap hinge. Here, h and α correspond to the flapwise deflection, w and the pitching motion, ϕ in the structural formulation, respectively.

As it is seen in Figure 3.1., the plunging motion is the flapwise bending motion that is positive downwards, the pitching motion occurs about the elastic axis and it is positive in the nose up direction and the flap angle is positive when the flap deflects downwards (Bisplinghoff et al., 1996).

3.3 Plain Blade Aerodynamics

3.3.1 Aerodynamic loads

In this subsection, Theodorsen’s theory for unsteady aerodynamics is used to model the plain blade aerodynamics. The trailing edge flap mechanism that is present in Figure 3.1 is discarded to model the plain blade as illustrated in Figure 3.2.

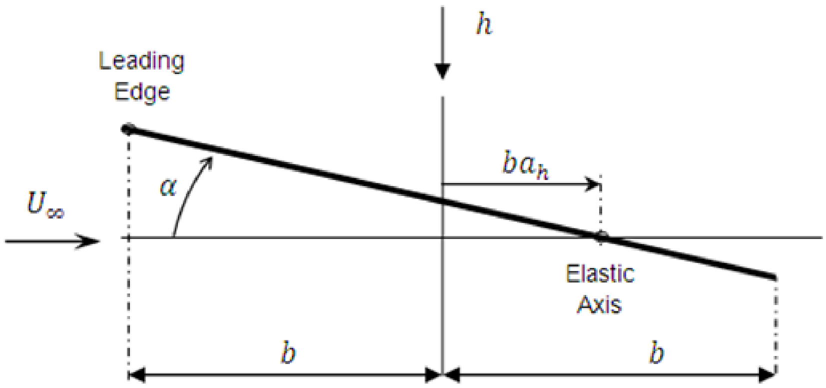

Figure 3.2: Typical wing cross-sectionof a plain blade.

Aerodynamic lift, L_b^A and aerodynamic moment, M_b^A expressions for a plain blade are given as follows(Bisplinghoff et al., 1996)

$$L_b^A = \pi\rho_\infty b^2\left[\ddot{h} + U_\infty\dot{\alpha} - ba_h\ddot{\alpha}\right] + \\ 2\pi\rho_\infty U_\infty bC(k)\left[\dot{h} + U_\infty\alpha + b\left(\frac{1}{2} - a_h\right)\dot{\alpha}\right] \quad \textbf{(3.1)}$$

$$M_b^A = \pi\rho_\infty b^2\left[ba_h\ddot{h} - U_\infty b\left(\frac{1}{2} - a_h\right)\dot{\alpha} - b^2\left(\frac{1}{8} + a_h^2\right)\ddot{\alpha}\right] + \\ 2\pi\rho_\infty U_\infty b^2\left(\frac{1}{2} + a_h\right)C(k)\left[\dot{h} + U_\infty\alpha + b\left(\frac{1}{2} - a_h\right)\dot{\alpha}\right] \quad \textbf{(3.2)}$$

where ρ_∞ is the free stream density and $C(k)$ is the Theodorsen deficiency function that is a complex valued function of the reduced frequency k

$$C(k) = F(k) + iG(k) = \frac{H_1^{(2)}(k)}{H_1^{(2)}(k) + iH_0^{(2)}(k)} \quad \textbf{(3.3)}$$

where $F(k)$ represents the real part and $G(k)$ represents the imaginary part of $C(k)$. Moreover, the $H_n^{(2)}(k)$ are Henkel functions of the second kind that are defined in terms of first and second kind Bessel functions, given respectively as follows

$$H_n^{(2)}(k) = J_n(k) - iY_n(k) \quad \textbf{(3.4)}$$

Here the reduced frequency is given by

$$k = \frac{\omega b}{U_\infty} \qquad \textbf{(3.5)}$$

where ω is the circular frequency.

Variation of the real and imaginary parts of $C(k)$ with respect to the reduced frequency, k are plotted in Figure 3.3.

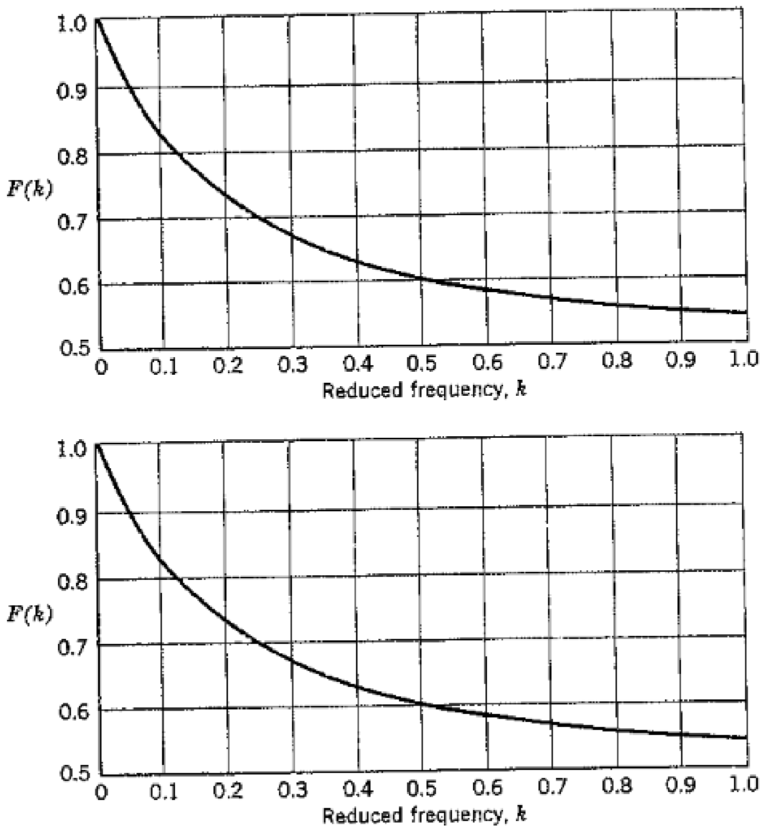

Figure 3.3: Variation of the real and the imaginary parts of the Theodorsen function, C(k) with respect to the reduced frequency, adapted from Fung (1969).

In Figure 3.3, it is seen that the real part, F(k) tends to 0.5 while the imaginary part, G(k), tends to infinity as the reduced frequency k goes to infinity (Fung, 1969).

The magnitude of the Theodorsen deficiency function, C(k), varies from 1 at low frequency to 0.5 at high frequency which means that C(k) is real and equals to unity for the steady case, i.e. k=0 and as the reduced frequency goes to infinity, C(k) approaches 0.5 (Hodges and Pierce, 2002).

The first set of terms in Eq. (3.1) and Eq.(3.2) are the results of flow acceleration and they are called noncirculatory terms while the second set of terms arise from the circulation about the airfoil and they are called circulatory terms. The Theodorsen's deficiency function, C(k), takes place in circulatory terms and it accounts for the effects of the shed wake on the unsteady airloads (Leishman, 2000).

3.3.2 Virtual work and aerodynamic matrix

The virtual work done by the aerodynamic loading is given by(Sivaneri and Chopra, 1982)

$$\delta W = \int_0^L L_b^A \delta h \, dx + \int_0^L M_b^A \delta\alpha \, dx \tag{3.6}$$

Substitutingthe shape functions whose expressions are derived in Section 2.5.1 into Eq.(3.6), terms of δW related to the aerodynamic lift, i.e. δW_L, and terms of δW related to the aerodynamic moment, i.e δW_M, are obtained as follows

$$\begin{aligned}\delta W_L = \int_0^L \{\delta q_e\}^T [N_w]^T \Big\{ & \pi\rho_\infty b^2 \Big[\underline{[N_w]\{\ddot{q}_e\} - ba\left[N_\phi\right]\{\ddot{q}_e\}} + \underline{\underline{U_\infty\left[N_\phi\right]\{\dot{q}_e\}}} \Big] + \\ & 2\pi\rho_\infty U_\infty b C(k) \Big[\underline{\underline{[N_w]\{\dot{q}_e\} + b\left(\frac{1}{2} - a\right)\left[N_\phi\right]\{\dot{q}_e\}}} + U_\infty\left[N_\phi\right]\{q_e\} \Big] \Big\} dx\end{aligned} \tag{3.7}$$

$$\begin{aligned}\delta W_M = \int_0^L \{\delta q_e\}^T \left[N_\phi\right]^T \Big\{ & \pi\rho_\infty b^2 \Big[\underline{ba[N_w]\{\ddot{q}_e\}} - \underline{\underline{U_\infty b\left[N_\phi\right]\{\dot{q}_e\}}} - \\ & \underline{b^2\left(\frac{1}{8} + a^2\right)\left[N_\phi\right]\{\ddot{q}_e\}} \Big] + 2\pi\rho_\infty U_\infty b^2 \left(\frac{1}{2} + a\right) C(k) \Big[\underline{\underline{[N_w]\{\dot{q}_e\}}} + \\ & \underline{\underline{b\left(\frac{1}{2} - a\right)}}\left[N_\phi\right]\{\dot{q}_e\} + U_\infty\left[N_\phi\right]\{q_e\} \Big] \Big\} dx\end{aligned} \tag{3.8}$$

As mentioned before, h and α correspond to the flapwise deflection, w and the pitching motion, ϕ in the structural formulation, respectively. Therefore, terms that are related to h and α in Eq.(3.1) and Eq.(3.2) are expressed by $[N_w]$ and $\left[N_\phi\right]$, respectively as it is seen in Eq.(3.7) and Eq.(3.8).

Here,thesingle underlined terms belong to the aerodynamic mass matrix, $\left[M_e^A\right]$, the double underlined terms belong to the aerodynamic damping matrix, $\left[C_e^A\right]$ while the terms with no underline are related to the aerodynamic stiffness matrix, $\left[K_e^A\right]$. These matrices can be expressed as one matrix, i.e. the aerodynamic matrix whose expression is given as follows

$$\left[A_e(k)\right]=\left[M_e^A\right]\{\ddot{q}_e\}+U_\infty\left[C_e^A\right]\{\dot{q}_e\}+U_\infty^2\left[K_e^A\right]\{q_e\} \tag{3.9}$$

3.4 Flap Aerodynamics

Before modeling flapped blade aerodynamics, validation of the flap aerodynamics is carried out in this section. Variation of the flap originated lift and moment coefficients with respect to time is inspected for validation.

Firstly, the terms that are related to the flap deflection in Theodorsen theory are given as follows (Theodorsen, 1934)

$$L_\beta^A=\rho_\infty b^2\left(U_\infty T_4\dot{\beta}+bT_1\ddot{\beta}\right)-2\pi\rho_\infty U_\infty bC(k)\left(\frac{T_{10}}{\pi}U_\infty\beta+b\frac{T_{11}}{2\pi}\dot{\beta}\right) \tag{3.10}$$

$$\begin{aligned}M_\beta^A=&-\rho_\infty b^2\left[\left(T_4+T_{10}\right)U_\infty^2\beta+\left(T_1-T_8-\left(c-a_h\right)T_4+\frac{T_{11}}{2}\right)bU_\infty\dot{\beta}-\right.\\&\left.\left(T_7+\left(c-a_h\right)T_1\right)b^2\ddot{\beta}\right]+2\pi\rho_\infty U_\infty b^2\left(\frac{1}{2}+a_h\right)C(k)\left(\frac{T_{10}}{\pi}U_\infty\beta+b\frac{T_{11}}{2\pi}\dot{\beta}\right)\end{aligned} \tag{3.11}$$

Here, T_i are the geometric constants that are defined by Theodorsen (1934) and that depend on the chord length, c and on the offset of the elastic axis from the midchord, a_h as introduced in App.A.

The assumption of simple harmonic motion is made for the flap deflection angle, β as follows

$$\beta=\bar{\beta}e^{i\omega t} \tag{3.12}$$

Substituting Eq. (3.12) into Eq.(3.10) and Eq. (3.11) gives

$$\begin{aligned}L_\beta^A=&-\rho_\infty b^2\left(-i\omega U_\infty T_4\bar{\beta}+\omega^2 bT_1\bar{\beta}\right)-\\&2\pi\rho_\infty U_\infty bC(k)\left(\frac{T_{10}}{\pi}U_\infty\bar{\beta}+i\omega b\frac{T_{11}}{2\pi}\bar{\beta}\right)\end{aligned} \tag{3.13}$$

$$M_{\beta}^{A}=-\rho_{\infty}b^{2}\Big[\left(T_4+T_{10}\right)U_{\infty}^{2}\bar{\beta}+i\omega\left(T_1-T_8-\left(c-a_h\right)T_4+\frac{T_{11}}{2}\right)bU_{\infty}\bar{\beta}+$$
$$\omega^{2}\left(T_7+\left(c-a_h\right)T_1\right)b^{2}\bar{\beta}\Big]+2\pi\rho_{\infty}U_{\infty}b^{2}\left(\frac{1}{2}+a_h\right)C\left(k\right)\left(\frac{T_{10}}{\pi}U_{\infty}\bar{\beta}+i\omega b\frac{T_{11}}{2\pi}\bar{\beta}\right) \quad \textbf{(3.14)}$$

Theflap originated lift and moment coefficients are defined as follows

$$C_{L_{\beta}}=\frac{L_{\beta}^{A}}{\rho_{\infty}U_{\infty}^{2}b} \quad \textbf{(3.15)}$$

$$C_{M_{\beta}}=\frac{M_{\beta}^{A}}{2\rho_{\infty}U_{\infty}^{2}b^{2}} \quad \textbf{(3.16)}$$

Substituting Eq.(3.13) and Eq.(3.14)into Eq. (3.15)and Eq.(3.16), respectively and expressing the resultant expressions in terms of the reduced frequency, Eq.(3.5), give

$$C_{L_{\beta}}=-\left(-ikT_4\bar{\beta}+k^{2}T_1\bar{\beta}\right)-2\pi C\left(k\right)\left(\frac{T_{10}}{\pi}\bar{\beta}+ik\frac{T_{11}}{2\pi}\bar{\beta}\right) \quad \textbf{(3.17)}$$

$$C_{M_{\beta}}=-\frac{1}{2}\Big[\left(T_4+T_{10}\right)\bar{\beta}+ik\left(T_1-T_8-\left(c-a_h\right)T_4+\frac{T_{11}}{2}\right)\bar{\beta}+$$
$$k^{2}\left(T_7+\left(c-a_h\right)T_1\right)\bar{\beta}\Big]+\pi\left(\frac{1}{2}+a_h\right)C\left(k\right)\left(\frac{T_{10}}{\pi}\bar{\beta}+ik\frac{T_{11}}{2\pi}\bar{\beta}\right) \quad \textbf{(3.18)}$$

Referring Eq. (3.17) and Eq. (3.18), an illustrative example that studies the variation of the flap originated lift and moment coefficients with respect to time is solved to validate the flap aerodynamics. The plotted results are compared with the ones of Koratkar (2000) inFigure 3.4and Figure 3.5where 2D flap originated sectional lift and pitching moment coefficients are compared, respectively.

In this example, reduced frequency is 0.087, the flap has a 20% chord and is deflected by ±5 deg at 67 Hz.

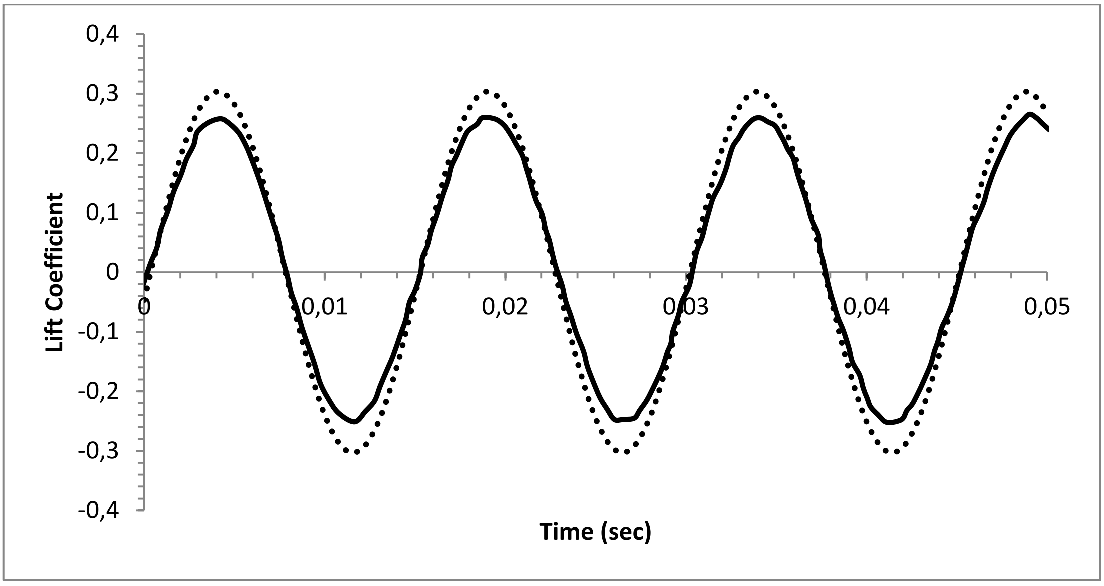

Figure 3.4: Variation of the flap originated sectional lift coefficient with respect to time, (....... Present, —— Koratkar).

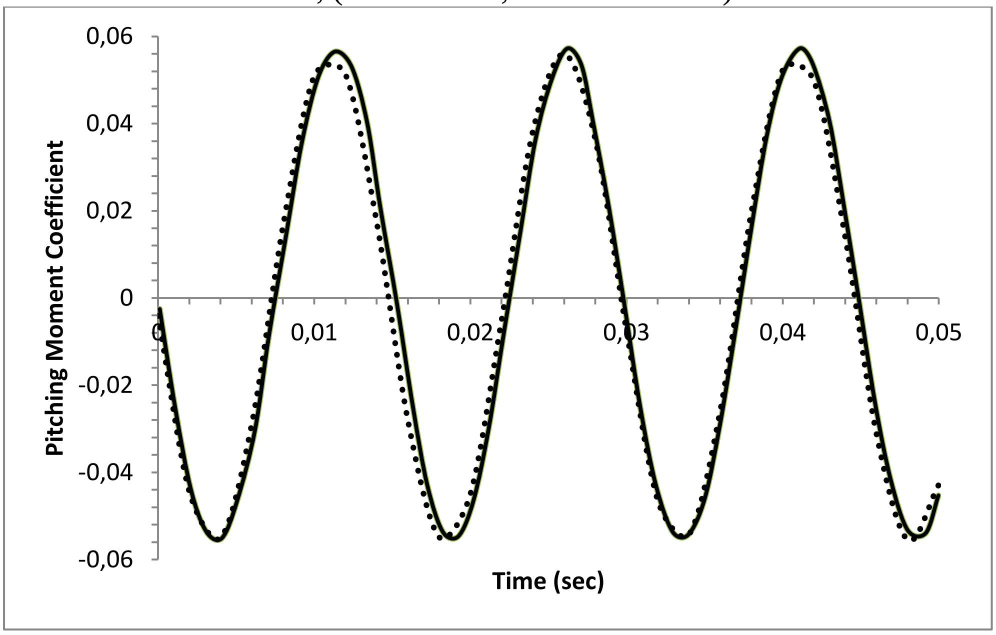

Figure 3.5: Variation of the flap originated sectional moment coefficient with respect to time, (....... Present, —— Koratkar).

3.5 Flapped Blade Aerodynamics

3.5.1 Aerodynamic loads

In this section, Theodorsen theory is generalized to include the flap mechanism as shown in Figure 3.1.

Expressions for sectional aerodynamic lift and aerodynamic moment of a flapped blade are given as follows (Theodorsen, 1934)

$$L^A = -\rho_\infty b^2\left[\pi\ddot{h} + U_\infty\pi\dot{\alpha} - \pi b a_h\ddot{\alpha} - U_\infty T_4\dot{\beta} - bT_1\ddot{\beta}\right] - \\ 2\pi\rho_\infty U_\infty bC(k)\left[\dot{h} + U_\infty\alpha + b\left(\frac{1}{2} - a_h\right)\dot{\alpha} + \frac{T_{10}}{\pi}U_\infty\beta + b\frac{T_{11}}{2\pi}\dot{\beta}\right] \tag{3.19}$$

$$M^A = -\rho_\infty b^2\left[U_\infty\pi b\left(\frac{1}{2} - a_h\right)\dot{\alpha} + \pi b^2\left(\frac{1}{8} + a_h^2\right)\ddot{\alpha} + \left(T_4 + T_{10}\right)U_\infty^2\beta + \right. \\ \left.\left(T_1 - T_8 - \left(c - a_h\right)T_4 + \frac{T_{11}}{2}\right)bU_\infty\dot{\beta} - \left(T_7 + \left(c - a_h\right)T_1\right)b^2\ddot{\beta} - \pi b a_h\ddot{h}\right] + \\ 2\pi\rho_\infty U_\infty b^2\left(\frac{1}{2} + a_h\right)C(k)\left[\dot{h} + U_\infty\alpha + b\left(\frac{1}{2} - a_h\right)\dot{\alpha} + \frac{T_{10}}{\pi}U_\infty\beta + b\frac{T_{11}}{2\pi}\dot{\beta}\right] \tag{3.20}$$

3.5.2 Coordinate systems

In this study two coordinate systems, i.e. undeformed coordinate system and blade fixed coordinate system, are considered and they are illustrated in Figure 3.6.

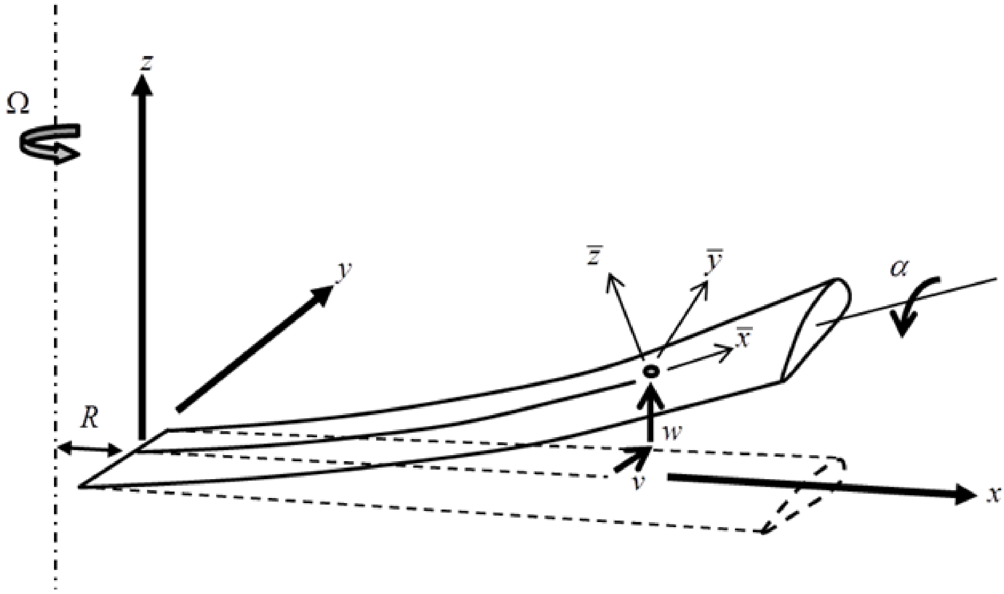

Figure 3.6: Undeformed and blade fixed coordinate systems, adapted from (Hodges and Ormiston, 1976).

The xyz axes represent the undeformed coordinate system. In this right-handed cartesian coordinate system, the x-axis coincides with the neutral axis of the blade in the undeflected position. The blade is rotating at a constant angular velocity Ω and the z-axis is parallel to the axis of rotation (but not coincident) and the y-axis lies in the plane of rotation.The principal axes of the beam cross-sections are, therefore, parallel to y and z directions, respectively.

The $\overline{xyz}$ axes represent the blade fixed coordinate system. This coordinate system is fixed to the blade and moves with the blade as it undergoes bending displacements and pitching rotation.

Projection of the rotor blade cross-section before and after deformation is illustrated in Figure 3.7.

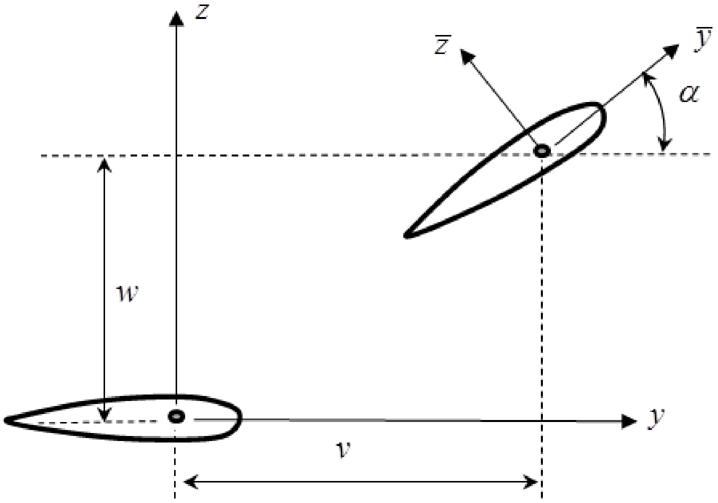

Figure 3.7:Rotor airfoil before and after deformation, adapted from (Hodges and Ormiston, 1976).

As it is seen in Figure 3.7, after the elastic axis undergoes flapwise and chordwise bending deformations, the blade undergoes pitching rotation which means that twisting occurs about the deformed blade coordinate system.

3.5.3 Application of Theodorsen's theory to helicopter aerodynamics

In order to apply the unsteady aerodynamic theory to helicopter blade aerodynamic environment, three steps have to be performed (Kaza and Kvaternik, 1981). These steps are

1.Resolving the free stream velocity U_∞ into its components, i.e. the radial, U_R, the tangential, U_T, and the perpendicular, U_P components.

2.Expressing the aerodynamic lift, L^A and the aerodynamic moment, M^A in terms of U_R, U_T, and U_P and $\dot{\alpha}$.

3.Deriving explicit expressions for U_R, U_T, and U_P and $\dot{\alpha}$ in terms of inflow ratio, λ, rotor rotational speed, Ω, blade motion variables, w,v,α, etc.

The velocity components that are present on an airfoil is shown inFigure 3.8.

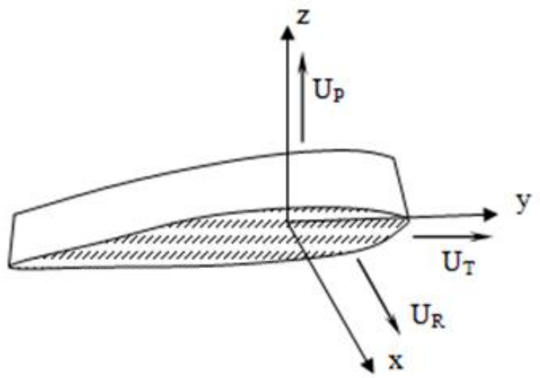

Figure 3.8:Velocity components that are present on the blade airfoil.

The perpendicular velocity, U_P is much smaller than the tangential velocity except at the blade root (Leishman, 2006). Additionally, in this section the rotor blade aerodynamic forces are formulated from strip theory in which only the velocity components perpendicular to the blade spanwise axis, x are considered (Hodges and Dowell, 1974). Therefore, the radial velocity component, U_R, can be neglected. Consequently, the free stream velocity, U_∞ can be written as follows

$$U_\infty = \sqrt{U_T^2 + U_P^2 + U_R^2} \cong U_T \tag{3.21}$$

Expression of the perpendicular velocity component, U_P can be obtained by referring Figure 3.9.

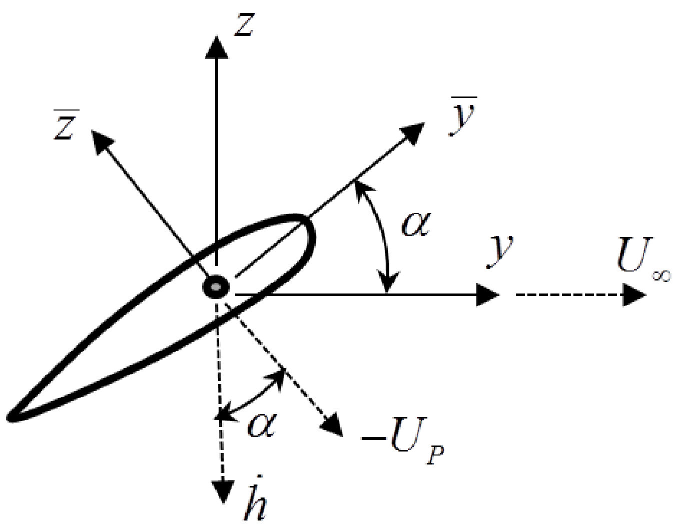

Figure 3.9:The perpendicular velocity, U_P.

Here, the blade twists at an angle α with respect to the free stream velocity, U_∞ and it plunges with a velocity, $\dot{h}$ that is positive downwards. Referring the Figure 3.9, the expression of the perpendicular velocity component is obtained as follows

$$-U_P = \dot{h}Cos\alpha + U_\infty \mathrm{Sin}\alpha \cong \dot{h} + U_\infty \alpha \qquad \textbf{(3.22)}$$

where small angle assumption, i.e. $Cos\alpha \cong 1$ and $\mathrm{Sin}\alpha \cong \alpha$, is made.

The expression in Eq.(3.22) is the same with the one given by Johnson (1980).Substituting Eq.(3.21) and Eq.(3.22) into Eq.(3.19) and Eq.(3.20)gives

$$\begin{aligned} L^A &= A_1\left(-\pi\dot{U}_P - \pi b a_h \ddot{\alpha} - U_T T_4 \dot{\beta} - bT_1 \ddot{\beta}\right) + \\ &\underline{\underline{A_2\left[-U_T U_P + b\left(\frac{1}{2} - a_h\right)U_T\dot{\alpha} + \frac{T_{10}}{\pi}U_T^2\beta + b\frac{T_{11}}{2\pi}U_T\dot{\beta}\right]}} \end{aligned} \qquad \textbf{(3.23)}$$

$$\begin{aligned} M^A &= B_1\left[\frac{\pi}{2}U_T b\dot{\alpha} + \pi b a_h \dot{U}_P + \pi b^2\left(\frac{1}{8} + a_h^2\right)\ddot{\alpha} + \left(T_4 + T_{10}\right)U_T^2\beta + \right. \\ &\left.\left(T_1 - T_8 - \left(c - a_h\right)T_4 + \frac{1}{2}T_{11}\right)bU_T\dot{\beta} - \left(T_7 + \left(c - a_h\right)T_1\right)b^2\ddot{\beta}\right] + \\ &B_2\left[-U_P U_T + b\left(\frac{1}{2} - a_h\right)U_T\dot{\alpha} + \frac{T_{10}}{\pi}U_T^2\beta + b\frac{T_{11}}{2\pi}U_T\dot{\beta}\right] \end{aligned} \qquad \textbf{(3.24)}$$

where

$$A_1 = -B_1 = \rho_\infty b^2 \qquad \textbf{(3.25)}$$

$$A_2 = 2\pi\rho_\infty bC\left(k\right) \qquad \textbf{(3.26)}$$

$$B_2 = 2\pi\rho_\infty b^2\left(\frac{1}{2} + a_h\right)C\left(k\right) \qquad \textbf{(3.27)}$$

Since the helicopter blade undergoes chordwise and flapwise bending deflections, it is desirable to express the aerodynamic forces and moments in the directions that are parallel and perpendicular to the airfoil chord line. In this way, the aerodynamic loads are transformed from the undeformed axis to the deformed axis, i.e. blade fixed axis as it is seen in Figure 3.10.

The lifting force has circulatory, L_C and non-circulatory, L_{NC} terms. The double underlined terms in Eq.(3.23) are the circulatory terms while the terms with no underline are the noncirculatory ones.The noncirculatory lift is taken to act normal to the airfoil chordline, and the circulatory lift is taken to act normal to the resultant blade velocity, V which is the resultant of aerodynamic and dynamic velocities at a point on the elastic axis. An aerodynamic profile drag force per unit length, acting parallel to the resultant blade velocity, is also included (Hodges and Ormiston, 1976). All the aerodynamic force components are shown in Figure 3.10.

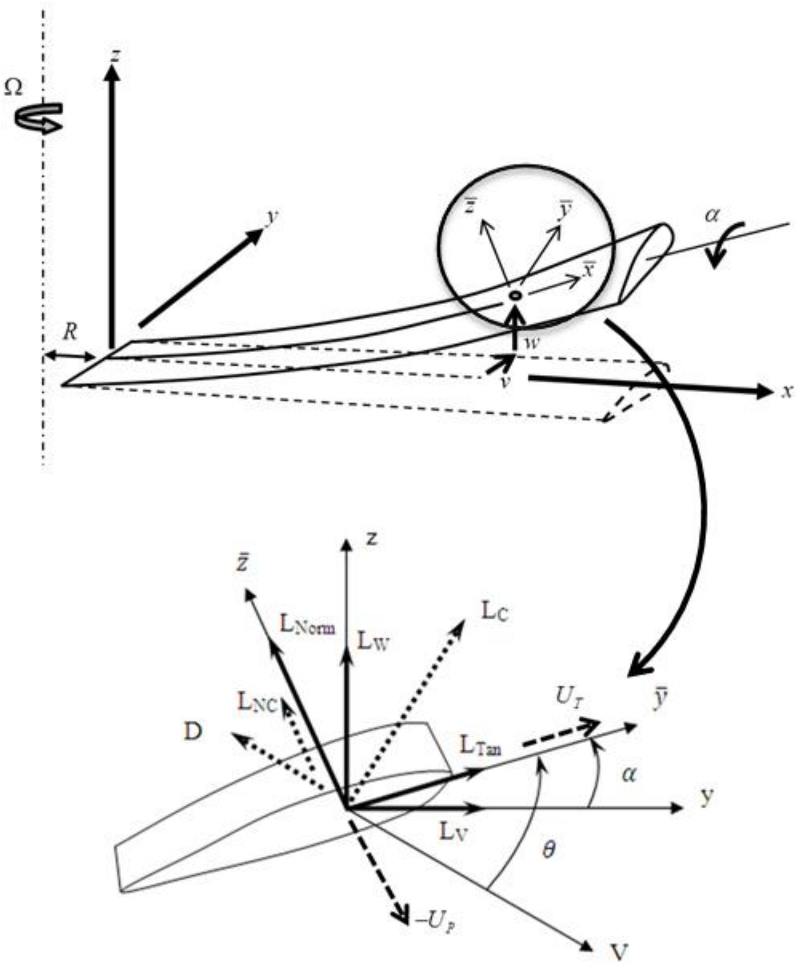

Figure 3.10: Components of the aerodynamic forces, adapted from (Hodges andOrmiston, 1976).

where θ is the angle of attack and D is the drag force that is in the opposite direction of the resulting velocity, V. Here the drag force, D is given by

$$D = \frac{\rho_\infty a_0 c}{2}\frac{C_d}{a_0}\left(U_T^2 + U_P^2\right) \cong \rho_\infty C_d U_T^2 \qquad \textbf{(3.28)}$$

where C_d is the drag coefficient and a_0 is the lift curve slope.

ReferringFigure 3.10, the normal component of the aerodynamic liftthat acts perpendicular to the airfoil chordline, L_{Norm} and the tangential componentof the aerodynamic lift that act in the direction that is parallel to the airfoil chord line, L_{Tan} are obtained as follows

$$L_{Norm} = L_{NC} + L_C Cos\theta - DSin\theta \tag{3.29}$$

$$L_{Tan} = -L_C Sin\theta - DCos\theta \tag{3.30}$$

Referring Figure 3.10, the following angle relations are obtained

$$Sin\theta = \frac{U_P}{\sqrt{U_T^2 + U_P^2}} \cong \frac{U_P}{U_T} \tag{3.31}$$

$$Cos\theta = \frac{U_T}{\sqrt{U_T^2 + U_P^2}} \cong 1 \tag{3.32}$$

Substituting Eq.(3.28), Eq. (3.31) and Eq. (3.32) into Eq.(3.29) and Eq.(3.30) gives

$$\begin{aligned} L_{Norm} = {} & \mathrm{A}_1\left(-\pi\dot{\mathrm{U}}_\mathrm{P} - \pi \mathrm{b}\mathrm{a}_\mathrm{h}\ddot{\alpha} - \mathrm{U}_\mathrm{T}\mathrm{T}_4\dot{\beta} - \mathrm{b}\mathrm{T}_1\ddot{\beta}\right) + \\ & \mathrm{A}_2\left[-\mathrm{U}_\mathrm{T}\mathrm{U}_\mathrm{P} + \mathrm{b}\left(\frac{1}{2} - \mathrm{a}_\mathrm{h}\right)\mathrm{U}_\mathrm{T}\dot{\alpha} + \frac{\mathrm{T}_{10}}{\pi}\mathrm{U}_\mathrm{T}^2\beta + \mathrm{b}\frac{\mathrm{T}_{11}}{2\pi}\mathrm{U}_\mathrm{T}\dot{\beta}\right] - \\ & \rho_\infty C_d U_T U_P \end{aligned} \tag{3.33}$$

$$\begin{aligned} L_{Tan} = {} & \mathrm{A}_2\left[-\mathrm{U}_P^2 + \mathrm{b}\left(\frac{1}{2} - \mathrm{a}_\mathrm{h}\right)\mathrm{U}_\mathrm{P}\dot{\alpha} + \frac{\mathrm{T}_{10}}{\pi}\mathrm{U}_\mathrm{P}\mathrm{U}_\mathrm{T}\beta + \right. \\ & \left. \mathrm{b}\frac{\mathrm{T}_{11}}{2\pi}\mathrm{U}_\mathrm{P}\dot{\beta}\right] - \rho_\infty C_d U_T^2 \end{aligned} \tag{3.34}$$

After obtaining the normal and the tangential force components, transformation from the “deformed axis” to the “undeformed axis” is performed to resolve the normal and tangential components of aerodynamic lift, L_{Norm} and L_{Tan} into L_v and L_w which are the force components parallel to the y and z axis of the the undeformed blade coordinate system. Thus considering Figure 3.10, we get

$$L_w = L_{Norm} + L_{Tan}\alpha \tag{3.35}$$

$$L_v = L_{Tan} - L_{Norm}\alpha \qquad \textbf{(3.36)}$$

Eq.(3.35) and Eq.(3.36) can be written in the extended form as follows

$$\begin{aligned} L_w = {} & \mathrm{A}_1\left(-\pi\dot{\mathrm{U}}_\mathrm{P} - \pi b a_h \ddot{\alpha} - \mathrm{U}_\mathrm{T}\mathrm{T}_4\dot{\beta} - b\mathrm{T}_1\ddot{\beta}\right) + \\ & \mathrm{A}_2\left[-\mathrm{U}_\mathrm{T}\mathrm{U}_\mathrm{P} + b\left(\frac{1}{2} - a_h\right)\mathrm{U}_\mathrm{T}\dot{\alpha} + \frac{\mathrm{T}_{10}}{\pi}\mathrm{U}_\mathrm{T}^2\beta + b\frac{\mathrm{T}_{11}}{2\pi}\mathrm{U}_\mathrm{T}\dot{\beta}\right] - \\ & \rho_\infty C_d U_T U_P + \left\{\mathrm{A}_2\left[-\mathrm{U}_P^2 + b\left(\frac{1}{2} - a_h\right)\mathrm{U}_\mathrm{P}\dot{\alpha} + \frac{\mathrm{T}_{10}}{\pi}\mathrm{U}_\mathrm{P}\mathrm{U}_\mathrm{T}\beta + \right.\right. \\ & \left.\left. b\frac{\mathrm{T}_{11}}{2\pi}\mathrm{U}_\mathrm{P}\dot{\beta}\right] - \rho_\infty C_d U_T^2\right\}\alpha \end{aligned} \qquad \textbf{(3.37)}$$

$$\begin{aligned} L_v = {} & \mathrm{A}_2\left[-\mathrm{U}_P^2 + b\left(\frac{1}{2} - a_h\right)\mathrm{U}_\mathrm{P}\dot{\alpha} + \frac{\mathrm{T}_{10}}{\pi}\mathrm{U}_\mathrm{P}\mathrm{U}_\mathrm{T}\beta + b\frac{\mathrm{T}_{11}}{2\pi}\mathrm{U}_\mathrm{P}\dot{\beta}\right] \\ & -\rho_\infty C_d U_T^2 - \left\{\mathrm{A}_1\left(-\pi\dot{\mathrm{U}}_\mathrm{P} - \pi b a_h \ddot{\alpha} - \mathrm{U}_\mathrm{T}\mathrm{T}_4\dot{\beta} - b\mathrm{T}_1\ddot{\beta}\right) + \right. \\ & \mathrm{A}_2\left[-\mathrm{U}_\mathrm{T}\mathrm{U}_\mathrm{P} + b\left(\frac{1}{2} - a_h\right)\mathrm{U}_\mathrm{T}\dot{\alpha} + \frac{\mathrm{T}_{10}}{\pi}\mathrm{U}_\mathrm{T}^2\beta + b\frac{\mathrm{T}_{11}}{2\pi}\mathrm{U}_\mathrm{T}\dot{\beta}\right] - \\ & \left. \rho_\infty C_d U_T U_P\right\}\alpha \end{aligned} \qquad \textbf{(3.38)}$$

Since there is no transformation about the x-axis, the aerodynamic pitching moment is not affected from coordinate transformations. Therefore, the following equality can be written

$$\bar{M} = \mathrm{M}^\mathrm{A} \qquad \textbf{(3.39)}$$

where M^A is the aerodynamic pitching moment whose expression is given in Eq.(3.20).

4. AEROELASTIC FORMULATION

4.1 Overview

The purpose of the present section is to assemble the results of the structural part and the aerodynamic part to build the aeroelastic model of the helicopter blade.

Firstly, the structural model of the flapwise bending-torsion coupled Euler Bernoulli beam, developed in Section 2.5, is combined with the aerodynamic model, developed in Section 3.3 to build the aeroelastic modelof a plain blade that does not have a trailing edge flap. An example that is present in open literature, Goland wing flutter, is chosen to validate the correctness and accuracy of this aeroelastic model. After the assembly of the structural matrices with the aerodynamic ones, modal analysis is carried out first. Afterwards, the flutter speed of the Goland wing and the reduced frequency value at which flutter occurs are calculated by applying the U-g method. The calculatedresults are in very good agreement with the ones in openliterature which is adequate for the validation of the plain blade aeroelastic model.

Secondly, the flapwise bending-chordwise bending-torsion coupled structural model of the helicopter blade, developed in Section 2.4, is combined with the aerodynamic formulation of the flapped blade, developed in Section 3.5, to inspect the vibration characteristics of the blade.A beam model that undergoes coupled motion is chosen and the cross-sectional properties of the beam are found by using a cross-sectional analysis program called VABS (Cesnik and Hodges, 1997). The aerodynamic characteristics are calculated by considering similar blade models that are present in open literature. Both the material and the aerodynamic properties are used in the developed aeroelastic computer codes and Runge-Kutta method is applied as the solution procedure.The analysis is carried out for both hover and forward flight conditions. Effects of several parameters, i.e. flap deflection angle, rotor disk angle of attack, advance ratio and voltage applied to the piezoelectric actuator, on the vibration characteristics of the blade are studied.

4.2 Plain Blade Flutter

Stability problems are the most common problems in aeroelasticity studies. The elastic moduli of a given structure is independent of the flight speed while the aerodynamic forces are strictly dependent on the speed of the aircraft. Therefore, in some cases aerodynamic forces are more powerful than the elastic restoring forces. When this occurs in such a way that the inertial forces have little effect, this static instability is called “divergence”. However, if the inertial forces are also effective, this dynamic instability is called “flutter”. Both instabilities can cause catastrophic results which lead to a sudden destruction of the vehicle (Hodges and Pierce, 2002). Flutter occurs during flight at a speed called the “flutter speed”. Since flutter may cause catastrophic disintegration of the airplane during flight and since it involves serious oscillatory distortions of the structural components, it must not occur during flight. Thus, the aircraft designers must know how to design lifting surfaces that do not undergo such instabilities (Goland, 1945).

The aim of the present section is to prove the correctness and the accuracy of the aeroelastic model that is developed for a plain blade that has no trailing edge flaps.Therefore, a numerical example that studies the flutter speed of Goland wing is solved in this section.

4.2.1 Aeroelastic formulation

In order to build the aeroelastic model for the plain blade, the structural matrices given by Eq. (2.243) and Eq.(2.244) are assembled with the aerodynamic matrix given by Eq.(3.9). Depending on the number of elements used in the developed aeroelasticity code, the element matrices are assembled by considering the finite element rules to obtain the global matrices.The boundary conditions at the cantilever end, Eq.(2.180), are applied to the global matrices to get the reduced matrices and the following governing matrix system of equations of the aeroelastic model are obtained for the plain blade.

$$\left[M^S\right]\{\ddot{q}\}+\left[K^S\right]\{q\}+\left[A\left(k\right)\right]=\{0\} \qquad \textbf{(4.1)}$$

4.2.2 Simple harmonic motion

In a classical flutter analysis, simple harmonic motion assumption is made for the displacement field as follows

$$\{q\} = \{\bar{q}\} e^{i\omega t} \quad \textbf{(4.2)}$$

Substituting Eq.(4.2) into Eq.(3.9) gives

$$\left[A(k)\right] = \omega^2 \left[\bar{A}(k)\right] \{\bar{q}\} e^{i\omega t} \quad \textbf{(4.3)}$$

where

$$\left[\bar{A}(k)\right] = -\left[M^A\right] + \frac{ib}{k}\left[C^A\right] + \frac{b^2}{k^2}\left[K^A\right] \quad \textbf{(4.4)}$$

The expressions of the element level aerodynamic mass matrix, $\left[M_e^A\right]$,aerodynamic damping matrix, $\left[C_e^A\right]$ and aerodynamic stiffness matrix, $\left[K_e^A\right]$ are given in App.B.

Substituting Eq.(4.2) and Eq.(4.3) into Eq.(4.1) gives

$$-\omega^2 [M] + [K] + \omega^2 \left[\bar{A}(k)\right] = \{0\} \quad \textbf{(4.5)}$$

4.2.3 Modal analysis

The modal matrix, $[\Phi]$, is obtained by using the eigenvectors obtained by solving the following determinant

$$\left|-\omega^2 [M] + [K]\right| = 0 \quad \textbf{(4.6)}$$

Premultiplying Eq.(4.5) by the transpose of the model matrix and postmultiplying it by the modal matrix give

$$-\omega^2 [I] + \left[\lambda^2\right] + \omega^2 \left[\bar{\bar{A}}(k)\right] = \{0\} \quad \textbf{(4.7)}$$

where $\left[I\right]$ is the identity matrix, $\left[\lambda^2\right]$ is the diagonal matrix of natural frequencies, and $\left[\bar{\bar{A}}(k)\right]$ is the aerodynamic matrix after being multiplied by the modal matrix.

4.2.4 Application of the U-g method

In the flutter analysis, it is common to include a parameter that simulates the effect of structural damping for each degree of freedom. In Theodorsen's theory, Section 3.2, plunging motion, h and pitching motion, α are considered. Therefore, damping parameters g_h and g_α are added to the system for each degree of freedom in this example. Depending on the structural configuration, damping parameters take values between 0.01 and 0.05. Scanlan and Rosenbaum (1948) suggested that damping coefficients, g_h and g_α, can be treated as unknowns as the circular frequency, ω. Thus, it is possible to remove the subscripts and express both of the damping coefficients as g (Hodges and Pierce, 2002).

A parameter Z whose expression is given below can be introduced.

$$Z = \frac{1+ig}{\omega^2} \qquad \textbf{(4.8)}$$

Referring Eq. (4.8), the following definitions are made

$$\omega = \frac{1}{\mathrm{Re}(Z)} \qquad \textbf{(4.9)}$$

$$g = \frac{\mathrm{Im}(Z)}{\mathrm{Re}(Z)} \qquad \textbf{(4.10)}$$

Adding the Z parameter to the system of equations, Eq.(4.7), gives

$$-\omega^2\left[I\right] + \left[\lambda^2\right] Z + \omega^2\left[\bar{\bar{A}}(k)\right] = \{0\} \qquad \textbf{(4.11)}$$

Referring Eq. (4.11), a set of Z values can be found by solving the following flutter determinant.

$$\left| -\omega^2 [I] + \left[\lambda^2\right] Z + \omega^2 \left[\bar{\bar{A}}(k)\right] \right| = 0 \qquad \textbf{(4.12)}$$

An iterative procedure is followed in the U-g method to calculate the flutter speed. The steps of this iterative procedure are

1. A set of trial reduced frequency values, k, say from 0.001 to 1 are specified.
2. For each value of k, the Theodorsen's deficiency function, $C(k)$ is calculated by referringEq.(3.3).
3. The flutter determinant, Eq.(4.12), is solved for Z.
4. After obtaining the essential Z values, pairs of real numbers, i.e. (ω_1, g_1), (ω_2, g_2), etc., are calculated by referring Eq.(4.9) and Eq.(4.10).
5. Free stream velocity values, U_∞, are calculated for each circular frequency, ω, as follows

$$U_\infty = \omega b / k \qquad \textbf{(4.13)}$$

6. Free stream velocity-virtual damping pairs, i.e. $(U_{\infty 1}, g_1)$, $(U_{\infty 2}, g_2)$, etc., are obtained for the k value.
7. After closing the first loop, repeat the steps 2-6 until all the trial k values are used.
8. When allsets of U_∞ and g are obtained, the $U_\infty - g$ graph that indicates the margins of stability at conditions near the flutter boundary, $g = 0$, is plotted.

The numerical values of g_i that are obtained for each value of k is interpreted as the required damping to achive simple harmonic motion at the circular frequency ω_i. The damping g is introduced as an artificial damping. Thus, it does not really exist and the value of U_∞ at which $g = 0$ is defined as the flutter speed (Hodges and Pierce, 2002).

4.2.5 Validation of the plain blade aeroelastic model

The flutter speed of Goland wing whose properties are given by Beran et al. (2004) and introduced in Table 2.18,is calculated by applying the $U_\infty - g$ method whose steps are defined in the previous section.Calculated flutter speed is illustrated in Figure 4.1.

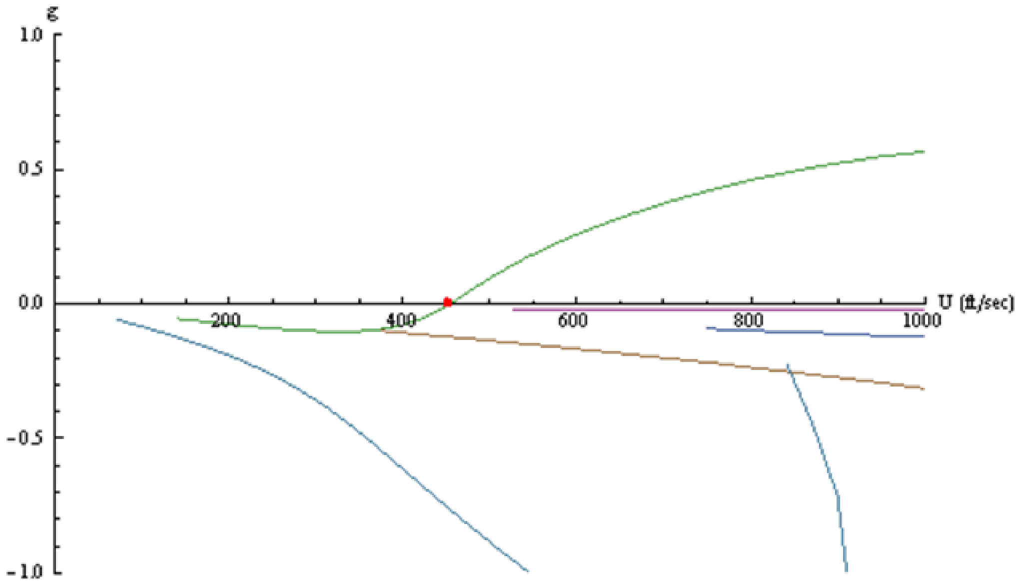

Figure 4.1: Flutter speed of the Goland wing.

Here, each set of $(U_{\infty i}, g_i)$ pairs that are calculated for a different reduced frequency value creats a brach and the free stream velocity at which one of the branchesintersect the U_∞ axis, i.e. $g = 0$, is called the "flutter speed". In Figure 4.1, one of the branches intersectsthe U_∞ axis at $U_\infty = 447\, ft/\sec$ and in Table 4.1, this calculated value is compared with the one found by Lin and Iliff (2000). Additionally, the reduced frequency value at which the flutter speed is calculated is also obtained and validated in Table 4.1.

Table 4.1: Validation of plain blade aeroelastic model.

Flutter Speed (ft/sec)		**Reduced Frequency**	
Present	Lin and Iliff (2000)	Present	Lin and Iliff (2000)
450	447	0.474	0.470

Here, it is seen that there is a very good agreement between the results which reveals that modeling and implementation of the aerodynamic matrix into the structural equations are performed correctly.

4.3 Aeroelastic Analysis of A Helicopter Blade with A Trailing Edge Flap

In this section, vibration characteristics of a helicopter blade with a trailing edge flap is studied. The structural formulation of the flapwise bending-chordwise bending-torsion coupled blade is completed in Section 2.4 and derivation of the aerodynamic matrices is made in Sections 4.3.3 and 4.3.4. The aerodynamic characteristics that are essential for the aerodynamic matrices are calculated in Section 4.3.6 by considering similar blade models which are present in open literature. Both the material and the aerodynamic properties are used in the developed aeroelastic computer codes and Runge-Kutta method is applied as the solution procedure. The analysis is carried out for both hover and forward flight conditions, i.e. Sections 4.3.8 and 4.3.9, respectively.. Effects of several parameters, i.e. flap deflection angle, rotor disk angle of attack, advance ratio and voltage applied to the piezoelectric actuator, on the vibration characteristics of the blade are studied.

4.3.1 Velocity components under hover conditions

Under hover conditions, the velocity components U_T, $\mathrm{U_P}$ and $\dot{\alpha}$, used in Eqs.(3.37)-(3.39), can be expressed in terms of blade motion variables,i.e. v, w and ϕ, in terms of induced flow, v_i and rotor rotational speed, Ω as follows (Hodges and Ormiston, 1976).

$$U_T = \Omega x + \dot{v} \tag{4.14}$$

$$\mathrm{U_P} = -\Omega \mathrm{x}\left(\phi + v'w'\right) - \dot{v}\phi - v_i + \dot{w} + \Omega \mathrm{v}w' \tag{4.15}$$

$$\dot{\alpha} = \dot{\phi} + \Omega \mathrm{w}' + \dot{v}'\mathrm{w}' \tag{4.16}$$

Substituting Eqs.(4.14)-(4.16) into Eqs.(3.37)-(3.39), gives the final expressions of aerodynamic loads that affect on a helicopter blade with a trailing edge flap under hover conditions.

4.3.2 Velocity components in forward flight

In forward flight, the velocity components U_T, $\mathrm{U_P}$ and $\dot{\alpha}$, used in Eqs.(3.37)-(3.39), can be expressed in terms of blade motion variables,i.e. v, w and ϕ in terms of induced flow, v_i, azimuth angle, ψ, pitch control angle, $\bar{\theta}$, precone angle, β_0, rotor rotational speed, Ω and advance ratio, μ as follows (Yoo, 1989).

$$U_T = \dot{v} + \Omega\left(x + \mu LSin\psi\right) + \mu\Omega Lv'Cos\psi \tag{4.17}$$

$$\begin{aligned} \mathrm{U_P} = \dot{w} + \mu\Omega L\left(\bar{\theta} + \phi\right)v'Cos\psi + \mu\Omega L\left(w' + \beta_0\right)Cos\psi - \\ v_i + \Omega\left(vw' + v\beta_0\right) - \dot{v}\left(\bar{\theta} + \phi\right) \end{aligned} \tag{4.18}$$

$$\dot{\alpha} = \dot{\bar{\theta}} + \dot{\phi} + \dot{v}'\mathrm{w}' + \Omega\left(\mathrm{w}' + \beta_0\right)\left(1 - \frac{v'^2}{2} - \frac{w'^2}{2}\right) \tag{4.19}$$

Substituting Eqs.(4.17)-(4.19)into Eqs.(3.37)-(3.39), gives the final expressions of the aerodynamic loads that affect on a helicopter blade with a trailing edge flap in forward flight.

4.3.3 Governing matrix equations of motion

The virtual work done by the aerodynamic loading is given by (Sivaneri and Chopra, 1982)

$$\delta W = \int_0^L L_w \delta w\, dx + \int_0^L L_v \delta v\, dx + \int_0^L M^A \delta\alpha\, dx \tag{4.20}$$

Substituting the final expressions of L_w, L_v and M^A, i.e. Eqs.(3.37)-(3.39) into Eq.(4.20) gives aerodynamic stiffness, aerodynamic mass and aerodynamic damping matrices that are going to be assembled with the structural matrices that are obtained in the structural formulation of the rotor blade in Section 2.4. During the assembly process of the structural and the aerodynamic matrices to obtain the governing matrix equations of motion,Hamilton's principle whose expression is given below is used.

$$\int_{t1}^{t2} \left(\delta U - \delta K - \delta W\right) dx = 0 \tag{4.21}$$

Here, δU, δK and δW are, respectively, the variation of strain energy, the variation of kinetic energy and the virtual work.

Consequently, the matrix equations of motion is obtained for the aeroelastic model of the helicopter blade with a trailing edge flap as follows

$$\left[M_e^S + M_e^A\right]\{\ddot{q}_e\} + \left[C_e^A\right]\{\dot{q}_e\} + \left[K_e^S + K_e^A\right]\{q_e\} = \left\{Q_e^A\right\} \tag{4.22}$$

where $[\ ]^S$ and $[\ ]^A$ present structural and aerodynamic matrices, respectively. Additionally, the term $\left\{Q_e^A\right\}$ that takes place on the right side of Eq.(4.22) is the force vector which is a result of the aerodynamic loads.

Depending on the number of elements used in the developed aeroelasticity code, the element matrices are assembled by considering the finite element rules to obtain the global matrices. The boundary conditions at the cantilever end, Eq.(2.180), are applied to the global matrices to get the reduced matrices and the following governing matrix system of equations of the aeroelastic model are obtained for the helicopter blade with a trailing edge flap.

$$[M]\{\ddot{q}\} + [C]\{\dot{q}\} + [K]\{q\} = \left\{Q^A\right\} \tag{4.23}$$

4.3.4 Aerodynamic matrices under hover conditions

Under hover conditions, expressions of the aerodynamic matrices, Eq.(4.22), are given by

$$\left[Q^A\right] = f_1\left[N_v\right]^T + g_1\left[N_w\right]^T + h_1\left[N_\phi\right]^T \tag{4.24}$$

$$\begin{aligned}\left[K_e^A\right] = {} & \left[N_v\right]^T\left(f_2\left[N_w\right]' + f_3\left[N_\phi\right]\right) + \\ & \left[N_w\right]^T\left(g_2\left[N_w\right]' + g_3\left[N_\phi\right]\right) + \left[N_\phi\right]^T\left(h_2\left[N_w\right]' + h_3\left[N_\phi\right]\right)\end{aligned} \tag{4.25}$$

$$\begin{aligned}\left[C_e^A\right] = {} & \left[N_v\right]^T\left(f_4\left[N_v\right] + f_5\left[N_w\right] + f_6\left[N_\phi\right]\right) + \\ & \left[N_w\right]^T\left(g_4\left[N_v\right] + g_5\left[N_w\right] + g_6\left[N_\phi\right]\right) + \\ & \left[N_\phi\right]^T\left(h_4\left[N_v\right] + h_5\left[N_w\right] + h_6\left[N_\phi\right]\right)\end{aligned} \tag{4.26}$$

$$\begin{aligned}\left[M_e^A\right] = {} & \left[N_v\right]^T\left(f_7\left[N_w\right] + f_8\left[N_\phi\right]\right) + \\ & \left[N_w\right]^T\left(g_7\left[N_w\right] + g_8\left[N_\phi\right]\right) + \\ & \left[N_\phi\right]^T\left(h_7\left[N_w\right] + h_8\left[N_\phi\right]\right)\end{aligned} \tag{4.27}$$

The coefficients of the aerodynamic matrices that are obtained for hover conditions are given in App. C.

4.3.5 Aerodynamic matrices in forward flight

Under forward flight conditions, expressions of the aerodynamic matrices, Eq.(4.22), are given by

$$\left[LvStiff\right]=\int_0^L\left[N_v\right]^T\left(m_1\left[N_v\right]+m_2\left[N_\phi\right]+m_3\left[N_v'\right]+m_4\left[N_w'\right]\right)dx \qquad \textbf{(4.28)}$$

$$\left[LwStiff\right]=\int_0^L\left[N_w\right]^T\left(n_1\left[N_v\right]+n_2\left[N_\phi\right]+n_3\left[N_v'\right]+n_4\left[N_w'\right]\right)dx \qquad \textbf{(4.29)}$$

$$\left[MomentStiff\right]=\int_0^L\left[N_\phi\right]^T\left(p_1\left[N_v\right]+p_2\left[N_\phi\right]+p_3\left[N_v'\right]+p_4\left[N_w'\right]\right)dx \qquad \textbf{(4.30)}$$

$$\left[K_e^A\right]=\left[LvStiff\right]+\left[LwStiff\right]+\left[MomentStiff\right] \qquad \textbf{(4.31)}$$

Here, $\left[LvStiff\right]$, $\left[LwStiff\right]$, $\left[MomentStiff\right]$ are the components of L_v, L_w and $\bar{M}$,i.e. Eqs.(3.37)-(3.39), that contribute to the aerodynamic part of the element stiffness matrix, $\left[K_e^A\right]$.

$$\left[LvDamp\right]=\int_0^L\left[N_v\right]^T\left(\bar{m}_1\left[N_v\right]+\bar{m}_2\left[N_\phi\right]+\bar{m}_3\left[N_w\right]+\bar{m}_4\left[N_w'\right]+\bar{m}_5\left[N_v'\right]\right)dx \qquad \textbf{(4.32)}$$

$$\left[LwDamp\right]=\int_0^L\left[N_w\right]^T\left(\bar{n}_1\left[N_v\right]+\bar{n}_2\left[N_w\right]+\bar{n}_3\left[N_\phi\right]+\bar{n}_4\left[N_w'\right]+\bar{n}_5\left[N_v'\right]\right)dx \qquad \textbf{(4.33)}$$

$$\left[MomentDamp\right]=\int_0^L\left[N_\phi\right]^T\left(\bar{p}_1\left[N_v\right]+\bar{p}_2\left[N_w\right]+\bar{p}_3\left[N_\phi\right]+\bar{p}_4\left[N_w'\right]+\bar{p}_5\left[N_v'\right]\right)dx \qquad \textbf{(4.34)}$$

$$\left[C_e^A\right]=\left[LvDamp\right]+\left[LwDamp\right]+\left[MomentDamp\right] \qquad \textbf{(4.35)}$$

Here, $\left[LvDamp\right]$, $\left[LwDamp\right]$, $\left[MomentDamp\right]$ are the components of L_v, L_w and $\bar{M}$,i.e. Eqs.(3.37)-(3.39), that contribute to the aerodynamic part of the element damping matrix, $\left[C_e^A\right]$.

$$\left[LvMass\right]=\int_{0}^{L}\left[N_v\right]^T\left(\bar{\bar{m}}_1\left[N_v\right]+\bar{\bar{m}}_2\left[N_w\right]+\bar{\bar{m}}_3\left[N_\phi\right]\right)dx \qquad \textbf{(4.36)}$$

$$\left[LwMass\right]=\int_{0}^{L}\left[N_w\right]^T\left(\bar{\bar{n}}_1\left[N_v\right]+\bar{\bar{n}}_2\left[N_w\right]+\bar{\bar{n}}_3\left[N_\phi\right]\right)dx \qquad \textbf{(4.37)}$$

$$\left[MomentMass\right]=\int_{0}^{L}\left[N_\phi\right]^T\left(\bar{\bar{p}}_1\left[N_v\right]+\bar{\bar{p}}_2\left[N_w\right]+\bar{\bar{p}}_3\left[N_\phi\right]\right)dx \qquad \textbf{(4.38)}$$

$$\left[M_e^A\right]=\left[LvMass\right]+\left[LwMass\right]+\left[MomentMass\right] \qquad \textbf{(4.39)}$$

Here, $\left[LvMass\right]$, $\left[LwMass\right]$, $\left[MomentMass\right]$ are the components of L_v, L_w and $\bar{M}$,i.e. Eqs.(3.37)-(3.39), that contribute to the aerodynamic part of the element mass matrix, $\left[M_e^A\right]$.

$$\left[LvConst\right]=\int_{0}^{L}\left(k_1\left[N_v\right]^T\right)dx \qquad \textbf{(4.40)}$$

$$\left[LwConst\right]=\int_{0}^{L}\left(k_2\left[N_w\right]^T\right)dx \qquad \textbf{(4.41)}$$

$$\left[MomentConst\right]=\int_{0}^{L}\left(k_3\left[N_\phi\right]^T\right)dx \qquad \textbf{(4.42)}$$

$$\left[Q_e^A\right]=\left[LvConst\right]+\left[LwConst\right]+\left[MomentConst\right] \qquad \textbf{(4.43)}$$

Here, $\left[LvConst\right]$, $\left[LwConst\right]$, $\left[MomentConst\right]$ are the components of L_v, L_w and $\bar{M}$,i.e. Eqs.(3.37)-(3.39), that contribute to the aerodynamic force vector, $\left[Q_e^A\right]$.

The coefficients of the aerodynamic matrices that are obtained for forward flight conditions are given in App. D.

4.3.6 Calculation of the aerodynamic properties

In this study, aeroelastic analysis of a single blade is carried out. However, most of the properties that are present in open literature are given for multi blade helicopters. Therefore, some calculations are carried out in this section to find the proper aerodynamic values for a single blade rotor.

Some geometrical properties of the BO-105 helicopter blade, which are introduced byViswamurthy and Ganguli, (2006) and given in Table 4.2, are used as the basic values to calculate the essential geometric properties of the blade used in this study.

Table 4.2 : Geometrical properties of the BO-105 helicopter blade.

Parameter	**Value**
R	5 m
$\bar{c}/R$	0.055
$\bar{c}_f/\bar{c}$	0.20
C_T/σ	0.007

where R is the length of the blade, $\bar{c}$ is the blade chord length, $\bar{c}_f$ is the flap chord length, σ is the rotor solidity and C_T is the trust coefficient.

4.3.6.1 Rotor solidity and thrust coefficient

Rotor solidity, σ, is defined as the ratio of the total blade area to the rotor disk area and for a rectangular blade, it is expressed as follows

$$\sigma = \frac{Blade\ Area}{Disk\ Area} = \frac{N_b \bar{c} R}{\pi R^2} = \frac{N_b \bar{c}}{\pi R} \qquad \textbf{(4.44)}$$

where N_b is the number of the blades.

Referring Table 4.2, the chord length of the blade is calculated to be $\bar{c} = 0.273m$ and as mentioned before, a single blade rotor is modeled in this study so $N_b = 1$ for this research. Substituting these values into Eq.(4.44), the rotor solidity is calculated to be $\sigma = 0.0174$.

ReferringTable 4.2 and the calculated rotor solidity, the thrust coefficient is found to be $C_T = 0.0012$.

4.3.6.2 Inflow ratio under hover conditions

Under hover conditions, the relation between the inflow ratio and the thrust coefficient is given by (Leishman, 2006)

$$\lambda_h = \sqrt{\frac{C_T}{2}} \qquad \textbf{(4.45)}$$

Substituting the calculated thrust coefficient, $C_T = 0.0012$, into Eq.(4.45), the hover inflow ratio is found to be $\lambda_h = 0.024$.

4.3.6.3 Inflow ratio in forward flight

In forward flight, the expression of the inflow ratio is given by (Leishman, 2006)

$$\lambda_f = \mu Tan\chi + \frac{C_T}{2\sqrt{\mu^2 + \lambda_f^2}} \tag{4.46}$$

where μ is the advance ratio and χ is the rotor disk angle of attack which appears when the rotor disk is tilted slightly forward to produce a propulsive force for the forward flight as seen in Figure 4.2.

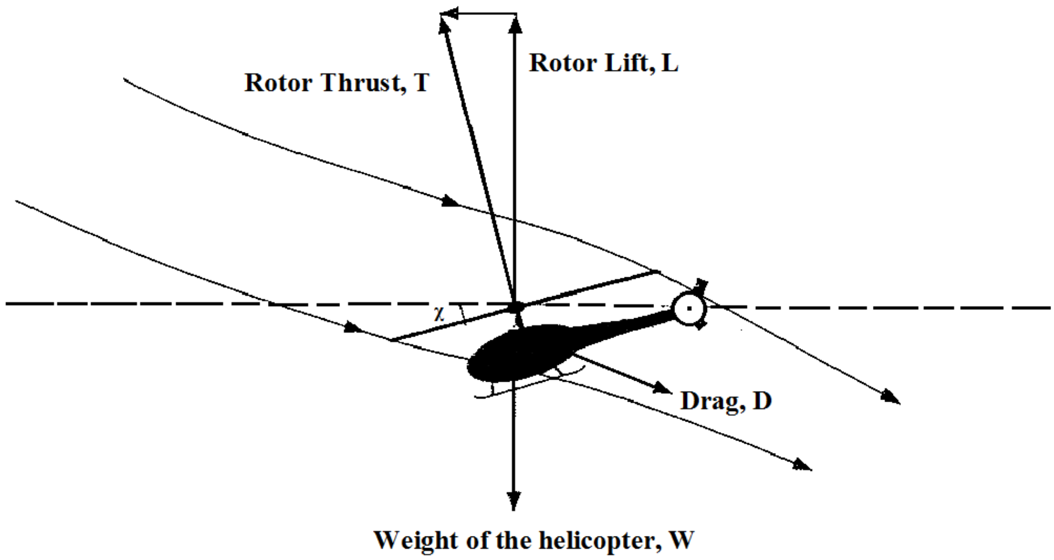

Figure 4.2: Rotor disk angle of attack in forward flight, adapted from(Leishman,2000).

In Eq.(4.46), it is noticed that λ_f appears on both sides of the equation which requires a numerical solution for λ_f. However, instead of applying a numerical solution, a graphic that illustrates the relationship between λ_h and λ_f can be used. The mentioned graphic is presented by Leishman (2000) andgiven in Figure 4.3.

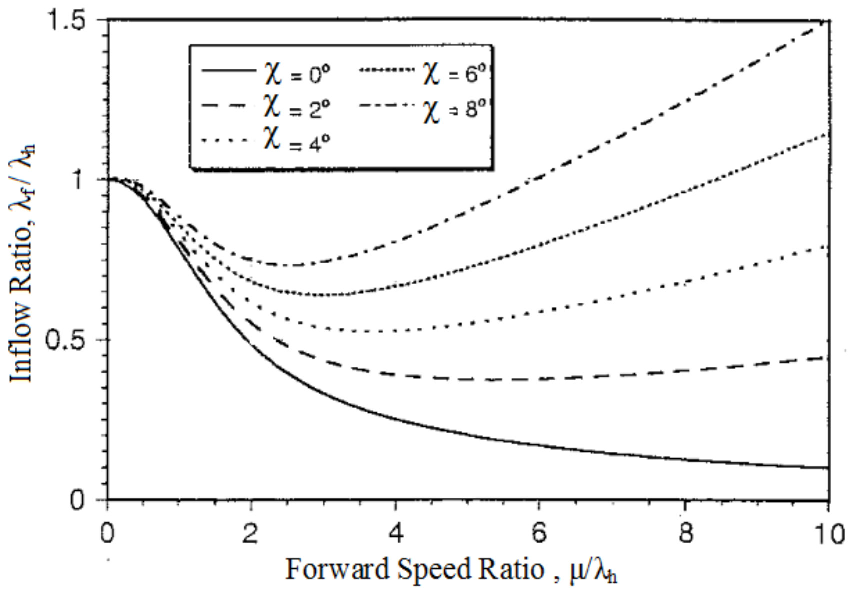

Figure 4.3: Variation of the inflow ratio with respect to the forward speed ratio and the rotor disk angle of attack, adapted from Leishman (2000).

In this study, a moderate forward flight speed is considered so the advance ratio is taken to be $\mu = 0.2$. Considering the hover inflow ratio that has already been calculated, $\lambda_h = 0.024$, the forward speed ratio is found to be $\mu/\lambda_h = 8.3$.

Referring Figure 4.3, the following table, Table 4.3, is prepared

Table 4.3: Forward flight inflow ratios for different values of rotor disk angle attack.

Rotor disk angle of attack (χ)	Forward flight inflow ratio (λ_f)
0^0	0.003
2^0	0.0096
4^0	0.0168
6^0	0.0235
8^0	0.0312

4.3.7 Blade model

The studied blade model, whose material and geometrical properties are given in Table 4.4, is illustrated in Figure 4.4.

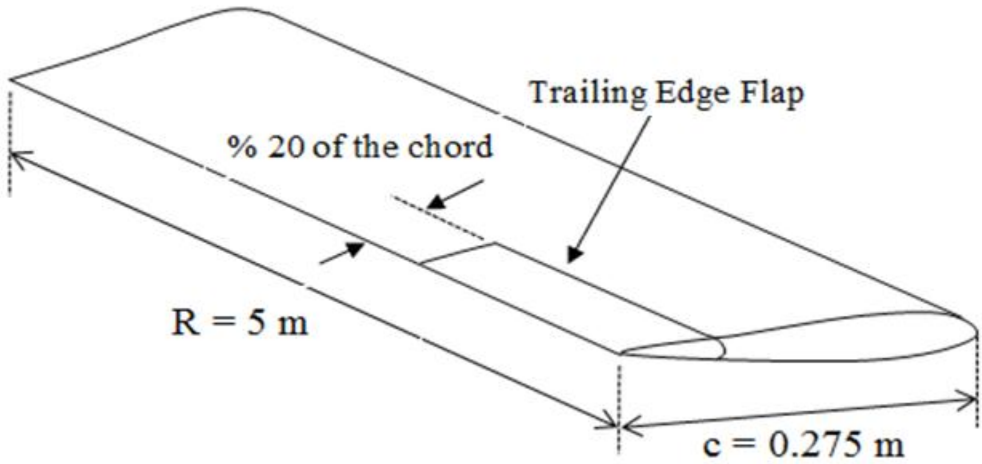

Figure 4.4: Helicopter blade configuration used for the vibration analysis.

Here, it is seen that the trailing edge flap is located at the tip of the blade and the flap chord is % 20 of the blade chord length.

Table 4.4: Material and geometricalproperties of the helicopter blade with a trailing edge flap.

Parameter	Value
E	70×10^{9} Pa
GJ	1.12599×10^{6} Nm^2
I_y	11.7187×10^{-6} m^4
I_z	14.5046×10^{-5} m^4
e_1	9.361×10^{-3} m
e_2	0 m
ρ	2700 kg/ m^3
A	22.5×10^{-3} m^2
a_h	-0.766

4.3.8 Vibration analysis under hover conditions

When the helicopter operates under hover conditions, flapwise bending deflection of the rotor tip with respect to time is illustrated in Figure 4.5 where $\lambda_h = 0.024$ and $\mu = 0$ .The air density is taken to be $\rho_\infty = 1.225$ kg/m^3 for the vibration analysis.

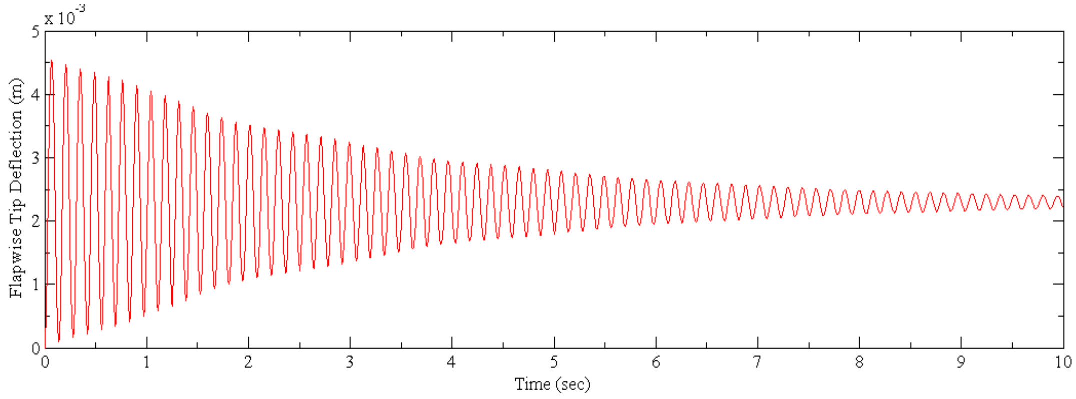

Figure 4.5: Flapping tip deflection under hover conditions.

As it is seen in Figure 4.5, the flapwise tip deflection of the rotor blade is damped under hover conditions due to the aerodynamic damping. Since under hover conditions vibration is damped on its own, in this case there is no need to study the effect of the flap deflection which is aimed to reduce vibration.

4.3.9 Vibration analysis in forward flight

In this section, effects of several parameters, i.e. trailing edge flap deflection, β, voltage that is applied to the piezoelectric bender type actuator, V,advance ratio, μ and, rotor disk angle of attack, χ on the flapwise tip deflection of the helicopter blade under forward flight conditions are inspected.

In Figure 4.6 – Figure 4.9, where χ = 2^0 and β = 0^0, variation of the blade flapwise tip deflection versus several values of advance ratio is illustrated where, it is seen that as the forward flight speed of the helicopter gets higher, the blade vibrates more and the blade tip deflection gets larger.

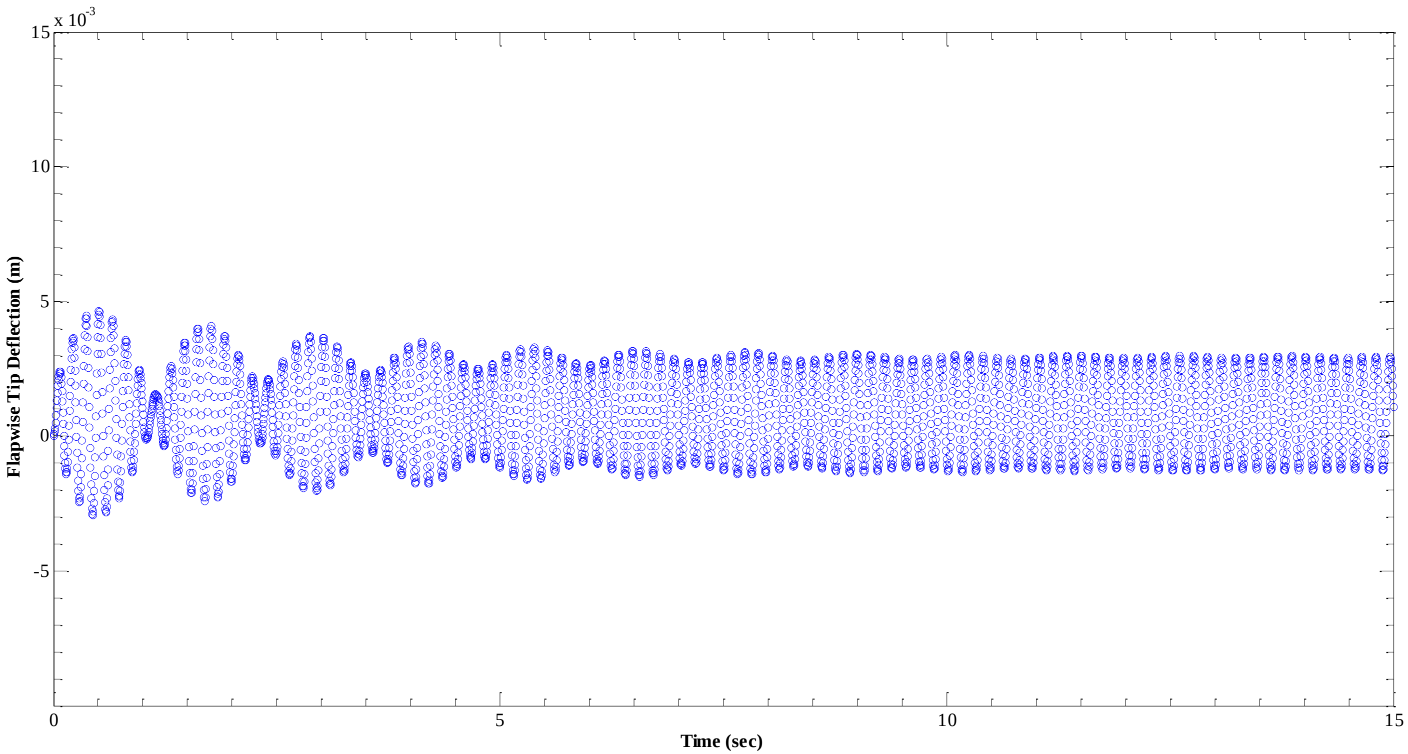

Figure 4.6 : Flapwise tip deflection of the blade versus time for the advance ratio, μ=0.1.

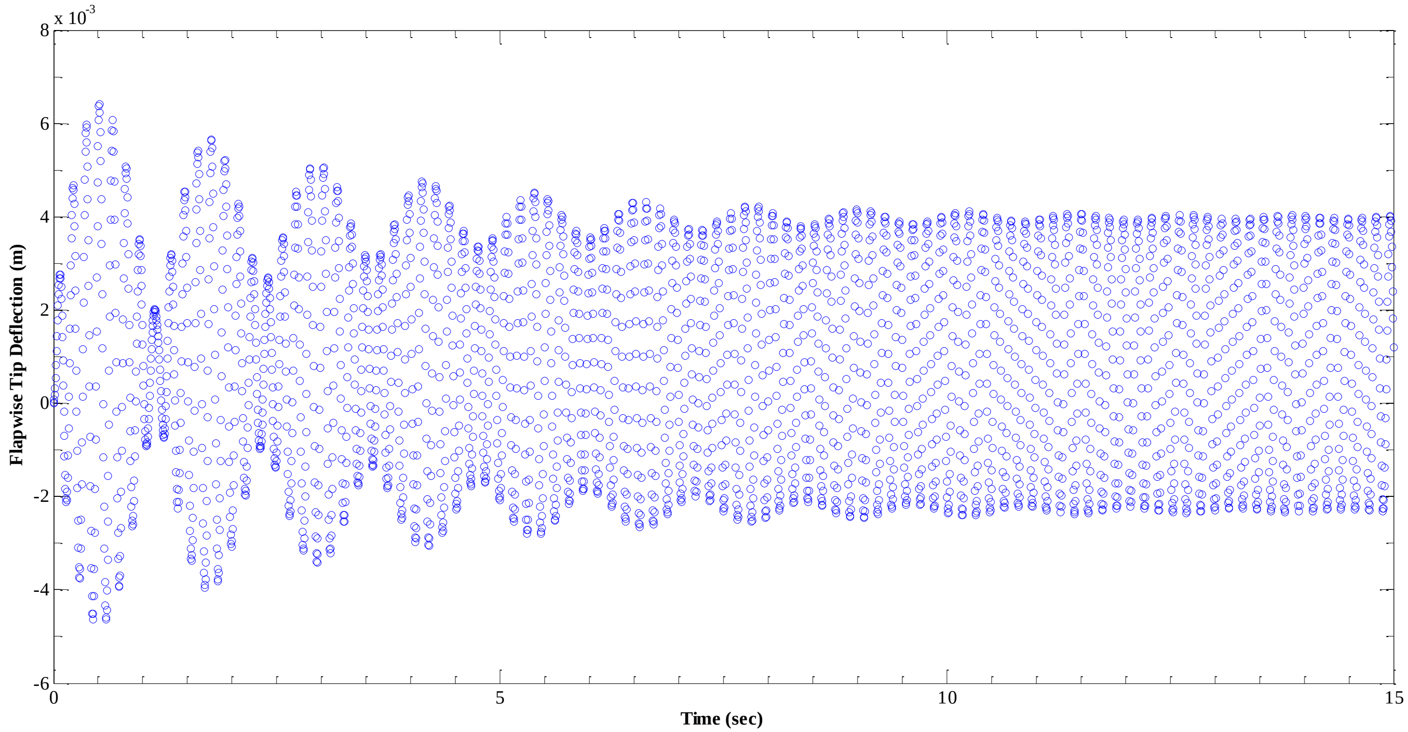

Figure 4.7 : Flapwise tip deflection of the blade versus time for the advance ratio, μ=0.15.

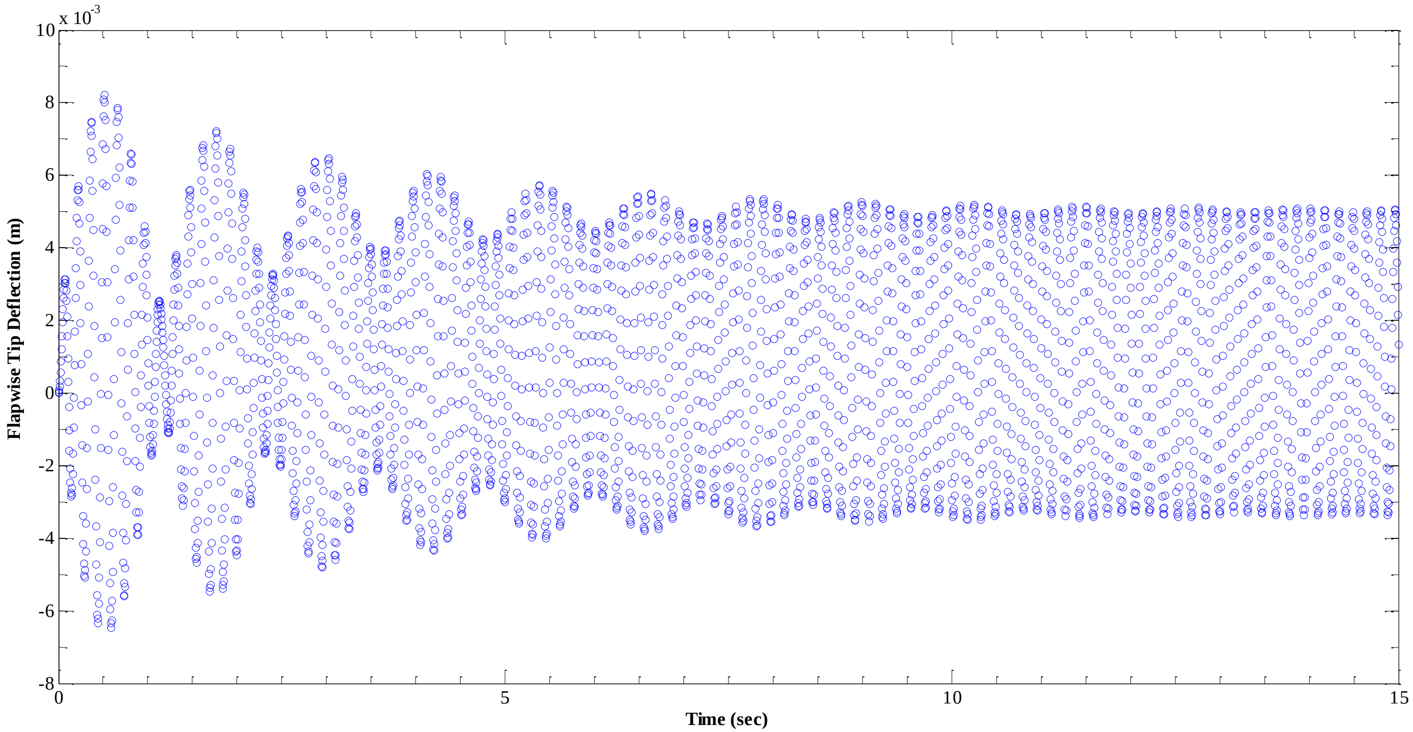

Figure 4.8 : Flapwise tip deflection of the blade versus time for the advance ratio, μ=0.2.

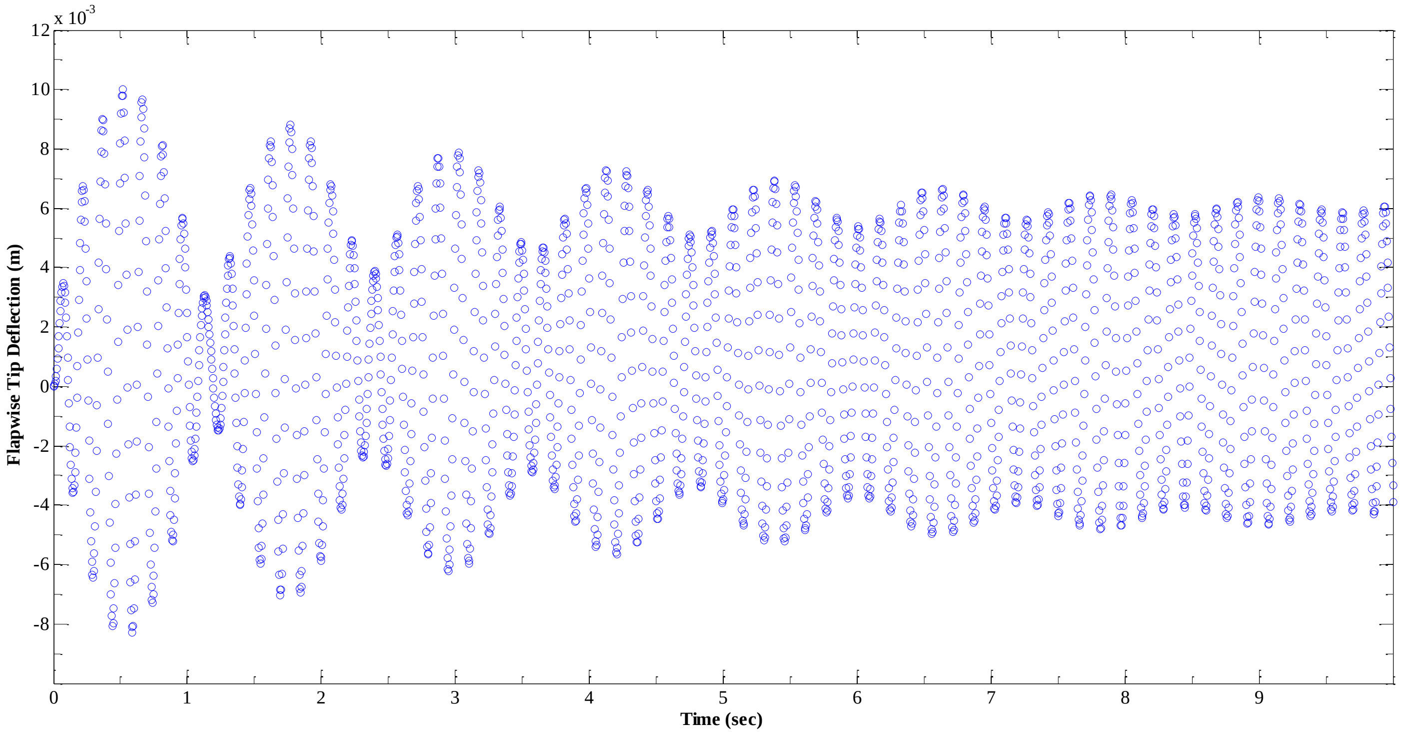

Figure 4.9 : Flapwise tip deflection of the blade versus time for the advance ratio, μ=0.25.

In Figure 4.10 and Figure 4.11, where, $\mu = 0.2$ and $\beta = 0^0$, variation of the blade flapwise tip deflection versus several values of the rotor disk angle of attack is illustrated.In forward flight, the rotor must always be tilted slightly forward to produce a propulsive force and $\chi = 0^0$ is not a realistic case but here, $\chi = 0^0$ value is used just to make comparison. In these figures, it is seen that as the rotor disk is tilted more, the blade vibrates more and the blade tip deflection gets larger.

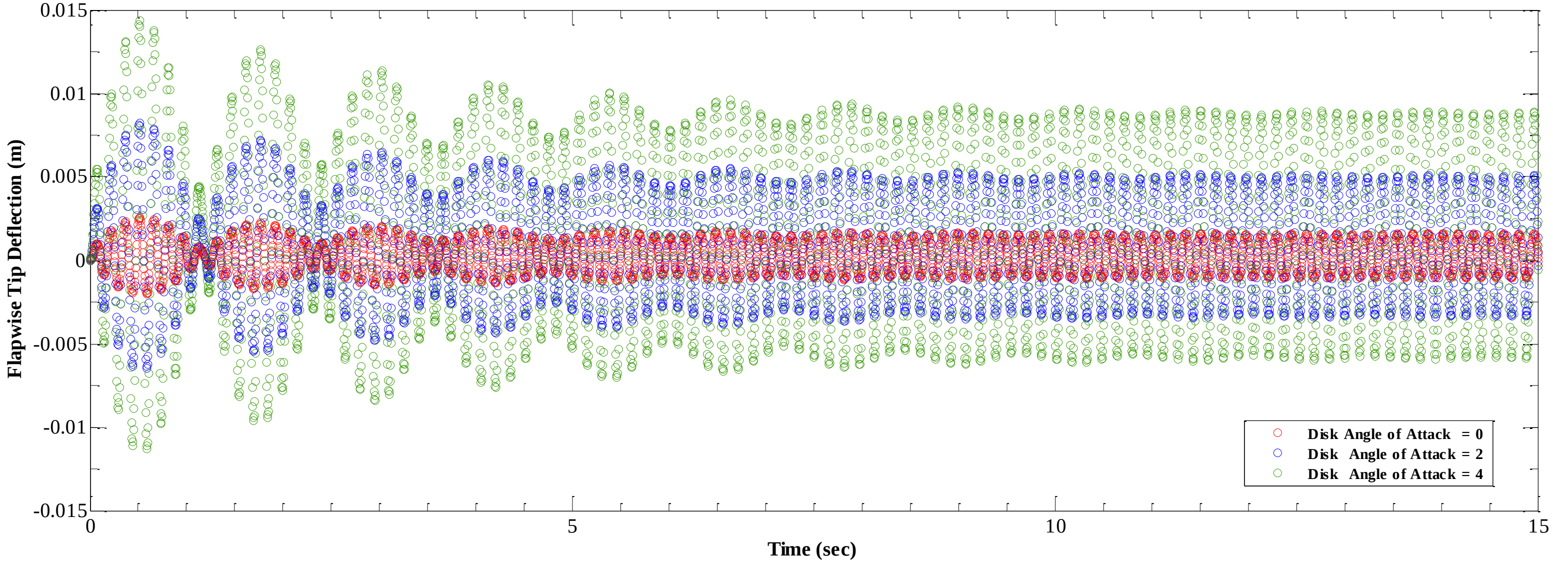

Figure 4.10 : Flapwise tip deflection of the blade versus time for the disk angle of attacks, χ=0^0, 2^0,4^0.

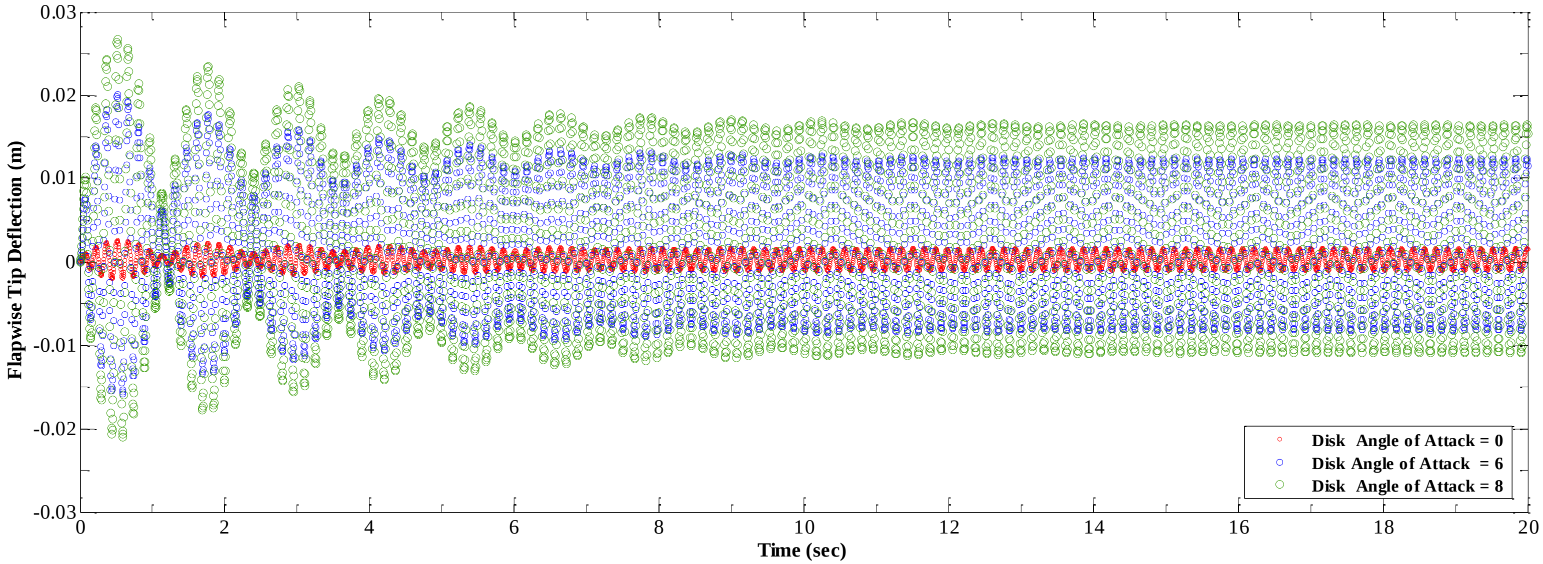

Figure 4.11: Flapwise tip deflection of the blade versus time for the disk angle of attacks,$\chi=0^0$, 6^0,8^0.

In Figure 4.12 – Figure 4.16, variation of the blade flapwise tip deflection versus several values of the trailing edge flap deflection is illustrated. In these figures, vibration levels of the rotor blade with and without trailing edge flap deflection are represented by the green and the red lines, respectively and here it is seen that the flapwise tip deflection is not damped on its own in forward flight, i.e. red lines, although under hover conditions, blade vibration is damped on its own, i.e. Figure 4.5. In Figure 4.17, flapwise tip deflection is plotted versus several flap angles just for comparison.

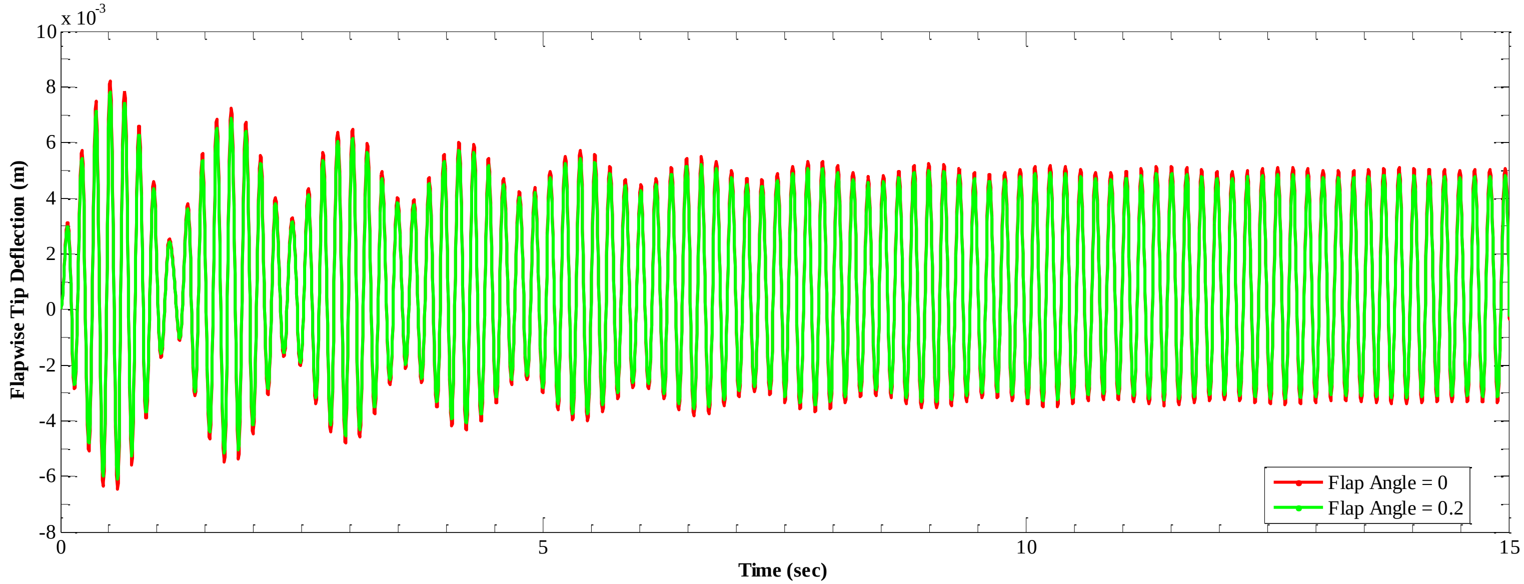

Figure 4.12: Flapwise tip deflection reduction versus time for the trailing edge flap angle, $\beta = 0.2^0$.

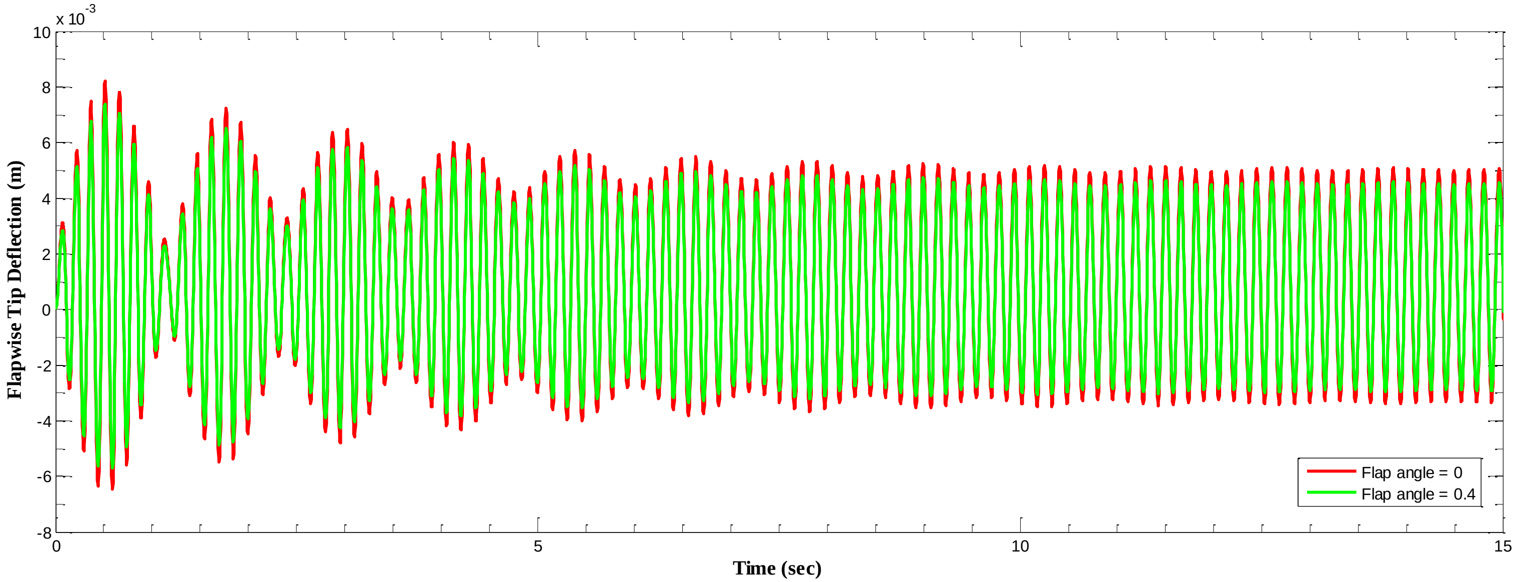

Figure 4.13: Flapwise tip deflection reduction versus time for the trailing edge flap angle, $\beta = 0.4^0$.

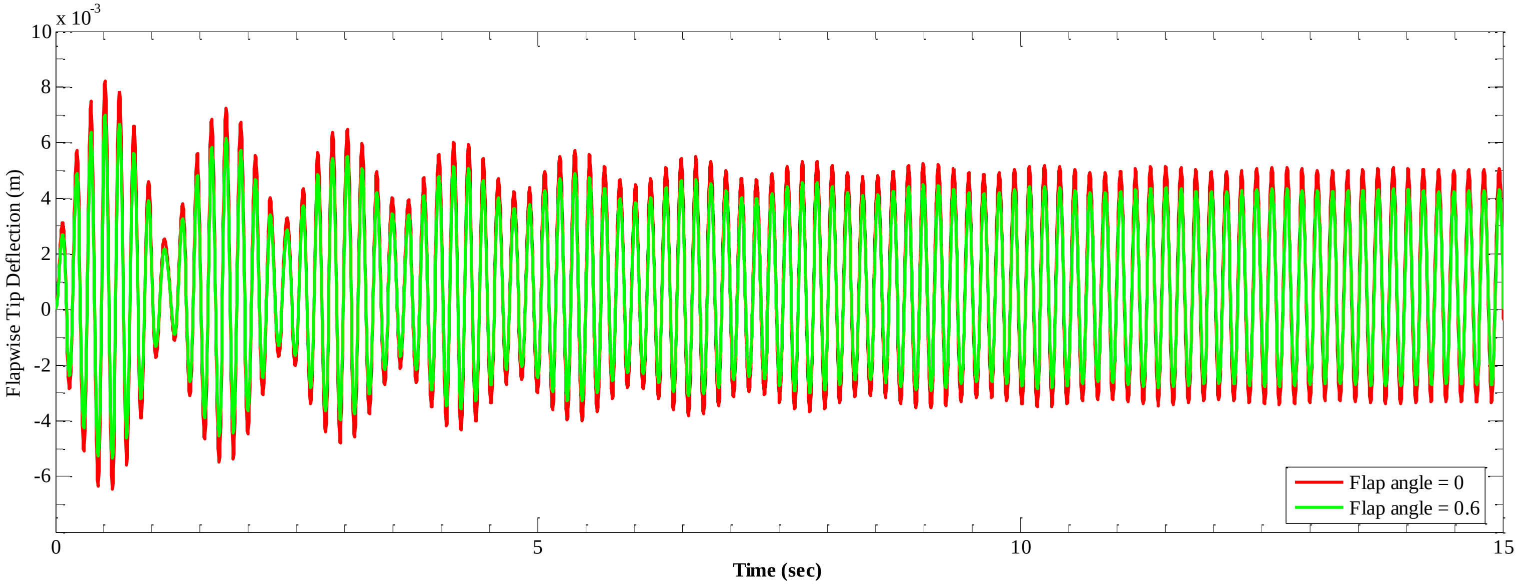

Figure 4.14: Flapwise tip deflection reductionversus time for the trailing edge flap angle, $\beta = 0.6^0$.

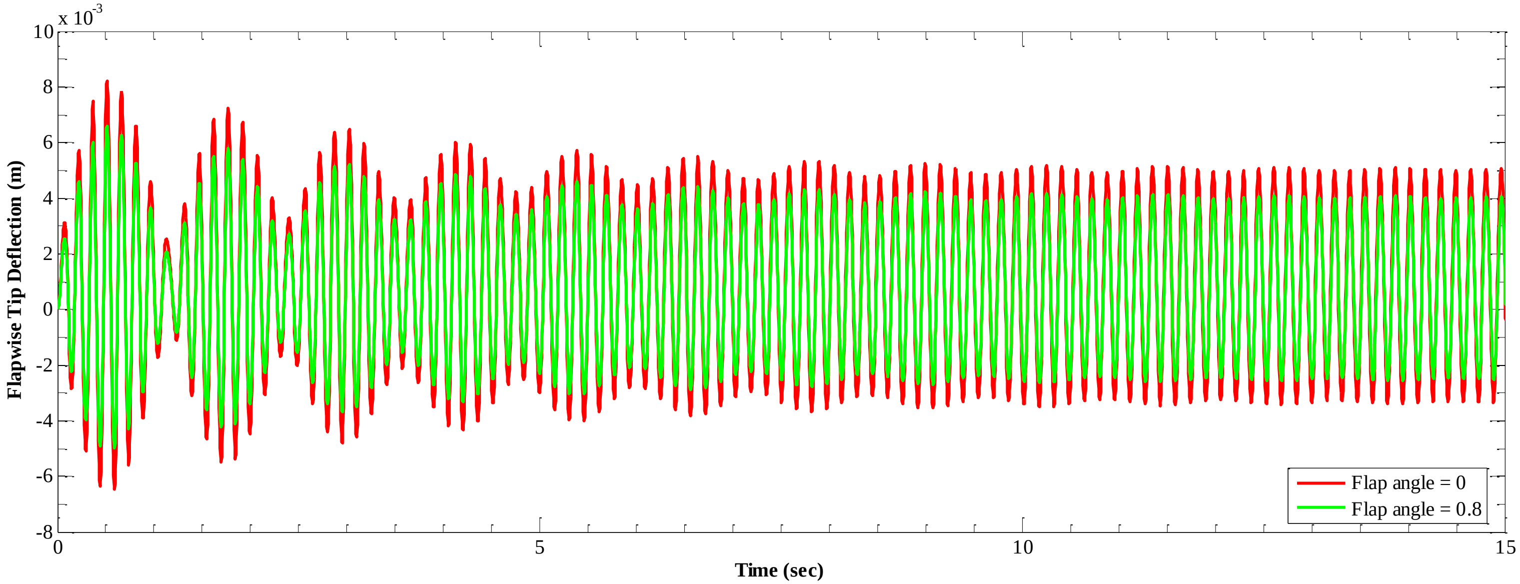

Figure 4.15: Flapwise tip deflection reductionversus time for the trailing edge flap angle, $\beta = 0.8^0$.

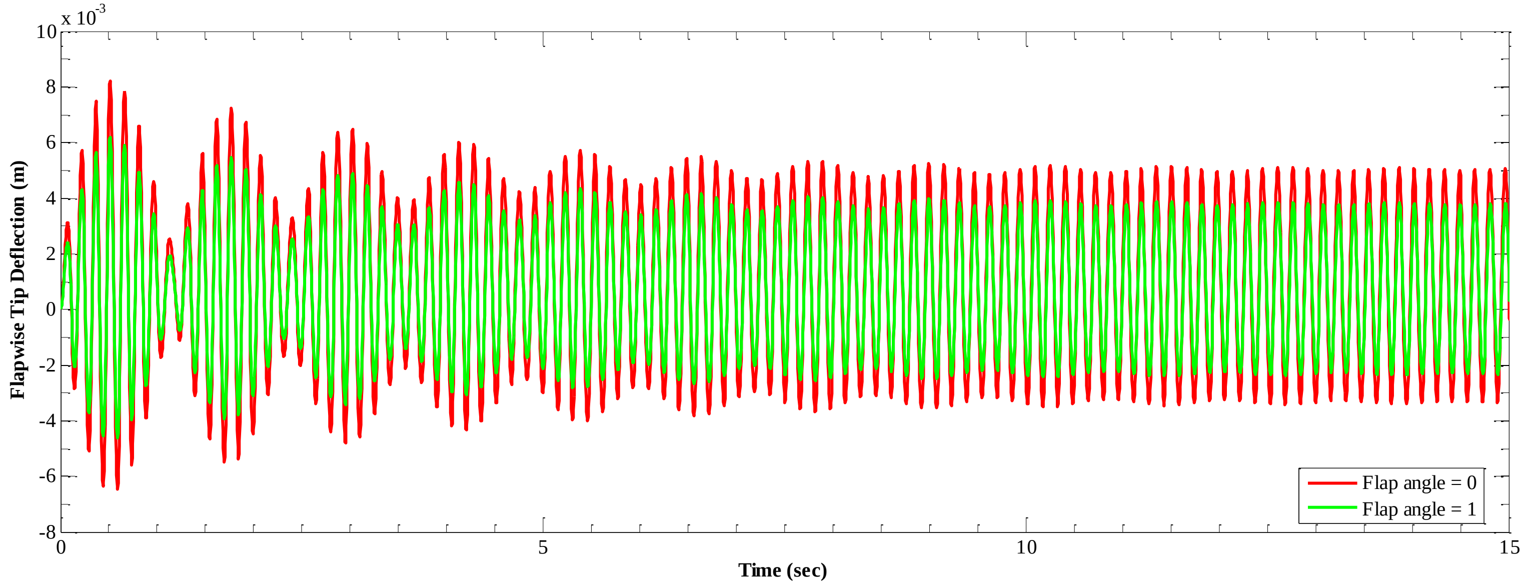

Figure 4.16: Flapwise tip deflection reductionversus time for the trailing edge flap angle, $\beta = 1^0$.

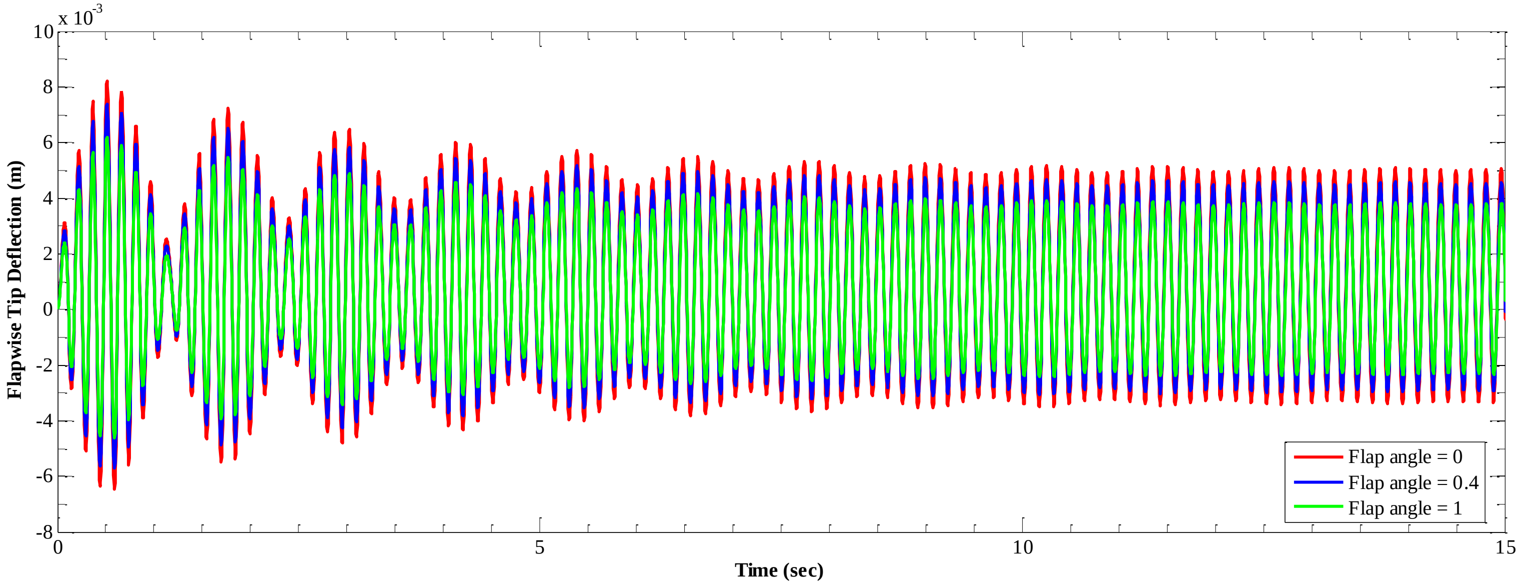

Figure 4.17: Flapwise tip deflection reductionversus time for the trailing edge flap angles, $\beta = 0^0, 0.4^0, 1^0$.

In Figure 4.12 – Figure 4.16, it is noticed that the flapwise tip deflection is suppressed more as the trailing edge flap deflects more. However, the trailing edge flap angle has a limit value at which the tip deflection is not suppressed any more since the structure fails as seen in Figure 4.18 where the flap deflection angle is $\beta = 3^0$ and the rotor disk angle of attack is $\chi = 2^0$.

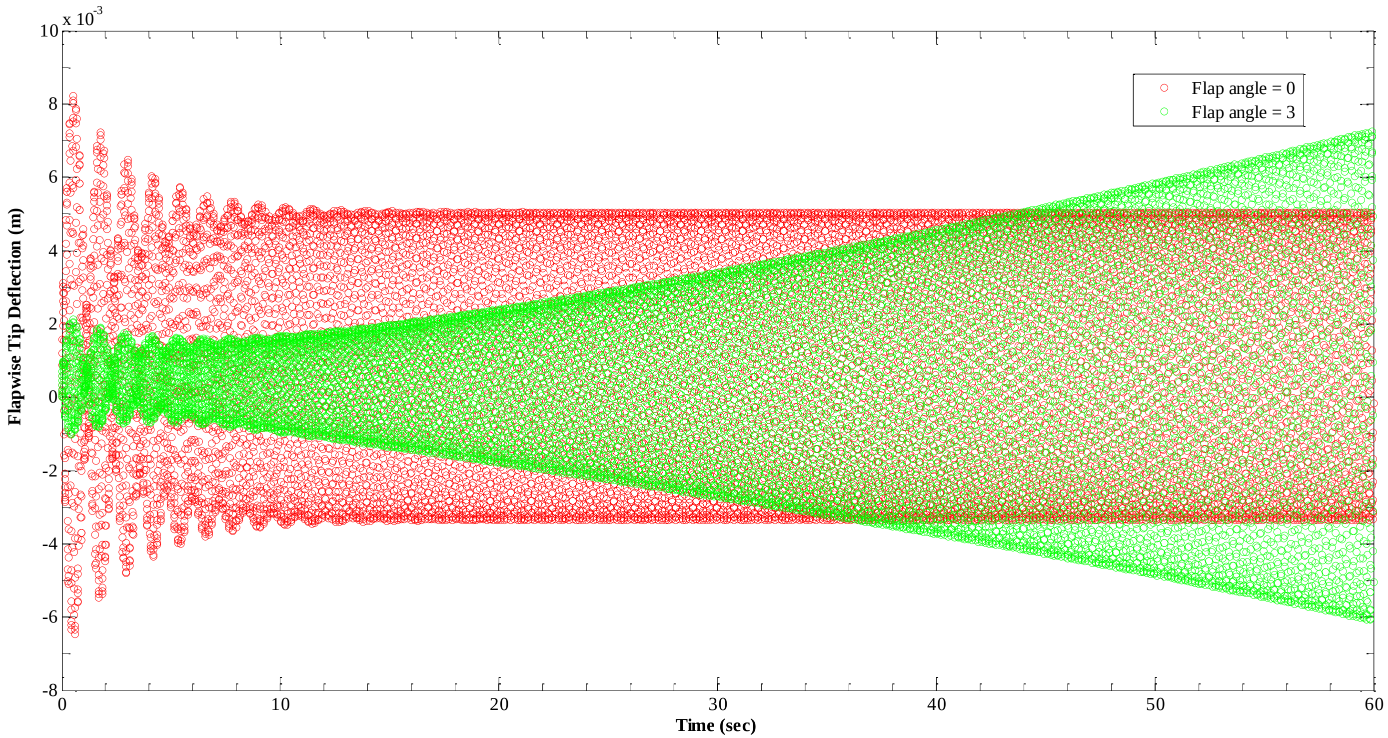

Figure 4.18: Flapwise tip deflection reduction, $\mu = 0.2$, $\chi = 2^0$, $\beta = 3^0$.

In Figure 4.19, the same flap deflection angle as in Figure 4.18, $\beta = 3^0$,is applied but the rotor disk angle of attack is taken to be $\chi = 6^0$. When Figure 4.18 is compared with Figure 4.19, it is seen that the same flap angle, $\beta = 3^0$, makes the structure fail at $\chi = 2^0$ while it just suppresses the tip deflection at $\chi = 6^0$ which shows that the limit value of the flap deflection angle depends on the rotor disk angle of attack, χ.

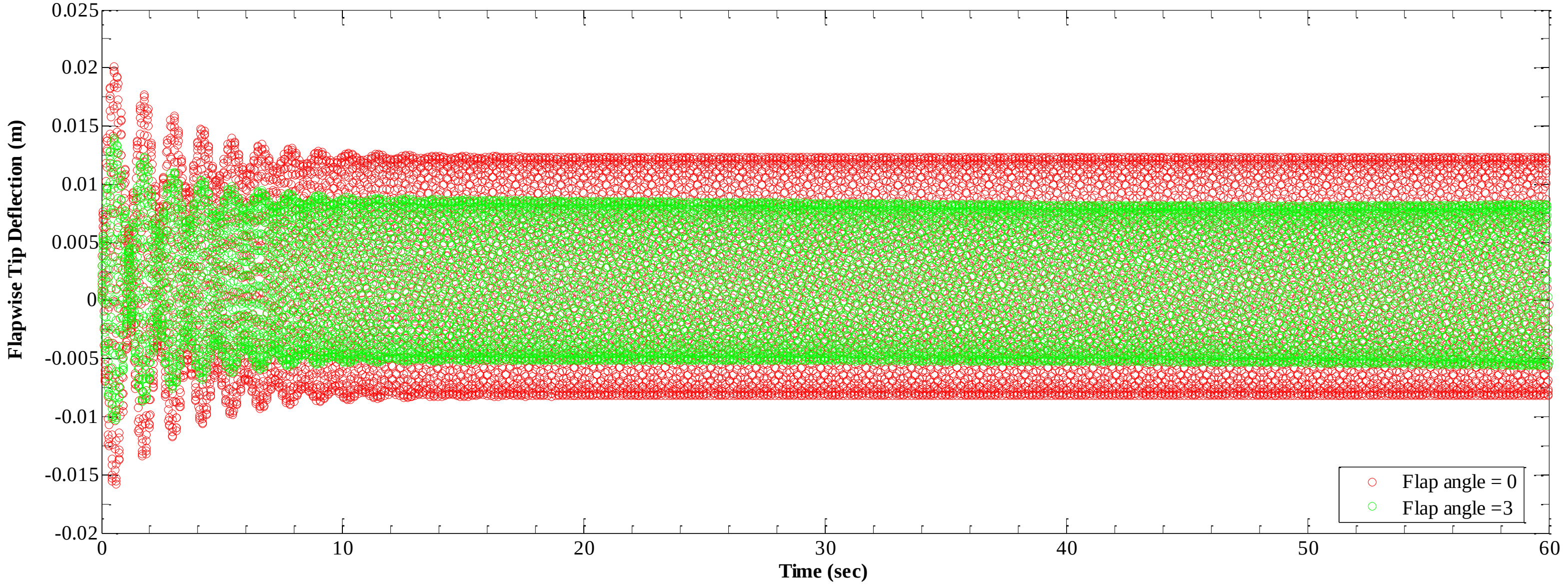

Figure 4.19: Flapwise tip deflection reduction, $\mu = 0.2$, $\chi = 6^0$, $\beta = 3^0$.

In Figure 4.20, percentage reduction in the flapwise tip deflection of the helicopter blade with respect to the voltage value applied to the piezoelectric bender type actuator is illustrated. All the calculations are carried out by using the material and geometrical properties given for the bimorph beam example in Section 2.3.8.1.In Figure 4.20, it is seen that as the voltage applied to the actuator is increased,flapwise tip deflection of the helicopter blade is reduced more since the trailing edge flap is deflected more. The percentage reduction is calculated with respect to the tip deflection of the plain blade in forward flight, i.e. red lines in Figure 4.12 – Figure 4.16.

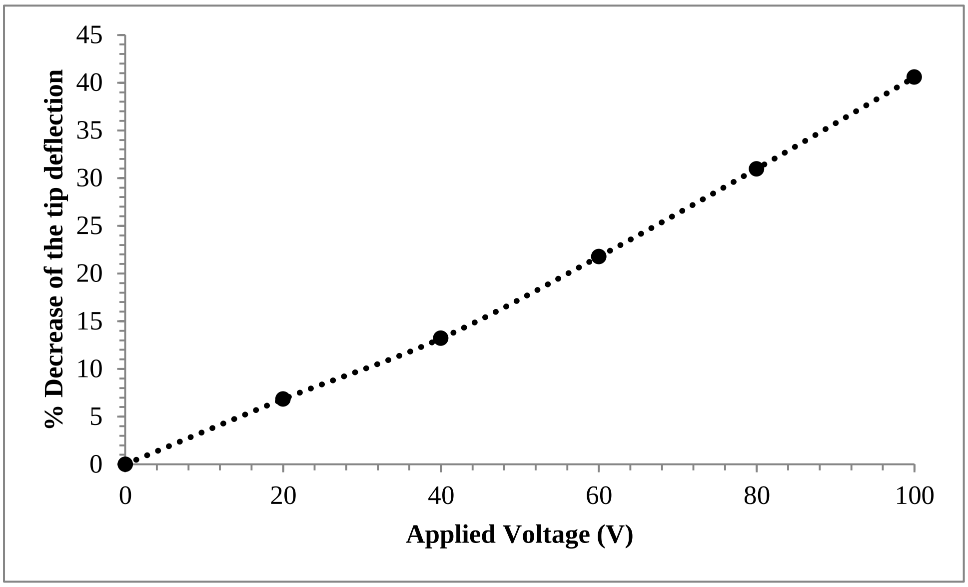

Figure 4.20: Voltage effect on the tip deflection of the helicopter blade, $\mu = 0.2$, $\chi = 0^0$

5. CONCLUSIONS AND RECOMMENDATIONS

5.1 Present Results

In the present study, formula derivations are made in great detail for all the sections, i.e. structural, aerodynamic and aeroelastic sections. Structural models are built both for the bender type piezoelectric actuator and the helicopter blade. The piezoelectric bender is connected to the trailing edge flap mechanism by calculating the length of the linkage arm. The Theodorsen's nonlinear aerodynamic theory is applied to rotary wing aerodynamic environment by making several transformations to build the aerodynamic model. The structural and aerodynamic models are assembled accurately to formulate the aeroelastic model. The correctness and accuracy of the models are revealed by validating the calculated results in several tables and figures. In the aeroelastic section, effects of several parameters, i.e. advance ratio, rotor disk angle of attack, trailing edge flap deflection and voltage applied to the piezoelectric actuator, on the vibration characteristics of a helicopter blade are investigated. In hover case, it is seen that the flapwise tip deflection of the rotor blade is damped due to the aerodynamic damping and since the vibration is damped on its own, there is no need to inspect the effect of the flap deflection which is aimed to reduce vibration. In forward flight case, it is seen that the tip deflection is not damped on its own. The flapwise tip deflection of the rotor blade is reduced after the flap is deflected which proves that the trailing edge flap has a reducing effect on the vibration characteristic of the rotor blade in forward flight which also reveals that the goal of the present thesis is achieved. Additionally, it is observed that as the voltage that is applied to the actuator is increased, tip deflection of the helicopter blade is reduced more since the trailing edge flap is deflected more. Moreover, it is noticed that advance ratio and the rotor disk angle of attack have an increasing effect on the blade vibration and that the limit value of the flap deflection angle at which the structure is destroyed depends on the rotor disk angle of attack, i.e. as the rotor disk angle of attack increases, the flap angle has a higher limit value.

5.2 Future Work

The following titles are recommended for the future work

- The flap deflection angle can be taken as a degree of freedom instead of using a prescribed flap angle.
- Inertial effects of the flap mechanism can be added to the structural formulation.
- Effects of the aerodynamic loads on the piezoelectric actuator can be inspected.
- A more advanced aerodynamic theory can be used.
- Instead of Euler-Bernoulli or Timoshenko beam theories, Geometrically Exact Beam theory can be used (Hodges, 2006).
- Instead of one flap, multiple flaps can be used and effects of flap location, flap chord length, number of flaps, etc. can be inspected.
- Hysteresis effect of the piezoelectric actuator can be included.

REFERENCES

Beran, P. S., Strganac, T. W., Kim, K., and Nichkawde, C. (2004). Studies of store-induced limit-cycle oscillations using a model with full system nonlinearities.*Nonlinear Dynamics,***37**, 323–339.

Ben-Zeev, O., and Chopra, I. (1996). Advances in the development of an intelligent helicopter rotor employing smart trailing-edge flaps. *Smart Materials and Structures,* 5, 11–25.

Bisplinghoff, R. L., Ashley, H., and Halfman, R. L. (1996). *Aeroelasticity.* Dover Publications, New York.

Booth, E. R. and Wilbur, M. L. (2004). Acoustic aspects of active twist rotor control. *Journal of the American Helicopter Society*, **49** (1), 3-10.

Borglund, D., and Kuttenkeuler, J. (2002). Active wing flutter suppression using a trailing edge flap. *Journal of Fluids and Structure,* **16** (3), 271-294.

Carnegie, W., and Dawson, B. (1971). Vibration characteristics of pre-twisted blades of asymmetrical aerofoil cross-section. *Aeronautical Quarterly,***22**, 257- 273.

Cesnik, C. E. S., and Hodges, D. H. (1997). VABS: A new concept for composite rotor blade cross-sectional modeling. *Journal of the American Helicopter Society,***42** (1), 27-38.

Cesnik, C. E. S., and Shin, S. (2001). On the modeling of integrally actuated helicopter blades. *International Journal of Solids and Structures*. 38 (10-13), 1765-1789.

Chen, P. and Chopra, I. (1996). Induced strain actuation ofcomposite beams and rotor blades with embedded piezoceramic elements. *Smart Materials and Structures,* **5**, 35–48.

Chen, P., and Chopra, I. (1997). Hover testing of smart rotor with induced-strain actuation of blade twist *AIAA Journal*, **35,** 6–16.

Cho, M. H., and Lee, I. (1994). Aeroelastic stability of hingeless rotor blade in hover using large deflection theory. *AIAA Journal*, **32** (7), 1472-1477.

Chopra, I. (2000). Status of application of smart structures technology to rotorcraft systems. *Journal of the American Helicopter Society,* **45** (4), 228-252.

Chopra, I. (2002). Review of state of art of smart structures and integrated systems. *AIAA*, **40** (11), 2145-2187.

Crawley, E. F. (1994). Intelligent structures for aerospace: A technology overview and assessment. *AIAA Journal,* **32** (8) 1689-1699.

Derham, R., and Hagood, N. (1996). Rotor Design Using Smart Materials to Actively Twist Blades.Proceedings of American Helicopter Society 52nd Annual Forum, Washington, DC, 4-6 June.

Donthireddy, P., and Chandrashekhara, K. (1996). Modeling and shape control of composite beams with embedded piezoelectric actuators. *Composite Structures*, **35** (2), 237-244.

Edery-Azulay, L., and Abramovich, H. (2006). Active damping of piezo-composite beams. *Composite Structures*,**74** (4), 458-466.

Eringen, A. C. (1980). *Mechanics of Continua*. Robert E. Krieger Publishing Company, Huntington, New York.

Eslimy-Isfahany, S.H.R., Banerjee, J.R.and Sobey, A.J. (1996).Response of a bending–torsion coupled beam to deterministic and random loads. *Journal of Sound and Vibration*, **195**(2), 267-283.

Fridman, Y., and Abramovich, H. (2008). Enhanced structural behavior of flexible laminated composite beams. *Composite Structures*,**82** (1), 140-154.

Friedmann, P. P. (2004). Rotary-wing aeroelasticity: Current status and future trends. *AIAA Journal*,**42** (10), 1953-1972.

Friedmann, P. P., de Terlizzi, M., and Myrtle, T. F. (2001). New developments in vibration reduction with actively controlled trailing edge flaps. *Mathematical and Computer Modelling*, **33** (10-11), 1055-1083.

Fuller, C. R., Elliott, S. J., Nelson. P. A. (1996). *Active Control of Vibration*. Academic Press, San Diego

Gaudenzi P., S. Y. (2005). Modelling of smart structures. *Computers and Structures*, **83**, 1151-1152.

Ghiringhelli, G. L., Masarati, P., and Mantegazza, P. (2000). Characterisation of a smart rotor blade incorporating active fibre composites. *Computational Methods for Smart Structures and Materials,* **7**, 119-128.

Gibson, R. F. (2007). *Principles of Composite Material Mechanics*. CRC Press, Boca Raton.

Goland, M. (1945). The flutter of a uniform cantilever wing, *Journal of Applied Mechanics*, **12** (4), A197–A208.

Gunston, B. and Spick, M. (1986). *Modern Fighting Helicopters*, Tiger Books International.

Hodges, D. H.. (2006). *Nonlinear Composite Beam Theory*. AIAA, Washington, D.C.

Hodges, D. H., and Dowell, E. H. (1974).Nonlinear equations of motion for the elastic bending and torsion of twisted nonuniform rotor blades, *NASA Technical Report*,**NASA TN D-7818.**

Hodges, D. H., and Ormiston, R. A. (1976). Stability of elastic bending and torsion of uniform cantilever rotor blades in hover with variable structural coupling, *NASA Technical Report,* **NASA TN D-8192.**

Hodges, D. H., and Pierce, G. A. (2002). *Introduction to Structural Dynamics and Aeroelasticity*,Cambridge University Press.

Hwang, W. S., and Park, H. C. (1993). Finite-element modeling of piezoelectric sensors and actuators. *AIAA Journal*,**31** (5), 930-937.

Johnson, W. (1980). Application of unsteady airfoil theory to rotary wings. *Journal of Aircraft*,**17** (4), 285-286.

Kaya, M. O. and Ozdemir Ozgumus O. (2007). Flexural–torsional coupled vibration analysis of axially loaded closed section composite Timoshenko beam by using DTM, *Journal of Sound and Vibration*, **306** (3-5), 495-506.

Kaya, M. O. and Ozdemir Ozgumus O.(2010). Energy expressions and free vibration analysis of a rotating uniform Timoshenko beam featuring bending-torsion coupling, *Journal of Vibration and Control*, **16** (6), 915-934.

Kaza, K. R. V., and Kvaternik, R. G. (1981). Application of unsteady airfoil theory to rotary wings. *Journal of Aircraft*,**18** (7), 604-605.

Kollar, L. R. and Springer, G. S. (2003). *Mechanics of Composite Structures*. Cambridge University Press, United Kingdom.

Koratkar, N. (2000). Smart helicopter rotor with piezoelectric bender actuated trailing edge flaps, *PhD Thesis*, University of Maryland, Maryland.

Koratkar, N. A., and Chopra, I. (2000). Analysis and testing of mach-scaled rotor with trailing-edge flaps. *AIAA Journal*, **38** (7), 1113-1124.

Koratkar, N. A., and Chopra, I. (2001). Wind tunnel testing of a mach-scaled rotor model with trailing-edge flaps. *Smart Materials and Structures*, **10**, 1–14.

Koratkar, N. A., and Chopra, I. (2002). Wind tunnel testing of a smart rotor model with trailing-edge flaps. *Journal of The American Helicopter Society*, **47** (4),263-272.

Lee, T., and Chopra, I. (1999). Development and Validation of a Refined Piezostack-Actuated Trailing-edge Flap Actuator for a Helicopter Rotor. Proceedings of SPIE, 3668, 9 June.

Lee, T., and Chopra, I. (2000).Design issues of a high-stroke, on-blade piezostack actuator for a helicopter rotor with trailing-edge flaps.*Journal of Intelligent Material Systems and Structures*, **11** (5),328-342

Lee, T., and Chopra, I. (2001). Design of piezostack-driven trailing-edge flap actuator for helicopter rotors. *Smart Materials and Structures*, **10**, 15–24.

Leishman, J. G., (2006). *Principles of Helicopter Aerodynamics.* Cambridge University Press, Cambridge; New York.

Li, J., Shen, R. Y., Hua, H. X., and Jin, X. D. (2004). Response of monosymmetric thin-walled timoshenko beams to random excitations. *International Journal of Solids and Structures*, **41** (22-23), 6023-6040.

Lin, J. and Iliff, K.W. (2000). Aerodynamic lift and moment calculations using a closed form solution of the Possio equation, *NASA Technical Report*, NASA/TM-2000-209019.

Liu, L., Friedmann, P. P., Kim, I. and Bernstein, D. S. (2006). Vibration Reduction and Performance Enhancement in Rotorcraft Using Active Flaps at High Advance Ratios. 47th AIAA/ASME/ASCE/AHS/ASC Structures, Structural Dynamics, and Materials Conference, Newport, Rhode Island, 1-4 May.

Loewy, R. G. (1984). Helicopter Vibrations: A Technological Prespective. *Journal of the American Helicopter Society*, **29** (4), 4-30.

Loewy, R. G. (1997).Recent developments in smart structures with aeronautical applications**,** *Smart Materials and Structures*, **6**, R11-R42.

Milgram, J., Chopra, I., and Straub, F. K. (1998). Rotors with trailing edge flap: analysis and comparison with experimental data. *Journal of the American Helicopter Society*,**43**, 319–332.

Mitrovic, M., Carman, G. P., and Straub, F. K. (1999)**.**Electro-Mechanical Characterization of Piezoelectric Stack Actuators. In Smart Structures and Materials 1999: Smart Structures and Integrated Systems, Proceedings of SPIE, Vol: 3668, Newport Beach, CA, USA, March.

Moheimani, S. O. R., and Fleming, A. J. (2006). *Piezoelectric Transducers for Vibration Control and Damping*. Springer, London.

Niezrecki, C., Brei, D., Balakrishnan, S. And Moskalik, A. (2001). Piezoelectric actuation: state of the art, *The Shock and Vibration Digest*, **33**(4), 269-280.

Ozdemir, O., **and Kaya, M. O.**(2006a). Flapwise bending vibration analysis of a rotating tapered cantilevered Bernoulli-Euler beam by Differential Transform Method, *Journal of Sound and Vibration*, **289** (1-2), 413-420.

Ozdemir O.,and Kaya, M. O.(2006b). Flexural vibration analysis of double tapered rotating Euler-Bernoulli Beam by using the Differential Transform Method, *Meccanica*, **41** (6), 661-670.

Ozdemir Ozgumus O., and Kaya, M. O. (2007a). Formulation for flutter and vibration analysis of a hingeless helicopter blade in hover: Part I, *Aircraft Engineering and Aerospace Technology: An International Journal*, **79** (2), 177–183.

Ozdemir Ozgumus O.,and Kaya M. O.(2007b). Results of flutter stability and vibration analysis of a hingeless helicopter blade in hover: Part II, *Aircraft Engineering and Aerospace Technology: An International Journal*, **79** (3), 231-237.

Ozdemir Ozgumus O. and Kaya M.O.(2007c).Energy expressions and free vibration analysis of a rotating double tapered Timoshenko beam featuring bending–torsion coupling, *International Journal of Engineering Science*, **45**(2-8), 562-586.

Ozdemir Ozgumus O., and Kaya, M. O.(2008). Flapwise bending vibration analysis of a rotating double tapered Timoshenko beam, *Archive of Applied Mechanics*, **78**, 379–392.

Ozdemir Ozgumus O. and Kaya M.O. (2010). Vibration analysis of a rotating tapered Timoshenko beam using DTM,*Meccanica*, **45**, 33–42

Ozdemir Ozgumus O. and Kaya M.O.(2012a).Energy expressions and free vibration analysis of a rotating Timoshenko beam featuring bending bending torsion coupling, *Archive of Applied Mechanics*, in publication process.

Ozdemir Ozgumus O. and Kaya M.O.(2012b).Energy derivation and extension-flapwise bending vibration analysis of a rotating piezolaminated composite

Timoshenko beam, *Mechanics of Advanced Materials and Structures*, in publication process.

Ozdemir Ozgumus O., Durmaz, S., and Kaya M.O. (2011).Flutter Analysis of Goland Wing, *International Forum On Aeroelasticity and Structural Dynamics (IFASD 2011)*, June 26-30, 2011, Paris, France.

Park, J. S. and Kim, J. H. (2008). Design and aeroelastic analysis of active twist rotor blades incorporating single crystal macro fiber composite actuators. *Composites: Part B,***39**, 1011–1025.

Pawar, P. M. and Jung, S. N. (2009).Active twist control methodology for vibration reduction of a helicopter with dissimilar rotor system, Smart Materials and Structures,**18**, 035013.

Preumont, A. (2006). *Mechatronics Dynamics of Electromechanical and Piezoelectric Systems,*Springer, The Netherlands.

Rao, J. S., and Carnegie, W. (1970). Solution of equations of motion of coupled-bending bending torsion vibrations of turbine blades by method of Ritz-Galerkin. *International Journal of Mechanical Sciences*, **12 (**10), 875-882.

Rodgers, J., and Hagood, N. (1997). Design, Manufacture, and Testing of An Integral Twist-Actuated Rotor Blade. 8th International Conference on Adaptive Structures and Technology, Wakayama, Japan, 29-31 October.

Sivaneri, N. T., and Chopra, I. (1982). Dynamic stability of a rotor blade using finite element analysis. *AIAA Journal*, **20** (5), 716-723.

S**pencer, B. T., and Chopra, I**. (1996). Design and Testing of a Helicopter Trailing Edge Flap with Piezoelectric Stack Actuators. In Smart Structures and Materials 1996: Smart Structures and Integrated Systems, Proceedings of SPIE, Vol: 2717, San Diego, CA, USA, February.

Straub, F. K., Ngo, H. T., Anand, V., and Domzalski, D. B. (2001). Development of a piezoelectric actuator for trailing edge flap control of full scale rotor blades. *Smart Materials and Structures*, **10**,25–34.

Tani J., T. T., Qiu J. (1998). Intelligent material systems: application of functional materials. *Applied Mechanics Review*,**51** (8), 505-521.

Thakkar, D., and Ganguli, R., (2005). Active twist control of smart helicopter rotor-A survey. *Aerospace Science and Technology,***57**, 429-448.

Theodorsen, T. (1934). General theory of aerodynamic instability and the mechanism of flutter. *NASA Technical Report*, **NASA RP-1050.**

Vinson, J. R. and Sierakowski, R. L., (2002). *The Behavior of StructuresComposed of Composite Materials*. Kluwer Academic Publishers, Secaucus, NJ, USA.

Viswamurthy, S. R., and Ganguli, R. (2006)**.** Effect of piezoelectric hysteresis on helicopter vibration control using trailing-edge flaps. *Journal of Guidance, Control, and Dynamics*, **29** (5), 1201-1209.

Viswamurthy, S. R., and Ganguli, R. (2007)**.** Optimal placement of trailing-edge flaps for helicopter vibration reduction using response surface methods. *Engineering Optimization*,**39**, 185–202.

Viswamurthy, S. R., and Ganguli, R. (2008). Optimal Placement of Piezoelectric Actuated Trailing-Edge Flaps for Helicopter Vibration Control, 49th AIAA/ASME/ASCE/AHS/ASC Structures, Structural Dynamics, and Materials Conference , Schaumburg, IL, 7 - 10 April.

Watkinson, J. (2004). *Art of The Helicopter.* Elsevier Butterworth-Heinemann, Oxford; Burlington, MA.

Wickramasinghe, V. K. and Hagood, N. W. (2004). Durability characterization of active fiber composite actuators for helicopter rotor blade applications. *Journal of Aircraft*, **41** (4), 931-937.

Wilbur, M. L., Mirick, P. H., Yeager, W. T., Langston, C. W., Cesnik, C. E. S., and Shin, S. (2002).Vibratory loads reduction testing of the NASA/Army/MIT active twist rotor. *Journal of The American Helicopter Society*, **47** (2), 123-133.

Yang, J. B., Jiang, L. J., and Chen, D. C. H. (2004). Dynamic modelling and control of a rotating Euler-Bernoulli beam. *Journal of Sound and Vibration,***274** (3-5), 863-875.

Yi, G., Liu, Y. J., and Leng, J. S. (2011). Active Vibration Control of Basic Structures Using Macro Fiber Composites.In Active and Passive Smart Structures and Integrated Systems, Proceedings of SPIE, Vol. **7977,** San Diego, California, USA, 7 March.

Yoo K.M. (1989).Unsteady vortex lattice aerodynamics for rotor aeroelasticity in hover and in forward flight, *PhD Thesis*, Georgia Institute of Technology, Atlanta.

Zhang, J. H., Smith, E. C., and Wang, K. W. (2004). Active-passive hybrid optimization of rotor blades with trailing edge flaps. *Journal of the American Helicopter Society*, **49** (1), 54-65.

Coppinger, R. (2006). Five-blade bearingless rotor flies. Date retrieved: 1.05.2012, adress:http://www.flightglobal.com/news/articles/five-blade-bearingless-rotor-flies-206508/

APPENDICES

APPENDIX A : Theodorsen Geometric Constants

$$T_1 = -\frac{2+c^2}{3}\sqrt{1-c^2} + \frac{c}{Cosc} \tag{A.1}$$

$$T_2 = c(1-c^2) - \frac{1+c^2}{Cosc}\sqrt{1-c^2} + \frac{c}{Cos^2 c} \tag{A.2}$$

$$T_3 = -(\frac{1}{8}+c^2)\frac{1}{Cos^2 c} + \frac{c(7+2c^2)}{4Cosc}\sqrt{1-c^2} - \frac{1}{8}(1-c^2)(5c^2+4) \tag{A.3}$$

$$T_4 = -\frac{1}{Cosc} + c\sqrt{1-c^2} \tag{A.4}$$

$$T_5 = -(1-c^2) - \frac{1}{Cos^2 c} + \frac{2c}{Cosc}\sqrt{1-c^2} \tag{A.5}$$

$$T_6 = T_2 \tag{A.6}$$

$$T_7 = -(\frac{1}{8}+c^2)\frac{1}{Cosc} + \frac{c(7+2c^2)}{8}\sqrt{1-c^2} \tag{A.7}$$

$$T_8 = -\frac{(1+2c^2)}{3}\sqrt{1-c^2} + \frac{c}{Cosc} \tag{A.8}$$

$$T_9 = \frac{1}{6}(\sqrt{1-c^2})^3 + \frac{a_h}{2}T_4 \tag{A.9}$$

$$T_{10} = \sqrt{1-c^2} + \frac{1}{Cosc} \tag{A.10}$$

$$T_{11} = \frac{1-2c}{Cosc} + \sqrt{1-c^2}(2-c) \tag{A.11}$$

$$T_{12} = \sqrt{1-c^2}(2+c) - \frac{2c+1}{Cosc} \tag{A.12}$$

$$T_{13} = -\frac{T_7}{2} - (c-a_h)\frac{T_1}{2} \tag{A.13}$$

$$T_{14} = \frac{1}{16} + \frac{1}{2}a_h c \tag{A.14}$$

APPENDIX B : Expressions of the Aerodynamic Matrices

$$\left[M_e^A\right] = b^2 L_b \pi \rho_\infty \begin{bmatrix} -\frac{13}{35} & -\frac{11L_b}{210} & \frac{7a_h b}{20} & -\frac{9}{70} & \frac{13L_b}{420} & \frac{3a_h b}{20} \\ -\frac{11L_b}{210} & -\frac{L_b^2}{105} & \frac{a_h b L_b}{20} & -\frac{13L_b}{420} & \frac{L_b^2}{140} & \frac{a_h b L_b}{30} \\ \frac{7a_h b}{20} & \frac{a_h b L_b}{20} & -\frac{1}{24}\left(1+8a_h^2\right)b^2 & \frac{3a_h b}{20} & -\frac{a_h b L_b}{30} & -\frac{1}{48}\left(1+8a_h^2\right)b^2 \\ -\frac{9}{70} & \frac{13L_b}{420} & \frac{3a_h b}{20} & -\frac{13}{35} & \frac{11L_b}{210} & \frac{7a_h b}{20} \\ \frac{13L_b}{420} & \frac{L_b^2}{140} & -\frac{a_h b L_b}{30} & \frac{11L_b}{210} & -\frac{L_b^2}{105} & -\frac{a_h b L_b}{20} \\ \frac{3a_h b}{20} & \frac{a_h b L_b}{30} & -\frac{1}{48}\left(1+8a_h^2\right)b^2 & \frac{7a_h b}{20} & -\frac{a_h b L_b}{20} & -\frac{1}{24}\left(1+8a_h^2\right)b^2 \end{bmatrix} \quad \textbf{(B.1)}$$

$$[K_e^A] = bC(k)\,\pi\rho_\infty \begin{bmatrix} 0 & 0 & \frac{7L_b}{10} & 0 & 0 & \frac{3L_b}{10} \\ 0 & 0 & \frac{L_b^2}{10} & 0 & 0 & \frac{L_b^2}{15} \\ 0 & 0 & -\frac{1}{3}(1+2a_h)bL_b & 0 & 0 & -\frac{1}{6}(1+2a_h)bL_b \\ 0 & 0 & \frac{3L_b}{10} & 0 & 0 & \frac{7L_b}{10} \\ 0 & 0 & -\frac{{L_b}^2}{15} & 0 & 0 & -\frac{L^2}{10} \\ 0 & 0 & -\frac{1}{6}(1+2a_h)bL_b & 0 & 0 & -\frac{1}{3}(1+2a_h)bL_b \end{bmatrix} \quad \textbf{(B.2)}$$

$$[C_e^A] = bL_b\pi\rho_\infty \begin{bmatrix} \frac{26C(k)}{35} & \frac{11L_bC(k)}{105} & \frac{7b(1+C(k)-2a_hC(k))}{20} & \frac{9C(k)}{35} & -\frac{13L_bC(k)}{210} & \frac{3b(1+C(k)-2a_hC(k))}{20} \\ \frac{11L_bC(k)}{105} & \frac{2L_b^2C(k)}{105} & \frac{bL(1+C(k)-2a_hC(k))}{20} & \frac{13L_bC(k)}{210} & -\frac{L_b^2C(k)}{70} & \frac{L_b(1+C(k)-2a_hC(k))}{30} \\ -\frac{7(1+2a_h)bC(k)}{20} & -\frac{(1+2a_h)bL_bC(k)}{20} & \frac{(-1+2a_h)b^2(-1+C(k)+2a_hC(k))}{6} & -\frac{3(1+2a_h)bC(k)}{20} & \frac{(1+2a_h)bL_bC(k)}{30} & \frac{(-1+2a_h)b^2(-1+C(k)]+2a_hC(k))}{12} \\ \frac{9C(k)}{35} & \frac{13L_bC(k)}{210} & \frac{3b(1+C(k)-2a_hC(k))}{20} & \frac{26C(k)}{35} & -\frac{11L_bC(k)}{105} & \frac{7b(1+C(k)-2a_hC(k))}{20} \\ -\frac{13L_bC(k)}{210} & -\frac{L_b^2C(k)}{70} & \frac{bL(-1+(-1+2a_h)C(k))}{30} & -\frac{11L_bC(k)}{105} & \frac{2L_b^2C(k)}{105} & \frac{bL_b(-1+(-1+2a_h)C(k))}{20} \\ -\frac{3(1+2a_h)bC(k)}{20} & -\frac{(1+2a_h)bL_bC(k)}{30} & \frac{(-1+2a_h)b^2(-1+C(k)+2a_hC(k))}{12} & -\frac{7(1+2a_h)bC(k)}{20} & \frac{(1+2a_h)bL_bC(k)}{20} & \frac{(-1+2a_h)b^2(-1+C(k)+2a_hC(k))}{6} \end{bmatrix} \quad \textbf{(B.3)}$$

APPENDIX C : Coefficients of The Aerodynamic Matrices In Hover

$$\mathrm{f}_1 = -\mathrm{A}_1(\mathrm{T}_4\Omega x\dot{\beta} + b\mathrm{T}_1\ddot{\beta}) - \mathrm{A}_2\mathrm{v}_\mathrm{i}(\frac{\mathrm{T}_{10}}{\pi}\Omega x\beta + \frac{\mathrm{T}_{11}}{2\pi}b\dot{\beta} - \mathrm{v}_\mathrm{i}) \quad \textbf{(C.1)}$$

$$\mathrm{f}_2 = -\mathrm{A}_2 b\mathrm{v}_\mathrm{i}(\frac{1}{2} - a_h)\Omega \quad \textbf{(C.2)}$$

$$\mathrm{f}_3 = \mathrm{A}_1(\mathrm{T}_4\Omega x\dot{\beta} + b\mathrm{T}_1\ddot{\beta}) - \mathrm{A}_2\Omega x\mathrm{v}_\mathrm{i} \quad \textbf{(C.3)}$$

$$\mathrm{f}_4 = -\mathrm{A}_1\mathrm{T}_4\dot{\beta} - \mathrm{A}_2\frac{\mathrm{T}_{10}}{\pi}\mathrm{v}_\mathrm{i}\beta \quad \textbf{(C.4)}$$

$$\mathrm{f}_5 = -\mathrm{A}_2(\frac{\mathrm{T}_{10}}{\pi}\Omega x\beta + \frac{\mathrm{T}_{11}}{2\pi}b\dot{\beta} - 2\mathrm{v}_\mathrm{i}) \quad \textbf{(C.5)}$$

$$\mathrm{f}_6 = \mathrm{A}_1\Omega x\pi - \mathrm{A}_2(\frac{1}{2} - a_h)b\mathrm{v}_\mathrm{i} \quad \textbf{(C.6)}$$

$$\mathrm{f}_7 = -\mathrm{A}_1\pi \quad \textbf{(C.7)}$$

$$\mathrm{f}_8 = -\mathrm{A}_1 a_h b\pi \quad \textbf{(C.8)}$$

$$g_1 = -A_1(T_4 \Omega x \dot{\beta} + b T_1 \ddot{\beta}) + A_2 \Omega x (\frac{T_{10}}{\pi} \Omega x \beta + \frac{T_{11}}{2\pi} b \dot{\beta} - 2\nu_i) \quad \textbf{(C.9)}$$

$$g_2 = A_2 b x (\frac{1}{2} - a_h) \Omega^2 \quad \textbf{(C.10)}$$

$$g_3 = -A_1(T_4 \Omega x \dot{\beta} + b T_1 \ddot{\beta}) + A_2 (\Omega x)^2 - A_2 \nu_i (\frac{T_{10}}{\pi} \Omega x \beta + \frac{T_{11}}{2\pi} b \dot{\beta} - \nu_i) \quad \textbf{(C.11)}$$

$$g_4 = -A_1 T_4 \dot{\beta} + A_2 (2 \frac{T_{10}}{\pi} \Omega x \beta + \frac{T_{11}}{2\pi} b \dot{\beta} - \nu_i) \quad \textbf{(C.12)}$$

$$g_5 = -A_2 \Omega x \quad \textbf{(C.13)}$$

$$g_6 = A_1 \Omega x \pi + A_2 (\frac{1}{2} - a_h) b \Omega x \quad \textbf{(C.14)}$$

$$g_7 = -A_1 \pi \quad \textbf{(C.15)}$$

$$g_8 = -A_1 a_h b \pi \quad \textbf{(C.16)}$$

$$h_1 = B_1\Big\{(T_{10}+T_4)\Omega^2 x^2\beta + a_h b(bT_1\ddot{\beta} + T_4\Omega x\dot{\beta}) - b^2(cT_1+T_7)\ddot{\beta} + b\left[T_1 + \frac{T_{11}}{2} - (cT_4+T_8)\right]\Omega x\Big\} + B_2\Omega x\left(\frac{T_{10}}{\pi}\Omega x\beta + b\frac{T_{11}}{2\pi}\dot{\beta} - v_i\right) \quad \textbf{(C.17)}$$

$$h_2 = B_1\frac{b}{2}\pi\Omega^2 x + B_2\left(\frac{1}{2} - a_h\right)b\Omega^2 x \quad \textbf{(C.18)}$$

$$h_3 = B_2(\Omega x)^2 \quad \textbf{(C.19)}$$

$$h_4 = B_1\left[2\Omega x(T_{10}+T_4)\beta + b\left(T_1 + \frac{T_{11}}{2} + (a_h - c)T_4 - T_8\right)\dot{\beta}\right] + B_2\left(2\frac{T_{10}}{\pi}\Omega x\beta + b\frac{T_{11}}{2\pi}\dot{\beta} - v_i\right) \quad \textbf{(C.20)}$$

$$h_5 = -B_2\Omega x \quad \textbf{(C.21)}$$

$$h_6 = (B_2 + B_1\pi)\left(\frac{1}{2} - a_h\right)b\Omega x \quad \textbf{(C.22)}$$

$$h_7 = B_1\pi b^2\left(\frac{1}{8} + a_h^2\right) \quad \textbf{(C.23)}$$

$$h_8 = B_1 a_h b\pi \quad \textbf{(C.24)}$$

APPENDIX D : Coefficients of The Aerodynamic Matrices In Forward Flight

$$m_1 = AA\left\{\beta_0\Omega\left[-\frac{bT_{11}\dot{\beta}}{2\pi} - 2\nu_i - \left(\frac{1}{2}-a_h\right)b\dot{\Phi} + \beta_0^2\Omega^2\left(2L_b\mu Cos\psi - \left(\frac{1}{2}-a_h\right)b\right)\right] - \beta_0\Omega^2\left(x + L_b\mu Sin\psi\right)\left(\frac{T_{10}\beta}{\pi}+\Phi\right)\right\} + C_d\Phi\Omega^2 b\rho_\infty\beta_0\left(x+L_b\mu Sin\psi\right) \tag{D.1}$$

$$\begin{aligned} m_2 = {} & AA\left(x\Omega\nu_i - L_b x\beta_0\mu\Omega^2 Cos\psi + L_b\mu\nu_i\Omega Sin\psi - L_b^2\beta_0\mu^2\Omega^2 Cos\psi Sin\psi\right) + \\ & BB\left\{\frac{bT_1\ddot{\beta}}{\pi} - \nu_i + \frac{T_4 x\dot{\beta}\Omega}{\pi} - x\Omega\dot{\Phi} + a_h b\ddot{\Phi} - \mu\Omega L_b\left[2\Phi\dot{\psi}Cos\psi + \left(\frac{T_4\dot{\beta}}{\pi} - \dot{\Phi} - \beta_0\dot{\psi}\right)Sin\psi\right]\right\} + \\ & C_d\rho_\infty\left[-\Omega b\left(x\nu_i + 2x^2\Phi\Omega + L_b\mu\nu_i Sin\psi\right) + \mu\Omega^2 L_b bx\left(\beta_0 Cos\psi - 4\Phi Sin\psi\right) + \right. \\ & \left. \mu^2\Omega^2 L_b^2 b\left(\beta_0 Cos\psi - 2\Phi Sin\psi\right)Sin\psi\right] \end{aligned} \tag{D.2}$$

$$\begin{aligned} m_3 = {} & AA\left[L_b\mu\Omega\nu_i\left(\frac{T_{10}\beta}{\pi}+\Phi\right)Cos\psi + L_b^2\mu^2\Omega^2\beta_0\left(\frac{L_b^2 T_{10}\beta}{\pi} - \Phi\right)Cos^2\psi\right] + \\ & BB\mu\Omega L_b\Phi\left[\left(\frac{T_4\dot{\beta}}{\pi} - \dot{\Phi}\right)Cos\psi + \Phi\dot{\psi}Sin\psi\right] + C_d\left[-L_b\mu\Omega b\rho_\infty\left(\nu_i\Phi + 2x\Omega + 2x\Phi^2\Omega\right)Cos\psi + \right. \\ & \left. L_b^2\mu^2\Omega^2 b\rho_\infty Cos\psi\left(\beta_0\Phi Cos\psi - 2Sin\psi - 2\Phi^2 Sin\psi\right)\right] \end{aligned} \tag{D.3}$$

$$m_4 = AA\left[b\nu_i\Omega\left(\frac{1}{2}-a_h\right) + L_b\mu\Omega\left(-\frac{bT_{11}\dot{\beta}}{2\pi} - 2\nu_i - b\beta_0\Omega + 2a_h b\beta_0\Omega - \frac{T_{10}x\beta\Omega}{\pi} - x\Phi\Omega - \left(\frac{1}{2}-a_h\right)b\dot{\Phi}\right)Cos\psi + \right.$$
$$\left. L_b^2\mu^2\Omega^2 Cos\psi\left(2\beta_0 Cos\psi - \frac{T_{10}\beta Sin\psi}{\pi} - \Phi Sin\psi\right)\right] - BB\left(L_b\mu\Phi\Omega\dot{\psi}Sin\psi\right) + C_d bL_b\mu\Omega^2\Phi\rho_\infty\left(x + L_b\mu\Omega Sin\psi\right)Cos\psi \qquad \textbf{(D.4)}$$

$$n_1 = AA\left[\beta_0\left(-\frac{bT_{11}\dot{\beta}\Phi}{2\pi} - 2\nu_i\Phi - x\Omega - \frac{T_{10}x\beta\Phi\Omega}{\pi} - 2x\Phi^2\Omega - \left(\frac{1}{2}-a_h\right)b\Phi\dot{\Phi}\right) + \beta_0 L_b\mu\Omega^2 Sin\psi\left(\frac{T_{10}\beta\Phi}{\pi} - 2\Phi^2 - 1\right) + \right.$$
$$\left. \beta_0^2\Phi\Omega^2\left(\left(\frac{1}{2}+a_h\right)b + 2L_b\mu Cos\psi\right)\right] - C_d\beta_0\rho_\infty b\Omega^2\left(x + L_b\mu Sin\psi\right) \qquad \textbf{(D.5)}$$

$$n_2 = AA\left(\frac{bT_{11}\dot{\beta}\nu_i}{2\pi} + \nu_i^{\,2} + b\nu_i\left(\frac{1}{2}-a_h\right)\left(\dot{\Phi} + \beta_0\Omega\right)b\beta_0\nu_i\Omega + \frac{T_{10}x\beta\nu_i\Omega}{\pi} + \frac{bT_{11}x\dot{\beta}\Phi\Omega}{\pi} + 4x\nu_i\Phi\Omega + x^2\Omega^2 + bx\beta_0\Phi\Omega^2 - \right.$$
$$2a_h bx\beta_0\Phi\Omega^2 + \frac{2T_{10}x^2\beta\Phi\Omega^2}{\pi} + 3x^2\Phi^2\Omega^2 - L_b\beta_0\mu\Omega Cos\psi\left(\frac{bT_{11}\dot{\beta}}{2\pi} + 2\nu_i\right) - bL_b\beta_0\mu\Omega Cos\psi\left(\frac{1}{2}+a_h\right)\left(\beta_0\Omega + \dot{\Phi}\right) -$$
$$L_b\beta_0\mu\Omega^2 Cos\psi\left(\frac{T_{10}\beta}{\pi} + 4\Phi\right)\left(x + L_b\mu Sin\psi\right) + L_b^2\beta_0^2\mu^2\Omega^2 Cos^2\psi + b\Phi\Omega\dot{\Phi}\left(1-2a_h\right)\left(x + L_b\mu Sin\psi\right)bx + \qquad \textbf{(D.6)}$$
$$\left(\frac{T_{10}\beta\nu_i}{\pi} + \frac{bT_{11}\dot{\beta}\Phi}{\pi} + 4\nu_i\Phi\right)L_b\mu\Omega Sin\psi + \left(2x + b\beta_0\Phi - 2a_h b\beta_0\Phi + \frac{4T_{10}x\beta\Phi}{\pi} + 6x\Phi^2\right)L_b\Omega^2\mu Sin\psi +$$
$$\left.\left(1 + \frac{2T_{10}\beta\Phi}{\pi} + 3\Phi^2\right)L_b^2\mu^2\Omega^2 Sin^2\psi\right) + BB\left(L_b\mu\Omega\dot{\psi}Cos\psi\right)$$

$$n_3 = AA\left[\left(\frac{bT_{11}\dot{\beta}}{2\pi} + \frac{bT_{11}\dot{\beta}\Phi^2}{2\pi} + \nu_i + \frac{T_{10}\beta\nu_i\Phi}{\pi} + 2\nu_i\Phi^2\right)L_b\mu\Omega Cos\psi - \left(1 + \frac{T_{10}\beta\Phi}{\pi} + 2\Phi^2\right)L_b^2\beta_0\mu^2\Omega^2 Cos^2\psi + \right.$$
$$\left. 2L_b\mu\Omega^2 Cos\psi\left(1+\Phi^2\right)\left(\frac{T_{10}\beta}{\pi} + \Phi\right)\left(x + L_b\mu Sin\psi\right) + bL_b\mu\Omega Cos\psi\left(1+\Phi^2\right)\left(\frac{1}{2} - a_h\right)\left(\dot{\Phi} + \beta_0\Omega\right)\right] + \quad \textbf{(D.7)}$$
$$BBL_b\mu\Omega\left(-\frac{T_4\dot{\beta}Cos\psi}{\pi} + \dot{\Phi}Cos\psi - \Phi\dot{\psi}Sin\psi\right) + C_d\rho_\infty b\mu\Omega L_b\left(\nu_i - L_b\beta_0\mu\Omega Cos\psi\right)Cos\psi$$

$$n_4 = AA\left[\left(\frac{1}{2} - a_h\right)\left(\nu_i\Phi + x\Omega + x\Phi^2\Omega\right)b\Omega - \left(\frac{bT_{11}\dot{\beta}}{2\pi} + 2\nu_i\right)L_b\mu\Phi\Omega Cos\psi - L_b\mu\Omega^2 Cos\psi\left(x + b\beta_0\Phi - 2ab\beta_0\Phi + \right.\right.$$
$$\left.\frac{T_{10}x\beta\Phi}{\pi} + 2x\Phi^2\right) + 2L_b^2\beta_0\mu^2\Phi\Omega^2 Cos^2\psi - \left(\frac{1}{2} - a_h\right)bL_b\mu\Phi\Omega\dot{\Phi}Cos\psi + \left(\frac{1}{2} - a_h\right)bL_b\mu\Omega^2 Sin\psi + \quad \textbf{(D.8)}$$
$$\left.\left(\frac{1}{2} - a_h\right)bL_b\mu\Phi^2\Omega^2 Sin\psi - \left(1+2\Phi^2\right)L_b^2\mu^2\Omega^2 Cos\psi Sin\psi - \frac{L_b{}^2T_{10}\beta\mu^2\Phi\Omega^2 Cos^2\psi Sin\psi}{\pi}\right) + BB\left(L_b\mu\Omega\dot{\psi}Sin\psi\right) -$$
$$C_d\mu\Omega^2 bL_b\rho_\infty Cos\psi\left(x\Omega + bL_b\mu Sin\psi\right)$$

$$p_1 = -AA\beta_0\Omega^2 b\left(\frac{1}{2} + a_h\right)\left(x + L_b\mu Sin\psi\right) \quad \textbf{(D.9)}$$

$$p_2 = AA\left[\Omega^2 b\left(\frac{1}{2} + a_h\right)\left(x^2 + L_b{}^2\mu^2 Sin^2\psi\right) + \left(1 + 2a_h\right)bL_b x\mu Sin\psi\right] + BB\left(a_h bL_b\mu\Omega\dot{\psi}Cos\psi\right) \quad \textbf{(D.10)}$$

$$p_3 = AA\Bigg[\left(\frac{1}{2}+a_h\right)\frac{b^2 L_b T_{11}\dot{\beta}\mu\Omega Cos\psi}{2\pi}+\left(\frac{1}{2}+a_h\right)bL_b\mu\nu_i\Omega Cos\psi+\left(\frac{1}{4}-a_h{}^2\right)b^2 L_b\beta_0\mu\Omega^2 Cos\psi +$$
$$\left(1+2a_h\right)\left(\frac{T_{10}\beta}{\pi}+2\Phi\right)bL_b x\mu\Omega^2 Cos\psi-\left(1+2a_h\right)\left(\beta_0 Cos\psi+\Phi Sin\psi\right)bL_b^2\mu^2\Omega^2 Cos\psi\Bigg]+$$
$$BB\Bigg[-\left(T_1+\frac{T_{11}}{2}\right)\frac{bL_b\dot{\beta}\mu\Omega Cos\psi}{\pi}-\left(\left(c+a_h\right)T_4-T_8\right)\frac{bL_b\dot{\beta}\mu\Omega Cos\psi}{\pi}-\left(\frac{1}{2}b\beta_0+\frac{2T_{10}x\beta}{\pi}+\right.$$
$$\left.\frac{2T_4 x\beta}{\pi}\right)L_b\mu\Omega^2 Cos\psi-\left(\frac{1}{2}-a_h\right)bL_b\mu\Omega\dot{\Phi}Cos\psi-\left(T_{10}+T_4\right)\frac{2L_b^2 T_{10}\beta\mu^2\Omega^2 Cos\psi Sin\psi}{\pi}-a_h bL_b\mu\Phi\Omega\dot{\psi}Sin\psi\Bigg] \quad \textbf{(D.11)}$$

$$p_4 = AA\left[b^2\Omega^2\left(\frac{1}{4}-a_h{}^2\right)\left(x+L_b\mu Sin\psi\right)-b\Omega^2 Cos\psi\left(\frac{1}{2}+a_h\right)\left(L_b x\mu+bL_b^2\mu^2 Sin\psi\right)\right]+$$
$$BB\left(-\frac{1}{2}bx\Omega^2-\frac{1}{2}bL_b\mu\Omega^2 Sin\psi+a_h bL_b\mu\Omega\dot{\psi}Sin\psi\right) \quad \textbf{(D.12)}$$

$$\overline{m}_1 = AA\left(\frac{T_{10}\beta\nu_i}{\pi}+\nu_i\Phi-\frac{L_b T_{10}\beta\beta_0\mu\Omega Cos\psi}{\pi}-L_b\beta_0\mu\Phi\Omega Cos\psi\right)+BB\left(\frac{T_4\dot{\beta}\Phi}{\pi}+\beta_0\Phi\Omega-\Phi\dot{\Phi}\right)+$$
$$C_d\rho_\infty\left(-b\nu\Phi-2bx\Omega-2bx\Phi^2\Omega+bL_b\beta_0\mu\Phi\Omega Cos\psi-2bL_b\mu\Omega Sin\psi-2bL_b\mu\Phi^2\Omega Sin\psi\right) \quad \textbf{(D.13)}$$

$$\overline{m}_2 = AAb\left(\frac{1}{2}-a_h\right)\left(\nu_i-L_b\beta_0\mu\Omega Cos\psi\right)-BB\Phi\Omega\left(x+L_b\mu Sin\psi\right) \quad \textbf{(D.14)}$$

$$\bar{m}_3 = AA\left[-\frac{bT_{11}\dot{\beta}}{2\pi} - 2\nu_i - b\left(\frac{1}{2}+a_h\right)\left(\beta_0\Omega+\dot{\Phi}\right) - \frac{T_{10}x\beta\Omega}{\pi} - x\Phi\Omega + 2L_b\beta_0\mu\Omega Cos\psi - L_b\mu\Omega Sin\psi\left(\frac{T_{10}\beta}{\pi}+\Phi\right)\right] + C_d b\rho_\infty\Phi\Omega\left(x+L_b\mu Sin\psi\right) \tag{D.15}$$

$$\bar{m}_4 = BB\Phi\Omega\left(a_h b + L_b\mu Cos\psi\right) \tag{D.16}$$

$$\bar{n}_1 = AA\left[\left(1+\Phi^2\right)\left(\frac{bT_{11}\dot{\beta}}{2\pi} + \frac{2T_{10}x\beta\Omega}{\pi} + 2x\Phi\Omega\right) + \left(\frac{1}{2}-a_h\right)\left(1+\Phi^2\right)b\left(\beta_0\Omega+\dot{\Phi}\right) + \left(1+2\Phi^2\right)\left(\nu_i - L_b\beta_0\mu\Omega Cos\psi\right) - \frac{L_bT_{10}\beta\beta_0\mu\Phi\Omega Cos\psi}{\pi} + \frac{T_{10}\beta\nu_i\Phi}{\pi} + 2L_b\mu\Omega Sin\psi\left(1+\Phi^2\right)\left(\frac{T_{10}\beta}{\pi}+\Phi\right)\right] - BB\left(\frac{T_4\dot{\beta}}{\pi} + \beta_0\Omega - \dot{\Phi}\right) + C_d\rho_\infty b\left(\nu_i - L_b\beta_0\mu\Omega Cos\psi\right) \tag{D.17}$$

$$\bar{n}_2 = AA\left(-\frac{bT_{11}\dot{\beta}\Phi}{2\pi} - 2\nu_i\Phi - \left(1+2\Phi^2\right)\left(x\Omega + L_b\mu\Omega Sin\psi\right) - b\Phi\left(\frac{1}{2}-a_h\right)\left(\beta_0\Omega+\dot{\Phi}\right) - \frac{T_{10}x\beta\Phi\Omega}{\pi} + 2L_b\beta_0\mu\Phi\Omega Cos\psi - \frac{L_bT_{10}\beta\mu\Phi\Omega Sin\psi}{\pi}\right] - C_d\rho_\infty b\Omega\left(x+L_b\mu Sin\psi\right) \tag{D.18}$$

$$\bar{n}_3 = AAb\left(\frac{1}{2}-a_h\right)\left(\nu_i\Phi + x\Omega + x\Phi^2\Omega - L_b\beta_0\mu\Phi\Omega Cos\psi + L_b\mu\Omega Sin\psi + L_b\mu\Phi^2\Omega Sin\psi\right) + BB\Omega\left(x+L_b\mu Sin\psi\right) \tag{D.19}$$

$$\bar{n}_4 = -BBb\Omega\left(a_h + L_b\mu Cos\psi\right) \tag{D.20}$$

$$\bar{n}_5 = -BB\left(L_b\mu\Omega\Phi Cos\psi\right) \quad \textbf{(D.21)}$$

$$\bar{p}_1 = AA\left\{\left(1+2a_h\right)b\left[\frac{bT_{11}\dot{\beta}}{4\pi}+\left(x\Omega+L_b\mu Sin\psi\right)\left(\frac{T_{10}\beta}{\pi}+\Phi\right)+L_b\beta_0\mu\Omega Cos\psi+\left(\frac{1}{2}+a_h\right)b\nu_i\right]+\right.$$
$$\left.\left(\frac{1}{4}-a_h^2\right)b^2\left(\beta_0\Omega+\dot{\Phi}\right)\right\}+BB\left\{\frac{b\dot{\beta}}{\pi}\left[-T_1-\frac{T_{11}}{2}+\left(c-a_h\right)T_4+\frac{bT_8}{\pi}\right]-\left(\frac{1}{2}+a_h\right)\Omega b\beta_0-\left(\frac{1}{2}-a_h\right)b\dot{\Phi}-\right. \quad \textbf{(D.22)}$$
$$\left.\frac{2}{\pi}\left(T_{10}+T_4\right)\Omega\beta\left(x+L_b\mu Sin\psi\right)\right\}$$

$$\bar{p}_2 = AA\left(\frac{1}{2}+a_h\right)b\Omega\left(x+L_b\mu Sin\psi\right) \quad \textbf{(D.23)}$$

$$\bar{p}_3 = AA\left(\frac{1}{4}-a_h^2\right)b^2\Omega\left(x+L_b\mu Sin\psi\right)-BB\left(\frac{1}{2}-a_h\right)b\Omega\left(x+L_b\mu Sin\psi\right) \quad \textbf{(D.24)}$$

$$\bar{p}_4 = BB\left(a_hbL_b\mu\Omega\Phi Cos\psi\right) \quad \textbf{(D.25)}$$

$$\bar{p}_5 = -BB\Omega\left[\left(\frac{1}{8}+a_h^2\right)b^2+a_hbL_b\mu Cos\psi\right] \quad \textbf{(D.26)}$$

$$\bar{\bar{m}}_1 = -BB\Phi^2 \quad \textbf{(D.27)}$$

$$\bar{\bar{m}}_2 = BB\Phi \tag{D.28}$$

$$\bar{\bar{m}}_3 = abBB\Phi \tag{D.29}$$

$$\bar{\bar{n}}_1 = \bar{\bar{m}}_2 \tag{D.30}$$

$$\bar{\bar{n}}_2 = -BB \tag{D.31}$$

$$\bar{\bar{n}}_3 = -a_h bBB \tag{D.32}$$

$$\bar{\bar{p}}_1 = a_h bBB\Phi \tag{D.33}$$

$$\bar{\bar{p}}_2 = \bar{\bar{n}}_3 \tag{D.34}$$

$$\bar{\bar{p}}_3 = -\mathrm{BB}b^2\left(\frac{1}{8} + a_h^2\right) \tag{D.35}$$

$$
\begin{aligned}
k_1 = AA\Bigg(&\frac{bT_{11}\dot{\beta}\nu_i}{2\pi} + \nu_i^{\ 2} + b\left(\frac{1}{2} - a_h\right)\left(\beta_0\nu_i\Omega - L_b\beta_0^2\mu\Omega^2 Cos\psi + \nu_i\dot{\Phi} - L_b\beta_0\mu\Omega\dot{\Phi}Cos\psi\right) + \frac{T_{10}x\beta\nu_i\Omega}{\pi} + x\nu_i\Phi\Omega - \\
&\frac{bL_bT_{11}\dot{\beta}\beta_0\mu\Omega Cos\psi}{2\pi} - 2L_b\beta_0\mu\nu_i\Omega Cos\psi - \frac{L_bT_{10}x\beta\beta_0\mu\Omega^2 Cos\psi}{\pi} - L_bx\beta_0\mu\Phi\Omega^2 Cos\psi + L_b^2\beta_0^2\mu^2\Omega^2 Cos^2\psi + \\
&\frac{L_bT_{10}\beta\mu\nu_i\Omega Sin\psi}{\pi} + L_b\mu\nu_i\Phi\Omega Sin\psi - \frac{L_b^2T_{10}\beta\beta_0\mu^2\Omega^2 Cos\psi\, Sin\psi}{\pi} - L_b^2\beta_0\mu^2\Phi\Omega^2 Cos\psi\, Sin\psi\Bigg) + \\
&BB\Bigg(\frac{bT_1\dot{\beta}\Phi}{\pi} - \nu_i\Phi + \frac{T_4x\dot{\beta}\Phi\Omega}{\pi} - x\Phi\Omega\dot{\Phi} + a_h\nu_i b\Phi\ddot{\Phi} - L_b\mu\Phi^2\Omega\dot{\psi}Cos\psi + \frac{L_bT_4\dot{\beta}\mu\Phi\Omega Sin\psi}{\pi} - \\
&L_b\mu\Phi\Omega\dot{\Phi}Sin\psi - L_b\beta_0\mu\Phi\Omega\dot{\psi}Sin\psi\Bigg) + C_d\rho_\infty\Big(-bx\nu_i\Phi\Omega - bx^2\Omega^2 - bx^2\Phi^2\Omega^2 + bL_bx\beta_0\mu\Phi\Omega^2 Cos\psi - \\
&bL_b\mu\nu_i\Phi\Omega Sin\psi - 2bL_bx\mu\Omega^2 Sin\psi + bL_b^2\beta_0\mu^2\Phi\Omega^2 Cos\psi\, Sin\psi - bL_b^2\mu^2\Phi^2\Omega^2 Sin^2\psi\Big)
\end{aligned}
\tag{D.36}
$$

$$
\begin{aligned}
k_2 = AA\Bigg(&\left(\frac{bT_{11}\dot{\beta}}{2\pi}+\nu_i\right)\left(\nu_i\Phi+x\Omega\right)+\left(\frac{1}{2}-a_h\right)b\beta_0\nu_i\Phi\Omega+\frac{T_{10}x\beta\nu_i\Phi\Omega}{\pi}+\left(\frac{bT_{11}\dot{\beta}}{2\pi}+2\nu_i\right)x\Phi^2\Omega+\\
&\left(\frac{1}{2}-a\right)\left(1+\Phi^2\right)bx\beta_0\Omega^2+\left(1+\Phi^2\right)\left(\frac{T_{10}x^2\beta\Omega^2}{\pi}+x^2\Phi\Omega^2\right)-\left(\frac{bT_{11}\dot{\beta}}{2\pi}+2\nu_i+x\Omega\right)L_b\beta_0\mu\Phi\Omega Cos\psi-\\
&\left(\frac{1}{2}-a_h\right)bL_b\beta_0^2\mu\Phi\Omega^2Cos\psi-\frac{L_bT_{10}x\beta\beta_0\mu\Phi\Omega^2Cos\psi}{\pi}-2L_bx\beta_0\mu\Phi^2\Omega^2Cos\psi+L_b^2\beta_0^2\mu^2\Phi\Omega^2Cos^2\psi+\\
&\left(\frac{1}{2}-a_h\right)\left(\nu_i\Phi+x\Omega+x\Phi^2\Omega\right)b\dot{\Phi}-\left(\frac{1}{2}-a_h\right)bL_b\beta_0\mu\Phi\Omega\dot{\Phi}Cos\psi+\left(\frac{bT_{11}\dot{\beta}}{2\pi}+\nu_i+\frac{T_{10}\beta\nu_i\Phi}{\pi}\right)L_b\mu\Omega Sin\psi+\\
&\frac{bL_bT_{11}\dot{\beta}\mu\Phi^2\Omega Sin\psi}{2\pi}+2L_b\mu\nu_i\Phi^2\Omega Sin\psi+\left(\frac{1}{2}-a_h\right)bL_b\beta_0\mu\Omega^2Sin\psi+\frac{2L_bT_{10}x\beta\mu\Omega^2Sin\psi}{\pi}+2L_bx\mu\Phi\Omega^2Sin\psi+\\
&\left(\frac{1}{2}-a_h\right)bL_b\beta_0\mu\Phi^2\Omega^2Sin\psi+\frac{2L_bT_{10}x\beta\mu\Phi^2\Omega^2Sin\psi}{\pi}+2L_bx\mu\Phi^3\Omega^2Sin\psi-\left(1+\frac{T_{10}\beta\Phi}{\pi}+2\Phi^2\right)L_b^2\beta_0\mu^2\Omega^2Cos\psi Sin\psi+\\
&\left(\frac{1}{2}-a_h\right)\left(1+\Phi^2\right)bL_b\mu\Omega\dot{\Phi}Sin\psi+\left(1+\Phi^2\right)\left(\frac{T_{10}\beta}{\pi}+\Phi\right)L_b^2\mu^2\Omega^2Sin^2\psi\Bigg)+\\
&BB\left(-\frac{bT_1\ddot{\beta}}{\pi}+\nu_i-\frac{T_4x\dot{\beta}}{\pi}+x\Omega\dot{\Phi}-ab\ddot{\Phi}+L_b\mu\Phi\Omega\dot{\psi}Cos\psi-\left(\frac{T_4\dot{\beta}}{\pi}+\dot{\Phi}+\beta_0\dot{\psi}\right)L_b\mu\Omega Sin\psi\right)+\\
&C_d\rho_\infty b\Omega\left(x+L_b\mu Sin\psi\right)\left(\nu_i-L_b\beta_0\mu\Omega Cos\psi\right)
\end{aligned}
\qquad \textbf{(D.37)}
$$

$$
\begin{aligned}
k_3 = AA\Bigg[&\left(\frac{1}{2}+a_h\right)\left(\frac{a_h b^2 T_{11} x\dot{\beta}\Omega}{2\pi}+bx\nu_i\Omega+\frac{bT_{10}x^2\beta\Omega^2}{2\pi}+bx^2\Phi\Omega^2-bL_b x\beta_0\mu\Omega^2 Cos\psi+\frac{b^2 L_b T_{11}\dot{\beta}\mu\Omega Sin\psi}{4\pi}+\right.\\
&\left. bL_b\mu\nu_i\Omega Sin\psi-bL_b^2\beta_0\mu^2\Omega^2 Cos\psi\, Sin\psi+bL_b^2\mu^2\Phi\Omega^2 Sin^2\psi\right)+\left(\frac{1}{4}-a_h{}^2\right)\left(b^2 x\beta_0\Omega^2+b^2 x\Omega\dot{\Phi}+\right.\\
&\left. b^2 L_b\beta_0\mu\Omega^2 Sin\psi+b^2 L_b\mu\Omega\dot{\Phi} Sin\psi\right)+\left(1+2a_h\right)bL_b\Omega^2 Sin\psi\left(\frac{T_{10}x\beta\mu}{\pi}+\frac{L_b T_{10}\beta\mu^2 Sin\psi}{2\pi}+x\mu\Phi\right)\Bigg]+\\
BB\Bigg\{&\frac{\ddot{\beta}b^2}{\pi}\left[\left(c-a_h\right)T_1+T_7\right]+\frac{\dot{\beta}bx\Omega}{\pi}\left[T_1-\frac{T_{11}}{2}+\left(c-a_h\right)T_4+T_8\right]+a_h b\nu_i-\frac{1}{2}bx\beta_0\Omega^2-\left(\frac{1}{8}+a_h{}^2\right)\frac{b^2\ddot{\Phi}}{8}-\\
&\left(T_{10}+T_4\right)\left(\frac{x^2\beta\Omega^2}{\pi}+\frac{2L_b x\beta\mu\Omega^2 Sin\psi}{\pi}+\frac{L_b^2\beta\mu^2\Omega^2 Sin^2\psi}{\pi}\right)-\left(\frac{1}{2}-a_h\right)b\Omega\dot{\Phi}\left(L_b\mu Sin\psi+x\right)+\\
&a_h bL_b\mu\Phi\Omega\,\dot{\psi} Cos\psi+\frac{bL_b\dot{\beta}\mu\Omega Sin\psi}{\pi}\left[-T_1-T_{11}+\left(c-a_h\right)T_4+T_8\right]-bL_b\beta_0\mu\Omega Sin\psi\left(\frac{1}{2}\Omega-a_h\dot{\psi}\right)\Bigg\}
\end{aligned}
\qquad \textbf{(D.38)}
$$

CURRICULUM VITAE

Name Surname: Özge ÖZDEMİR ÖZGÜMÜŞ

Place and Date of Birth: İstanbul, 12 November 1981

Address: İstanbul Technical University, Faculty of Aeronautics and Astronautics, 34469, Maslak, İstanbul

E-Mail: ozdemirozg@itu.edu.tr

B.Sc.: Aeronautical Engineering

M.Sc.: Aeronautical and Aerospace Engineering Programme

Professional Experience and Rewards:

2004-2005: Structure Team Research Engineering, Istanbul Technical University, Faculty of Aeronautics and Astronautics, Rotorcraft Center of Excellence

List of Publications and Patents:

Ozdemir, O., and Kaya, M. O**.**, 2004a:Askıda Kalma Durumundaki Bir Helikopter Palinin Aeroelastik İncelemesi, *Havacılıkta İleri Teknolojiler ve Uygulamaları Sempozyumu*, Air Force Academy, December9-10, 2004, Istanbul, Turkey.

Ozdemir, O, and Kaya, M. O**.**, 2004b:Dönen Bir Kirişin Flaplama-Eğilme Titreşiminin Diferansiyel Dönüşüm Yöntemi ile İncelenmesi, *Havacılıkta İleri Teknolojiler ve Uygulamaları Sempozyumu*, Air Force Academy, December 9-10, 2004, Istanbul, Turkey.

Ozdemir, O., and Kaya, M. O**.**, 2004c:Düzgün Daralan Bir Euler Kirişinin Eğilme Titreşiminin Diferansiyel Dönüşüm Yöntemi ile İncelenmesi, *V. Havacılık Sempozyumu*, Erciyes University, May 13-14, 2004, Kayseri, Turkey.

Ozdemir, O., and Kaya, M. O**.**, 2005a:Vibration Analysis of Double Tapered Rotating Euler-Bernoulli Beam by Using Differential Transform Method, *The 2nd International Basic Research Conference on Rotorcraft Technology*, Nanjing University of Aeronautics and Astronautics, November 7-9, 2005, Nanjing, China.

Ozdemir, O., and Kaya, M. O**.**, 2005b:Free Vibration Analysis of A Rotating Tapered Timoshenko Beam with Bending Torsion Coupling, *The 2nd International Basic Research Conference on Rotorcraft Technology*, Nanjing University of Aeronautics and Astronautics, November 7-9, 2005, Nanjing, China.

Ozdemir, O., and Kaya, M. O., 2005c: Free Vibration Analysis of A Rotating Tapered Timoshenko Beam, *3rd Ankara International Aerospace Conference*, Middle East University, August 22-25, Ankara, Turkey.

Ozdemir, O., and Kaya, M. O., 2005d:İleri Uçuşta Bir Helikopter Palinin Kanat Çırpma-Gecikme Dinamiğinin İncelenmesi, *XIV. Ulusal Mekanik Kongresi*, Mustafa Kemal Üniversity, September 12-16, Antakya, Turkey.

Ozdemir, O., and Kaya, M. O., 2005e:Askıda Kalma Durumundaki Menteşesiz Bir Helikopter Palinin Kanat Çırpma-Gecikme-Burulma Dinamiğinin İncelenmesi, *XIV. Ulusal Mekanik Kongresi*, Mustafa Kemal Üniversity, September 12-16, Antakya, Turkey.

Kaya, M. O., and **Ozdemir, O.**, 2005a: Flexural-Torsional Coupled Vibration Analysis of A Thin-Walled Closed Section Composite Timoshenko Beam by Using The Differential Transform Method, *The Seventh International Conference on Vibration Problems (ICOVP-2005),* Isik University, September 5-9, 2005, Istanbul, Turkey.

Kaya, M. O., and **Ozdemir, O**, 2005b: Flutter and Vibration of A Hingeless Helicopter Blade in Hover, *3rd Ankara International Aerospace Conference*, Middle East University, August 22-25, Ankara, Turkey.

Ozdemir, O., and Kaya, M. O**.,** 2006a: Flapwise bending vibration analysis of a rotating tapered cantilevered Bernoulli-Euler beam by Differential Transform Method, *Journal of Sound and Vibration*, 289 (1-2), 413-420.

Ozdemir O., and Kaya, M. O**.,**2006b: Flexural vibration analysis of double tapered rotating Euler-Bernoulli Beam by using the Differential Transform Method, *Meccanica*, 41 (6), 661-670.

Ozdemir Ozgumus O., and Kaya, M. O**.,** 2006c:Bir Helicopter Palinin Dinamik ve Aeroelastik Analizi, *I. Ulusal Havacılık ve Uzay Konferansı*, Middle East University, September, 21-23, 2006, Ankara, Turkey.

Kaya, M. O**.,** and **Ozdemir Ozgumus O.,** 2006a:Menteşesiz Bir Rotor Sisteminde Yer Alan Önburulmalı Elastik Palin Kanat Çırpma-Gecikme-Yunuslama Hareketlerinin Aeroelastik İncelemesi, *Kayseri VI. Havacılık Sempozyumu*, May 12-14, 2006, Nevşehir, Turkey.

Kaya, M. O**.,** and **Ozdemir Ozgumus O.,** 2006b:İki Düzlemde Doğrusal Daralan ve Eğilme-Burulma Etkileşimli Timoshenko Kirişinin Titreşim İncelemesi, *Kayseri VI. Havacılık Sempozyumu*, May 12-14, 2006, Nevşehir, Turkey.

Ozdemir Ozgumus O., and Kaya, M. O**.,** 2007a: Formulation for flutter and vibration analysis of a hingeless helicopter blade in hover: Part I, *Aircraft Engineering and Aerospace Technology: An International Journal*, 79 (2), 177–183.

Ozdemir Ozgumus O., and Kaya M. O**.**

Ozdemir Ozgumus O. and Kaya M.O**.,** 2007c:Energy expressions and free vibration analysis of a rotating double tapered Timoshenko beam featuring bending–torsion coupling, *International Journal of Engineering Science*, 45(2-8), 562-586.

Ozdemir Ozgumus O. and Kaya M.O**.,** 2007d: Flexural–Torsional Coupled Vibration Analysis of A Rotating Closed Section Composite Timoshenko Beam by Using DTM, *4th Ankara International Aerospace Conference*, Middle East University, September 10-12, 2007, Ankara, Turkey.

Kaya, M. O. and**Ozdemir Ozgumus O.,** 2007, Flexural–torsional coupled vibration analysis of axially loaded closed section composite Timoshenko beam by using DTM, *Journal of Sound and Vibration*, 306 (3-5), 495-506.

Durmaz, S., **Ozdemir Ozgumus O.** and Kaya M.O**.,** 2007: Aeroelastic Analysis of A Tapered Aircraft Wing, *4th Ankara International Aerospace Conference*, Middle East University, September 10-12, 2007, Ankara, Turkey.

Ozdemir Ozgumus O., and Kaya, M. O., 2008, Flapwise bending vibration analysis of a rotating double tapered Timoshenko beam, *Archive of Applied Mechanics*, 78, 379–392.

Durmaz, S., **Ozdemir Ozgumus O.,** Ozuncer, A.D.,and Kaya M.O**.,** 2008: Sesaltı Bir Kanadın P-K Metodu ile Flutter Analizi, *Kayseri VII. Havacılık Sempozyumu*, Erciyes University, May 15-16, 2008, Kayseri, Turkey.

Oktay, T.,**Ozdemir Ozgumus O.** and Kaya M.O**.,** 2008: Dönen ve Daralan Euler-Bernoulli Kirişinin Titretim Kontrolü, *II. Ulusal Havacılık ve Uzay Konferansı*, Istanbul Technical University, October 15-17, 2008, Istanbul, Turkey.

Ozdemir Ozgumus O. and Kaya M.O**.,** 2009: Tailoring and Active Damping of Piezo-Laminated Composite Rotor Blades by Using DTM, *International Forum On Aeroelasticity and Structural Dynamics (IFASD 2009)*, June 21-25, 2009, Seattle, USA.

Ozdemir Ozgumus O. and Kaya M.O**.,** 2010, Vibration analysis of a rotating tapered Timoshenko beam using DTM,*Meccanica*, 45, 33–42

Kaya, M. O. and**Ozdemir Ozgumus O.,** 2010, Energy expressions and free vibration analysis of a rotating uniform Timoshenko beam featuring bending-torsion coupling, *Journal of Vibration and Control*, 16 (6), 915-934.

Durmaz, S., **Ozdemir Ozgumus O.,** and Kaya M.O**.,** 2010a: Finite Element Analysis of A Thin Walled Composite Wing by Including Warping Effects, *Proceedings of ASME International Mechanical Engineering Congress and Exposition*, November 12-18, 2010, Vancouver, British Columbia.

Durmaz, S., **Ozdemir Ozgumus O.,** and Kaya M.O**.,** 2010b:İnce Cidarlı Kompozit Bir Kirişin Statik ve Dinamik Cevabı, *III.Havacılık ve Uzay Konferansı*, Anadolu University, September 16-18, Eskişehir, Turkey.

Ozdemir Ozgumus O., Durmaz, S.,and Kaya M.O**.,** 2010:Dönen Kompozit Timoshenko Kirişin Titreşim Analizi, *III.Havacılık ve Uzay Konferansı*, Anadolu University, September 16-18, Eskişehir, Turkey.

Ozdemir Ozgumus O.ve Kaya M.O., 2011:Energy Derivation and Extension-Flapwise Bending Vibration Analysis of A Rotating Piezolaminated Composite Timoshenko Beam, *Recent Advances in Space Technologies (RAST'2011)*, June 9-11, Istanbul, Turkey.

Ozdemir Ozgumus O., Durmaz, S.,and Kaya M.O**.,** 2011:Flutter Analysis of Goland Wing, *International Forum On Aeroelasticity and Structural Dynamics (IFASD 2011)*, June 26-30, 2011, Paris, France.

Ozdemir Ozgumus O. and Kaya M.O**.,** 2012a, Energy expressions and free vibration analysis of a rotating Timoshenko beam featuring bending bending torsion coupling, *Archive of Applied Mechanics*, in publication process.

Ozdemir Ozgumus O. and Kaya M.O**.,** 2012b, Energy derivation and extension-flapwise bending vibration analysis of a rotating piezolaminated composite Timoshenko beam, *Mechanics of Advanced Materials and Structures*, in publication process.

Ozdemir Ozgumus O. and Kaya M.O., 2012c: Vibration Analysis of A Smart Helicopter Blade with Piezoelectric Actuated Trailing Edge Flaps, *AIAA 53rd Structures, Structural Dynamics, and Materials and Co-located Conferences*, April 23-27, 2012, Honolulu, Hawaii.